POLITECNICO
MILANO 1863

Dipartimento di Chimica, Materiali e Ingegneria Chimica "G. Natta"
Doctoral Programme In Industrial Chemistry and Chemical Engineering

A Kinetic Model of Thermochemical Conversion of Biomass

Doctoral Dissertation of:
Paulo Eduardo Amaral DEBIAGI 822440

Supervisor
Prof. Tiziano FARAVELLI

Tutor
Prof. Andrea MELE

The Chair of the Doctoral Program
Prof. Alessio FRASSOLDATI

2018

To the superior spirituality.

To my Family.

To my partner in life.

“It is during our darkest moments that

we must focus to see the light.”

Aristotle

Acknowledgements

In the first place, my sincere gratitude to the spirituality and my spiritual guides. I am sure that this work would have never become truth, without their guidance and enlightenment.

I would like to express my sincere acknowledgements to:

All the members of CRECK modeling group, for the warm welcoming and continuous support. In special, Professor Tiziano Faravelli for accepting to be my Ph.D. supervisor, for always being present with great ideas, for pushing the edges and providing solid support during the development of this work. Professor Eliseo Ranzi, who spent much of his time teaching me the essence of his knowledge and being a great mentor and friend. For Professors Alessio Frassoldati and Alberto Cuoci, and for Giancarlo Gentile, Matteo Pelucchi, Alessandro Stagni and Mattia Bissoli who were present when I first arrived and provided me pleasurable talks and ideas about work and life. Professors Stephen Dooley and Christian Hasse for accepting to be part of the evaluating board of this thesis, contributing with many important comments and ideas.

Politecnico di Milano, for providing a great scientific environment and the access to the tools required for this work. CAPES foundation, for providing the financial support for the development of this work. The friends I met during these years in Milan, who made my stay much more pleasurable and enriching. My first mentor in science, Professor Regildo Marcio Gonçalves da Silva, for his support and friendship.

My partner in life, Francyelle Tostes, for being by my side and giving me support and love in the darkest moments. For believing in me when I could not. For persisting that I can always become a better person. For awakening the real feeling of pure love inside of me. For providing me so many precious lessons and unforgettable moments, that I will carry for all my life. For being this special human being that destiny made me encounter.

Finally, the acknowledgements to my family. My parents, for being always present and available during my whole life, for allowing and encouraging me to grow up and to be independent. For raising me and providing limitless love and care. For showing me the value of education. My sisters, for being supportive and kind when I most needed. For giving birth to my nephews, who provide me memorable moments of joy. My grandmother, the strongest person I ever met, who is my inspiration for resilience, persistence and peace.

All the people that I did not mentioned, but were part of this journey, my sincere thank you!

Publications

- Debiagi, P. E. A., C. Pecchi, G. Gentile, A. Frassoldati, A. Cuoci, T. Faravelli and E. Ranzi (2015). "Extractives extend the applicability of multistep kinetic scheme of biomass pyrolysis." Energy & Fuels 29(10): 6544-6555.
- Debiagi, P. E. A., G. Gentile, M. Pelucchi, A. Frassoldati, A. Cuoci, T. Faravelli and E. Ranzi (2016). "Detailed kinetic mechanism of gas-phase reactions of volatiles released from biomass pyrolysis." Biomass and Bioenergy 93: 60-71.
- Gentile, G., P. E. Debiagi, A. Cuoci, A. Frassoldati, T. Faravelli and E. Ranzi (2016). "A CFD Model for Biomass Flame-Combustion Analysis." Chemical Engineering Transactions 50.
- Gentile, G., P. E. A. Debiagi, A. Cuoci, A. Frassoldati, E. Ranzi and T. Faravelli (2017). "A computational framework for the pyrolysis of anisotropic biomass particles." Chemical Engineering Journal 321: 458-473.
- Ranzi, E., P. E. A. Debiagi and A. Frassoldati (2017). "Mathematical modeling of fast biomass pyrolysis and bio-oil formation. Note I: Kinetic mechanism of biomass pyrolysis." ACS Sustainable Chemistry & Engineering 5(4): 2867-2881.
- Ranzi, E., P. E. A. Debiagi and A. Frassoldati (2017). "Mathematical Modeling of Fast Biomass Pyrolysis and Bio-Oil Formation. Note II: Secondary Gas-Phase Reactions and Bio-Oil Formation." ACS Sustainable Chemistry & Engineering 5(4): 2882-2896.
- Debiagi, P. E. A., M. Trinchera, A. Frassoldati, T. Faravelli and E. Ranzi (2017). Third Generation Biomass. Classification and Characterization of Algae Fuels. 40th Meeting of the Italian Section of the Combustion Institute. Rome.
- Debiagi, P. E. A., M. Trinchera, A. Frassoldati, T. Faravelli, R. Vinu and E. Ranzi (2017). "Algae characterization and multistep pyrolysis mechanism." Journal of Analytical and Applied Pyrolysis 128: 423-436.
- Debiagi, P. E. A., G. Gentile, A. Cuoci, A. Frassoldati, T. Faravelli and E. Ranzi (2018). "Yield, Composition and Active Surface Area of Char from Biomass Pyrolysis." Chemical Engineering Transactions 65.
- Debiagi, P. E. A., G. Gentile, A. Cuoci, A. Frassoldati, E. Ranzi and T. Faravelli (2018). "A predictive model of biochar formation and characterization." Journal of Analytical and Applied Pyrolysis. (Accepted - In press).

Participation in Events

- Joint Meeting – French and Italian sections of the combustion institute. Pisa, April 23-24, 2014.
- IConBM – Second international conference on biomass. Italy, June 19-22, 2016. Work presented: A CFD Model for Biomass Flame-Combustion Analysis.
- 40th Meeting Italian Section of the Combustion Institute, Rome – Italy. May-2017. Work presented: Third Generation Biomass. Classification and Characterization of Algae Fuels.
- 3rd General Meeting and Workshop on SECs in Industry of SMARTCATs Action. Work presented: Update and Validation of Hemicellulose Pyrolysis Kinetic Mechanism
- Gas-phase Reaction Kinetics of Biofuels Oxygenated Molecules. Milan, April 23-24, 2018.
- Doktorandenkolloquium OxyFlame project. WSA RWTH Aachen – Germany. 06 June 2018. Work Presented: A general model for the thermochemical conversion of biomass.
- IConBM – Third international conference on biomass. Italy, June 17-20, 2018. Work presented: Yield, Composition and Active Surface Area of Char from Biomass Pyrolysis.

ABSTRACT

Biomass is promising as renewable resource, comprising a broad range of different types of biomaterials, such as wood, forest and agricultural residues, waste from wood and food industry, algae, energy grasses, straw, bagasse and sewage sludge. These materials are widely available and many of them are residues from different economic activities, generating costs for disposal and sometimes even environmental issues. Harvesting these materials is a possible solution for substitution of fossil fuels and treatment of residues.

The thermochemical route of biomass conversion is promising. By providing heat to the feedstock, it releases its volatile matter giving multiple products, depending on the feedstock and the operating conditions. The yield of these products can be enhanced by selecting the proper technologies. This conversion path is a very complex multicomponent, multiphase, and multiscale problem. Because of its complexity, modeling this process is still a challenge, but consists an essential step to better understand the aspects involved and provide tools to the design of optimized reactors and processes.

A predictive and comprehensive model for both characterization and chemical kinetics of biomass thermochemical conversion was developed. The workflow consists on: Collection of literature experimental data, characterization of feedstocks, kinetic mechanisms that describe each step of the process, validation of the simulations with the collected experimental data.

The model proposes some innovative and interesting features:

- Comprehensiveness – Can be applied for a wide range of feedstock composition, covering both lignocellulosic and algae biomass;
- Flexibility – Can be further improved in order to account for new experimental evidences;
- Predictivity – The models were developed and validated for many feedstocks in several different conditions. In this way, no experimental data is needed to perform the simulations. All the information needed are the characteristics of your feedstock and the operating conditions. When experimental data is available, the user can choose whether to use it or rely on the model predictions;
- Compatibility of Kinetic Mechanisms– A combination of semi-detailed and detailed kinetic mechanisms are present for the different facets of the problem.

They are proposed in a CHEMKIN-like format, which make them compatible with each other;

- Species – The reference components and the products released are defined with a combination of real and lumped species;
- Computational cost – As a result of the simplification degree adopted in this model, it is efficient for more complex simulations, involving particle and reactor scales. Despite these simplifications, the model generates a great level of details.

The validation of large amounts of experimental data shows the robustness of the model. It remains flexible to include new experimental evidences and to be extrapolated when required. It was not found in literature another model that covers all these steps of biomass thermochemical conversion in a single formulation, being able to simulate the majority of processes currently available. The model is a useful tool to the development of optimized reactor designs for improving industrial processes efficiency. Besides providing reliable predictions in many cases, uncertainties still exist due to the level of simplification adopted in the selection of reference species and the definition of the reactions. The model could be further improved in the future by considering the catalytic effect of each metal present in the ashes, the intra-component interactions, the effect of the polymerization and branching degrees, among others.

Contents **Page**

List of Tables

List of Figures

CHAPTER 1

INTRODUCTION

1. Mankind, Biomass, Energy and Materials

The development of human life into the modern society we live today was aided by technological improvements along the time span of our species existence. At first, primitive human being developed tools for aiding daily tasks for life support, such as hunting and defending from predators. The technological achievements were always useful for a period of time, until a better technology overcome the previous, including the discovery of new materials and methods of production. Using energy for supporting human activities started with the discovery of fire, but it took a long time from its discovery to its mastery. According to Gowlett [1], interaction with fire occurred in three steps, evolving from passive to active use: fire foraging for resources across landscapes; social/domestic hearth fire, for protection and cooking; and fire used as tool in technological process, such as pottery and metallurgy. When mankind mastered the technics of starting and manipulating fire, there was a revolution on the way to produce, manage and consume food, equipment, protection, hunting and other activities, and an expansion of environments that humans could survive took place [1]. Fire provided means of modifying and greatly extending the range of

properties available in materials themselves [2]. From the beginning, biomass was the main source of fuel to generate heat by combustion, until mankind discovered other sources [3].

Human activities also evolved supported by the sources of power available to perform daily tasks. An important concept in this discussion is “prime mover”, which consist of any tool/mechanism that can convert a prime form of energy into mechanical power [4]. Figure 1 schematically shows different sources used by man to power the prime movers. Chronologically, mechanical power was produced by human power, then by animal power, followed by water and wind flows (sails, waterwheels and windmills). Up to this moment, fire was used to generate heat and the prime movers to generate mechanical power. A revolution started when mankind learned how to transform heat into mechanical power, through the invention of steam engines, which could be powered by mostly any fuel, despite the low efficiency of about 0.5% of chemical energy conversion in the early 18^{th} century [4]. This was a great technological achievement, as fuels could be stored and used on demand, differently than relying on weather conditions for wind and seasons for water flows. Further developments on steam engines significantly increased efficiency, using higher pressure regimes and separate condensers, allowing the application in trains and ships, which lead to affordable and regular intercontinental freight and passengers transport [4]. Later, internal combustion engines were invented, which have significantly improved power conversion efficiency and reduced the equipment size, due to skipping the steam generation step. However, most of the efficiency improvements were attained by making the machines progressively more specific in terms of operating conditions and fuel. The range of possible fuels to be used was shrank, massively driving the economy to liquid and gas fossil fuels systems. Efficiency in these modern engines and turbines reach about 40% conversion efficiency [4].

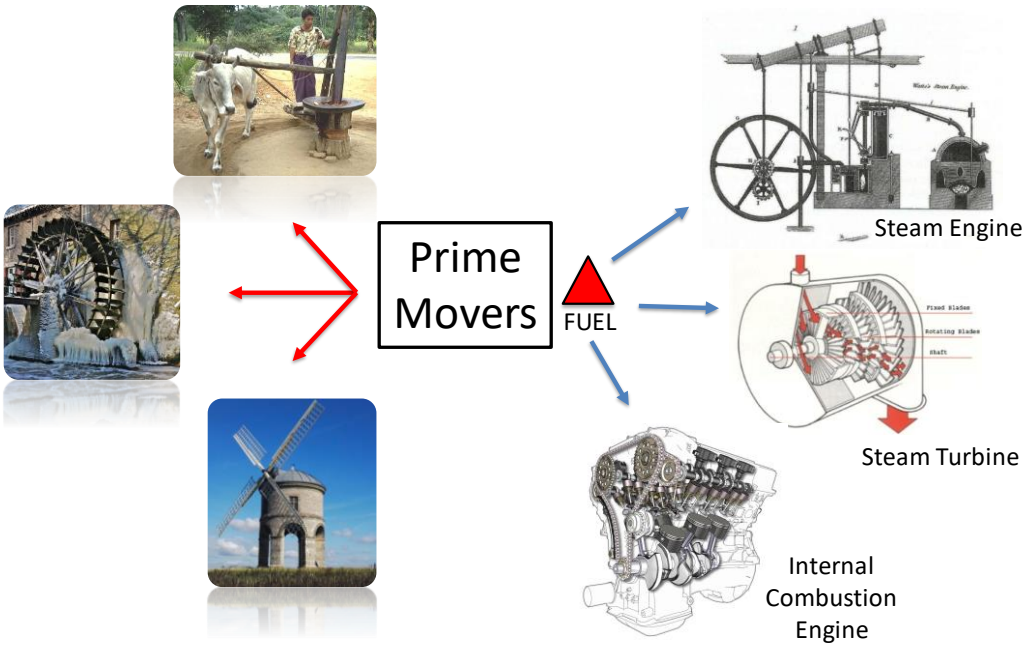

Figure 1 - Sources of power used by man on prime movers

Not only energy, but also the access to materials was determining to mankind evolution. Early human beings used to build with the available and ready-to-use materials such as stones, wood, bones and fibers [2]. With increasing capacity of manipulating materials and energy, refined materials such as bricks, metals, glass and plastics could be made. Nowadays, materials science not only try to increase size and speed of production and reduce costs, but also can design specific materials for each purpose [2]. Most of the materials and tools produced nowadays use petroleum-derivate compounds at some degree, either in its composition or in the production process, that it becomes very hard to imagine our current society without petroleum reserves. The greatest concern regarding using petrol as both fuel and raw material is that once used as fuel, it cannot be recycled. The USA, for example, transform about 97% of crude petroleum to produce a variety of fuels, while only 3% is used as petrochemical feedstock, lubricants and waxes [5]. With our current technology, there is no affordable option to fully substitute crude petroleum as feedstock for materials. Despite the issue on costs of production, it is already possible to obtain similar molecules from biomass. However, crude oil transformation into fuels and chemicals is still much easier for several reasons including the infrastructure present, the transportation of the raw material and its chemical properties.

Looking back into human history, it becomes clear that in order to put aside one technology, a better one must be able to substitute. Taking a step back and resume the

exploration of renewable resources is necessary for the sustainable development of our society and economy. However, this time we must put our efforts into developing technologies to transform renewable materials into compounds that can fit and substitute non-renewable materials, and perhaps that can even work in a better way. Not only as a challenge to our capability of improving technologies, substituting fossil fuels is also a required task to keep our civilization in this level of development.

2. World Energy Scenario

As energy plays a key role in most of our daily tasks and in the development of our economy [6], the combination of global population growth and constant rising in living standards is significantly impacting the worldwide demand for energy and materials over the last several decades [7]. The extensive exploration of fossil fuels in the last century provided the necessary boost for this worldwide development. However, we have reached a point that fossil fuel reserves are shortening and the atmospheric pollution is rising to critical levels in several countries. As a result of the combustion process, fuels introduce CO_2 to the atmosphere, which is the major responsible for greenhouse effect. This effect actually is necessary to maintain life conditions on earth, by reflecting partially the infrared waves emitted from earth. However, this increase in atmospheric CO_2 concentration is breaking the balance and rising the global temperatures. Moreover, not only greenhouse gases are emitted from fossil fuel combustion, several other pollutants like soot, partially unburned fuels, carbon monoxide, SO_x and NO_x compounds are also emmited. These pollutants are responsible for acid rain, smog effect and increasing number of respiratory problems mainly in metropolitan areas.

The International Energy Agency (IEA) recently released the report “Key world energy statistics - 2017” [8], which reports interesting numbers of the global energy scenario. Some important data was extracted from this report and is shown in Table 1. Figure 2 shows the area plots of different fuels distribution in the world energy matrix of 1973 and 2015. The plot divides fuels in oil, coal, natural gas, nuclear, hydroelectricity, biofuels and waste, and the remaining sources are grouped in others, accounting for geothermal, solar, wind and tide/wave/ocean.

Fuel			1973		2015		Growth (%)		2040 (EIA)	
			Mtoe	%	Mtoe	%	In capacity	In share	Mtoe	%
Fossil	Non-Renewable	Oil	2819	46.2	4326	31.7	53.5	-31.4	5670	30.0
		Coal	1495	24.5	3835	28.1	156.6	14.7	4032	21.3
		Natural Gas	976	16	2948	21.6	202.0	35.0	4662	24.7
Non-Fossil		Nuclear	55	0.9	669	4.9	1117.8	444.4	1134	6.0
	Renewable	Hydro	110	1.8	341	2.5	210.7	38.9		
		Biofuels & Waste	641	10.5	1324	9.7	106.6	-7.6	3402	18.0
		Other	6	0.1	205	1.5	3255.3	1400.0		
Total			6101	100	13647	100	123.7	-	18900	100

Table 1 – World energy scenario in 1973 and 2015. Global capacity by energy source and their share on the global energy matrix

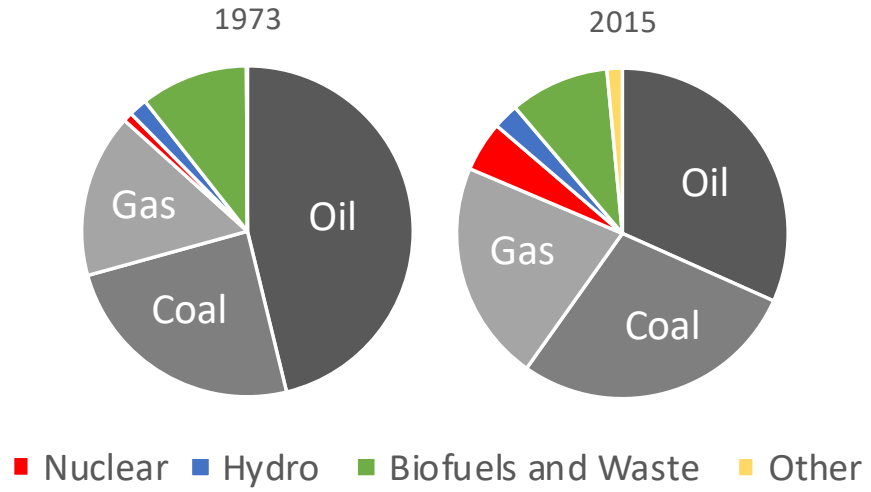

Figure 2 – Percentual share of fuels in the world energy matrix (1973 – 2015)

By grouping the fuels in just two categories (Figure 3) we can say that, global energy matrix in 2015 was majorly composed by fossil fuels, with only 18.6% contribution of non-fossil fuels. If we sort these fuels by their renewability, we have an overwhelming 86.3% share of non-renewable fuels in the matrix.

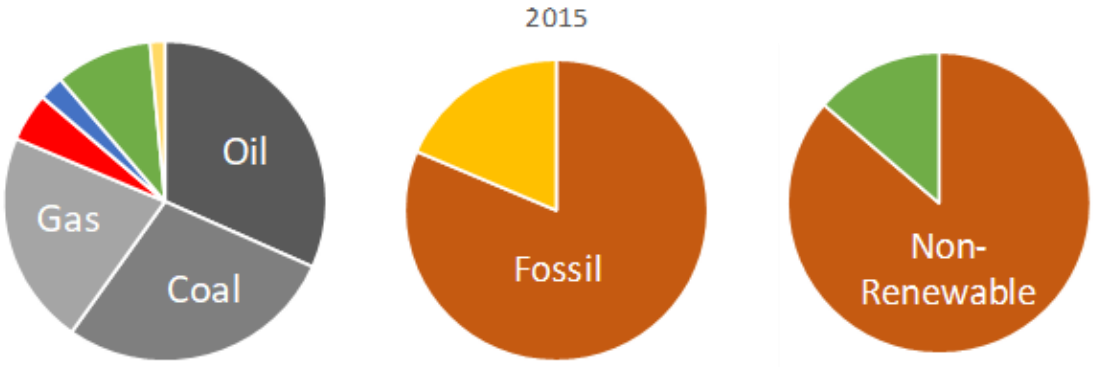

Figure 3 – World energy scenario (2015), comparison of different grouping of the fuels by their characteristics

From 1973 to 2015, the world total primary energy consumption more than doubled, increasing from 6101 to 13647 Million Tons of Oil Equivalent (Mtoe) (Figure 4). This growth in demand was supported by increasing energy production by all means, but they have increased in different rates. The bar plots in

Figure 5 reports the growth of each category, comparing with the global growth. In terms of share growth in the matrix, hydroelectricity increased by 40%, nuclear power by 5.5 times, and geothermal, solar, wind, tide/wave/ocean significantly increased 15 times. In terms of capacity growth, these numbers become even more interesting: Biofuels and waste production doubled, hydroelectricity tripled, nuclear power increased 12 times, and together geothermal, solar, wind, tide/wave/ocean energy production increased by remarkable 33.5 times. This means that many efforts were done and new technologies are rising and they are being progressively refined, allowing this energy resources to fulfill a significant share of the global energy demand. Besides being the largest producer of electricity from coal in 2015 (4109 TWh), China has shown remarkable achievements in production of renewable energy from all means (1398 TWh), generating more than twice the USA production (the second place). China alone consumes about 22% of the world energy demand. Together with the USA, they reach about 40% of the world energy demand.

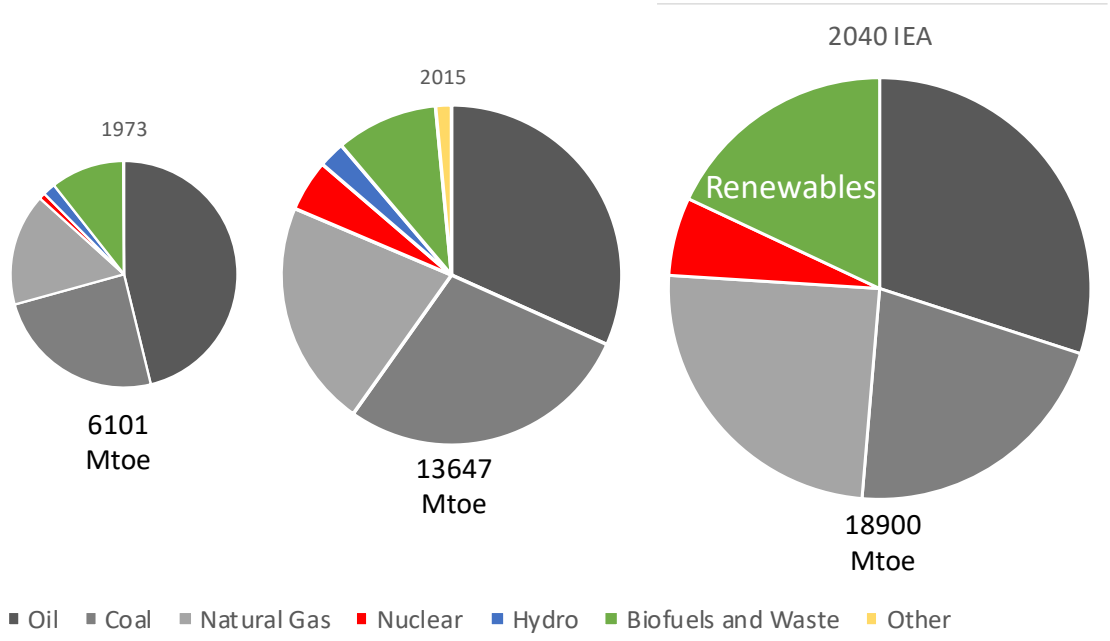

Figure 4 - Absolute share of fuels in the world energy matrix (1973 – 2015 – 2040 (IEA projection))

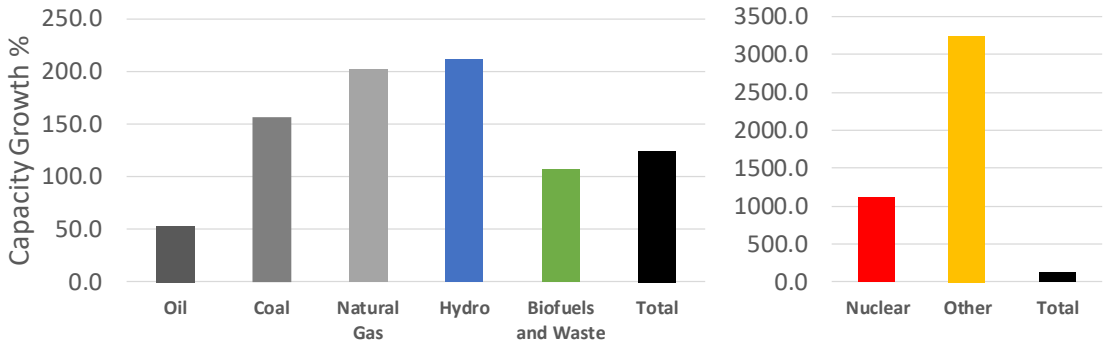

Figure 5 - Growth of absolute fuels demand from 1973 to 2015

The energy demand for the next 20 years was projected by the US Energy Information Administration (EIA) in the International Energy Outlook 2017 (IEO2017) [9], and an increase of about 30% is expected, as shown in Figure 4. The projection reports that renewables will be have the largest capacity growth, followed by natural gas, petroleum and nuclear, while coal consumption should stop increasing and remain almost constant. As the energy demand increase, CO_2 emissions tends to follow the trend.

When compared to 1971, the global emissions of CO_2 doubled, and the most significant increase came from intense use of coal (as seen in Figure 6) in the industrialization of Asiatic countries (as seen in Figure 7). The Organization for Economic Co-operation and Development (OECD) is an intergovernmental economic organization with 37 member countries, founded in 1961 to stimulate economic progress and world trade. Most of the

OECD members are high-income economies with a very high Human Development Index (HDI) and are regarded as developed countries. Because of their developed economy, it is expected to observe higher energy demands from countries that are part of this group. On the other hand, their growth rate in terms of energy demand is not elevated, as they are already highly industrialized. The non-OECD countries, highlighted in Figure 7, show that the non-members of the OECD had largest increase in energy demand, mostly in Asia and Africa.

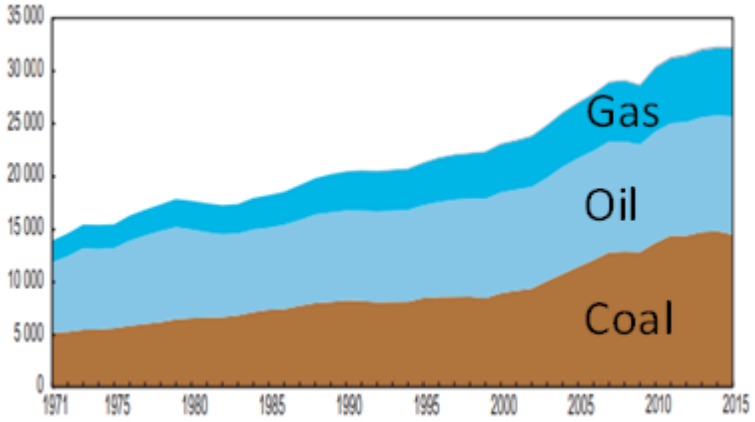

Figure 6 - World CO_2 emissions by fuel combustion from 1971 to 2015 (Mt of CO_2) (after [8])

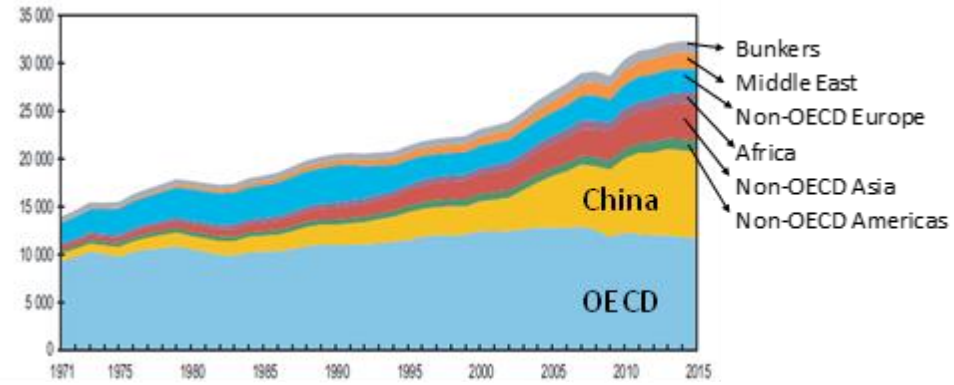

Figure 7 - World CO2 emissions by regions from 1971 to 2015 (Mt of CO2) (after (IEA 2017))

This increase in emissions are causing global climatic effects which are being discussed internationally since 1988 in the Toronto Conference on the Changing Atmosphere, followed by a series of global meetings and discussions, finally culminating in a formal international commitment for reduction of greenhouse gases emissions with the Kyoto protocol. This commitment expired in 2012 and it is being a hard task to meet a new global agreement for climate purposes. The reason is clear, the development of national economies relies on more energy production and consequently, more greenhouse gasses emissions. Countries with a more developed environment consciousness are putting more efforts into

developing new technologies and putting barriers to the expansion of fossil fuels. Moreover, countries with a more developed economy can afford to invest in science and technology, and also to set political barriers to the exploration of non-renewable fuels. This is a critical point for economies in development, which cannot afford to invest and rely only on full developed technology imported, that already has a degree of economical attractiveness.

From the information observed in these reports, it becomes clear that the energy profile around the world and along the past decades is very dynamic. Some interesting facts were reported by the World Energy Council, in the "World Energy Trilemma Index - 2017"[10], where they evaluate and rank countries in base of three indicators: energy security, energy equity and environmental sustainability. Except for New Zealand and the USA (9th and 15th rank), the other top 15 ranked countries in the index are European. This is a result of commitments and policies that push the exploration of alternative resources and development of new technologies, which enhances the diversification of the energetic matrix of the country. These policies reduce the need of non-renewable resources and the dependency of importation from foreign countries, paving the way to self-sustainability in energy production. In other words, transiting from an oil-based economy to a multi-resources economy is not only cleaner but safer, as it protects against reserve shortages and price wars, also promotes the development of local economies.

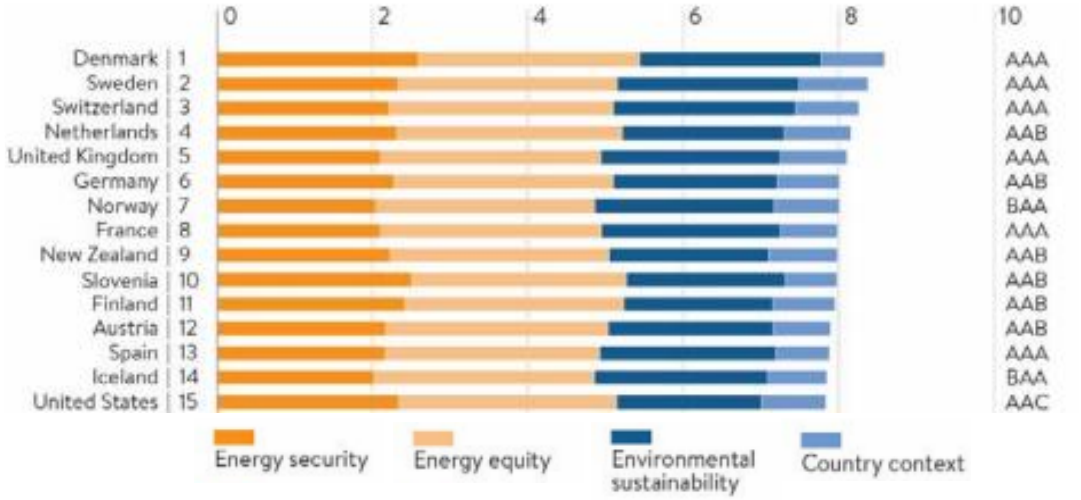

Figure 8 – Top 15 ranked countries by the World Energy Council, in the "World Energy Trilemma Index - 2017"[10].

Furthermore, the British Petroleum recently released an updated report of the global energy status, the "BP Statistical Review of World Energy - June 2017" [11]. Agreeing to the IEA and WEC reports, and adding some interesting facts, Figure 9 clearly shows that besides

a global increase in energy demand, each region of the world has particularities on their energy matrix. The availability of natural resources in a territory drives the selection of means to produce energy. For example, the large reserves in Russia provides natural gas with attractive prices for European countries, which are short on fossil fuel resources. Nevertheless, relying only on importation is not safe, and the economical position of Europe allows the promotion of nuclear and renewables to provide a bigger share of the demand. The European energy matrix is the most diversified and, therefore, the safest. Brazil is rich in water bodies which can constantly provide hydroelectricity, but the country is also rich in petrol reserves. Venezuela and Bolivia have vasts reserves of petrol and natural gas. These facts strongly impact the South and Central America matrix, which as almost absent in nuclear and coal energy production. Controversially, Asiatic countries strongly rely their energy production on coal (~50%), which is the cheapest and dirtiest fossil resource. The last decades boom in Asiatic industrialization pushed the intense exploration of this abundant local resource, mainly present in China and India.

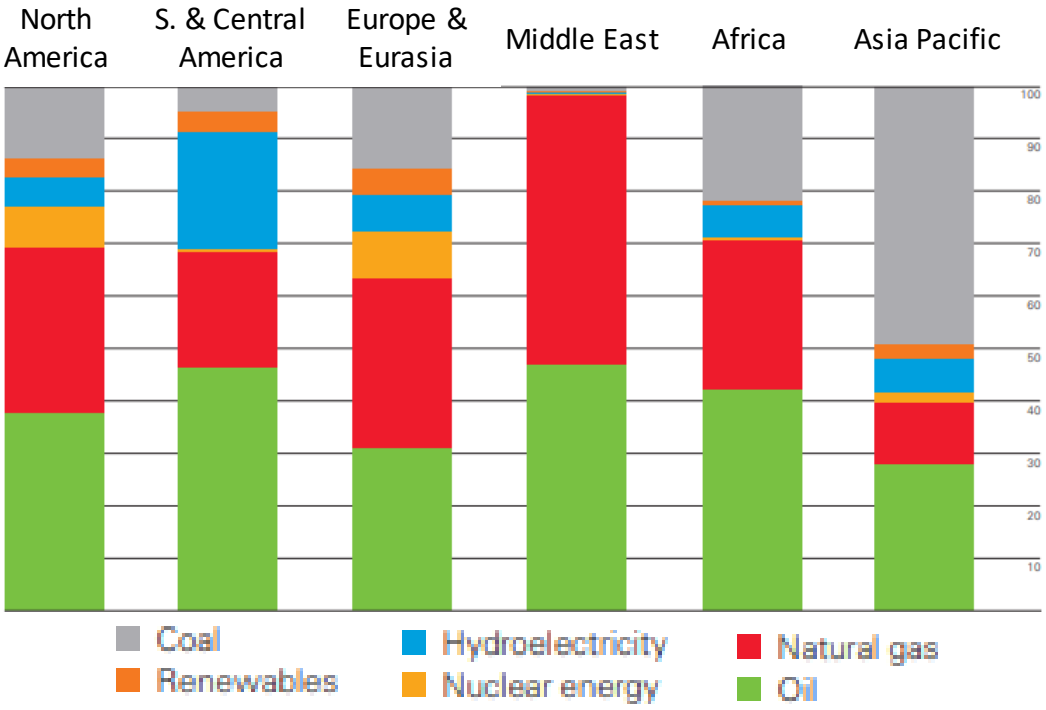

Figure 9 – 2016 energy matrix by world regions. Share of each fuel in total energy production.

Together, the shortening of fossil fuels reserves, the problems caused by its usage, and the constraints of having a highly dependent energy matrix are boosting the interests into the development of a renewable and sustainable economy. Most of the energy available in our planet is directly or indirectly coming from the sun. Exceptions are geothermal, nuclear

and partially tidal energies. Solar panels directly harvest the sunlight into electricity. The energy moving a wind turbine is the result of temperature gradients caused by earth's surface heating by the sun. Hydroelectricity harvests the potential gravitational energy of water bodies, which only exists due to the water cycle, result of the sun's energy. Fossil fuels are the result of transformation of ancient biomass into solid (coal), liquid (petrol) and gas (natural gas) fuels. However, this process takes millions of years and is much long compared to human life span, we must assume that they are non-renewable. On the other hand, biomass can provide energy and chemicals in a time scale that we can consider renewable in the lifespan of mankind.

3. Biomass as Renewable Source of Fuels and Materials

Biomass is another indirect form of solar energy resource, as plants grow by absorbing carbon dioxide from the atmosphere as well as water and nutrients from soils followed by converting them into hydrocarbons through photosynthesis, a process that consumes energy provided by sunlight.

All carbon contained in biomass is gained from carbon dioxide. Therefore, carbon is cycled in the atmosphere when biomass is consumed as a fuel, which makes biomass a carbon neutral fuel when it is burned. Controversies exist to assume that biomass is carbon neutral, as the processing is not perfect and losses and residues needs to be accounted. Nevertheless, biomass is far more neutral when compared to fossil fuels. When planning the transition to a renewable and sustainable economy, several technologies can be applied to solve the energy problem, but biomass also play several other essential roles. The exploration of biomass with advanced technology aids the solution of multiple problems: diversifies the energy matrix, provides raw material for the production of advanced materials, explore and treat industrial and municipal residues, promotes local economy.

Biomass resources are widely and quite fairly distributed on the Earth's surface, differently from fossil fuel reserves. It comprises a broad range of different types of biomaterials, such as wood, forest and agricultural residues, waste from pulp and food industry, algae, energy grasses, straw, bagasse, sewage sludge, municipal solid wastes, among others. The common aspect of all these materials is that they are result of biological metabolism, and that they can be produced in a short time spam (a few days up to a few years). However, these materials widely differ in their chemical composition and physical properties. Therefore, the use of different types of biomass results in different challenges

and solutions for transportation, storage, feeding, and finally for converting these raw materials into more useful chemicals and substitutes for fossil fuels [12, 13].

First generation biofuels, those derived from food crops, represent a temporary answer to the energetic problem. Countries like Brazil and the USA have remarkably developed the production of bioethanol from sugarcane and corn respectively, which substitutes gasoline with few engine modifications. Also Biodiesel production from oilseeds has been significant in Brazil and Europe. Great concern lies on the expansion of first generation biofuels production, as it impacts food availability and market prices. Substituting whole countries demand of gasoline and diesel with bioethanol and biodiesel would require vasts areas of agriculture destined to fuel production, if not causing further deforestation [14]. Nevertheless, these technologies are simple and well stablished, which promoted a first push into biofuels. On the other hand, second generation biofuels, also known as advanced biofuels are based on non-food crop biomaterials [15]. These biofuels require specific pre-treatments and application of high technology for production and replacement of fossil fuels in large scale [6, 15]. Third generation biofuels are derived from micro and macro algae. Modern biotechnology is capable of genetically modify algae allowing them to direct produce target molecules, such as alcohols and acids, which can be direct used as liquid fuels. Algae outcomes for their fast growth rate and elevated lipid production per land area occupied.

While first generation biofuels technology use fermentation to transform sugars into alcohols (bioethanol) and triglycerides in methyl/ethyl-esters (biodiesel), second generation biofuels rely on several different technologies to transform a wide range of raw materials into fuels and chemicals. Biochemical and thermochemical are the main routes for this transformation. The first uses microorganisms, enzymes and/or acid/alkali to break down the complex structure and separate the components, which is an interesting process for high moisture feedstock, as the process usually occurs in aqueous medium. Products are usually biogas (methane) and alcohols from fermentation. Figure 10 schematically shows the biomass conversion routes and the products obtained.

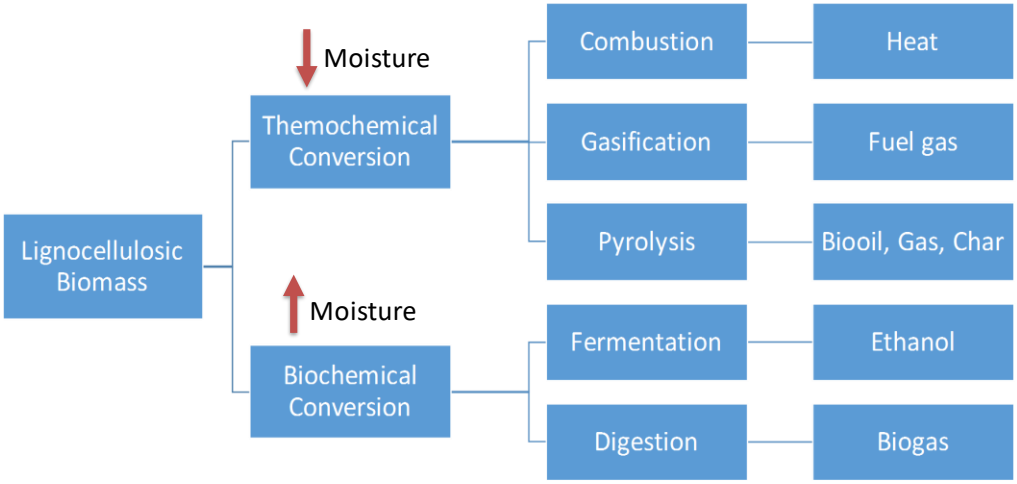

Figure 10 – Biomass conversion routes into fuels.

The thermochemical route uses heat to break down biomass structure. The main thermochemical transformations of biomass are pyrolysis, combustion, gasification, hydrothermal liquefaction and hydrothermal carbonization.

Pyrolysis is the thermal degradation of a material in the absence of an oxidizing agent. The process releases condensable and non-condensable volatiles (tar and light gases), together with a solid residue (biochar). Figure 11 shows a scheme of typical biomass pyrolysis process and the resulting products.

Tars condense when cooled down, forming the bio-oil, which can be used as substitute for crude petrol oil, directly employed for power and heat generation or even upgraded to liquid fuels for internal combustion engines [16, 17]. For this last purpose, reducing the oxygen content of bio-oil via catalytic hydrotreating/hydrogenation [18] or catalytic cracking [19] must be required to improve its heating value. The wide range of chemical components in the bio-oil supports its use in a biorefinery concept. Light gases can be directly used for heat and power generation in burners, turbines and internal combustion engines. Biochar can be employed as soil amendant, as a domestic cooking fuel instead of wood, upgraded to high-value activated carbon for cosmetic and pharmaceutical purposes, or used in the metallurgical industry instead of coal, among others [20]. Light gases can be used also in internal combustion engine.

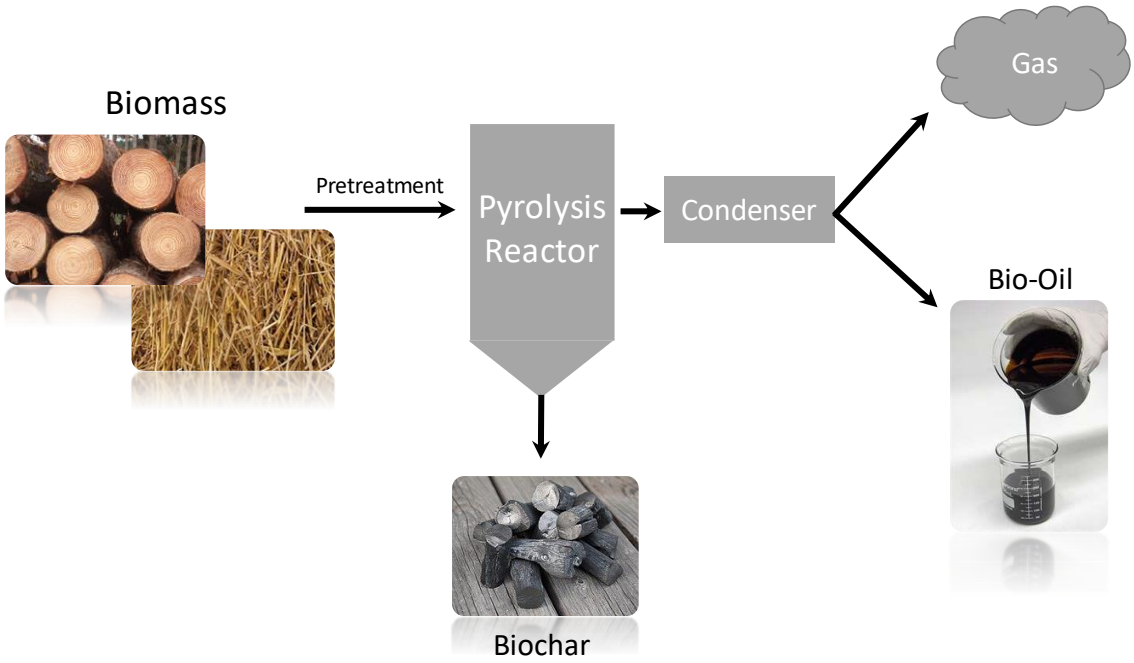

Figure 11 - Scheme of thermochemical conversion of biomass. Typical products obtained after pyrolysis.

Pyrolysis operating conditions can be adjusted to improve the yield of desired products. In this sense, torrefaction, slow pyrolysis, fast pyrolysis and flash pyrolysis are the possible variations to this process. Torrefaction is a pyrolysis performed at low temperatures (180-300°C) for long residence times, improving some properties of the material such as grindability, hydrophobicity, heating value, and reduce biological activity. In this process, the main components partially decompose and re-polymerize, releasing some oxygen-rich functional groups. This process starts to form the typical polyaromatic char structures, while the solid loses about 20% of initial mass. Slow pyrolysis (300-400°C) is typically used with large particle sizes for biochar production, with hours of residence time and slow heating rates, allowing also cross-reticulation and tar repolymerization. Fast pyrolysis (400-600°C) aims the production of liquids by using temperatures and residence times adequate for devolatilization, but not for tar cracking. Flash pyrolysis (above 600°C) uses small particle sized and very high heating rates to force the conversion into gases by promoting complete devolatilization and tar cracking.

Gasification is the thermal degradation of biomass in the presence of an oxidizing agent (Air, pure oxygen, steam or CO_2). The material is partially oxidized generating a mixture of gases (producers gas), mainly composed by CO, CO_2, H_2O, CH_4, H_2, N_2 (when air is used), together with reduced amounts of tars, char and ashes. The aim of this process is increasing

significantly the yield of gases, in comparison to the pyrolysis alone. This mixture of gases, also called producers gas, can be used for the same purposes as the light gases from pyrolysis, but can also be employed to make liquid fuels through Fischer-Tropsch synthesis [21-23].

Combustion is the complete oxidation of the feedstock, producing mainly CO_2 and H_2O, together with minor amounts of secondary combustion sub-products. This process does not consist in a fuel conversion technology, it is a heat/electrical energy generation process.

The hydrothermal liquefaction is a process that direct liquefies organic matter suspended in an aqueous medium, without the drying step. Temperatures at 250-400°C and high pressure (up to 200 bar) promotes this transformation method [24]. Hydrothermal carbonization uses similar technology, but at lower temperatures (180-250°C) and longer residence times, promoting the formation of higher solid yields.

Figure 12 shows schematically the typical distribution of products from different thermochemical conversion processes of biomass. In addition, Table 2 reports these processes and the characteristic residence times of volatiles and solids

Mode	Temperature [°C]	Residence time volatiles	solid	Product Yields (wt.%) Liquid	solid	gas
Fast Pyrolysis	500	1-2 s		75	12	13
Intermediate Pyrolysis	500	5-30 s		50	25	25
Slow (Carbonization)	400	hours-days	hours	30	35	35
Torrefaction	280		10-60 min	0	80	20
Gasification	750-900	1-5 s		3	1	95

Table 2 - Biomass pyrolysis, torrefaction, and gasification processes [13]

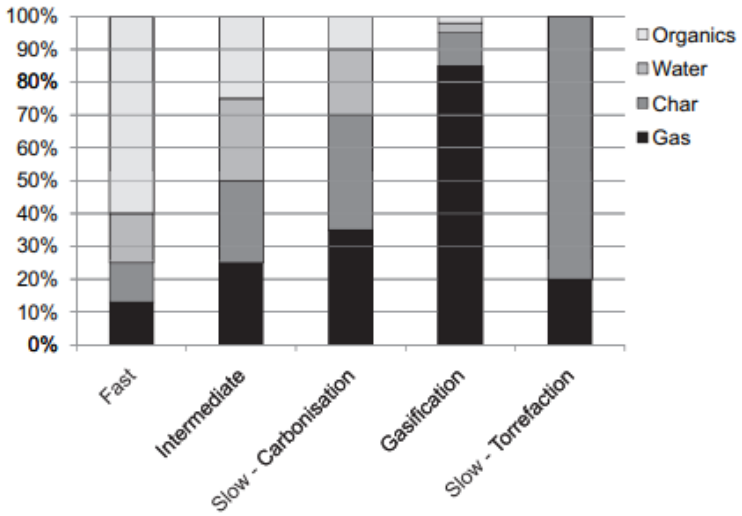

Figure 12 – Typical product spectrum from thermochemical conversion processes (After Bridgwater [13])

These thermochemical processes can be used also as a complementary method for residue treatment from other industrial activities. These residues could either be costly to dispose or even cause environmental issues. The non-convertible compounds in a biochemical conversion leave residues, such as bagasse from sugarcane. Pulp industry and food processing produce large amounts of organic residues (e.g. black liquor, soybean/olive cake). Solid municipal waste and sewage sludge are daily produced in large amounts and represent a big problem for metropolitan areas. Cattle and poultry manure is produced in rural areas and release CH_4, which is much more hazardous than CO_2. All these residues can be treated through thermochemical conversion, solving the problem of waste dumping and creating additional value to the whole process.

Thermochemical conversion of biomass open paths to very promising technologies, not only for remediation of immediate problems but to find long term solutions for human activities. Much information was already acquired in the past decades, but many efforts are still required to build knowledge and develop efficient and affordable technologies. In the next section, a brief review of the state-of-the-art both on experimental activities and modeling will be reported.

4. State-of-the-Art of thermochemical conversion of biomass

4.1. The Multi-Complexities of the Problem

Fully understanding of the thermochemical conversion of biomass is very challenging as its complexity occurs at several levels:

- Multi-component problem: Biomass is a complex feed and also its composition widely varies, requiring a proper characterization.
- Multi-phase problem: The biomass first reacts in a condensed phase and forms a solid (biochar), a liquid (bio-oil), and a gas phase. Successive heterogeneous gas-solid reactions involve the bio-char, while gas and bio-oil react in the gas-phase.
- Multi-scale problem: The chemical reactions occurs at the molecular level, but transport phenomena compete with chemical kinetics and needs to be

considered both at particle and reactor scale. Different time scales also take place in the overall process.

Because of its complexity, understanding all the aspects involved in this process require extensive experimental activity to produce data, followed by the mathematical modelling activities that process these data and help the understanding of the phenomena. Modeling this process is still a challenge, but constitutes an essential step to better understand the aspects involved and provide tools to the design of improved systems and reactors.

Much is already understood about the multicomponent aspect of biomasses. Most of this information derives from intense experimental activity to unveil the composition and properties of these materials. Institutions such as the National Renewable Energy Laboratory (NREL) and the American Society for Testing and Materials (ASTM) propose standard preparation procedures and complete analytical methodologies [25]. The analytical methods and sort of experimental data obtained with them will be discussed later.

4.2. Pyrolysis: Measurements and Analysis of Products

4.2.1. Kinetic and Thermal Regimes

Investigating and developing general kinetic mechanism of solids decomposition require especial attention to avoid fluid dynamics effects. Data must be gathered from experiments in which heat and mass transfer characteristic times are negligible to allow proper observance of the kinetics of the process. These aspects define the reactive regime that is taking place in the experiment. For this matter, two dimensionless parameters essentially define four different regimes. The Biot number (BI) introduces the ratio of heat transfer resistances inside of and at the surface of a particle. This ratio determines whether or not the temperatures inside the solid has significant variation in temperature profile along the space. The Pyrolysis number (Py), on the other hand, introduces the ratio of heat exchange and the kinetic characteristic times. This ratio indicates whether the chemical kinetics of the process or the global heat transfer is determining the evolution of the system. The equation (1) describes the Biot number, which is defined by the external heat exchange coefficient (hext), the diameter of the particle (Dp) and the thermal conductivity of the material (λ). Equations (2) and (3) define the Pyrolysis number in two different cases, when the internal or external heat transfer, respectively, are controlling the heat exchange. The definition of the Pyrolysis number involves also the density of the particle (ρ), the specific heat ($\hat{C}$), and the kinetic constant (K).

$$Bi = \frac{h_{ext} \cdot D_p}{\lambda_p} \tag{1}$$

$$Py^{\text{int}} = \frac{\lambda_p}{\rho_p \cdot \hat{C} \cdot K \cdot D_p^2} \tag{2}$$

$$Py^{ext} = \frac{h_{ext}}{\rho_p \cdot \hat{C} \cdot K \cdot D_p} \tag{3}$$

When plotting the values of BI and Py for different particle sizes and external temperatures, the four different pyrolysis regime can be defined, as seen in Figure 13. At high temperatures, for particles larger than 100 µm, the pyrolysis assumes a conduction-limited process (lower-right), while for smaller particles, the process becomes convection-limited (lower-left). On the other hand, by working with smaller particles and/or low temperatures, the regime becomes kinetically-limited (upper-right) or even can reach kinetically-limited with isothermal conditions (upper-left).

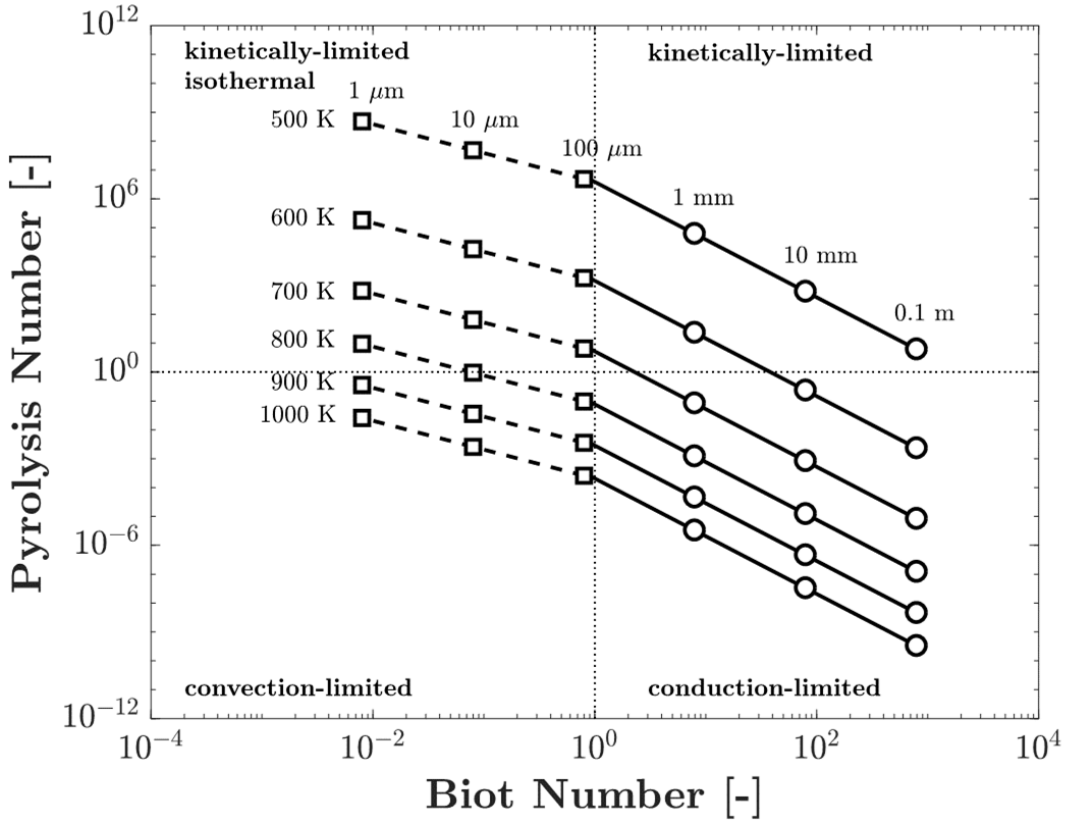

Figure 13 - The four pyrolysis regimes defined by Biot and Pyrolysis numbers.

Therefore, the experiments considered in this work take place preferably in the kinetically-limited region, meaning that BI<<<1 and Py>>>1. Several experimental apparatuses are nowadays available and frequently used for this kind of investigation. It is worthwhile to describe the most relevant ones.

4.2.2. Experimental Devices for Kinetic Measurements

A thermogravimetric analyzer (TGA) provides a simple but very useful way to investigate the thermal behavior of a sample (Bach & Chen, 2017; Cai et al., 2018; Murillo, Biernacki, Northrup, & Mohammad, 2017; Shurong Wang et al., 2016). The derivative of mass loss (DTG) is contemporaneously produced. The analysis can be performed isothermally or with a temperature program, under normal or pressurized, inert or oxidizing atmosphere, with tiny or relevant sample sizes (micro and macro-TGA). This versatile method identifies the mass loss profile under different conditions, providing information for understanding the decomposition mechanisms, which can even support forest fire prevention. Once individuated the thermal behavior of each major component of biomass, the method can also be used to quickly estimate their amounts in a biomass sample [26]. Recently, TGA apparatus incorporates also differential thermal analysis (DTA) and differential scanning calorimetry (DSC), which gives information on the endo/exothermicity of the process. TGA has been performed for decades to gather global kinetics of biomass and its components but no intrinsic kinetics can be measured.

TGA provides good conditions for slow heating rates, by exchanging heat through the controlled temperature of the flowing gas. However, different set-ups are required for fast pyrolysis experiments, providing faster heating rates to the sample.

Micro-pyrolyzers serve this purpose by providing a pre-heated environment where the solid is dropped, and sometimes a second-stage reactor is also present for gas-phase kinetic studies. The two stage allow to investigate separate residence times and temperatures for solid and gases. It also offers the possibility to couple analytical techniques like gas-chromatography coupled with mass spectrometry (MS), time-of-flight mass spectrometry (TOF-MS) or Flame Ionization Detector (FID), for qualitative and quantitative measurement of volatiles [27-29]. Similar apparatus, U-shaped two-stage reactor, was used from Norinaga and collaborators for both cellulose and lignin studies [30-34]. Pyro-probe offers similar conditions, but in a horizontal set-up. However, the heat is electrically provided through the sample holder, not by the surrounding atmosphere. It allows precise controlling

of the heating rate from between 0.1-20000˚C s-1 and temperatures up to 1400˚C. Online products detection can be performed using FTIR [35]. Drop tube reactors and entrained-flow reactors have longer vertical reaction zones, in which the samples are either simply dropped from the top or inserted pneumatically by the flue gas [36]. The phenomenon can be captured using high speed cameras [37].

These reactors, however, are not able to investigate very short residence times, mainly for the volatiles. For this aim, hyperthermal nozzle or tubular reactors can be heated up to 1500 ˚C and have residence times as short as 100 µs for the volatiles. Such short residence times attained because of the vacuum exit of the reactor [38-41]. This hinders the effect of secondary gas phase-reactions, and clearer analysis of the nascent volatiles [42].

Several other reactors are being employed for these kinetically-limited experiments, like curie-point, laser ablation, micro-fluidized bed and jet stirred reactors, and also Pulse-Heated Analysis of Solid Reaction kinetics (PHASR).

In addition to the importance of understanding the mechanisms of biomass thermal decomposition, the knowledge of products and yields obtained are of utmost importance to design economically attractive processes. Several analytical methods exist and are widely used for this purpose.

Volatiles compounds that are released during biomass thermochemical conversion can be identified and quantified by global and real-time gas-chromatography coupled with mass-spectrometry and flame ionization. While global analysis is capable of giving the total yields of products detected, the more advanced real-time analysis provides also the rate of release of each product along the experiment.

Biochar, on the other hand, is typical analyzed with methods that provide information on the elemental and proximate composition, on the types and amounts of chemical functionalities, and to obtain physical properties such as surface area, porosity and density. The ^{13}C Nuclear magnetic resonance (NMR), Fourier-transform infrared spectroscopy (FTIR), and Raman spectroscopy for investigating functional groups and degree of crystallization [43-45]; Brunauer-Emmett-Teller (BET) is the most common method to obtain surface area and pore size distribution. [44].

Condensable volatiles can be refined to produce chemicals. Biochar can be used directly as fuel, or be gasified yielding more light gases, that can be joined in the production of chemicals by fischer-tropsch process.

Knowing the properties and the fate of each biomass compound supports the development of biorefinery approaches and the designing of processes in all aspects: choose proper feedstock, define required pre-treatments, operating conditions and reactor sizes.

Reactor scale experimental activities go ahead in the study of biomass thermochemical conversion, providing data that not only consider ideal conditions, but also investigate more aspects of the multiscale aspects of the problem. While the previous analysis mentioned focus on the molecular scale, transport phenomena involving heat and mass transfer have undeniable effects in real industrial processes. These experiments focus on the investigation of particle and reactor scale and were not considered in the present work.

4.3. Modeling Activity

Together with experimental data, modeling activities complement the overall knowledge in the field. Models are capable of rationalizing experimental data, providing predictive tools that aid technological improvements with just a fraction of the cost of running experiments. There are several levels of detail in the modeling approaches, and they evolved in parallel with the improvements in analytical methods. In the past decade, several model approaches were proposed, and their adequacy changes depending on the objective of the investigation. Prakash and Karunanithi [46], describes the evolution of mathematical models of thermochemical conversion of biomass and Anca-Couce [47] recently published a review updating the last decade models developed.

Several authors proposed one-step single-component global models [48-54]. These models were useful as first approaches to this complex problem but fairly represent the real situation, and are only able to describe a strict range of conditions with good agreement. Even nowadays this kind of models are still used and proposed, usually with kinetic parameters derived empirically from TGA.

Thurner and Mann [55] proposed an empirical model, in which a single-component “biomass” decomposes in competing reactions for the formation of generic gas, tar and char. This became a classical reference for the time. No secondary reactions were accounted.

Multi-component Parallel Reaction Models [56-59] have the advantage of considering biomass heterogeneous, with a few reference model components decomposing in parallel. This allowed the models to be applied for different feedstock by attributing different shares of each single components, thus introducing a characterization step to each sample. For being more comprehensible and flexible, this approach was adopted in the modeling activities of this thesis. Despite this advantages, some compositional information on the biomass studied is required.

Secondary tar cracking was further introduced both in single and multi-component kinetic models [60-67]. This step is very important for a good prediction of the process, as volatiles are quite reactive at temperatures above 500°C, producing light gases in exchange of tars (bio-oil). Tar interactions with char in repolymerization reactions are also considered in some models.

Broido, Evett [68] increases the complexity of models by proposing a multi-step kinetic mechanism for cellulose decomposition at low temperatures. Later, Bradbury, Sakai [69] have simplified Broido's reaction work. This simplified reaction scheme, called the 'Broido-Shafizadeh model', which was the reference model for a significant period. This mechanism accounts for the formation of an active solid with a reduced degree of polymerization and two competing reaction pathways: intermolecular dehydration, predominating at low temperatures, leading to char and gas; and depolymerization reaction, predominating at high temperatures, leading to tar. The reactions are endothermic and their rates are represented as first order in the mass and with Arrhenius form kinetic parameters. The Bradbury, Sakai [69] model was extended to include a simple step of secondary reactions [64]

Di Blasi [70], Koufopanos, Lucchesi [71], Koufopanos, Papayannakos [72], proposed some multi-step models, which were further tuned by Jalan and Srivastava [73], Babu and Chaurasia [74], Babu and Chaurasia [75], Babu and Chaurasia [76], and Chaurasia and Kulkarni [77], aiming to improve predictions base on additional experimental data. Varhegyi, Jakab [78] modified the 'Broido-Shafizadeh' model, adding some reactions of cellulose in the presence of moisture. Boutin, Ferrer [79] simplified the Varhegyi, Jakab [78] model for flash pyrolysis conditions. Branca and Di Blasi [80] proposed a semi-global mechanism accounting for the biomass and two intermediate solid components. Their decomposition produces

different lumped volatiles following Arrhenius form for the temperature dependency. She proposed an update in another work, after studying non isothermal pyrolysis data [81].

Ranzi, Cuoci [82] have proposed a new multi-component multi-step kinetic mechanism of biomass pyrolysis. The author considers that feedstock is a mixture of cellulose, hemicellulose, and three types of lignin, which combined in varying ratios characterize the samples. The reaction mechanism assumes independent decomposition of each reference component. The model introduces real species both for gases and volatiles, which incorporate theoretically calculated thermodynamic properties. This allowed a better agreement in the estimation of heats of reactions. The model also describes the biochar as a mixture of a pure carbon species (CHAR) and metaplastics species, which refers to trapped gases and oxygen and hydrogen rich functional groups connected to the carbonaceous matrix. This feature allowed the estimation of elemental composition of the solid. The reactions are stoichiometrically balanced, allowing to track the fate of each atomic species in the system.

The most simple kinetic models, such as single-component and one step models require low computational power, but fail to address reliable results with slight changes in feedstock and operating conditions. More sophisticated models tend to be computationally expensive, but are more flexible and provide much more information and good agreement in a wide range of conditions.

5. Objectives

The main objectives of the present work are:

- Investigate the variety of biomass feedstock, their properties and composition;
- Individuate and propose a minimum set of reference species that together are able to characterize the largest amount of these feedstocks;
- Develop a general characterization method that can account for the variations in feedstock composition;
- Investigate the available experimental data on the literature, mainly on experiments that are in kinetically-limited conditions, in order to derive the main thermochemical reaction paths with their rate constants, and the released products, accounting for the different operating conditions;

- Couple the biomass pyrolysis mechanism with the CRECK kinetic mechanism of secondary gas phase reactions, allowing to describe the fate of volatile species;
- Investigate the available literature experimental data on biochar composition, functionalities, and physical characteristics, with particular attention to the effect of feedstock and operating conditions.
- Develop a kinetic mechanism of heterogeneous reactions of char with oxidizing agents, which can be applied both for biochar and charcoal.
- Validate the overall model involving biomass pyrolysis, secondary gas-phase reactions, and char gas-solid reactions. Determine the minimum amount of experimental data needed from a sample for predicting reliable results.

This mathematical model of biomass thermochemical conversion is a very useful predictive tool that can be used at particle and reactor scale, for optimal design and operation of thermochemical conversion units and processes.

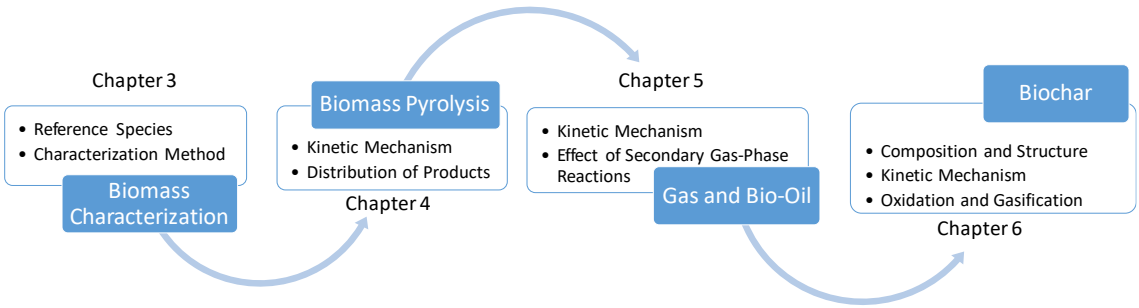

Figure 14 – Scheme of the sub-models proposed and discussed in the present thesis

The activities developed during the period of the Ph.D. focused on attaining these objectives, and the results were published in peer-reviewed journals and conferences, as soon as relevant subjects were investigated. Therefore, this thesis gives an overall critical view, mainly referring to the published works, showing the ideas and approaches proposed, and the results obtained. After this general introduction, the thesis is organized as following: Chapter 2 describes the biomass composition and the main components present in typical feedstock, together with the analytical methods typically used for this kind of experiments. As schematically reported in Figure 14, Chapter 3 starts the modeling activity, discusses and

defines the reference components for both lignocellulosic and algae biomass, together with a general characterization method for lignocellulosic and for algae biomasses. Chapter 4 explains the methods used for the development of multistep kinetic mechanisms of the pyrolysis of reference species. The kinetic validation is supported by an extensive database of biomass pyrolysis experiments. Chapter 5 discusses the importance of secondary gas phase reactions and proposes a detailed kinetic approach that accounts for the fate of volatiles from the primary pyrolysis. In fact, these reactions can strongly affect the yield and composition of gas and tars (bio-oil) under different operating conditions. Chapter 6 discusses the predictions of biochar composition and characteristics, and also presents a kinetic mechanism for the heterogeneous gas-solid reactions involved in gasification and combustion processes.

CHAPTER 2

BIOMASS COMPOSITION

The present chapter starts discussing the main analytical methods used to investigate biomass composition. Then, because of large heterogeneity of chemical components found in biomass, we identify, describe and classify the main groups of components present. Moreover, after investigating biomass both in their compositional and thermochemical properties, we sort biomass in two larger groups, the ones with lignocellulosic structure and algae. The discussion of the components present in these two groups will be carried separately, as well as the further discussions on characterization and pyrolysis.

1. Analytical Methods and Biomass Composition

The capability to define the chemical composition of complex biomass materials is a first key and necessary feature for the modeling of thermochemical processes of biomass conversion to fuels and valuable chemicals [83].

Biomass samples are heterogeneous and demand reliable preparation methods. Drying, milling, acid and basic treatments with or without organic solvents, followed by chromatographic analysis, are applied in order to separate moisture, organic and inorganic compounds, for further measurement of their contents. Institutions such as the National Renewable Energy Laboratory (NREL) [84] and the American Society for Testing and Materials

(ASTM) often release new standard preparation procedures and complete analytical methodologies for these purposes [25].

The analysis of biomass composition consists in several degrees of detail. Proximate, ultimate, and structural or biochemical analyses are the typical methods to investigate and provide the composition of biomass.

Proximate analysis is a gravimetric method that puts a sample under inert atmosphere, following an increasing temperature program. It can be carried out with thermogravimetric analysis (TGA) in accordance with the ASTM procedure [85], resulting in the measurement of moisture content and volatile matter. The resulting solid after devolatilization is the fixed carbon. When no further mass loss is detected, oxygen is introduced in the system until complete burnout of the solid. The remaining material is the ash content.

For on line applications and environmental analyses, the fast and sensitive mass spectrometry allows to determine the elemental composition from electron ionization [86].

Elemental analysis, also called ultimate analysis, provides the atomic composition of a certain material. It consists in fully oxidizing the sample, and determine the composition of main atoms (Carbon, Hydrogen, Nitrogen, and Sulphur) through measurement of the corresponding oxidized gases (CO_2, H_2O, NO_x and SO_x). Usually, oxygen is calculated by difference, while minor elements can be detected with additional methods. This method, together with the proximate analysis provide most of the literature data available on biomass composition. For on-line applications and environmental analyses, the fast and sensitive mass spectrometry allows to determine the elemental composition from electron ionization [86]

Biochemical or structural analysis measures the amount of organic compounds present. For this aim, there are numerous wet methods to fractionate and isolate biomass components, which can be further quantified through conventional analytical methods [26]. Some methods, focused on providing data to agriculture and livestock farming, measure the components in terms of nutritional value, revealing contents of digestible nutrients, such proteins, sugars and fats, together with fibers. On the other hand, biochemical analysis for energy and materials purpose sort the components in term of their relative structure and properties, mainly quantifying cellulose, hemicellulose, lignin and sometimes proteins and extractive components, which are the major components of interest for thermochemical

conversion. Different isolation and analytical methods lead to significant divergences in this kind of data. Unfortunately, isolation methods can also induce some degree of decomposition to the raw material, impacting the thermal behavior of the natural components. Raman and Fourier transform infrared spectroscopy provide fast and very promising results with minimal sample processing [25, 87, 88]. These analyses are time consuming, labor-intense and complex both in materials and methods necessary, which explains the little number of experimental data on biochemical composition in the literature, compared to proximate and ultimate.

Table 3 (After Demirbas [89]) reports a list of standard analytical procedures usually applied for determining some chemical and physical properties, together with proximate and ultimate composition of biomass samples.

property	analytical method(s)
heating value	ASTM D2015, E871
particle size distribution	ASTM E828
Proximate Composition	
moisture	ASTM E871
ash	ASTM D1102 (873 K), ASTM E830 (848 K)
volatile matter	ASTM E 872, ASTM E897
fixed carbon	by difference
Ultimate Elemental Analysis	
carbon, hydrogen	ASTM E777
nitrogen	ASTM E778
sulfur	ASTM E775
chlorine	ASTM E776
oxygen	by difference
elemental ash	ASTM D3682, ASTM D2795, ASTM D4278, AOAC 14.7

Table 3 - Standard analytical procedures of biomass fuel analysis. After Demirbas [89]

The results of these analytical methods can be reported in different calculation bases. For instance, the most used bases are “as received” (AR), “dry” and “dry and ash-free” (DAF). Despite the fact that many authors do not inform these details, this information is very important for precise understanding of the data and comparison between different sources. “AR” composition includes the content of both moisture and ashes/inorganics. “Dry” composition excludes the moisture content, and “DAF” excludes both moisture and ashes, considering only the organic matter. Table 4 (After Williams, Jones [90]) reports the composition of several biomass feedstock, including woods, grasses, cereals, and residues. The proximate analysis is reported with moisture and ash in “as received” basis, whilst ultimate analysis is considered in “DAF” basis.

	Proximate Analysis				Ultimate Analysis					
biomass	moisture	volatile matter, VM	fixed carbon, FC	ash	C	H	O	N	S	Cl
wood pine chips	4.00	81.30	14.60	0.10	52.00	6.20	41.59	0.12	0.08	0.01
willow, SRC	6.96	75.70	16.31	1.03	51.62	5.54	42.42	0.38	0.03	0.01
Miscanthus giganteus	14.20	70.40	14.10	1.30	49.10	6.40	43.98	0.26	0.13	0.13
switchgrass	7.17	73.05	15.16	4.62	49.40	5.70	44.25	0.45	0.10	0.10
wheat straw	7.78	68.83	17.09	6.30	49.23	5.78	43.99	0.64	0.10	0.26
rice husks	9.40	74.00	13.20	12.80	42.30	6.10	50.56	1.10	0.10	0.04
palm PKE	7.60	72.12	16.18	4.10	51.12	7.37	38.21	2.80	0.30	0.20
sugar cane bagasse	10.40	76.70	14.70	2.20	49.90	6.00	43.15	0.40	0.04	0.51
olive residue	6.40	65.13	19.27	9.20	54.42	6.82	37.29	1.40	0.05	0.04
cow dung	13.90	60.50	11.90	13.70	54.00	6.40	36.70	0.83	0.03	1.00
lignin	9.00	73.50	1.50	16.00	72.00	6.60	21.34	0.00	0.00	0.00

[a] After Williams et al.[15]

Table 4 - Proximate and ultimate composition of some typical biomass feedstock. Proximate composition is reported in "As received" basis, whilst ultimate composition is "DAF". After Williams, Jones [90].

The more complex structural or biochemical analysis measures the main components cellulose, hemicellulose, lignin, and sometimes also extractives and proteins. Figure 1 shows the relative concentration of several carbohydrates, lignin, extractives, and ash in different lignocellulosic biomass samples [91].

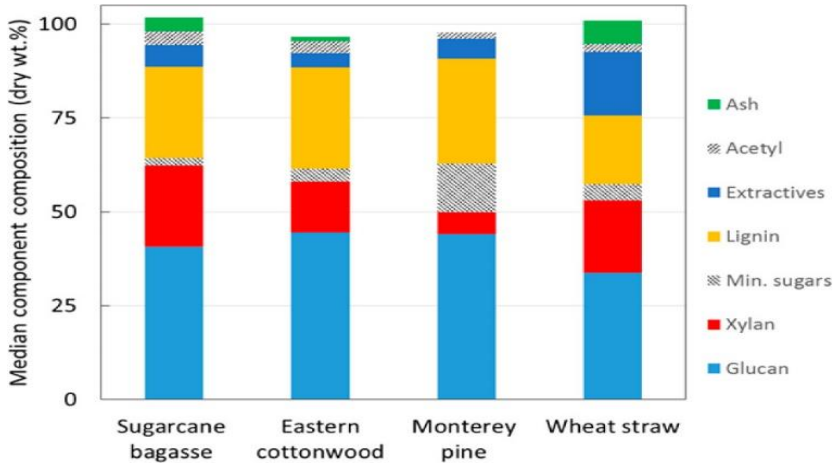

Figure 15 - Typical biochemical compositions of four biomass samples [91].

Proximate and ultimate analysis information are not sufficient to describe the devolatilization process. A reliable structural analysis of biomass samples, giving significant information on the relative content of carbohydrates (glucose, xylose, galactose, arabinose, and mannose), lignin, extractives, protein, and ash, is a valuable element if the interest is to analyze the successive biomass decomposition. Unfortunately, thermal and extraction methods can also induce some degree of decomposition [92]. Current wet chemical methods for biomass analysis are not only time-consuming and labor-intensive but also unable to provide accurate structural information. Raman and Fourier transform infrared spectroscopy provide fast and very promising results with minimal sample processing [25, 87, 88]

Despite the large amount of data available for proximate and ultimate analysis information, they are not sufficient to describe the devolatilization process. A reliable structural analysis of biomass samples, giving significant information on the relative content of carbohydrates (glucose, xylose, galactose, arabinose, and mannose), lignin, extractives, protein, and ash, is a valuable element if the interest is to analyze the successive biomass decomposition. However, detailed biochemical analysis are not commonly available, and experimental data reporting both elemental and biochemical composition remain quite scarce. This lack of information creates some difficulties in the characterizing biomass for modeling purposes, because different components undergo various decomposition pathways.

In biomass, volatile matters typically span between 60 and 80%, with a fixed carbon in the range 10−20%. In lignocellulosic biomass, carbon, hydrogen, and oxygen sum up to more than 95%, whereas only a few percent of nitrogen and minor amounts of sulfur and chlorine complete the elemental analysis. Cellulose, hemicellulose, and lignin are the major building blocks of lignocellulosic biomass, whereas extractives are usually lower than 15−20%.

The biochemical composition of algae widely differs from lignocellulosic. They in general do not have lignin, their sugars are organized in other kinds of polymers and have much more oils/fats and proteins. The amount of ash significantly varies among the different biomass samples, but are clearly present in larger amounts in algae. For instance, the very high content of nitrogen (i.e. reaching up to 15 wt.% of algae in a dry basis) is what motivated the study of algae, aiming to understand in which forms this element is present and how it relates to the pyrolysis products and formation of nitrogenated pollutants.

In order to highlight the compositional variations among algae, Table 5 reports the typical elemental and biochemical composition of different algae groups. Unicellular or micro algae are typical of yellow-green, blue-green, and diatom groups, whereas multicellular or macro algae characterize the brown ones. Both micro and macro algae are present in green and red algae. It is clear that algae are generally richer in hydrogen, nitrogen and sulfur when compared to ligno-cellulosic biomasses, whereas carbon content is within the same range [93]. The higher H content in micro algae is because of the large presence of fatty acids, whereas the higher N and S content is due to the abundance of proteins. Mineral content of algae is generally higher than plants and sodium (Na), potassium (K), and calcium (Ca), usually

bonded to carbonate ions, are the most present metals [94, 95]. Brown algae and diatoms are particularly rich in silicon (Si) [96].

Elemental and biochemical composition (Dry and ash-free wt.%)									
GROUP		C	H	N	S	O	Protein	Sugars	Lipids
Green	Micro	40 - 60	6 - 8	7 - 13	0.1 -2	25 - 55	10 - 60	5 - 40	2 - 35
	Macro	30 - 50	4 - 8	2 - 6	0.1 - 2.5	35 - 55	2 - 15	25 - 50	2 -7
Yellow-Green	Micro	47 - 70	7 - 10	5 - 10	0.1 - 2	17 - 38	20 - 50	10 - 30	20 - 40
Blue-Green	Micro	46 - 55	6 - 8	6 - 14	0.1 - 1	24 - 38	40 - 65	10 - 30	3 - 15
Brown	Macro	30 - 50	5 - 10	1 - 6	0.1 - 4	35 - 65	3 - 30	30 - 50	0.5 - 5
Red	Micro	45 - 52	6 - 8	6 - 8	0.1 - 1.5	30 - 40	30 - 65	20 - 55	8 - 15
	Macro	40 - 46	4 - 8	1 - 7	0.1 - 1.5	30 - 40	4 - 30	20 - 55	1 - 7
Diatoms	Micro	20 - 55	3 - 8	3 - 7	n.d.	30 - 75	30 - 40	20 - 35	15 - 35

Table 5 - Typical elemental and biochemical composition of main groups of algae.

In order to understand and build a big picture of biomass composition, a large collection of literature data was organized in database format, available in the Appendix A, and reports all the data found on proximate, elemental and biochemical composition. The data is divided in lignocellulosic and algae materials, and accounts for about 600 and 150 entries, respectively.

Lignocellulosic materials accounts for wood (treated and non-treated), bark, pits, needles, seeds, shells, energy crops, grasses, stalks, hull-husk, residual cakes, etc. Algae materials contain most of the species studied for energy purposes and are divided in micro and macro algae, which are subdivided in base of their dominant pigment color. From this collection of data, it was possible to define the main components present in biomass, which will be described in this chapter. Moreover, an innovative biomass characterization method was proposed, which will be presented after describing the main components. In the next session, the biochemical compounds in lignocellulosic and algae biomasses will be discussed in detail.

2. Biomass Molecular Structure

2.1. Lignocellulosic Biomass

Wood and lignocellulosic biomasses are renewable and complex products usually sorted as gymnosperms and angiosperms. Gymnosperms or softwoods are evergreen, seed-producing, nonflowering plants, whose seeds are unenclosed on cones or leaves, whereas angiosperms are seasonal, seed-producing, flowering plants, whose seeds are enclosed

within the fruits. Among the gymnosperms, only the conifers are major competitors with the dominant angiosperm trees. Angiosperms also include cereals and grasses.

Lignocellulosic biomass materials are mainly constituted by a combination of polysaccharides, which can be generally grouped into holocellulose (cellulose and hemicellulose) and lignin species. Moisture, together with other components such as acetyl groups, extractives, and minerals are also present [47, 97]. Biomass has a porous structure where cellulose microfibril represents the important element surrounded by hemicellulose and pectin, which act as ligand and embed lignin materials [98]. Figure 16 (After Bidlack [99]) shows the microscopic organization of sugar monomers into polysaccharides, forming the fibrils, and Figure 17 (After Mettler, Vlachos [100]) shows the multiscale structure of biomass, highlighting the progressive resulting macroscopic structure of plant cells, tissues and the whole organism.

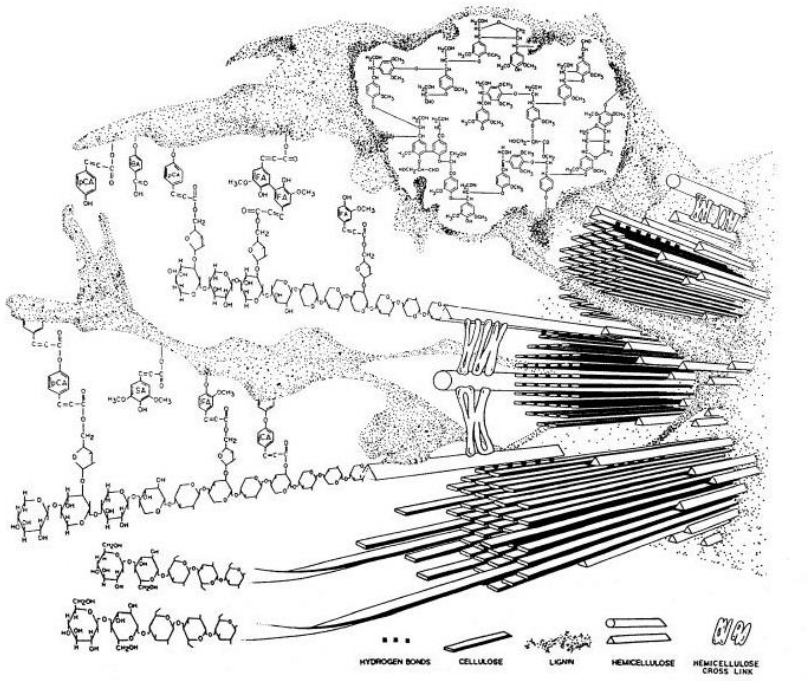

Figure 16 - Microscopic organization of lignocellulosic fibers. After Bidlack [99].

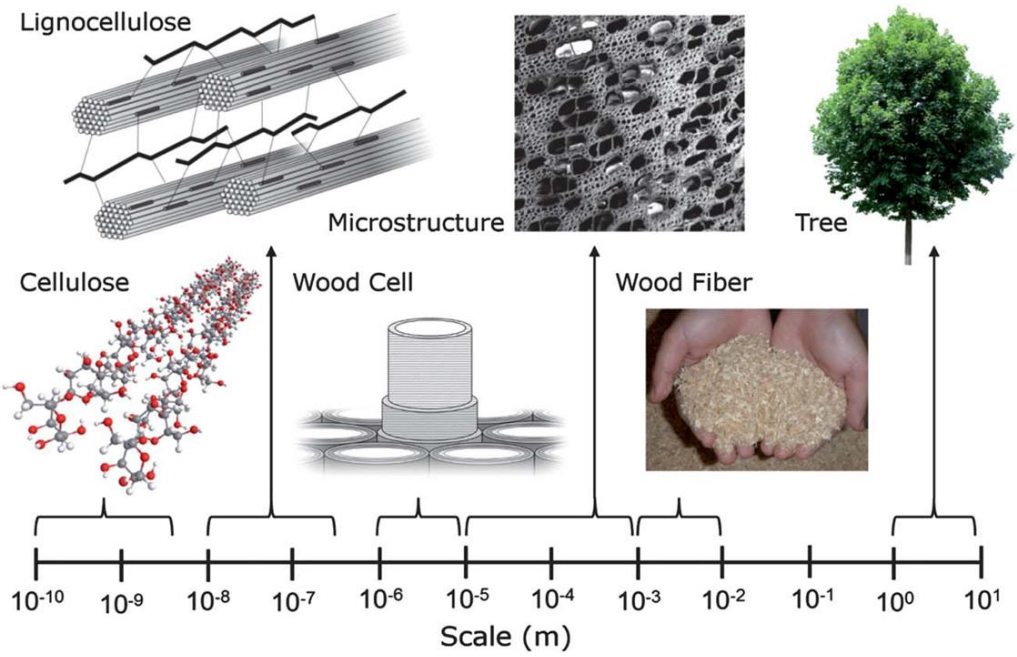

Figure 17 - Multiscale lignocellulosic biomass structure: from molecules to cells, tissues and organism. After Mettler, Vlachos [100]

2.1.1. Sugars and Carbohydrates

Sugars and carbohydrates are polyhydroxylated aldehydes or ketones. Cyclic sugars with a six membered ring are called pyranoses (e.g., glucose), whereas cyclic sugars containing a five membered ring are called furanoses (e.g., fructose). There are two different isomers of glucose. In fact, the hemiacetal carbon (anomeric center) in the ring can present two configurations (anomers) with hydroxyl group in the axial plane (β) or orthogonal to the ring (α). Figure 18 shows the α and β anomers of glucose, together with the α-1,4 and β-1,4 glycosidic bond to form maltose and cellobiose, respectively. In maltose, two glucose molecules are linked by a α-1,4-glycosidic bond between the α-anomeric form of C-1 on one sugar and the hydroxyl oxygen atom on the C-4 of the adjacent sugar. Various glycosidic bonds are possible, because glucose has multiple hydroxyl groups. Cellobiose consists of two β-glucose molecules linked by a β-1,4 glycosidic bond, and is found as a repeat unit in cellulose. Maltose is found as a repeat unit in amylose, the linear polysaccharide in starch. The slight difference in the bond type creates strong differences between cellulose and starch, the first mainly have structural function while the other has energy storage role. Moreover, as enzymes are substrate specific, most of the animals are incapable of digesting cellulose as an energy source and it acts as dietary fiber only. Exceptions are some insects like termites and ruminants like horses and cattle, which rely on symbiotic microorganisms

in their digestive system, that produce proper enzymes for breaking cellulose structure. On the other hand, most organisms easily hydrolyze the bonds connecting glucose in starch.

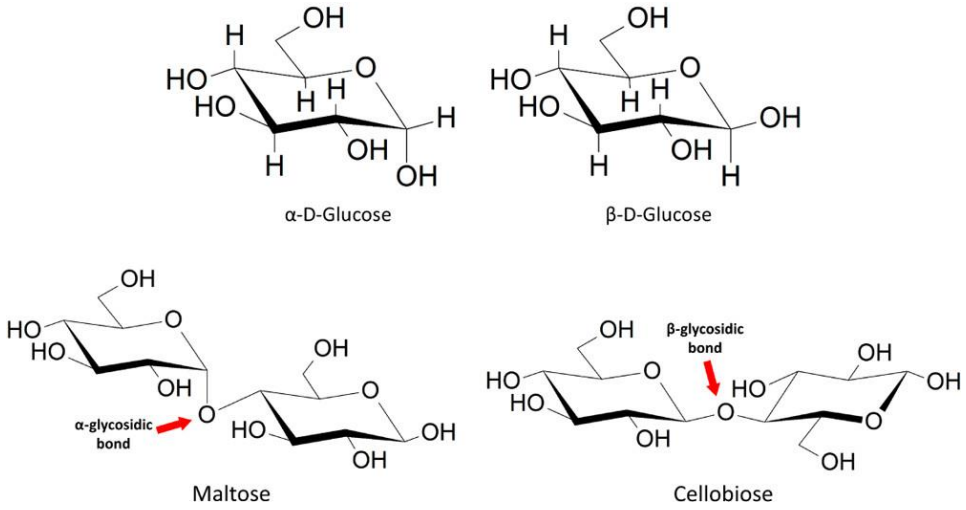

Figure 18 - α and β anomers of glucose; glycosidic bonds in maltose and cellobiose.

2.1.1.1. Cellulose

Cellulose, the most abundant structural polysaccharide in cell walls, comprises 15–50% of the dry weight of plant biomass. It is a linear polysaccharide composed of β-d-glucopyranose units linked by β-1,4 glycosidic bonds, which can be summarized as $(C_6H_{10}O_5)_n$, so that mass elemental composition is C = 44.4%, H = 6.2%, and O = 49.4%. Cellulose chains have a degree of polymerization (DP) of approximately 10–15 thousand of glucopyranose units in chair conformation [101]. DP of cellulose is a structural property that has a high impact on enzymatic hydrolysis, solubility, and mechanical properties of lignocellulosic biomass. The presence of several strong hydrogen bonds contributes to the recalcitrance of cellulose toward hydrolysis and enzyme activity. Intersheet H-bonds connect atoms between different sheets. The inchain and interchain H-bonds connect chains and thus stabilize the overall structure of cellulose fibrils, as clearly shown in Figure 19. Cellulose crystallization is directly related to the formation of these intermolecular hydrogen bonds [102], in which the sugar polymer chains strongly interact with each other to form a stable microfibril. The cellulose chains, whose sugar rings are located in the same plane, form a sheet and these sheets are stacked above one another to form the fibril. Cellulose elementary fibril may contain 36 crystalline and subcrystalline chains with linear cross-section dimensions ranging between 2 and 10 nm and a different degree of disorder.

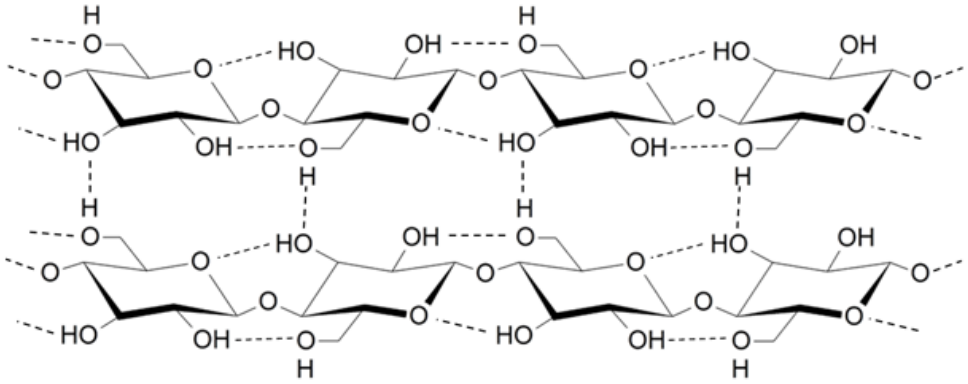

Figure 19 - Intra and inter hydrogen bonds in cellulose.

Hemicelluloses and pectins are closely associated with the surface of cellulose fibrils with non-covalent linkages forming a micro-fibril network. Cell walls are further reinforced by lignin, a three-dimensional polymer of phenyl propanoid units, which is covalently linked to hemicellulose. Variations in the crystalline structure affect pyrolysis products, for example the compound levoglucosan yield is more abundant for higher crystallinity samples [103, 104].

2.1.1.2. Hemicellulose

Hemicellulose accounts for 25–30 wt.% of total biomass and is a heterogeneous complex polysaccharide derived from hexose and pentose monosaccharide units such as xylose, galactose, mannose, glucose, and arabinose. Linear or branched hemicellulose polymers are named according to the main sugar units. Mostly, sugars on hemicellulose structure are linked together by β-1,4 glycosidic bonds. Ebringerová [105] highlights three major classes of hemicellulose structures:

- Xylans: Linear homoxylan polysaccharides are characterized by β-1,3 and β-1,4 linkages, whereas glucuronoxylans present single side chains of α-d-glucuronic acid. l-Arabino side chains are also present in cellular wall of cereal grains.
- Mannans: Galactomannan, glucomannan, and galactoglucomannan polysaccharides depend on the various branching at position 6. Glucomannan is the main component in softwoods, and less abundant in hardwoods and grasses.
- Xyloglucans: d-Xylo-d-glucan represents the major building material of primary cell walls of all higher plants. Mixed-linkage β-glucans are present in cereals.

Hemicellulose in softwood biomasses is prevailing of type galacto-glucomannan (mannose/glucose/galactose residues in a ratio 3:1:1) and glucomannan (mannose/glucose

residues in a ratio of 3:1). Mannose units are acetylated at the C2 or C3 positions with one substitution every three to four units. Figure 20 shows the structure of xylan and glucomannan polymers [106].

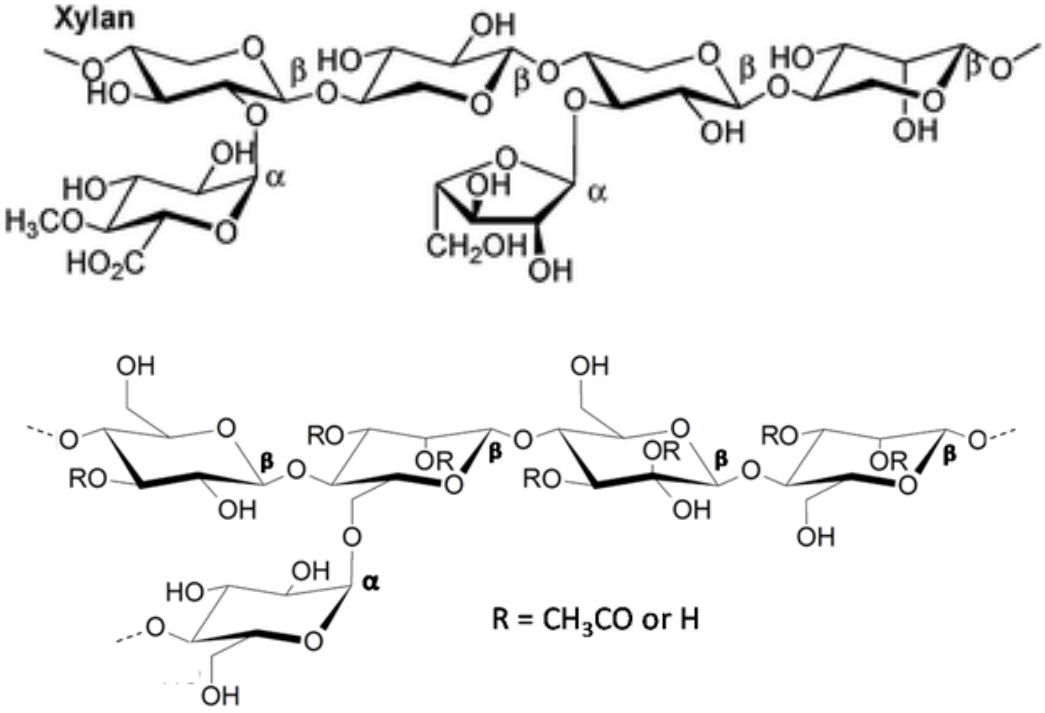

Figure 20 – Xylan and glucomannan polymeric structure [106].

Hemicellulose in hardwood is mainly of xylan type with variable amounts of galactose, arabinose, rhamnose, methylglucuronic acid units, and acetyl groups. Grass and cereals, for being a subgroup of hardwood plants (angiosperms), usually have hemicellulose of xylan type, but with some structural differences that reflects in the pyrolysis behavior.

The polymerization degree of hemicelluloses is relatively small (DP = 70–200), with larger molecules in hardwoods and smaller in softwoods. Very recently, Zhou et al [107]. presented detailed information on monomeric composition of hemicellulose. In most grasses and hardwoods, the xylose polymer is the primary hemicellulose constituents, and xylan conversion is important for utilization of biomass feedstocks such as corn stover, *Miscanthus*, switchgrass, and poplar [106]. Because of the strain in furanose units, their decomposition is faster compared with pyranose, thus indicating a greater recalcitrance of xylose with respect to arabinose. Together with hemicellulose, pectin is a major component of primary cell walls of biomass and contains highly branched polysaccharides (DP = ∼100–1000) rich in galacturonic acid [102].

2.1.2. Lignin

Lignins are aromatic polymers resulting from the oxidative coupling of 4-hydroxy-phenyl-propanoid units. They contribute to make rigid and impervious the walls of secondarily thickened cells. Although lignins shield cell wall polysaccharides from microbial degradation, this protection is a limiting factor in the conversion to pulp or biofuels. Lignins are complex racemic polymers derived from three hydroxycinnamyl alcohol monomers that differ in their methoxylation degree: p-coumaryl, coniferyl, and sinapyl alcohols. These monolignols produce p-hydroxyphenyl (H), guaiacyl (G), and syringyl (S) propanoid units, and these are the main building blocks of lignin [108, 109]. Figure 21 schematically shows the monolignols and the corresponding phenyl-propanoid units.

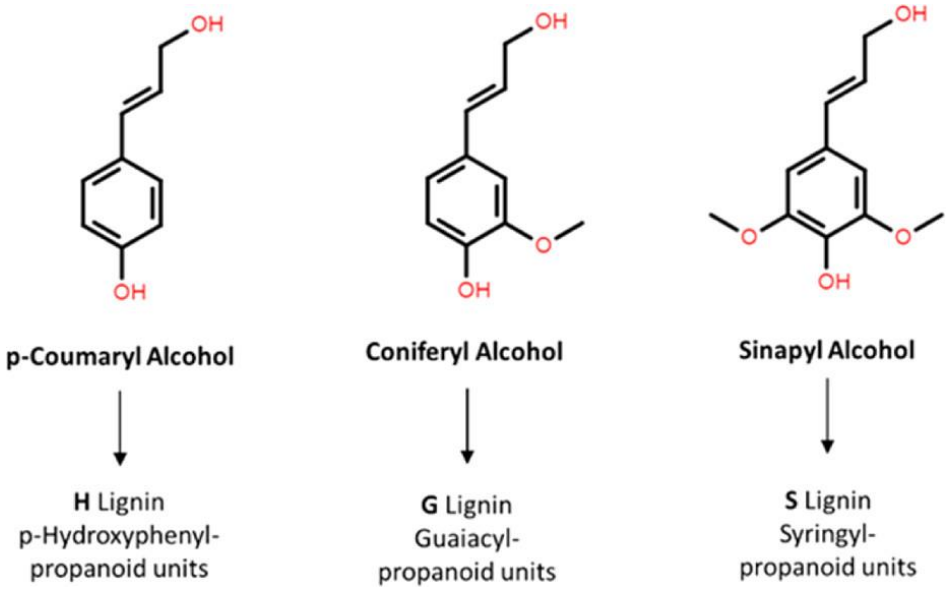

Figure 21 - Monolignols and derived phenyl-propanoid units.

Hardwood lignins are mainly constituted of guaiacyl (G) and syringyl (S) units with only traces of p-hydroxyphenyl (H) units. Softwood lignins are mostly composed by guaiacyl (G) units with low amounts of p-hydroxyphenyl. Lignins in forages are composed primarily of H, G, and S units. H-units are elevated in softwood compression wood and are slightly higher in grasses [87, 108].

The main linkages in lignins are described in Figure 22. They are β-O-4 and β-5 from monomer-oligomer couplings, 5-5 and 4-O-5 from oligomer–oligomer couplings, β-β and β-1. Even 8-membered rings may be produced through the coupling of a monolignol and a 5-5 unit (at one of its 4-O position), which forms a structure known as dibenzodioxocin. These structures make up almost the entire spectrum of functionalities in the lignin family. Branch-

points in the lignin structure are mainly due to the presence of 5-5 and 4-O-5 bonds. The minor resinol units may come from the direct coupling of monolignols forming a dehydrodimer, or from a 5-coupling of a monolignol to the growing polymer, mainly in softwood lignin. β-1 coupling is observed in many combinations: in birch the syringyl–syringyl type is the most abundant, while β-1-structure formation in lignin is likely to produce dienones.

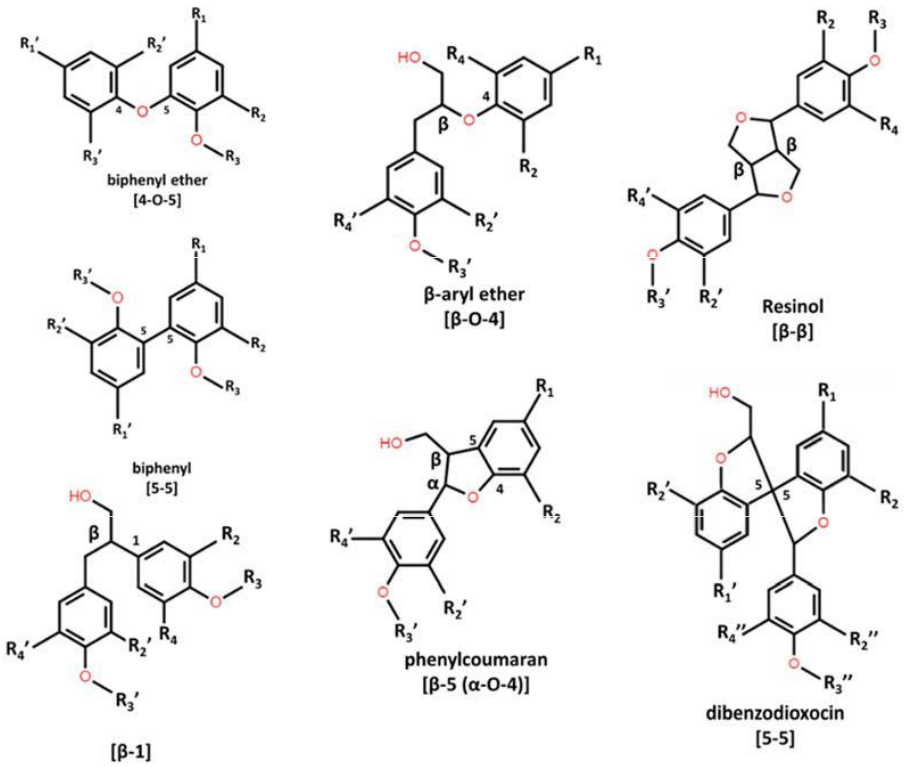

Figure 22 - Typical bonds in lignin polymer structures.

The β-O-4 linkage is typically the most abundant and most labile bond, readily cleaved by most pretreatment methods. The β-aryl ether structure (β-O-4) of isolated lignins strongly depends on the separation method and severity of its conditions [87, 92].

The relative abundance of methoxyl groups (OCH_3) is useful for characterizing different lignins. Hardwood plants contain a larger amount of (OCH_3) groups with respect to softwood and herbaceous biomasses. The lignin monomeric units usually refer to nine carbon atoms and are expressed in terms of a C9 formula with the indication of the number of (OCH_3) groups, e.g. $C_9H_{8.3}O_{2.7}(OCH_3)_{0.97}$ for Picea abies and $C_9H_{8.7}O_{2.9}(OCH_3)_{1.57}$ for *Eucalyptus regnans*. Table 6 reports a detailed set of elemental composition of different lignins. Lignins are generally more branched in gymnosperms than in angiosperms, because of the lack of S

units. The G/S-rich lignin of angiosperms is rich in β-O-aryl ether linkages and cross-linked to cell wall polysaccharides [92].

	C (wt.%)	H (wt.%)	O (wt.%)	Reference
Hardwood				
Liquidambar styraciflua	57.6	5.6	36.8	[Alt, 2006]
Liriodendrum tulipifera	58.4	5.8	35.8	[Jakab, 1995]
Betula verrucosa	58.5	6.5	35.0	[Alt, 2006]
Ball-milled enzyme cottonwood	58.9	6.1	35.1	[Jakab 2, 1995]
Eucalyptus regnans	59.2	6.3	34.5	[Alt, 2006]
Prunus serotina	59.7	5.9	34.4	[Jakab, 1995]
Populus tremuloides	60.0	6.1	33.9	[Alt, 2006]
Casearia praecox	60.0	5.9	34.1	[Jakab, 1995]
Olea sp.	60.2	5.9	34.0	[Jakab, 1995]
Fagus sylvatica	60.3	6.3	33.4	[Alt, 2006]
Juglans regia L.	60.3	5.9	33.7	[Jakab, 1995]
Acer macrophyllum	60.4	5.7	33.9	[Alt, 2006]
Entandrophragma cylindricum	60.6	5.8	33.6	[Jakab, 1995]
Manilcara sp.	60.7	5.9	33.4	[Jakab, 1995]
Tieghemella heckelii	61.2	5.8	33.1	[Jakab, 1995]
Millettia laurentii	62.3	5.7	32.0	[Jakab, 1995]
Afzelia sp.	62.3	5.6	32.1	[Jakab, 1995]
Dalbergia granadillo	62.6	6.0	31.5	[Jakab, 1995]
Dalbergia melanoxylon	62.7	5.8	31.5	[Jakab, 1995]
Steam explosion yellow poplar sc	63.4	5.9	30.7	[Jakab 2, 1995]
Pseudotsuga menziessi	64.8	5.8	29.4	[Alt, 2006]
Alcell organosolv mixed hardwoo	66.8	6.2	27.0	[Jakab 2, 1995]
Average Hardwood	**60.9**	**5.9**	**33.1**	
Softwood				
Steam explosion aspen softwood	61.4	6.1	32.5	[Jakab 2, 1995]
Pinus ponderosa	62.5	6.0	31.5	[Alt, 2006]
Metasequoia glyptostrobides	62.9	5.9	31.2	[Jakab, 1995]
Picea abies	63.3	6.0	30.6	[Jakab, 1995]
Tsuga heterophylla	63.4	6.3	30.3	[Alt, 2006]
Picea mariana	63.7	6.3	30.0	[Alt, 2006]
Larix occidentalis	63.7	6.1	30.2	[Alt, 2006]
Thuja plicata	63.8	6.1	30.1	[Alt, 2006]
Picea sylvestris	64.0	6.1	29.9	[Alt, 2006]
Indulin kraft mixed softwoods	65.8	6.1	28.1	[Jakab 2, 1995]
Acetosolv pine sawdust	66.0	5.5	30.2	[Moore, 2015]
Average Softwood	**63.7**	**6.0**	**30.4**	
Grass/Cereal				
Miscanthus sinensis	60.3	5.8	34.0	[Jakab, 1995]
Arachis hypogaea	63.1	5.7	31.2	[Jakab, 1995]
Sucrolin sugar cane bagasse	66.1	5.8	28.1	[Jakab 2, 1995]
Average Grass/Cereal	**63.2**	**5.8**	**31.1**	

Table 6 - Elemental composition of different lignins.

2.1.3. Extractives

The aforementioned biomass components are already widely studied. However, there is a large gap in the understanding of extractives species for thermochemical conversion purposes. For instance, these compounds grasp all nonstructural substances produced by plants and are highly valuable for the pharmaceutical and cosmetics industry,

receiving great attention in other research fields. Thousands of different extractives were already identified and they present a great variety of composition, structure, and biological functions, also depending on the different seasons. They are also distributed in different ways among the organs of the plant, being more abundant in leaves and barks. Typical content of extractives in lignocellulosic biomass varies from 5 to 15 wt %, and gymnosperms generally are richer in extractives, which can even reach more than 20% in bark samples. Oil seed plants can also present high content of extractives. Because of the large variety of extractive species, it is necessary to drastically simplify the complexity of the overall system. Water solubility is a simple and useful way to classify extractive components. Hydrophilic extractives are the soluble molecules in high-polarity solvents, such as ethanol and water, while hydrophobic extractives are only soluble in low-polarity solvents, such as hexane and ether.

2.1.3.1. Resins

Resins comprehend all those compounds such as terpenes, acid resins, fatty acids and esters present in various parts of the plant, from leaves, bark to wood itself, not soluble in water but in neutral organic solvents such as (alcohols, ethers, chloroform). First of all, an important distinction must be made between the resins present in hardwood and those present in softwood plants[110]: the first contain wood resin, consisting mainly of fatty acids (60-90%), which is present in small quantities (≤ 1%), while the second, in addition to wood resin, also contain terpenic resins (oil resin) in much more appreciable quantities. The overall resin amount in softwoods can sometimes represent as much as 15% of the total weight of the plant. It should also be noted that the genus Pinus is the one with the most abundant resinous content compared to other species, which makes these plants widely used by the glue and pharmaceutical industry.

As represented schematically in Figure 23, the compounds present in oil resins can be further subdivided according to their molecular weight:

- Turpentine: the volatile, low molecular weight fraction, is mostly composed by monoterpenes ($C_{10}H_{16}$) and sesquiterpenes ($C_{15}H_{24}$), which the most recurrent are: α-Pinene, β-Pinene, Δ-Carene, limonene, phellandrene, among many other with smaller quantities. This fraction represents about 25-30% of oil resins [111]. These compounds, in particular monoterpenes, are difficult to characterize

because they are very thermolabile and tend to decompose, rearrange or condense if subjected to abrupt heating or aggressive acid treatments .

- Colophony: the non-volatile, high molecular weight fraction of oil resin, also called rosin, represents 70-75% of oil resins. Diterpenes ($C_{20}H_{32}$), mostly pimaric and abietic acid, represent 30-40% by weight of colophony in softwoods, and are almost absent in hardwoods. The remaining compounds are fatty acids and minor amounts of unsaponifiable compounds [111].

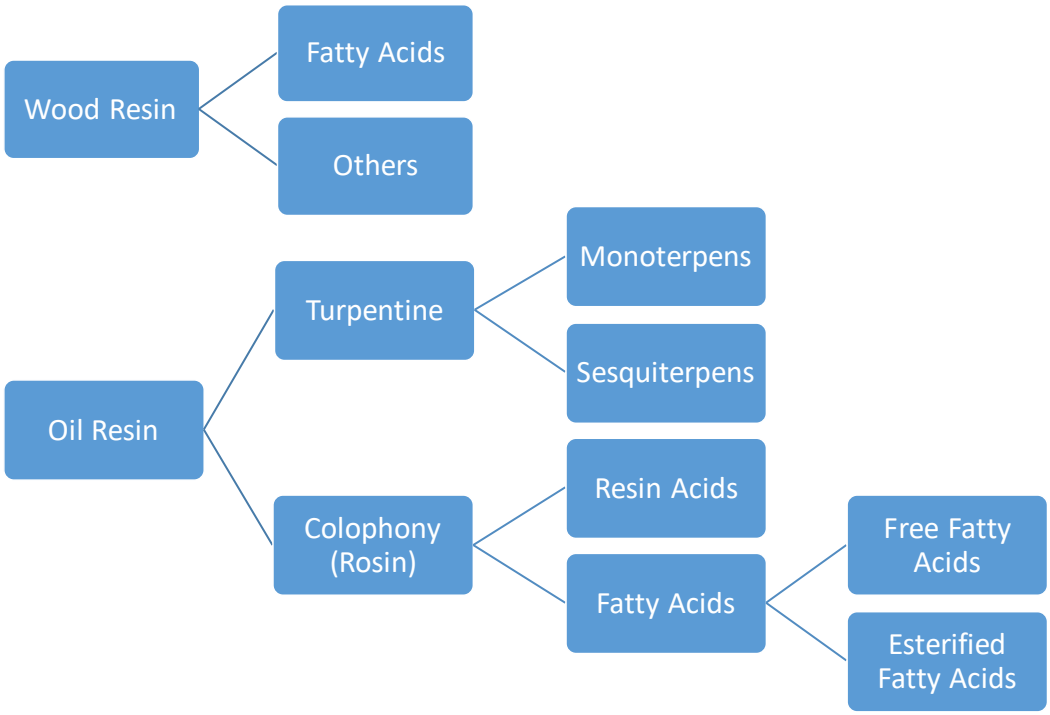

Figure 23 - Scheme for the classification of compounds in resins

Terpenes are hydrocarbons derived from isoprene monomers, with or without substituted groups. Figure 24 shows the molecular structure of the main terpenes found in lignocellulosic biomass. β-Carotene is an example of politerpene. It has high market value and consists in an antioxidant pigment found in many plants, but is not commonly found in appreciable amounts in wood.

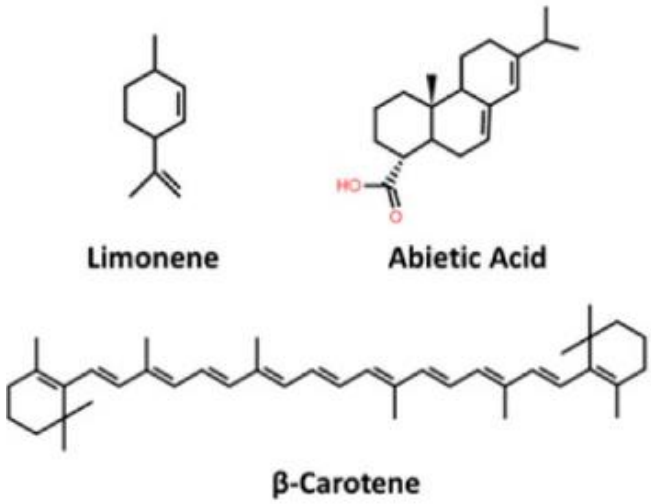

Figure 24 - Typical terpenes present in lignocellulosic biomass: Monoterpene limonene, diterpene abietic acid and politerpene β-Carotene.

Fatty acids are long hydrocarbon chains with a terminal carboxylic group. In lignocellulosic biomass they are frequently esterified (forming mono, di and triglycerides), only with minor amounts in free form [111]. They reach 60-90 wt.% of extractives in hardwoods, forming the fraction of woody resin mentioned above, while in the softwoods they comprehend 30-50% of the extractives [111]. There are several fatty acids in biomass, and the differences are mainly in the chain length and degree of unsaturation. In plants, most of the fatty acids have unsaturated 16-20 carbon chains. Table 7 shows the distribution of fatty acids extracted from *Betula verrucosa.* Very similar to oil seed plants, the most abundant fatty acid is linoleic acid.

TABLE IX
FATTY ACIDS OF *Betula verrucosa*[a]

Saturated	Per cent of total acids	Unsaturated	Per cent of total acids
C_{12}	0.24	C_{16} (1)	2.05
C_{14}	0.33	C_{16} (2)	0.46
C_{16} Ac. Palmitico	8.90	C_{16} (2)	0.22
C_{18} Ac. Stearico	4.60	C_{18} (1) Ac. Oleico	3.46
C_{20}	1.86	C_{18} (2) Ac. Linoleico	65.60
C_{22}	1.86	C_{18} (3)	9.95
C_{24}	0.46	—	—
	18.25		81.74

[a] Selleby (1960).

Table 7 - Distribution of fatty acids extracted from Betula verrucosa [112].

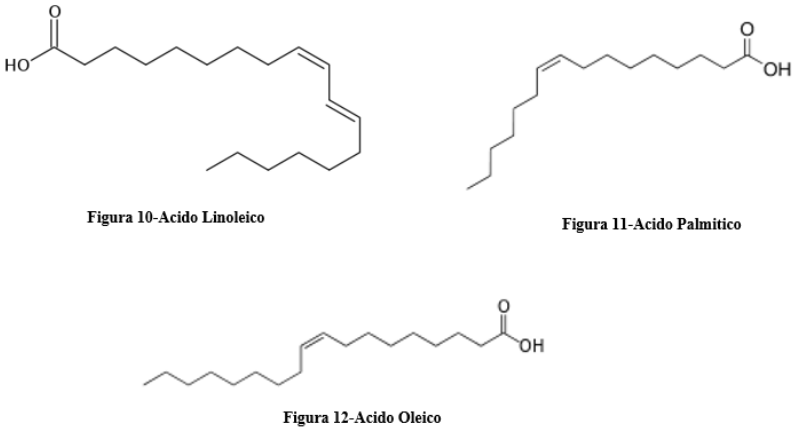

Figure 25 - Molecular structure of some typical fatty acids found in lignocellulosic biomass

The heavy fraction of oil resin can contain also minor amounts of waxes and unsaponifiable compounds. Waxes are a mixture of long chain alcohols, aldehydes, ketones, esters and acids. Not able to be hydrolyzed by alkali, the unsaponifiable compounds are mostly steroids like β-Sitosterol and β-Sitostanol. Both these compounds are of minor importance for the overall composition of biomasses.

2.1.3.2. Phenolic Compounds

Phenolic compounds are the second big group of extractives and it is important to understand the composition and the role they play within the plant. Some tissues have been found richer in phenolic compounds (e.g. bark, leaves, sprouts), and the same applies to some plants (e.g. apple, pear, wheat, rice, tobacco, onion) when compared to others [111]. These compounds play a defensive role in plants because of their antioxidant activity, protecting from free radicals, and sometimes for their odor that manage to keep away some parasites. Some of them also act as pigments, that attract pollinizing agents. They can be extracted with various solvents such as water, ether, methanol, acetone or slightly acidic and heated solutions of sodium carbonate. The quantity and variety differs among the species or even among samples of the same species due to external factors such as the geographical area in which the plant has grown, climatic conditions or biological mutations.

The phenolic compounds comprehend a wide class of compounds, often presenting similar structures, but with different properties that distinguish them in different categories. In this present work, an attempt of classification for these compounds was done, as reported in Figure 26.

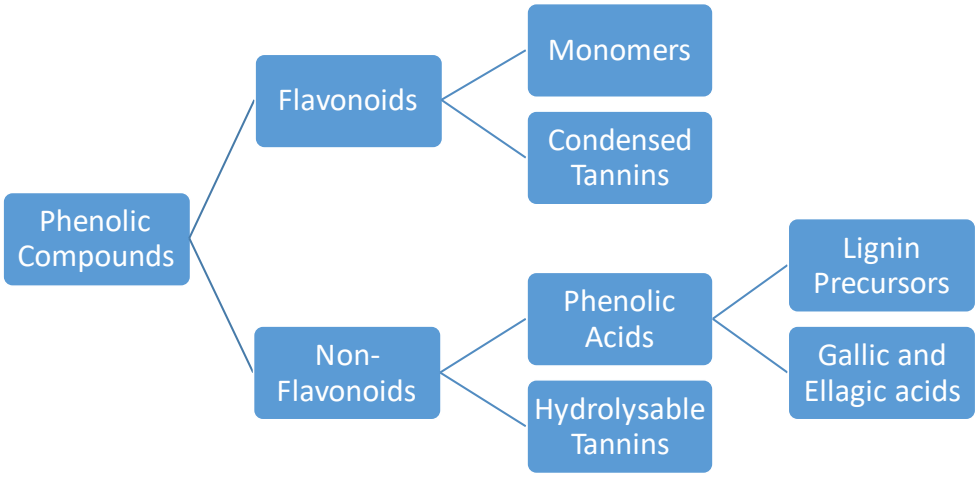

Figure 26 - Schematic classification of phenolic compounds

The first major division is made between flavonoids and non-flavonoids. Flavonoids are a large class of more than 5000 compounds [113] formed by two aromatic rings connected by a bridge of three carbons and one of oxygen as seen in Figure 27. They can also be connected to sugars or other complex molecules. By changing the functional groups bonded to the general structure, the varieties of flavonoids are formed, as exemplified in Figure 27.

Basic structure	Anthocyanidin	R_3'	R_4'	R_5'	R_3	R_5	R_6	R_7
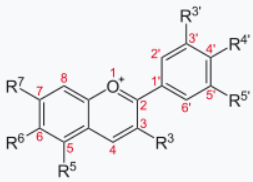	Aurantinidin	–H	–OH	–H	–OH	–OH	–OH	–OH
	Cyanidin	–OH	–OH	–H	–OH	–OH	–H	–OH
	Delphinidin	–OH	–OH	–OH	–OH	–OH	–H	–OH
	Europinidin	$-OCH_3$	–OH	–OH	–OH	$-OCH_3$	–H	–OH
	Pelargonidin	–H	–OH	–H	–OH	–OH	–H	–OH
	Malvidin	$-OCH_3$	–OH	$-OCH_3$	–OH	–OH	–H	–OH
	Peonidin	$-OCH_3$	–OH	–H	–OH	–OH	–H	–OH
	Petunidin	–OH	–OH	$-OCH_3$	–OH	–OH	–H	–OH
	Rosinidin	$-OCH_3$	–OH	–H	–OH	–OH	–H	$-OCH_3$

Figure 27 - General structure of anthocyanidins, and the position of functional groups characteristic of some species.

Flavonoids can be subdivided into anthoxanthins, flavanones, flavanonols, flavans, anthocyanidins, isoflavonoids, among others. In addition to the free form, these species can also build oligomeric and polymeric structures, which are called condensed tannins (or also protoantocianidins), present in quantities that reach 40 wt.% in the bark of some trees. Figure 28 shows the structure of condensed tannins, flavonoid monomers connected by 4-8 bonds, also presenting branches on the 4-6 bonds.

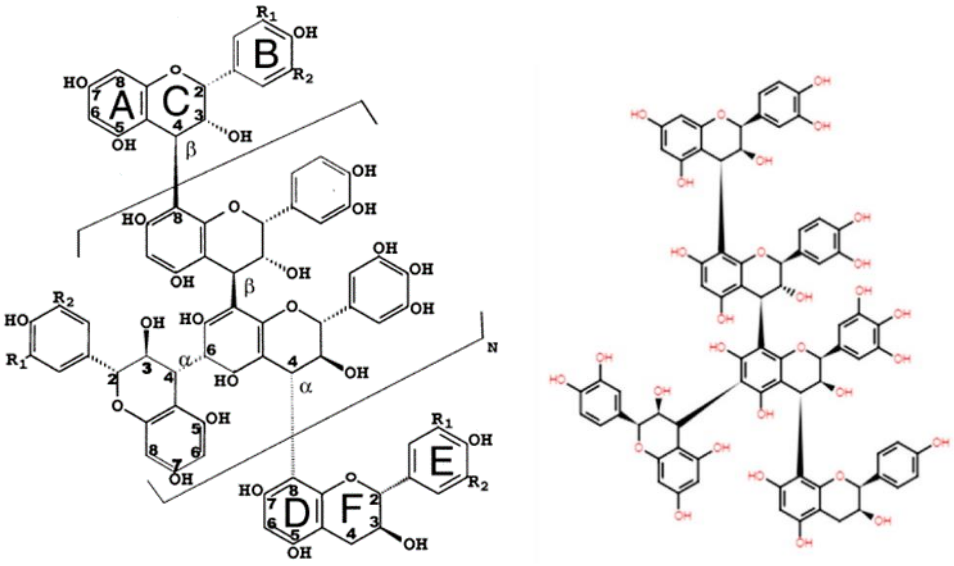

Figure 28 - Example of condensed tannin

Phenolic acids are derivatives of benzoic and cinnamic acids (Benbrook, 2005) whose molecular structure is reported in Figure 29. The most abundant benzoic acid derivatives are p-hydroxybenzoic, vanillic, syringic and gallic acids, while common cinnamic acid derivatives include p-coumaric, caffeic, ferulic and sinapic acids. The derivatives differ in the degree of hydroxylation and methoxylation of the aromatic ring. Caffeic acid is the most abundant phenolic acid in berry fruits (Mattila et al., 2006), while coumaric acid is usually present at lower concentrations (Rice-Evans et al., 1997). Ferulic acid comprises 90% of total phenolic acids in cereals (Manach et al., 2004; Scalbert and Williamson, 2000). Benzoic acid is precursor of many extractive species, while cinnamic acid is precursor of the lignin building blocks.

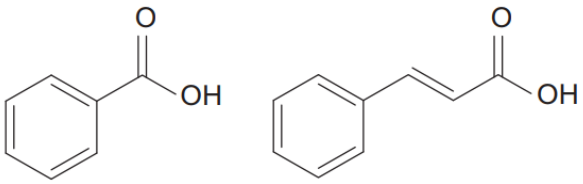

Figure 29 - Molecular structure of benzoic and cinnamic acids, precursors of the phenolic acids.

Hydrolysable tannins comprehend the chemical compounds formed by esterification of one or more gallic and/or ellagic acid units with a carbohydrate. In the free form, these acids tend to be less soluble in water than in the condensed form. Ellagic acid is formed after combination of two gallic acids by two esterification steps, whose structures are shown in Figure 30.

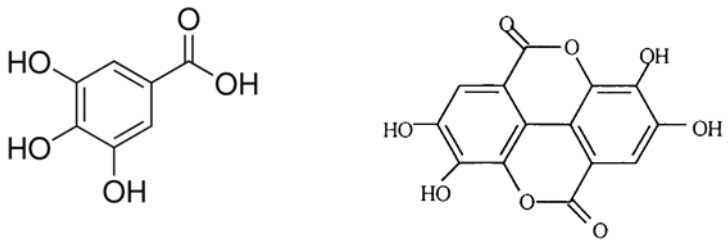

Figure 30 - Gallic and ellagic acid. The second is the result of combination of two gallic acids by two esterification steps.

The sugars in these type of tannins can be removed by hydrolysis in acid conditions, providing the name hydrolysable. These compounds are more commonly found in the leaves and bark of plants. Figure 31 shows two different hydrolysable tannins, glucogallin and corilagin, the first with one phenolic acid unit, and the second with three units. Some other species found are di- and tri-galloilglucose, acertannin, hamameltannin.

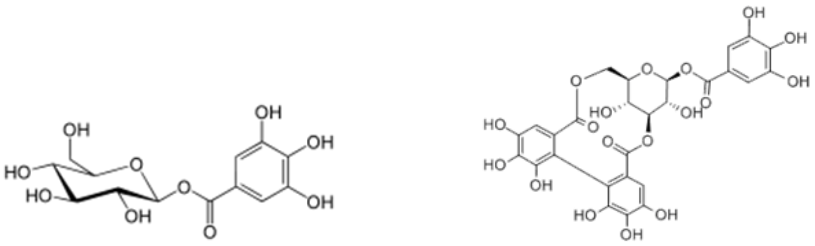

Figure 31 - Hydrolysable tannins. Glucogallin and corilagin.

In order to summarize this discussion, Table 8 reports and propose a classification the extractive compounds typically present in lignocellulosic biomass.

Classification		Species	Formula	C	H	O
Terpenes	Monoterpenes	α/β-Pinene	C10H16	0.882	0.118	0.000
		δ-Carene	C10H16	0.882	0.118	0.000
		Phellandrene	C10H16	0.882	0.118	0.000
		Camphene	C10H16	0.882	0.118	0.000
		Terpinolene	C10H16	0.882	0.118	0.000
		Terpinene	C10H16	0.882	0.118	0.000
		Limonene	C10H16	0.882	0.118	0.000
		Myrcene	C10H16	0.882	0.118	0.000
	Sesquiterpenes	α-Muurolene	C15H24	0.882	0.118	0.000
		Longifolene	C15H24	0.882	0.118	0.000
		α/β/γ/δ-Cadinene	C15H24	0.882	0.118	0.000
		Caryophyllene	C15H24	0.882	0.118	0.000
	Diterpenes	Abietic Acid	C20H30O2	0.795	0.099	0.106
		Pimaric Acid	C20H30O2	0.795	0.099	0.106
		Palustric Acid	C20H30O2	0.795	0.099	0.106
	Triterpenes	Squalene	C30H50	0.878	0.122	0.000
		Malabaricane	C30H56	0.865	0.135	0.000
		Oleanane	C30H52	0.874	0.126	0.000
	Tetraterpenes	β-Carotene	C40H56	0.896	0.104	0.000
		Lycopene	C40H56	0.896	0.104	0.000
		Lutein	C40H56O2	0.845	0.099	0.056
Fatty Acids	Free-fatty acids	Linoleic Acid	C18H32O2	0.771	0.114	0.114
		Oleic Acid	C18H34O2	0.766	0.121	0.113
		Palmitic Acid	C16H32O2	0.750	0.125	0.125
		Linolenic Acid	C18H30O2	0.777	0.108	0.115
		Capronic Acid	C6H12O2	0.621	0.103	0.276
		Butyric Acid	C4H8O2	0.545	0.091	0.364
	Triglicerydes	Trilinolein	C57H98O6	0.779	0.112	0.109
Unsaponifiable	Steroids	Retinol	C20H30O	0.795	0.099	0.106
		β-sitosterol	C29H50O	0.841	0.121	0.039
		β-sitostanol	C29H50O	0.841	0.121	0.039
Phenolic Compounds	Flavonoids	Catechin	C15H14O6	0.621	0.048	0.331
		Cyanidin	C15H11O6	0.627	0.038	0.334
		Gallocatechin	C15H14O7	0.588	0.046	0.366
		Taxifolin	C15H12O7	0.592	0.039	0.368
	Phenolic acids	Gallic Acid	C7H6O5	0.494	0.035	0.471
		Ellagic Acid	C14H6O8	0.556	0.020	0.424
		Caffeic Acid	C9H8O4	0.600	0.044	0.356
		Coumaric Acid	C9H8O3	0.659	0.049	0.293
		Salicylic Acid	C7H6O3	0.609	0.043	0.348
		Gentisic Acid	C7H6O4	0.545	0.039	0.416
		Benzoic Acid	C7H6O2	0.689	0.049	0.262
		Ferulic Acid	C10H10O4	0.619	0.052	0.330
		Sinapinic Acid	C11H12O5	0.566	0.057	0.377
	Hydrolysable Tannins	Corilagin	C27H22O18	0.511	0.035	0.454
		Chebulagic acid	C41H30O27	0.516	0.031	0.453
		Chebulinic acid	C41H32O27	0.515	0.033	0.452
		β-Glucogallin	C13H16O10	0.470	0.048	0.482
		Digalloyl glucose	C20H20O14	0.496	0.041	0.463
		Trigalloyl glucose	C27H24O18	0.509	0.038	0.453
		Acertannin	C20H20O13	0.513	0.043	0.444
		Hamamelitannin	C20H20O14	0.496	0.041	0.463

Table 8 - Summary and classification of extractive compounds typically found in lignocellulosic biomass.

2.1.4. Nitrogen, Sulfur, Ash, and Inorganics

Together with C/H/O, elemental analysis gives nitrogen and sulfur content by measuring NOx and SOx. Both N and S components are present in greater amounts in fast-growing and young tissues such as leaves and stems. Together with minor amounts of nucleic acids, chlorophyll, amino sugars, and alkaloids, most of nitrogen and around 60% of sulfur is present as amino acids.(35) The residual sulfur content, in the form of sulfates, remains partially in ash. Ash is formed by combusting inorganics under controlled conditions. The ashing temperature for biomass is 550 °C, whereas is 780 °C for coals. Chlorine, potassium, and sodium are readily released during high temperature combustion. The wood ash content is typically less than 1 wt %, whereas in grass it ranges from 2% to 10% or even up to 25% in rice husks. The ash content is sorted as major and minor elements. Major elements include Al, Ca, Fe, Mg, P, K, Si, Na, and Ti and are expressed in terms of their oxides. They have a major impact on ash melting, fouling and corrosion, whereas they have a low impact on environment. Herbaceous biomass are rich in K and Na have higher Si, and lower Ca content compared to wood. Typically, Ca and Mg increase the ash melting temperature, whereas Si, K, and Na decrease it. Thus, grass ashes have low melting temperatures, whereas higher melting temperatures are expected for wood samples. Minor elements include As, Cd, Co, Cr, Cu, Hg, Mn, Mo, Ni, Pb, Sb, V, and Zn. With respect to coal, biomass has higher amounts of K2O and Na2O. The content of phosphorus oxide, especially in willow, is quite larger than in coal lignite.(36) The Catalytic Effect of Ash section briefly discusses and models the relevant catalytic effect of ash in pyrolysis process.

2.2. Algae Biomass

As already mentioned, the compositional profile of algae widely differs from lignocellulosic biomass. They are eukaryotes macro or micro photosynthetic organisms that can substantially be found in every natural or artificial water environments (oceans, seas, lakes, rivers, ponds, and wetlands), where solar or artificial light is present [114]. They can be classified in several ways by different criteria such as structural characteristics, membrane composition, pigments color, and energy-storing molecules [115]. A univocal taxonomical classification of algae is complex and is not yet available. We propose to simply classify algae depending on their unicellular or multicellular nature, and on their predominant pigment color. In this way, six groups were defined: green, yellow-green, blue-green, brown, red, and diatoms [6, 114]. Cyanobacteria constitute the blue-green group, and they are not real algae. They are frequently called algae because they are photosynthetic unicellular organisms

(prokaryotes) [114]. Table 9 reports the most common algae species studied and their classification with the proposed criteria.

Group	Species	
Green	Chlorella sp., Cladophora sp., Dunaliella sp.	Unicellular and Multicellular
Yellow-Green	Nannochloropsis sp., Schizochytrum sp.	Mostly Unicellular
Blue-Green	Arthrospira sp. (Spirulina), Synechoccus sp.	Unicellular (prokaryotes)
Brown	Fucus sp., Macrocyctis p., Laminaria sp.	Mostly Multicellular
Red	Gracilaria sp., Hypnea sp.	Mostly Multicellular
Diatoms	Phaeodactylum sp., Nitzschia sp.	Unicellular

Table 9 - Classification of algae species

For inhabiting aquatic environments, they do not need to develop a solid support structure, which in lignocellulosic biomass is a complex matrix of cellulose, hemicellulose and lignin. Thus, algae constituents are mainly active metabolic compounds, whose distribution is highly influenced by nutritional and environmental conditions [95, 116-118]. As seen in Table 5, proteins and lipids are dominant in unicellular algae. Carbohydrates are higher in macro algae, which require extracellular polysaccharides for protection and cell-to-cell adhesion. The algae degradation products are usually classified as originated from protein, carbohydrate, and lipid species. In particular, the lipid content can vary significantly from species to species. A wide range of furan derivatives is also observed, which are more numerous than those from terrestrial biomass, although some similar bio-markers such as furfural and furaldehyde are present in both [117]. In addition, important sugar structural units for macroalgae appears to be di-anhydrous mannitol. Thermogravimetric analysis of algae fuels show large differences with respect to the decomposition of lignocellulose type materials. The main differences between the thermal decomposition of aquatic and terrestrial biomass are that algae release a significant amount of nitrogen containing compounds, linear chain alcohols, and an absence of methoxy-phenols, typically attributed to lignin pyrolysis [119]. The nitrogen-released compounds are mainly in the form of organic nitrites, nitriles, amines, amides, indoles, pyrroles and their derivatives [120, 121].

2.2.1. Proteins and nitrogen species

As already shown in Table 5, nitrogen content in algae overcomes 10 wt.%, and proteins account generally for 75–90 wt.% of this quantity [122, 123]. The remaining portion is contained in inorganics, chlorophylls, and nucleic acids.

2.2.1.1. Proteins

Proteins are long chains of polymerized amino acids, also involved in cell structure. They are very active in the metabolism, they act as catalyst for reactions, antibodies, and are vehicle for the transport of atoms and small molecules. They are produced based on DNA and RNA instructions, which determine the sequence of amino acids composing proteins. Algae rich in proteins are of high interest for food and feed industries [124]. Table 10 reports the composition and the range and average frequency of different amino acids in each algae group [125]. Amino acids are also sorted by their side substitutions in terms of aliphatic, aromatic, acid, sulfur, alcoholic, basic, and cyclic. The individual frequency of aliphatic and acid groups sums up to more than 50% of the total amino acids, with the highest frequency of aspartic and glutamic acids, together with alanine, leucine, arginine, lysine and glycine [126, 127].

Amino Acid (wt.%)	Green macro	Green micro	Red macro	Red micro	Brown	Blue–green	Yellow–green	Diatoms	Average	Group
Alanine $C_3H_7NO_2$	6–8	6–12	5–9	6–8	5–10	7–10	5–12	6–8	8.18	Aliphatic
Leucine $C_6H_{13}NO_2$	6–10	6–11	4–10	6–9	4–9	5–10	9–10	6–9	8.17	
Glycine $C_2H_7NO_2$	5.5–7.5	5–8	5–7	5.3–7.3	6–10	5–8	6–10	4–6.5	6.26	
Isoleucine $C_6H_{13}NO_2$	3–5	3.5–4.5	3.5–5	4–5.7	2.5–5	4–6.5	4–5	4.3–6	4.34	
Valine $C_5H_{11}NO_2$	4.5–7	4–6.5	4–6.2	4.8–5.4	4.5–6.5	6–8.5	3.5–6.5	5–7	5.97	
Glutamic acid $C_5H_9NO_4$ + Glutamine $C_5H_{10}N_2O_3$	9–16	10–14.5	5.5–17	5.5–7.5	9–22	10–15	11–14	11.5–18	12.5	Acid
Aspartic acid $C_4H_7NO_4$ + Asparagine $C_4H_8N_2O_3$	9–16	8.5–14	0.7–14.7	1–2	10–15	7.5–13	9–10.5	10–14	11.22	
Cysteine $C_3H_7NO_2S$	0.5–3	0.2–2	3.5–5.5	4–6	0.5–1.5	0.1–1	0.2–1.3	0.5–5	0.73	Sulfur c.
Methionine $C_5H_{11}NO_2S$	0.7–3	0.2–2.5	0.7–9.7	6–7	1–3	1–2	0.3–3	1–3	1.96	
Phenylanine $C_9H_{11}NO_2$	4–7	4.5–6.3	5–9	6–9	1.5–6	1–6	5–5.5	4.7–6.5	5.13	Aromatic
Tryptophan $C_{11}H_{12}N_2O_2$	n.d	1.8–6.5	0.5–4	2.5–3	0.5–8	0.2–6.6	1.3–2.3	n.d	1.28	
Tyrosine $C_9H_{11}NO_3$	1–4.5	2.8–4.4	2.5–6	3–5	2–6.5	4–8	2.5–4	2–4	3.37	
Lysine $C_6H_{14}N_2O_2$	5–7.5	5.5–8.5	5–8	6–8.5	4–7.5	4.6–7	6.5–7	4.5–7.5	6.39	Basic
Histidine $C_6H_9N_3O_2$	1.5–3.5	1–3	2–7	5–9	1.5–3	1–2	1–2	1.5–2.5	2.54	
Arginine $C_6H_{14}N_4O_2$	3.5–7	4–10	4.5–6	4.4–6.4	4–10	5.5–10	6–6.5	5–8	6.51	
Serine $C_3H_7NO_3$	5–6.5	4–7.5	5–7	2.5–5.5	4–7.5	4.5–7.5	4.5–7	4.5–7.5	5.31	Alcoholic
Theronine $C_4H_9NO_3$	3.7–6	3–6	4–5.5	4.5–7	4–6	4.5–6.5	4.4–6.4	4.5–6	4.95	
Proline $C_5H_9NO_2$	4.5–8	3–6	2–5.5	4.5–6	4–8	2–4.5	4.5–9	4–6.7	4.62	Cyclic

Table 10 - Average frequency of amino acids in algae

Although the frequency of amino acid distribution from one algae group to another is not deeply different, this information refers to global quantities of amino acids in the sample. One single cell produces thousands of different proteins with different amino acid composition. It remains important to identify the specific composition of some typical proteins produced by algae. summarizes the composition of some of these proteins from algae samples, as estimated through the dedicated NCBI database [128].

PROTEINS IN ALGAE	O/C (wt.)	H/C (wt.)
Actin. Chlorella $C_{1406}H_{2204}O_{419}N_{366}S_{16}$	0.40	0.13
Actin. Spirulina $C_{1270}H_{2000}O_{399}N_{326}S_{14}$	0.42	0.13
Histone H3. Spirulina $C_{543}H_{904}O_{151}N_{170}S_2$	0.37	0.14
NADH dehydrogenase subunit 2. Spirulina $C_{1425}H_{2060}O_{349}N_{334}S_{17}$	0.33	0.12
Photosystem II D2 protein. Nannochloropsis g. $C_{1859}H_{2738}O_{489}N_{460}S_9$	0.35	0.12
S-adenosylmethionine mitochondrial carrier protein. Nannochloropsis g. $C_{2156}H_{3463}O_{651}N_{607}S_{14}$	0.40	0.13
RNA binding protein. Nannochloropsis g. $C_{1941}H_{2942}O_{609}N_{552}S_{16}$	0.42	0.13
Actin. Nannochloropsis g. $C_{1862}H_{2921}O_{561}N_{491}S_{20}$	0.40	0.13
Photosism Fucus v. $C_{1827}H_{2681}O_{476}N_{453}S_{12}$	0.35	0.12
30S Ribosomal protein. Fucus v. $C_{1399}H_{2226}O_{372}N_{350}S_5$	0.35	0.13
Hypothetical protein. Spirulina subsalsa $C_{8234}H_{12895}O_{2419}N_{2269}S_{57}$	0.39	0.13
Hypothetical protein CHLNCDRAFT_142385$C_{2993}H_{4694}O_{973}N_{800}S_{17}$	0.43	0.13
GDP-4-keto-6-deoxy-D-mannose epimerase-reductase. partial [Laminaria digitata]$C_{1557}H_{2412}O_{456}N_{416}S_{19}$	0.39	0.13
Photosystem II thylakoid membran protein. partial (plastid) [Laminaria digitata] $C_{1752}H_{2568}O_{455}N_{428}S_9$	0.35	0.12
Phosphoglycerate kinase. partial [Laminaria digitata] $C_{163}H_{2654}O_{508}N_{430}S_{11}$	0.41	0.13
Poly(A) binding protein I. partial [Nannochloris bacillaris] $C_{3813}H_{5984}O_{1173}N_{1060}S_{23}$	0.41	0.13
Peptidyl-prolyl *cis*-trans isomerase [Nannochloris bacillaris] $C_{1922}H_{3026}O_{630}N_{550}S_{23}$	0.44	0.13
Glycoprotein [Porphyridium sp. UTEX 637] $C_{2878}H_{3942}O_{813}N_{686}S_{19}$	0.38	0.11
Lipoprotein [Arthrospira platensis str. Paraca] $C_{2724}H_{4379}O_{879}N_{777}S_{14}$	0.43	0.13
Low-density lipoprotein [Nannochloropsis gaditana] $C_{5591}H_{8724}O_{1572}N_{1552}S_{45}$	0.37	0.13

Table 11 - Typical proteins produced by some algae species.

2.2.1.2. Other nitrogen containing components

Nitrogen is also present as nitrites (NO_2^-), nitrates (NO_3^-), ammonium (NH_4^+). These species devolatilize at high temperatures under pyrolysis and combustion conditions leaving metal oxides as ash. The inorganic fraction usually does not exceed 10-15% of total nitrogen in algae [123]. Nevertheless, this fraction can become significant when global contents of nitrogen are elevated.

Besides the essential role of nucleic acids for the existence of life, transmitting the genetic code of species on reproduction, they are present only in reduced fractions of the total biomass weight. They are N-containing species which form linear polymers of nucleotides which are made up of three specific units: a nitrogenous base, a pentose sugar, ribose or deoxyribose and a phosphate group. When the sugar is a ribose, it forms a single strand folded onto itself called RNA (ribonucleic acid). A DNA (deoxyribonucleic acid) paired double strand chain is formed when deoxyribose is the connecting sugar. The nitrogenous bases are adenine, cytosine, guanine, thymine (in DNA only) and uracil (in RNA only) and are attached to sugar by an N-glycosidic bond. The phosphate group connects to two sugar rings through a phosphodiester bond, forming the polymer chain. Figure 32 shows the five possible conformations of the nucleotides.

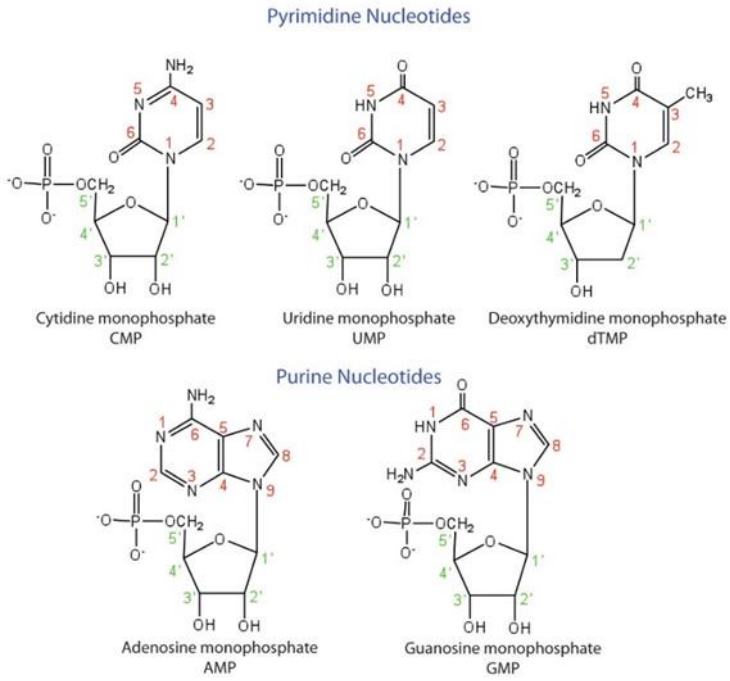

Figure 32 - The five possible nucleotides

Together with the nucleic acids, the pigments play an essential role for the maintenance of life. They are responsible for the absorption of energy from light, providing the necessary input to fix CO_2 and H_2O into sugar molecules. Chlorophyll is present in different configurations, having a cyclic polypyrrolic structure with a magnesium atom in the center in common for all variations [129]. The differences in the structure allow to capture different light wave lengths, providing also different colors to the species. Figure 33 shows the structure of chlorophylls of type a, b, c1 and c2, which are the most common. Despite their essential role, pigments are only present in minor or even negligible percentages compared to main compounds.

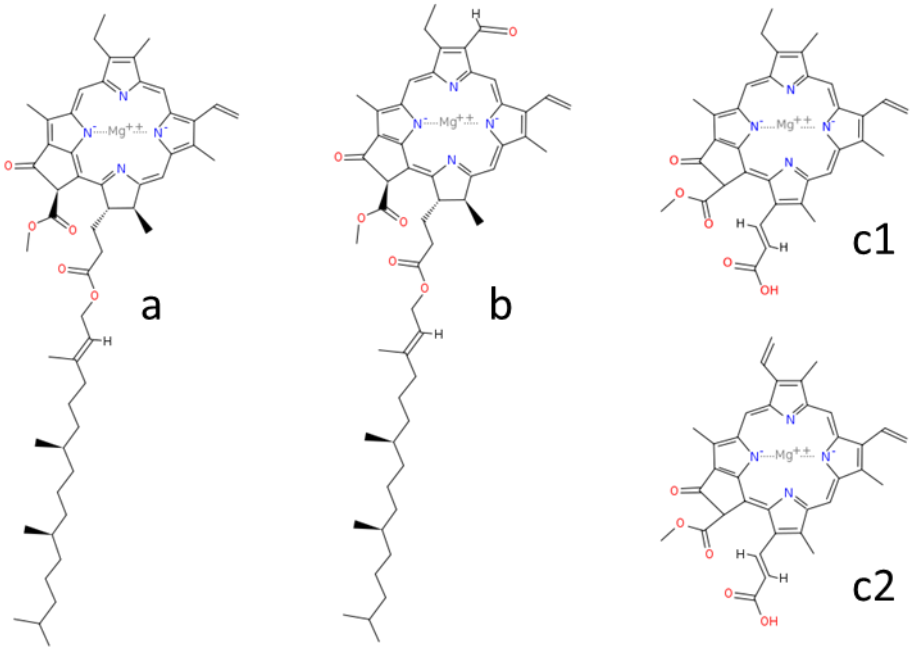

Figure 33 - Main chlorophyll configuration present in plants and algae.

2.2.2. Carbohydrates

Sugars or carbohydrates are the main products of photosynthesis, having different distributions in the different algae species. Glucose is often the most present monomer for many species [91], cellulose, hemicellulose and pectin are present in the cell membranes mainly of green algae, whereas starch is found in the cytoplasm as energy storage. Lipopolysaccharides and peptidoglycan are the main sugars in blue algae [130]. Red algae produce agar, carrageenan and cellulose in the cell walls, together with a more branched starch in cytoplasm [131]. Mainly mannitol ($C_6H_{14}O_6$), laminarin $(C_6H_{10}O_5)_n$, alginic acid $(C_6H_8O_6)_n$, and fucans are found in brown algae. Mannitol is a primary product of photosynthesis, it is a sugar alcohol derived from the six carbon sugar D-mannose and can

reach 5–25 dry wt.%. Fucans or fucoidan are the sulphated polysaccharides present in brown algae up to 5–20% of algae dry weight. They are mainly composed of L-fucose (a six carbon sugar) with small proportions of other sugars, such as mannose, galactose, xylose and glucuronic acid. These different sugars are richer in oxygen when compared to cellulose $(C_6H_{10}O_5)_n$, which is present only in minor amounts [132]. Most of the sugars are polysaccharides and their respective monomers are very similar, with different substitutions to the same original molecule [131, 133].

The degradation of algae carbohydrate is different from cellulose pyrolysis. Alginates are linear unbranched polymers constituted by (1,4)-linked D-mannuronic and L-guluronic acid residues. This polymer decomposes in a different way than cellulose, which consists of D-glucose monomers linked by β-glycosidic bonds. There are two main types of carbohydrates in brown seaweed, those with β-1,3 linkages (e.g. laminarin and mannitol) and those with β-1,4 linkages (e.g. amylopectin, amylose) roughly equivalent to starch in lignocellulosic biomass. These structural differences explain the large formation of anhydrous mannitol rather than levoglucosan [117]. Figure 34 shows the different structures of sugars found in algae. When compared to the typical structure of cellulose and hemicellulose, algae sugars are quite different, providing important features for the algae metabolism.

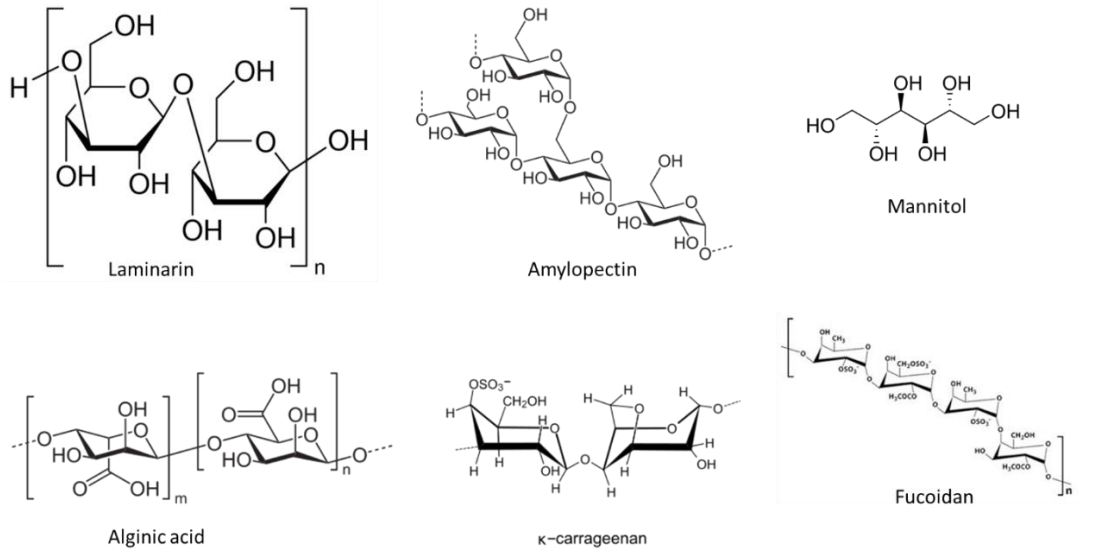

Figure 34 - Some sugars present in algae.

2.2.3. Lipids

When compared to lignocellulosic biomass, algae produce very similar lipids, that also play both structural and energy storage roles as they are present as phospholipids,

glycolipids, fatty acids and triglycerides. Different from higher plants, algae have most of the lipids as free fatty acids, with particular presence of eicosapentanoic acid, quite rare in plants [134]. Total amount of lipids widely varies among different algae, ranging from less than 5% in brown, up to 50% in yellow-green algae [135, 136]. Fatty acid chains commonly contain 14–20 carbon atoms, and 18 carbon fatty acids are the most frequent [137]. Weight composition of typical fatty acids found in algae show very similar elemental composition (C=73-78% and H=11-13%), with moderate variations in carbon number and unsaturation degree [138]. Unsaturated fatty acids in cis configuration, are the most abundant [139].

2.2.4. Inorganics and ash

As already mentioned in discussing nitrogen content, the inorganics in algae are measured through the ash content, which is usually obtained through standard analytical methods, under complete combustion at 550 or 800 °C. The metal oxides contained in ash (e.g. sodium (Na), calcium (Ca), potassium (K), magnesium (Mg), among others) are mainly present in the raw algae as carbonates (CO_3^{2-}), nitrates (NO_x^-), sulphates (SO_x^{2-}), phosphates(PO_x^{3-}), and chlorates (ClO_x^-). Thus, these inorganics decompose into oxides, releasing a volatile fraction during the combustion process. Their presence can promote catalytic effects during the thermochemical conversion of organic matter, both on pyrolysis and oxidation steps.

3. Conclusions

Under the light of a large set of experimental data collected and reported in the Appendix A, this chapter provided essential information to support all the steps of the activities developed during this thesis. This investigation revealed the complexity of lignocellulosic and algae biomass composition. Despite some similarities, these two groups present significant differences in both the biochemical species present and their distribution in the samples. Significant compositional variability also exists among different plants and algae species, their different organs and also depending on environmental and nutritional conditions.

There are many analytical methods often used by the scientific community. However, these methods not always provide similar results, creating some uncertainties about the sample composition. The most abundant and standardized data is the elemental/ultimate composition, which provides the composition in terms of the main atoms carbon, hydrogen, oxygen and nitrogen, sometimes with other elements of minor concentration. For modeling biomass thermochemical conversion, the elemental composition is not sufficient, as the biochemical species distribution in the sample is required for describing their decomposition path.

Moreover, for modeling purposes, the whole spectrum of compounds described above need to be reduced into a few representative compounds. Therefore, the next chapter will describe the selection and definition of these compounds, which will be called reference species. Furthermore, in order to overcome the gap between the compositional data available in the literature, a characterization method will be presented. The method requires only the elemental composition of the sample, and returns a biochemical composition in terms of these reference species

CHAPTER 3

BIOMASS CHARACTERIZATION

The discussion presented in this chapter is the first modeling step of this work. From all the compositional information obtained and discussed in chapter 2, we first present a selection of chemical species that are essential for the modeling the thermochemical conversion of both lignocellulosic and algae biomass. This selected species will be called reference species along this work. They are the representation of real and lumped species, and will be used to both characterize and describe the thermal behavior or complex biomass. After the definition of the reference species, we describe the proposed characterization method which allows to estimate the biochemical composition of a sample simply using the elemental composition. Then, the validity and correlation index of this method is evaluated.

1. Selection and definition of reference species

The distribution of biomass decomposition products (water, sugars together with smaller quantities of aldehydes, ketones, alcohols, phenolic compounds, along with light gases, and biochar) significantly changes depending on the biochemical composition. As already mentioned, biomass composition is often available only in terms of ultimate and elemental analysis. Referring to the database reported in the appendix A, Figure 35 and Figure 36 show the scatter diagrams of cellulose, hemicellulose, lignin, and extractive

amounts versus the weight content of carbon and hydrogen in the different lignocellulosic biomass samples. Just a fraction of the database is reported in these plots because only some samples had both their elemental and biochemical analysis available. It is clear that there is a large variability of the amounts of these components, and it seems difficult to find well-defined trends. In order to allow some observations, the data is represented with different symbols for hardwood, softwood, cereals, and grasses. From this perspective, it is possible to recognize that relevant differences exist between the composition of wood and grass/cereal samples. For example, cellulose is more abundant in wood biomass, while hemicellulose amounts are larger in grasses and cereals. Thus, wood plants have higher cellulose/ hemicellulose ratios. Extractives are more abundant in grass plants, while lignins are more abundant in shells.

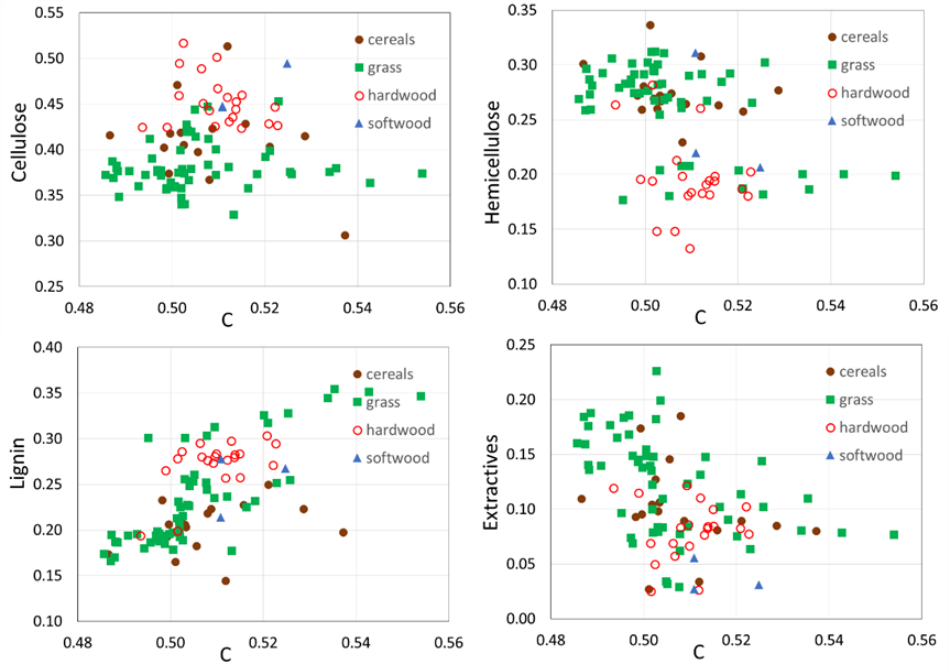

Figure 35 - Scatter plots of biomass composition (cellulose, hemicellulose, lignin, and extractives) versus the carbon content (weight fraction).

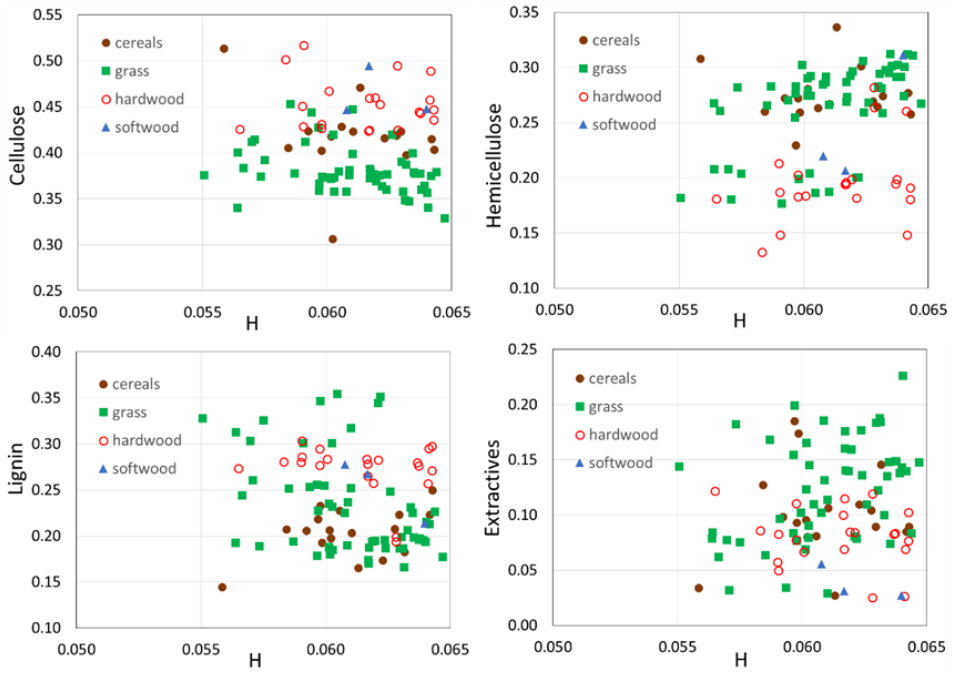

Figure 36 - Scatter plots of biomass composition (cellulose, hemicellulose, lignin, and extractives) versus the hydrogen content (weight fraction).

When direct information on biochemical composition is unavailable, cellulose, hemicellulose, lignin, and extractive content can be derived through the elemental biomass composition in terms of C/H/O [82, 109, 140]. The C/H/O atomic balances allow to estimate a suitable combination of a few reference species. Cellulose, hemicellulose, lignin, and extractives constitute the largest portion of the lignocellulosic biomass. Therefore, despite some specific sample variabilities such as polymerization degree, these components must be represented by reference species. This first simplification step is similar to defining lumped species that allow the definition of surrogate fuels. For example, gasoline is often described as a mixture iso-octane and n-heptane, and the ratio is defined based on the fuel octane number.

1.1. Lignocellulosic Biomass

Despite the crystallinity and polymerization degrees, cellulose remains very similar in all lignocellulosic biomass sources. Because of the homogeneity of the monomers composing its structure, one single species is capable of proper describing the composition of cellulose. Therefore, the monomer anhydrous glucose, for now on called CELL, is the reference species for cellulose.

As the spectra of sugars building hemicellulose chain, similarly to those of cellulose, have a global molecular formula of $C_n(H_2O)_n$, no significant difference exists in their elemental

composition. However, these sugars are present as pentoses and hexoses, and their decomposition behavior is significantly different, not only on reactivity, but also on the products released. This said, we defined two monomers: HCE1 and HCE2, that have the same molecular composition but decompose in different paths, as will be shown in the next chapter. The idea behind this definition is to describe the decomposition of HCE1 as hexoses and HCE2 as pentoses. Thus, a linear combination of those two reference species are able to, in a very simple approach, characterize the decomposition of different hemicelluloses according to the sugars distribution in the chain. Furthermore, we could identify that both sugar distribution and decomposition profile is similar within the same group of plants (softwood, hardwood, and grass/cereal), but quite different among these groups. Therefore, a standard ratio HCE1:HCE2 for each group was defined. By using these combinations, we defined three standard reference hemicelluloses: GMSW for softwoods, XYHW for hardwoods, and XYGR for grasses and cereals.

Different from the previously mentioned components, lignin samples differ both in composition, decomposition profile and distribution of pyrolysis products. In this context, a single reference species is not enough to characterize this complex and amorphous component. After understanding that, despite these complexities, lignin could be represented by the combination of three reference species, all deriving from the same parent molecule, but with different degrees of methoxylation. This definition allows the characterization of a wide range of lignin samples as a linear combination of those three reference species, that have significant different elemental composition. Because of these differences, the reference species received the names LIG-C, LIG-H and LIG-O, of which the last letter on their names represents the element of major presence when compared to the others. All these species are based on a β–O–4 skeleton. The reference unit LIG–C is representative of a softwood lignin, without methoxyl groups and with the largest amount of carbon. LIG–O and LIG–H, which are richest in O and H respectively, contain methoxyl groups and are more representative of the structures of hardwood lignin. These reference compounds also differ in terms of the aliphatic and oxygenated side groups bound to the basic structure of β–O–4.

The diversity of extractive compounds present in biomass makes the definition of reference species a hard task. In order to keep the simplicity and characterize with good global agreement, choosing the species that are present in a larger number of samples and in higher amounts is the best option. In terms of elemental composition, hydrophobic

extractives share more similarities, containing high amounts of hydrogen. Most lignocellulosic biomass have triglycerides in their composition, and the most common chain of fatty acid has 18 carbons with one unsaturation. Therefore, the trilinolein molecule was defined the reference species for this group of extractives. Hydrophilic extractives, on the other hand, are generally rich in oxygen, and condensed tannin is quite common to be found in many feedstock. Thus, a single monomer from the polymeric structure of condensed tannins was defined as the reference species for this group. In this very simplified approach, two lumped extractive species, trilinolein (TGL) and condensed tannin (TANN) represent the whole variety of extractive compounds. Of course this selection is not the only possible, and the flexibility of this model allow the inclusion of many more species if wanted or needed. For atypical biomasses, containing other extractives in high amounts, using more specific reference species could be useful. Nevertheless, the present work aims to propose a global model, remaining flexible when additional information is available.

Figure 37 shows the molecular structure of the reference species for lignocellulosic biomass characterization. It is clear that, except for TGL, these species are monomers representing larger polymeric structures. The composition of trilinolein is $C_{57}H_{98}O_6$, but for simplicity reasons, one water molecule was added to this structure, resulting in the TGL composition reported in Figure 37. The reason for this modification will be explained in the chapter 4 and 5.

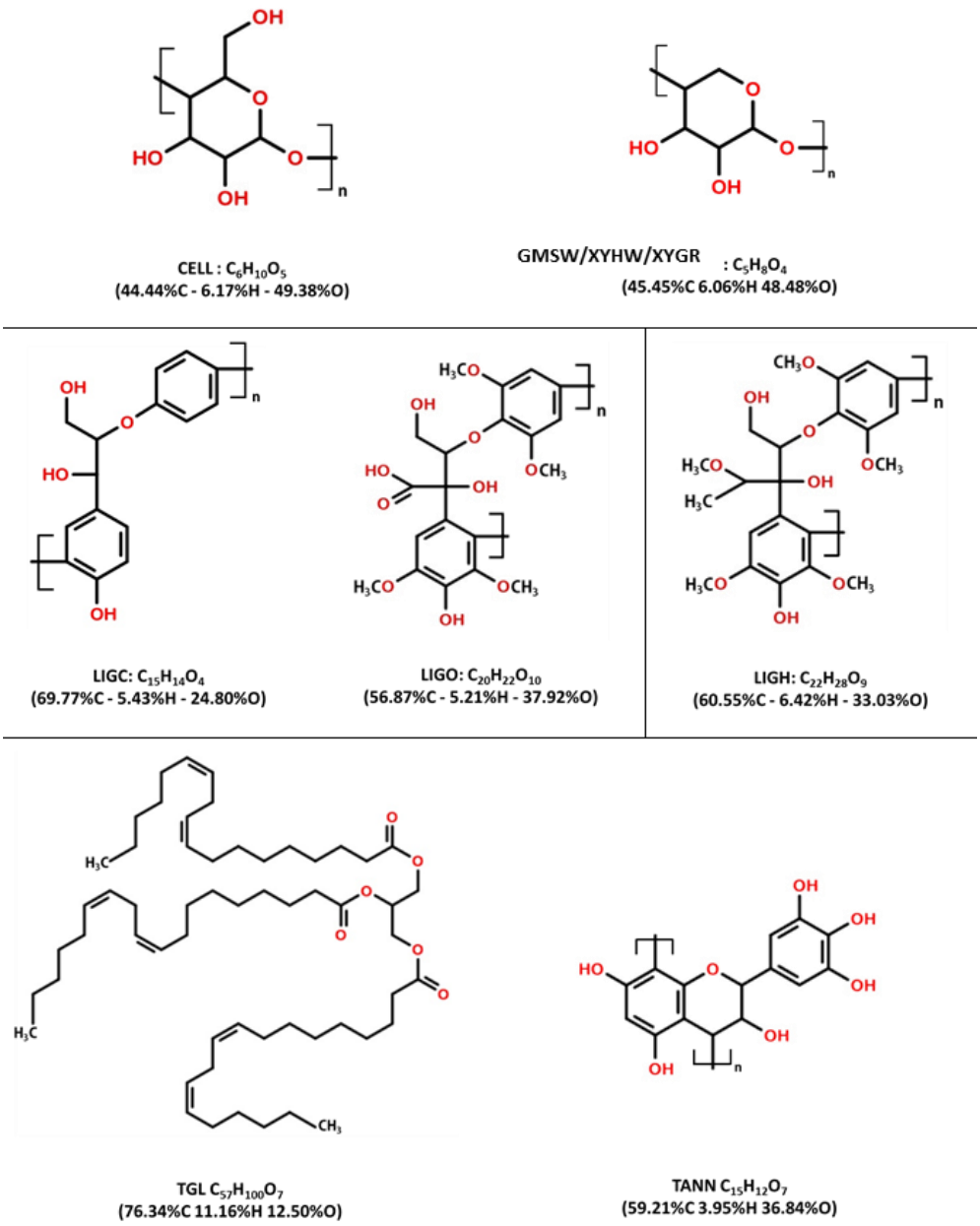

Figure 37 - Reference species for biomass characterization

1.2. Algae Biomass

As macroalgae are significantly richer in sugars than microalgae, the definition of a reference species must take into account the distribution of polysaccharides present in the first group. A lumped reference component with the same formula of alginic acid, here called simply as SUGAR $C_6H_8O_6$ is selected as representative of carbohydrates in algae. This species groups and lumps the average mixture of alginic acid, glucose, mannitol, laminarin and fucoidan [141].

For having a similar distribution of fatty acids, it would be very convenient to use TGL as reference species for lipids in algae. However, as already explained, algae contain lipids as free fatty acids, and they have a very different pyrolysis profile. Together with this molecules, some other heavier hydrophobic compounds are also present, which are usually extracted and accounted together with lipids. Therefore, we defined the reference species LIPID ($C_{18}H_{32}O_2$), which received the composition of linoleic acid, the most abundant species.

As already discussed in Chapter 2, nitrogen content in algae can overcome 10%, and proteins account generally for 75–90% of total nitrogen content[122, 123]. Thousands of different proteins with different amino acid composition are present in a single cell. The selection of one single reference protein is not flexible enough, because of the large amount and variety of proteins in algae. In a very similar approach to lignins, three lumped reference proteins were defined: PROT-C ($C_{500}H_{450}O_{65}N_{80}$), PROT-H ($C_{400}H_{900}O_{150}N_{86}$) and PROT-O ($C_{250}H_{500}O_{200}N_{72}$), which are richer in C, H and O, respectively. These reference proteins are equivalent to asymptotic protein fragments or oligomers of different amino acids, and their linear combination allows to represent the whole variety of elemental composition of proteins contained inside the triangle defined by these reference proteins.

Moreover, based on their internal composition, a fixed nitrogen amount of 13 wt.% is assumed as average protein composition. Although the weight fraction of nitrogen is different among the amino acids, the global nitrogen in typical algae proteins do not vary in the same proportion. Assuming that all the organic nitrogen is in proteins is a reasonable assumption as no other organic compound is present in such high amounts. However, mainly in samples containing elevated amounts of nitrogen, the inorganic fraction of nitrogen becomes significant and must not be neglected. This contribution proved to be useful in order to characterize algae with high ash and nitrogen content, which will be explained along the text.

In order to better characterize the volatiles from the pyrolysis of algae with high ash content, dissociation of carbonates, nitrites/nitrates and ammonium salts are considered by assuming a release of CO2, NO and NH3 species as a function of the amount of ash, given from the proximate and elemental analysis. Indeed, there is a significant presence of carbonates in algae and we assume that CO2 is released as volatile. From a quantitative point of view, we assume that about 1/3 of inorganics are carbonates, able to release CO_2 [142]. Similarly, about 10% of total algae nitrogen is assumed as an equimolar mixture of NO and

NH3, released by inorganics. Of course, a complete knowledge of ash composition and relating salts could improve these assumptions.

2. Van Krevelen Diagram

The Van Krevelen diagram is a graphical plot developed by Dirk Willem van Krevelen (TU Delft) and which was originally used to explain the origin and maturity of fossil fuels. The diagram cross-plots the hydrogen:carbon (hydrogen index) as a function of the oxygen:carbon (oxygen index) atomic ratios of carbon compounds. Figure 38 shows an example of this diagram, highlighting the composition evolution of solid fuels from fresh biomass to the highest rank anthracites. It is worth to mention that a progressive dehydration takes place from biomass to lignite, whilst dehydrogenation is the main process from medium rank coals to anthracites. Synthetic compounds such as graphene and carbon nanotubes are structures with no hydrogen and oxygen, and would be represented in the intersection of the x and y axis of this plot.

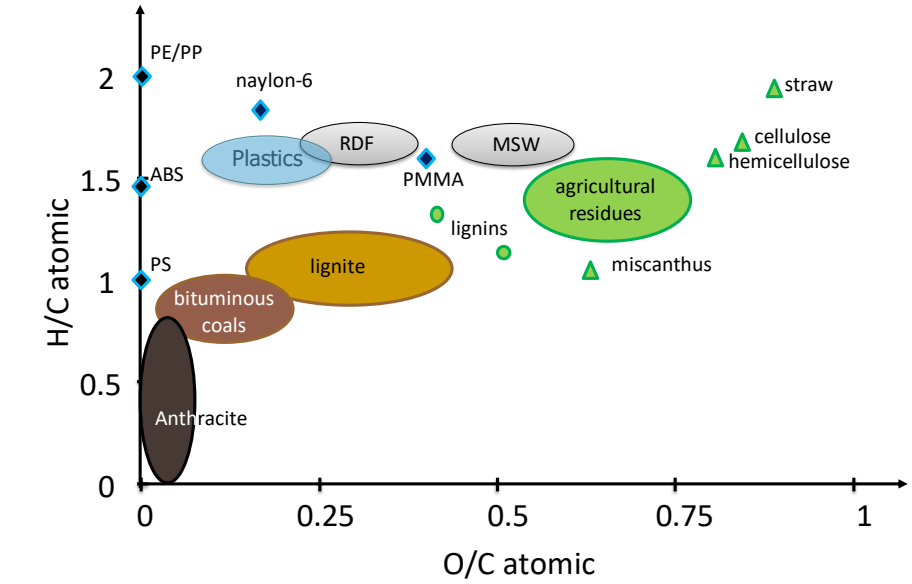

After: R.H. Hurt (1998) "Structure, properties, and reactivity of solid fuels." 27th *Symposium on Combustion*. 2887-2904

Figure 38 - Van Krevelen diagram reporting the composition of some solid fuels (after Hurt [143])

Table 12 summarizes the composition of both lignocellulosic and algae reference species. Lignocellulosic reference species are then reported in Figure 39 in a Van Krevelen diagram, together with the biomass samples from the database, which is quite useful to provide an overall graphical view of the problem. In the present work, we prefer to use mass index ratios instead of molar.

Biomass Compound	Ref. Species	Formula	Wt.%				Wt. ratio	
			C	H	O	N	H/C	O/C
Lignocellulosic Biomass								
Cellulose	CELL	$C_6H_{10}O_5$	44.4	6.2	49.4	-	0.139	1.111
Hemicellulose	GMSW	$C_5H_8O_4$	45.5	6.1	48.5	-	0.133	1.067
	XYHW							
	XYGR							
Lignin	LIG-C	$C_{15}H_{14}O_4$	69.8	5.4	24.8	-	0.078	0.355
	LIG-H	$C_{22}H_{28}O_9$	60.6	6.4	33.0	-	0.106	0.545
	LIG-O	$C_{20}H_{22}O_{10}$	56.9	5.2	37.9	-	0.092	0.667
Extractives	TANN	$C_{15}H_{12}O_7$	59.2	3.9	36.8	-	0.067	0.622
	TGL	$C_{57}H_{100}O_7$	76.3	11.2	12.5	-	0.146	0.164
Algae Biomass								
Sugars	SUGAR	$C_6H_8O_6$	40.9	4.6	54.5	-	0.111	1.333
Lipids	LIPID	$C_{18}H_{36}O_2$	77.2	11.4	11.4	-	0.148	0.148
Proteins	PROT-C	$C_{500}H_{450}O_{65}N_{80}$	69.7	5.2	12.1	13.0	0.075	0.173
	PROT-H	$C_{400}H_{900}O_{150}N_{86}$	51.5	9.7	25.8	13.0	0.188	0.500
	PROT-O	$C_{250}H_{500}O_{200}N_{72}$	38.9	6.5	41.6	13.0	0.167	1.067
Carbonates	CO2i	CO_2	27.3	-	72.7	-	-	-
Inorganic N.	NH3NO	N_2H_3O	-	6.4	34.0	59.6	-	-

Table 12 – Summary of elemental composition of reference species for biomass characterization.

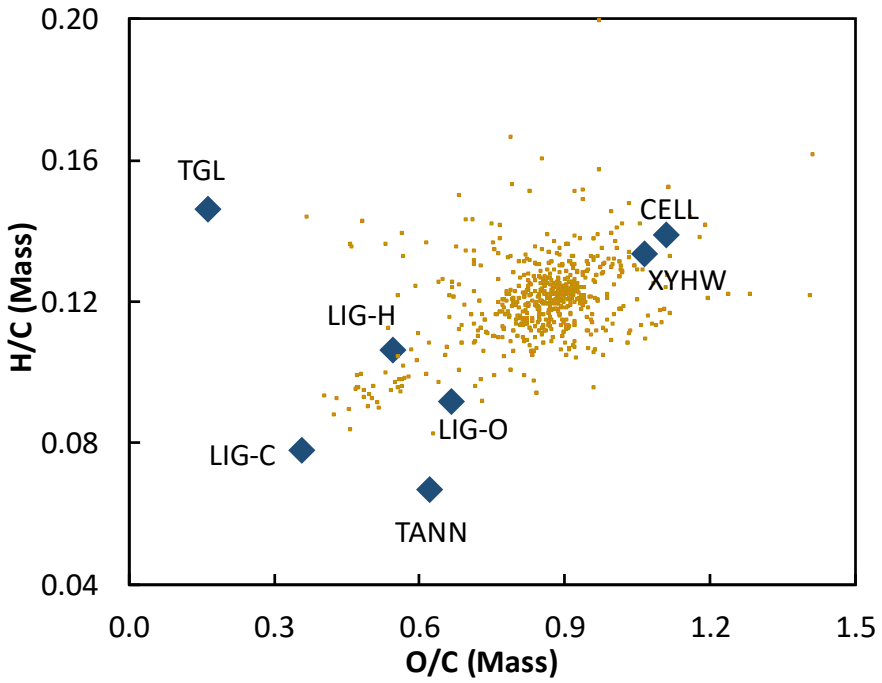

Figure 39 - Van Krevelen diagram: lignocellulosic biomass samples and the reference species

It is clear that the composition of biomass samples is very spread on the plot. The reference species have boundary composition towards different directions. Any sample can easily be characterized by combining two reference species, respecting the atomic mass balances, when it falls within the line connecting those two reference species. It is also possible to characterize a sample by linear combination of three reference species, when it falls within the triangle formed by using these reference species as vertices. However, it is well known that biomasses are a combination of several species, which makes the characterization a very complex process, when only the elemental composition is known. The solution found for stablishing a general characterization method is to consider, not two or three, but all the reference species. This solution, however, involves several degrees of freedom, which are only properly defined by knowing the general biochemical composition of biomass, and how it tends to change from one group to another. This knowledge was only possible to obtain after having access to a large amount of experimental data, contained in the database.

3. Characterization of Lignocellulosic Biomass

3.1. Characterization when biochemical composition is available

As already discussed, not many samples have a detailed biochemical composition available. But in the cases that it is present, we can directly benefit from these data for characterization. For example, Hybrid Poplar [84] composition and proposed characterization is reported in Table 13. The experimental amounts of Cellulose, Hemicellulose, Lignin and Extractives is 42.50/18.10/27.30/12.10 wt.%. Using only the available data, without taking further assumptions, the characterization considers all cellulose as CELL and all hemicellulose as XYHW (because the biomass is a hardwood sample). Lignin content is considered an equal combination of the three reference species of lignin. Finally, extractives are also considered to be equally distributed among the two reference species TGL and TANN.

Experimental data		Characterization	
Cellulose	42.50	CELL	42.50
Hemicellulose	18.10	XYHW	18.10
Lignin	27.30	LIG-C	9.10
		LIG-H	9.10
		LIG-O	9.10
Extractives	12.10	TGL	6.05
		TANN	6.05

Table 13 - Characterization of Hybrid Poplar (NREL). Direct correspondence of biochemical composition with reference species.

This is the simplest possible characterization for such a biomass. Of course, a more accurate and refined characterization could be done in case more information was available, such as the distribution of sugar monomers, the composition of the lignin, the nature of extractive species, allowing both lignin and extractives to be custom characterized.

3.2. Characterization of Lignin Samples

This section will start explaining the characterization method for lignin samples, which was the first step into the development of the more complex lignocellulosic and algae biomass characterization methods. Despite the complexity, all the methods rely on solving atomic mass balances. The characterization of lignin is simpler because we have three reference species (LIG-C, LIG-H and LIG-O) and tree atomic mass balances to solve (Carbon, Hydrogen and Oxygen). Thus, knowing the C/H/O composition of each reference species

involved and of the sample to be characterized, it is straightforward to write a system of linear equations as reported in Figure 40. In these equations, ω is mass fraction of an element (indicated as subscript) in a sample or reference species (indicated as superscript). The solution of the system returns the mass fraction of each reference species (α, β, and γ) that are able to characterize the sample, respecting the atomic mass balances.

$$\begin{aligned}
\alpha \cdot \omega_C^{S1} + \beta \cdot \omega_C^{S2} + \gamma \cdot \omega_C^{S3} &= \omega_C^{solid} \\
\alpha \cdot \omega_H^{S1} + \beta \cdot \omega_H^{S2} + \gamma \cdot \omega_H^{S3} &= \omega_H^{solid} \\
\alpha \cdot \omega_O^{S1} + \beta \cdot \omega_O^{S2} + \gamma \cdot \omega_O^{S3} &= \omega_O^{solid}
\end{aligned}$$

Figure 40 - System of equations used to find the solution for the samples characterization.

Once again, in order to better illustrate the method, Figure 41 shows the Van Krevelen diagram, this time only reporting the three reference species for lignin. The triangle formed using them as vertices creates a characterization range (i.e. the area corresponding to the composition of samples that are able to be characterized by linear combination of the chosen reference species).

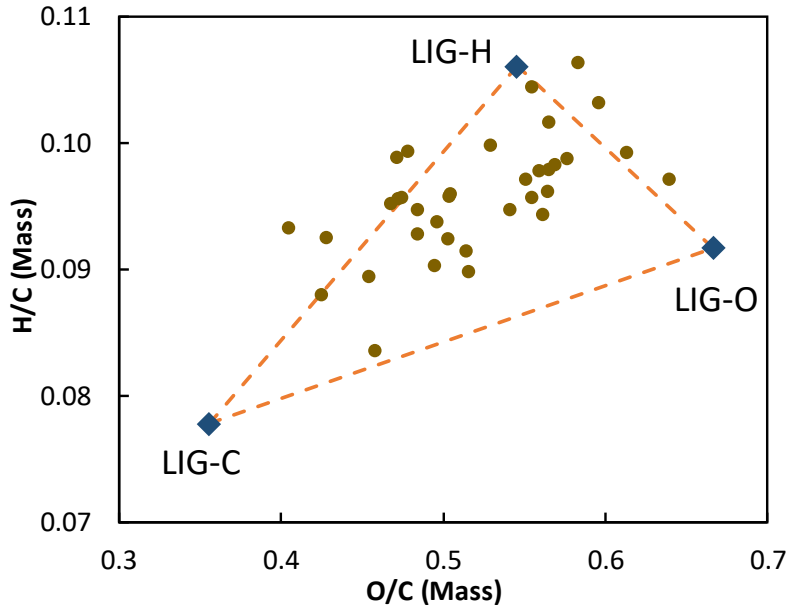

Figure 41 - Composition of typical lignin samples, lignin reference species and characterization range

For example, taking the lignin extracted from *Afzelia sp.*, with elemental composition (C/H/O = 62.3/5.6/32.1 wt.% as reported in Table 14), we find that it falls within this characterization range and is characterized by 34.7/25.9/39.4 wt% of LIG-C/LIG-H/LIG-O.

When applied to all these lignin samples reported in the previous chapter, the characterization returns the results reported in the same table.

Some samples of lignin still fall outside of this characterization range. These samples are atypical or they are not purely composed by lignin. Lignin extraction methods can often leave some other compounds, like phenolics, lipids and sugars from hemicellulose. Thus, the characterization can be extended to include a few percent of a proper reference species, allowing to treat all samples and still respect the atomic mass balances.

	C (wt.%)	H (wt.%)	O (wt.%)	LIG-H (wt.%)	LIG-O (wt.%)	LIG-C (wt.%)	Reference
Hardwood							
Liquidambar styraciflua	57.6	5.6	36.8	31.9	67.7	0.4	[Alt, 2006]
Liriodendrum tulipifera	58.4	5.8	35.8	48.5	51.2	0.3	[Jakab, 1995]
Betula verrucosa	58.5	6.5	35.0	n.d.	n.d.	n.d.	[Alt, 2006]
Ball-milled enzyme cottonwood	58.9	6.1	35.1	71.7	28.3	0.0	[Jakab 2, 1995]
Eucalyptus regnans	59.2	6.3	34.5	n.d.	n.d.	n.d.	[Alt, 2006]
Prunus serotina	59.7	5.9	34.4	55.8	38.2	6.0	[Jakab, 1995]
Populus tremuloides	60.0	6.1	33.9	72.7	23.8	3.5	[Alt, 2006]
Casearia praecox	60.0	5.9	34.1	55.3	36.2	8.5	[Jakab, 1995]
Olea sp.	60.2	5.9	34.0	55.0	34.9	10.1	[Jakab, 1995]
Fagus sylvatica	60.3	6.3	33.4	89.7	9.3	1.0	[Alt, 2006]
Juglans regia L.	60.3	5.9	33.7	54.9	34.2	10.9	[Jakab, 1995]
Acer macrophyllum	60.4	5.7	33.9	37.3	46.0	16.7	[Alt, 2006]
Entandrophragma cylindricum	60.6	5.8	33.6	45.7	38.4	15.9	[Jakab, 1995]
Manilcara sp.	60.7	5.9	33.4	54.3	31.5	14.2	[Jakab, 1995]
Tieghemella heckelii	61.2	5.8	33.1	44.9	34.4	20.8	[Jakab, 1995]
Millettia laurentii	62.3	5.7	32.0	34.6	33.2	32.2	[Jakab, 1995]
Afzelia sp.	62.3	5.6	32.1	25.9	39.4	34.7	[Jakab, 1995]
Dalbergia granadillo	62.6	6.0	31.5	60.3	12.5	27.2	[Jakab, 1995]
Dalbergia melanoxylon	62.7	5.8	31.5	42.7	24.3	33.0	[Jakab, 1995]
Steam explosion yellow poplar sc	63.4	5.9	30.7	49.5	13.8	36.7	[Jakab 2, 1995]
Pseudotsuga menziessi	64.8	5.8	29.4	39.7	10.1	50.2	[Alt, 2006]
Alcell organosolv mixed hardwoo	66.8	6.2	27.0	n.d.	n.d.	n.d.	[Jakab 2, 1995]
Average Hardwood	**60.9**	**5.9**	**33.1**	**51.1**	**32.0**	**17.0**	
Softwood							
Steam explosion aspen softwood	61.4	6.1	32.5	73.3	12.5	14.2	[Jakab 2, 1995]
Pinus ponderosa	62.5	6.0	31.5	60.4	13.2	26.4	[Alt, 2006]
Metasequoia glyptostrobides	62.9	5.9	31.2	51.1	16.7	32.2	[Jakab, 1995]
Picea abies	63.3	6.0	30.6	59.3	7.8	32.9	[Jakab, 1995]
Tsuga heterophylla	63.4	6.3	30.3	n.d.	n.d.	n.d.	[Alt, 2006]
Picea mariana	63.7	6.3	30.0	n.d.	n.d.	n.d.	[Alt, 2006]
Larix occidentalis	63.7	6.1	30.2	65.8	0.8	33.4	[Alt, 2006]
Thuja plicata	63.8	6.1	30.1	65.7	0.1	34.2	[Alt, 2006]
Picea sylvestris	64.0	6.1	29.9	65.8	0.8	33.4	[Alt, 2006]
Indulin kraft mixed softwoods	65.8	6.1	28.1	n.d.	n.d.	n.d.	[Jakab 2, 1995]
Acetosolv pine sawdust	66.0	5.5	30.2	13.6	19.5	66.9	[Moore, 2015]
Average Softwood	**63.7**	**6.0**	**30.4**	**56.9**	**8.9**	**34.2**	
Grass/Cereal							
Miscanthus sinensis	60.3	5.8	34.0	46.2	40.4	13.4	[Jakab, 1995]
Arachis hypogaea	63.1	5.7	31.2	33.4	27.8	38.8	[Jakab, 1995]
Sucrolin sugar cane bagasse	66.1	5.8	28.1	38.7	0.6	60.8	[Jakab 2, 1995]
Average Grass/Cereal	**63.2**	**5.8**	**31.1**	**39.4**	**22.9**	**37.6**	

Table 14 - Elemental composition of different lignins and characterization in terms of reference components

3.3. Characterization of Lignocellulosic Biomass samples

When the number of reference species involved in the characterization exceeds the number of atomic mass balances, several feasible solutions are possible (physically acceptable, no negative mass fractions, and the sum of mass fractions sum up to 1). From one side, is means that the system becomes more flexible. But from another side, most of these solutions are far from the biochemical composition of real biomass samples. In all cases, it is necessary to define a three mixtures of reference species, allowing the determination of a characterization area. There are many degrees of freedom in this approach, and they can be used to improve the characterization range of the model, allowing to characterize most of the samples, but some rules must be followed in order to keep reasonable characterization. For example, the average mass ratio cellulose: hemicellulose is 1.5:1, but this ratio changes from one biomass to another, and this can be taken into consideration when the type of biomass is known. Also, through the characterization of the lignin samples, it was possible to see some trends, such as hardwoods lignins in average are richer in oxygen reflecting in higher amounts of LIG-O. This fact well agrees with the dominant presence of syringyl propanoid units in hardwood species. Softwood lignins, on the other hand, are usually richer in carbon and require more LIG-C for its characterization.

For this aim, we define three standard mixture of the main reference species, which will be called reference mixtures (RM-1, RM-2 and RM-3). The ratio that define these RM's will be called splitting parameters. RM-1 is representative of holocellulose, combining the reference species for cellulose and hemicellulose through the splitting parameter α. RM-2 is a mixture of LIG-H and LIG-C defined by β. Finally, RM-3 is a mixture of LIG-O and LIG-C defined by γ. The standard splitting parameters of these mixtures are defined from experimental findings and can be easily modified. The values below show the meaning of the splitting parameters

	α=0.6		β=0.8		γ=0.8
CELL	0.6	LIG-H	0.8	LIG-O	0.8
XYHW	0.4	LIG-C	0.2	LIG-C	0.2

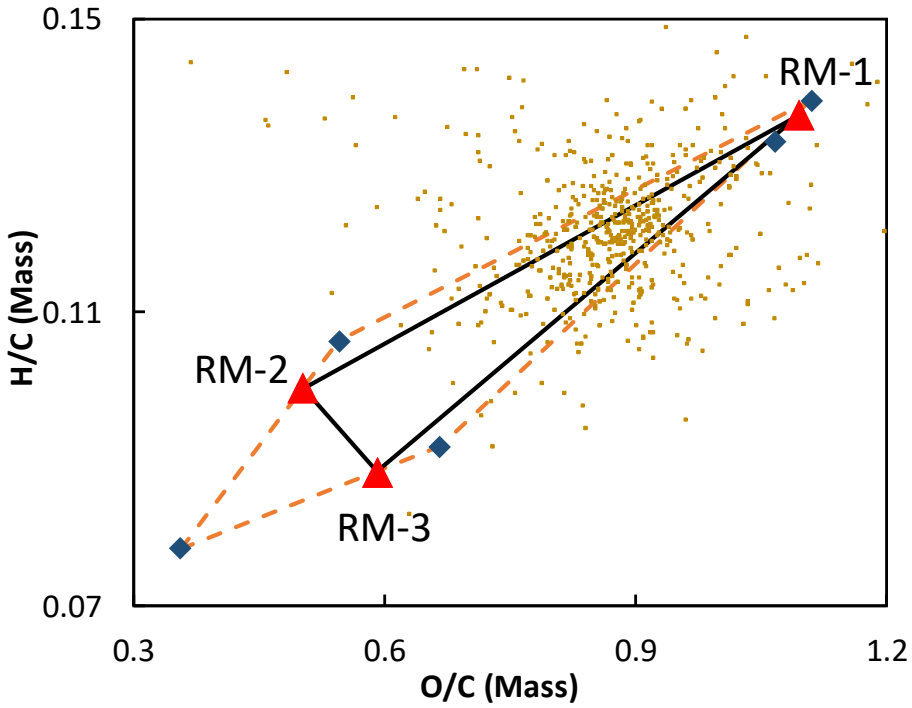

Figure 42 - Composition of biomass samples, the reference species (except extractives) and the reference mixtures that allow to determine a mobile characterization range.

As an example, the almond shell [144] with elemental composition C/H/O = 0.500/0.060/0.440 on a dry and ash free (daf) basis is characterized by the following mass composition:

CELL	XYHW	LIG-C	LIG-H	LIG-O
0.4314	0.2344	0.0437	0.1529	0.1376

The values reported above are obtained by using the default splitting parameters: α/β/γ = 0.6/0.8/0.8. With the same splitting parameters, the softwood bark[110] with C/H/O = 0.534/0.06/0.406 is characterized by the following mass composition:

CELL	GMSW	LIG-C	LIG-H	LIG-O
0.2946	0.1595	0.0713	0.2934	0.1822

The plot in Figure 42 shows that there are several biomass samples whose compositions fall outside this area and thus cannot be represented by a feasible combination of only those reference components. These biomasses are generally rich in extractives, as reported in Table 15 for a few samples.

Sample	C	H	O	Extractives	Solvent(s)	Reference
Hybrid Poplar	50.92	5.65	43.43	6.89	Ethanol	[84]
Switchgrass	50.19	5.64	44.17	16.99	Ethanol	[84]
Olive Husks	54.89	6.96	38.15	9.40	Alcohol, benzene (1/1, v/v)	[145]
Pinewood	49.00	6.40	44.60	14.90	Ethanol, water, hexane	[145]

Table 15 - Biomass samples rich in extractives

It is clear that the characterization range is quite narrow when the extractives TGL and TANN are not considered. Therefore, another two splitting parameters δ and ε can be included, and represent the amount of TGL and TANN to be included in the previously mentioned RM-2 and RM-3, extending the characterization range. Standard values for these parameters are reported below, and different values can also be used when appropriate. This further step can be skipped when the sample is easily characterized without extractives, or when it is known that extractives content is low.

	δ=0.8		ε=0.8
LIG-H + LIG-C	0.8	LIG-O + LIG-C	0.8
TGL	0.2	TANN	0.2

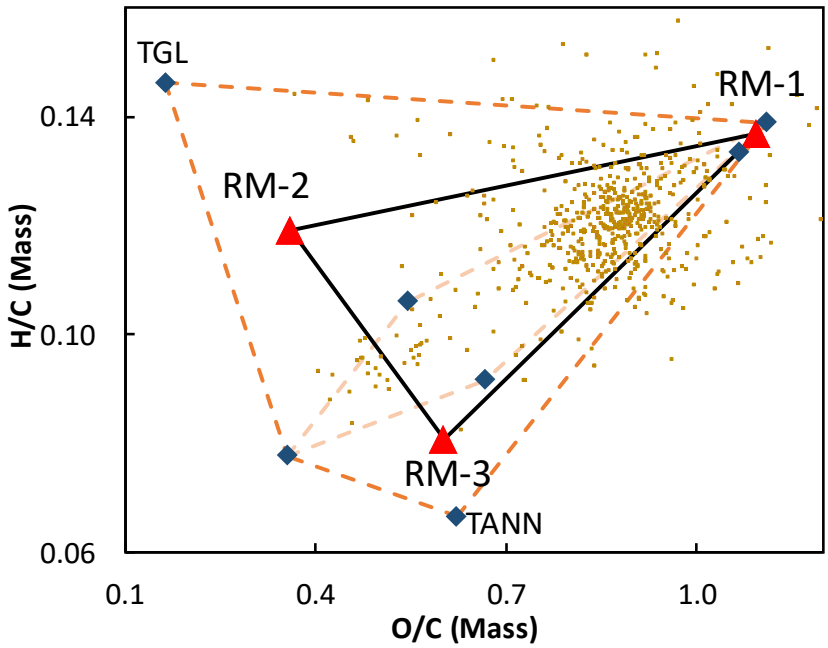

Figure 43 - Van Krevelen diagram: The reference mixtures defined with standard ratios of reference species and the characterization range.

As an example to explain the characterization procedure with extractives, the same hybrid poplar, characterized in section 3.1 of this chapter, whose elemental composition is C/H/O = 0.509/0.057/0.434 (highlighted as A in Figure 43), is characterized including 20% of TANN in RM-3. It means that 80% of lignins (LIG-O and LIG-C) and 20% of TANN are combined to obtain RM-3, and this condition allows this biomass with low H content to enter the characterization range. The linear system of C/H/O balance equations first gives the mass fraction of the reference mixtures:

RM-1	RM-2	RM-3
0.5597	0.0020	0.4384

The reference mixture RM-2 is only present in a very limited amount because of the low hydrogen content of this sample, and RM-1 and RM-3 are major constituents of this biomass. From these values and the internal composition of the reference mixtures, the following mass fractions of the seven reference species are obtained:

CELL	XYHW	LIG-C	LIG-H	LIG-O	TGL	TANN
0.3627	0.1970	0.0489	0.0017	0.3181	0.0000	0.0716

Similarly, olive husk [145], with C/H/O = 0.5489/0.0696/0.3815 is characterized including 20% of TGL in RM-2. It means that 80% of lignins (LIGH and LIGC) and 20% of TGL are combined to obtain RM-2, and this condition allows this biomass with high H content to enter the characterization range. The solution using these parameters is:

CELL	XYHW	LIG-C	LIG-H	LIG-O	TGL	TANN
0.3484	0.1892	0.0392	0.2474	0.0170	0.1589	0.0000

While the default values of α/β/γ remained unchanged, the splitting parameters δ and ε were progressively reduced, increasing in this way the extractive content, in order to respect a feasible composition (i.e., non-negative values for all the seven reference components).

By changing the splitting parameters that define the reference mixtures, linear combinations of all the reference species are able to describe all the biomasses contained in the shadow area of Figure 43. The capability to process all these biomass samples, which are spread on a wide range of composition, was only possible through the inclusion of extractive species.

3.4. Estimation of optimal characterization splitting parameters

In order to allow a non-random definition of the splitting parameters, optimal values were obtained by minimizing the square deviations between the predicted and experimental, in terms of cellulose, hemicellulose, lignin, and extractives. TGL is expected to increase with the H content of the biomass sample, while TANN will increase when H content is decreasing. A non-linear regression method [146, 147] was applied in order to find the optimal splitting parameters taking also into account the relative Hi and Ci content of the biomass sample. In this way, α, β, γ, δ, and ε are calculated through the correlations:

$$\alpha = \alpha_1 + \alpha_2 . C_i + \alpha_3 . H_i \quad [1]$$

$$\beta = \beta_1 + \beta_2 . C_i + \beta_3 . H_i \quad [2]$$

$$\gamma = \gamma_1 + \gamma_2 . C_i + \gamma_3 . H_i \quad [3]$$

$$\delta = \delta_1 + \delta_2 . C_i + \delta_3 . H_i \quad [4]$$

$$\varepsilon = \varepsilon_1 + \varepsilon_2 . C_i + \varepsilon_3 . H_i \quad [5]$$

Table 16 reports the optimized parameters for these correlations, when separating the samples into wood and grass samples. The same procedure could be performed for other subgroups of biomass, if a relevant amount of experimental data is available and show evidence of significant differences exist.

		α	β	γ	δ	ε
OPT1: Overall	1	-0.586	0.995	1.015	0.294	0.734
	2	2.255	-0.012	-0.045	0.986	-0.372
	3	0.000	0.162	-0.005	0.002	0.021
OPT2: Wood	1	1.503	2.079	12.697	-1.750	-2.339
	2	-0.037	-2.160	-25.284	3.428	1.303
	3	-13.807	-0.207	12.461	13.422	41.335
OPT3: Grass	1	0.626	0.155	6.944	-2.249	-3.501
	2	0.877	-2.110	-13.983	0.731	3.038
	3	-8.681	29.643	13.707	33.856	45.092

Table 16 - Optimized parameters for different ligno-celullosic feedstocks

In order to verify the reliability and the uncertainty of the characterization method, Figure 44 reports the parity diagrams of the calculated and experimental composition of the biomass reported in the Appendix A whose structural composition was determined

experimentally. To perform this analysis, both experimental and predicted values were organized into cellulose, hemicellulose, lignin, and extractives. For the model predictions, lignin represents the sum of LIGH, LIGC, and LIGO, while the extractives are the sum of TGL and TANN. The complete comparisons between model predictions and experimental data are reported in the Appendix A. Figure 44 distinguishes the biomass families, in terms of hardwood, softwood, grass, and cereals. Relevant differences exist between the compositions of wood and grass/cereal samples. Namely, wood plants have higher cellulose/hemicellulose ratios, while extractives are more abundant in grass plants.

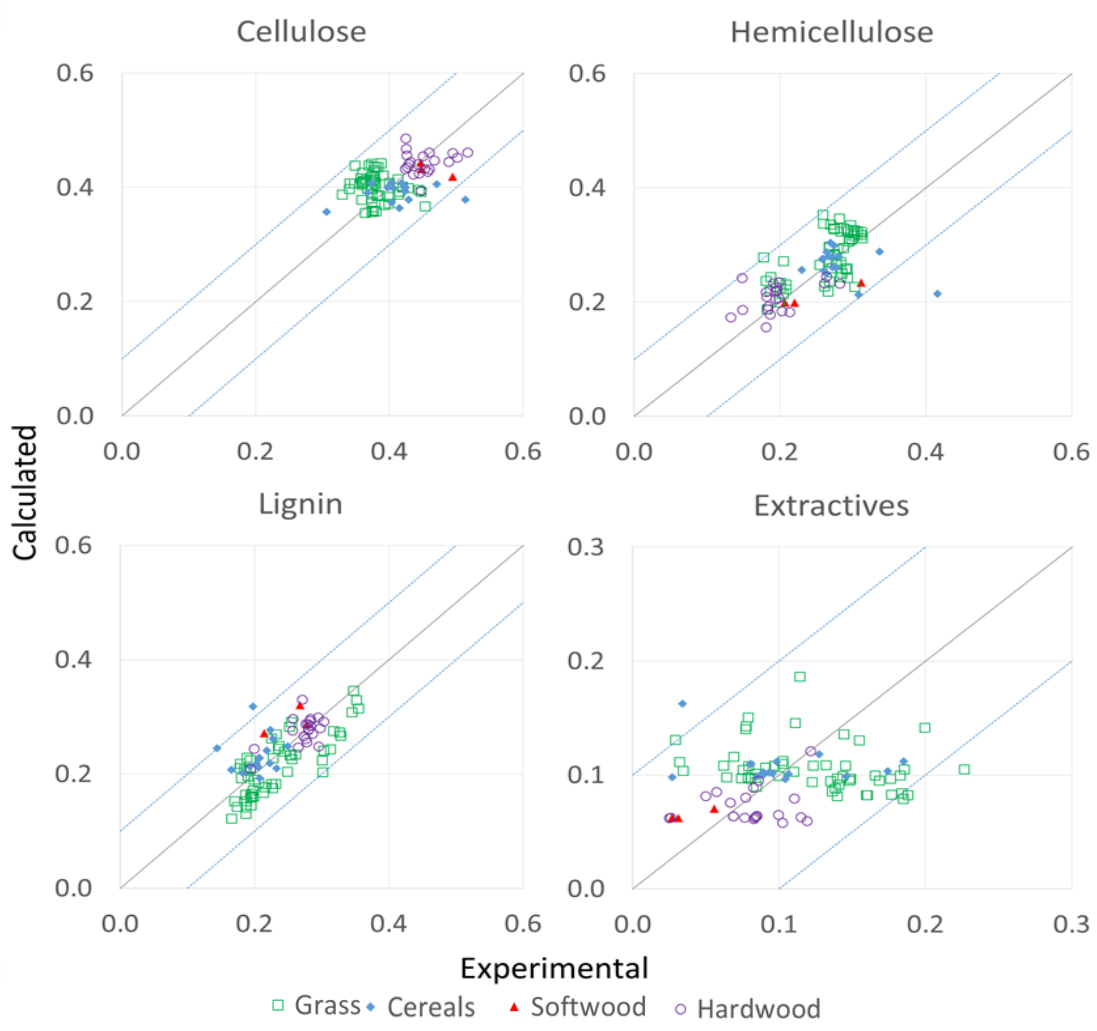

Figure 44 - Parity diagrams of experimental and predicted biomass composition in terms of cellulose, hemicellulose, lignin, and extractives.

Table 17 reports the corresponding average and standard deviations for the global results of the characterization method, using the optimized parameters. The mean square deviations can be at least partially explained by considering, on one hand, the strong

simplifications in the selection of reference species, but on the other hand, also the large variety of analytical methods for the determination of structural and biochemical composition, as well as the different uncertainties of the experimental information. It is also important to highlight that predicted extractives are the sum of two reference components, tannins and triglycerides, whose compositions are very different. Experimental data with a distinction between these two classes of components would be useful to improve the characterization method and to reduce the large scatter of extractives.

	Cellulose	Hemicellulose	Lignin	Extractives
Characterization with Extractives (96 Biomass Samples)				
Exp. Average	0.4045	0.2521	0.2366	0.1068
Calc. Average	0.4101	0.2603	0.2322	0.0974
Avg. Deviation	-0.0057	-0.0087	0.0051	0.0093
Mean Square Deviation	0.0017	0.0018	0.0014	0.0025
Characterization without Extractives (42 Biomass Samples)				
Exp. Average	0.4094	0.2466	0.2470	0.069
Calc. Average	0.3691	0.2406	0.3902	-
Avg. Deviation	0.0403	0.0060	-0.1432	0.069
Mean Square Deviation	0.0719	0.0572	0.1548	-
Sheng and Azevedo [148] Characterization (73 Biomass Samples)				
Exp. Average	0.4031	0.2394	0.2567	0.1008
Calc. Average	0.3749	0.3587	0.2665	-
Avg. Deviation	0.0329	-0.1188	-0.0155	0.1008
Mean Square Deviation	0.0545	0.1448	0.0760	-

Table 17 - Mean square and average deviations of cellulose, hemicellulose, lignins, and extractives.

The average content of extractive species inside these biomass samples is ~10%. Therefore, despite the persisting deviation, there is a clear improvement when the mean square deviations of predicted values are compared with the original and extended model. Only 42 biomass samples whose biochemical compositions are known can be characterized by the previous model. In particular, there is a large overestimation (~14%) of the lignins and an underestimation of ~4% cellulose. This result is mainly due to the chemical similarity of LIGO and condensed tannins. Table 17 also compares these characterization methods with the method proposed by Sheng and Azevedo [148]. This characterization method was applied for using the CPD model [149] when biochemical composition was not available[150]. The

mass fractions of cellulose and lignin are evaluated as a function of the ratios of oxygen and hydrogen to carbon (O/C and H/C, respectively) in biomass and the volatile matter (VM). Then, it is necessary to have both proximate and ultimate elemental analysis for each biomass. As a consequence, only 73 biomass samples are considered here. The analysis of Table 17 clearly highlights the great improvements of the proposed extended characterization method, when compared with the other two.

Figure 45 clearly confirms how the optimal splitting parameter α, widely scattered when considering the overall set of data, become more correlated with hydrogen content when considering the two separate biomass classes. Namely, the ratio between cellulose and holocellulose ranges between 0.6-0.7 for wood, while it is lower than 0.6 for the grass and cereals.

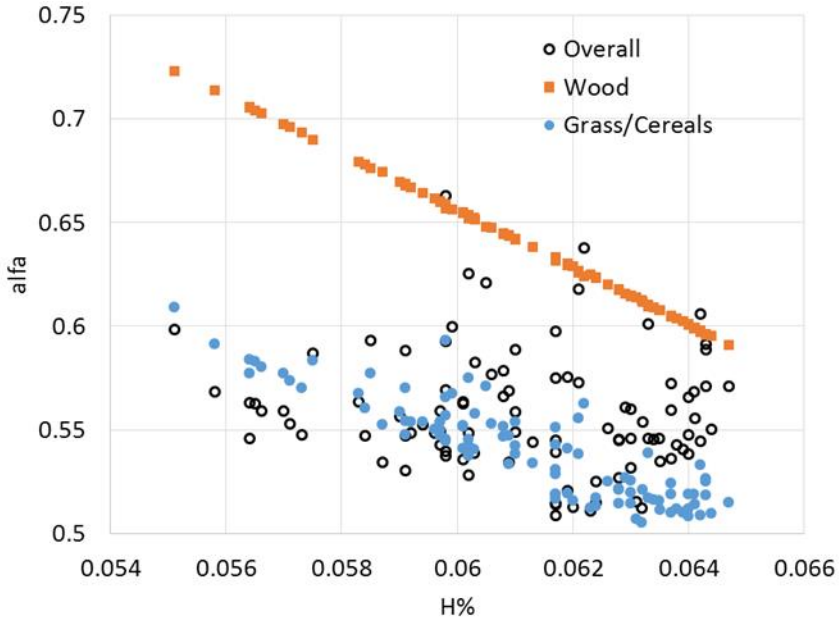

Figure 45 - Optimal splitting parameter α (ratio between cellulose and holocellulose) as a function of H% for the overall database, for the wood, and for the grass/cereal samples

Moreover, based on the splitting parameters of Table 16, it is also possible to derive simpler correlations to define the mass fractions of reference components. These correlations, simply obtained by linear regression methods [151], are reported in Table 18, in the following form for each reference species:

$$REF_K = \alpha_0 + \alpha_1.C_i + \alpha_{11}.C_i^2 + \alpha_2.H_i + \alpha_{22}.H_i^2 + \alpha_{12}.C_i.H_i \qquad \text{(K=1, 7)}$$

GRASS Linear characterization																				
CELL	=	6.153	+	-21.875	Ci	+	20.483	Ci^2	+	6.803	Hi	+	3.925	Hi^2	+	-11.744	Ci* Hi
HECELL	=	4.178	+	-18.098	Ci	+	18.187	Ci^2	+	30.983	Hi	+	7.512	Hi^2	+	-42.778	Ci* Hi
LIGH	=	-1.411	+	4.574	Ci	+	-3.935	Ci^2	+	5.047	Hi	+	10.413	Hi^2	+	-7.619	Ci* Hi
LIGO	=	-10.653	+	53.328	Ci	+	-62.901	Ci^2	+	-85.335	Hi	+	-54.471	Hi^2	+	173.332	Ci* Hi
LIGC	=	12.623	+	-52.992	Ci	+	56.568	Ci^2	+	6.285	Hi	+	-2.564	Hi^2	+	-20.184	Ci* Hi
TGL	=	-3.898	+	11.971	Ci	+	-10.847	Ci^2	+	14.575	Hi	+	3.230	Hi^2	+	-7.411	Ci* Hi
TANN	=	-5.993	+	23.091	Ci	+	-17.554	Ci^2	+	21.642	Hi	+	31.954	Hi^2	+	-83.595	Ci* Hi
WOOD Linear characterization																				
CELL	=	11.814	+	-46.121	Ci	+	47.910	Ci^2	+	33.934	Hi	+	22.352	Hi^2	+	-79.165	Ci* Hi
HECELL	=	5.124	+	-22.635	Ci	+	23.302	Ci^2	+	25.813	Hi	+	19.902	Hi^2	+	-34.972	Ci* Hi
LIGH	=	-14.550	+	61.143	Ci	+	-70.524	Ci^2	+	-75.695	Hi	+	-49.969	Hi^2	+	212.321	Ci* Hi
LIGO	=	-16.513	+	72.616	Ci	+	-75.716	Ci^2	+	-16.957	Hi	+	-70.433	Hi^2	+	19.080	Ci* Hi
LIGC	=	18.745	+	-84.434	Ci	+	96.927	Ci^2	+	68.397	Hi	+	35.378	Hi^2	+	-165.043	Ci* Hi
TGL	=	-1.574	+	4.203	Ci	+	-3.779	Ci^2	+	10.470	Hi	+	10.271	Hi^2	+	-7.296	Ci* Hi
TANN	=	-2.045	+	15.229	Ci	+	-18.120	Ci^2	+	-45.961	Hi	+	32.499	Hi^2	+	55.075	Ci* Hi

Table 18 - Correlations obtained by linear regression of the optimized values.

Figure 46 shows that the validity range of these expressions, to maintain the feasibility of biomass composition, is indeed quite limited. This is due to the prediction of unfeasible values above zero of some reference species outside this region.

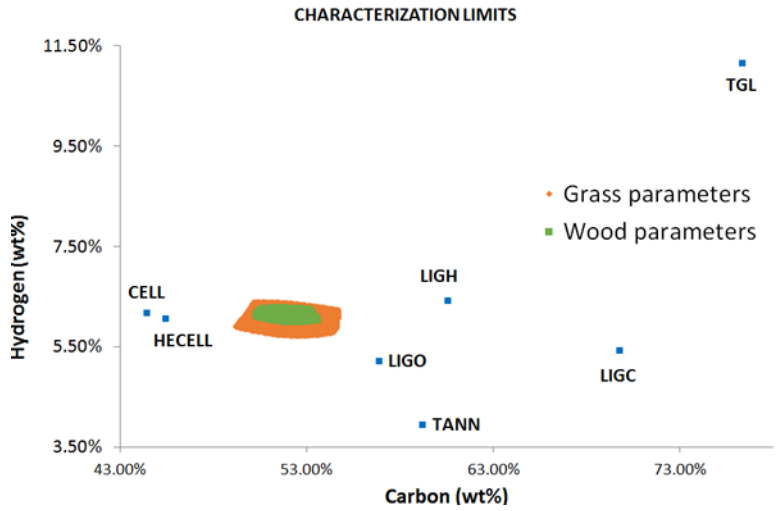

Figure 46 - Characterization limits for both grass and wood set of equations. The colored area represents the region in which no reference specie return unfeasible values.

Figure 47 shows iso-lines of the surface of estimated amounts for TANN and TGL, thus indicating the region of feasibility values. The resulting intersection of the two feasible regions is indeed very limited. In order to enlarge this region of applicability of the characterization method, it should be necessary to drastically modify the regressions accounting for these feasibility boundaries. This is outside the purposes of this work. For this reason, and to warrant a complete respect of the C/H/O balances, it is preferable to refer to the three reference mixtures and to solve the corresponding linear system of equations.

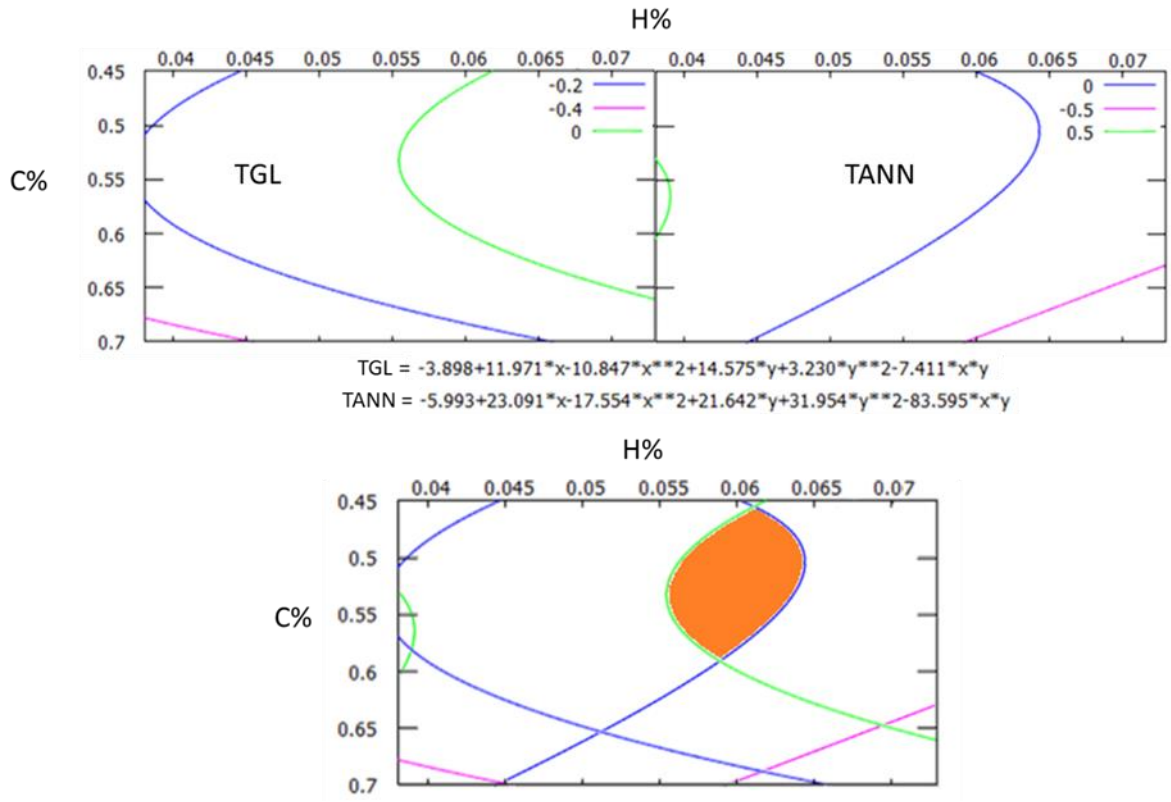

Figure 47 - Grass/Cereal Samples. Contour map of TGL and TANN estimated values. Feasible region from the intersection of TANN and TGL surfaces.

Moreover, referring to the large scatter of extractive species, as seen in Figure 44, it is important to highlight that predicted extractives are the sum of the two reference components, tannins (TANN) and triglycerides (TGL), whose compositions are highly different. Figure 48 clearly shows how tannin species decreases when hydrogen content of the biomass increases, while the reverse is observed for the triglycerides. Figure 49 highlights the correlation between these extractive species. Comparisons reported in the parity diagram of Figure 44 only refers to the sum of these two classes. Experimental data with a distinction between these two classes of components would be useful to improve the characterization method and to reduce the large scatter of extractives.

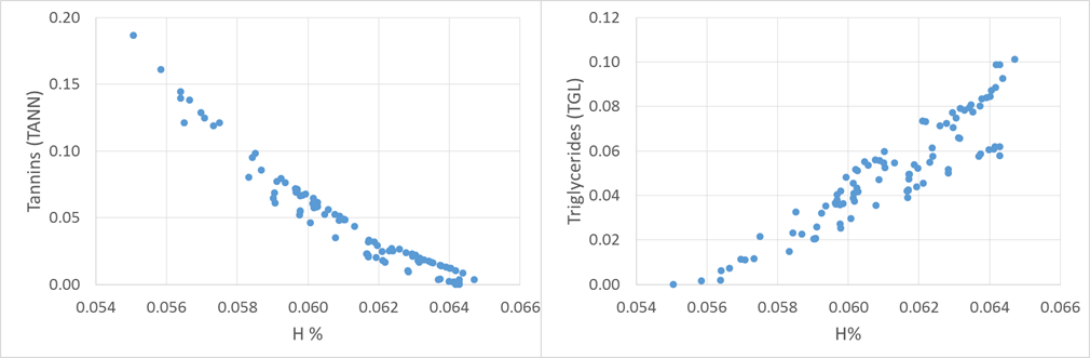

Figure 48 – TANN and TGL species versus biomass hydrogen content.

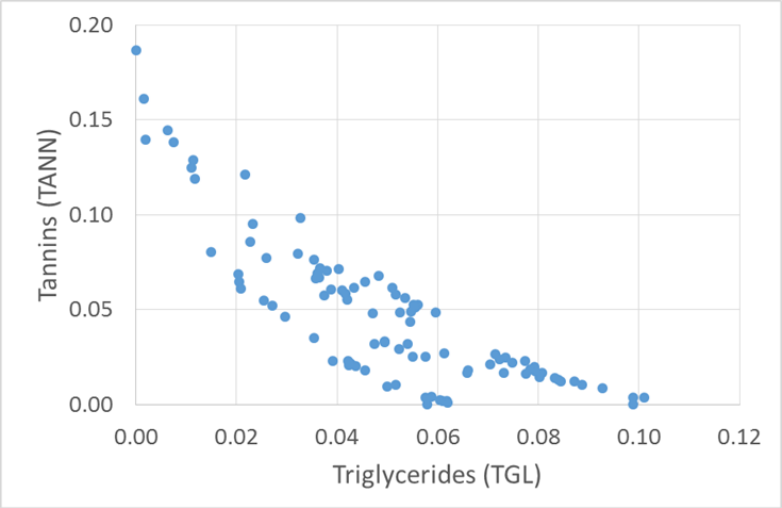

Figure 49 - Correlation between TANN and TGL species

4. Algae Characterization

4.1. Characterization procedure

While nitrogen content in the characterization of lignocellulosic biomass can often be neglected, this assumption would bring strong deviations. Similar to lignocellulosic, when biochemical composition of algae biomass is available, characterization can be directly done by correlation with the aforementioned algae reference species. In the absence of this information, the elemental composition can be processed in order to obtain the characterization. Once again, it is necessary to define a suitable characterization procedure, because of the higher number of degrees of freedom, with respect to the atomic balances. Figure 50 schematically shows the sequential phases of this procedure.

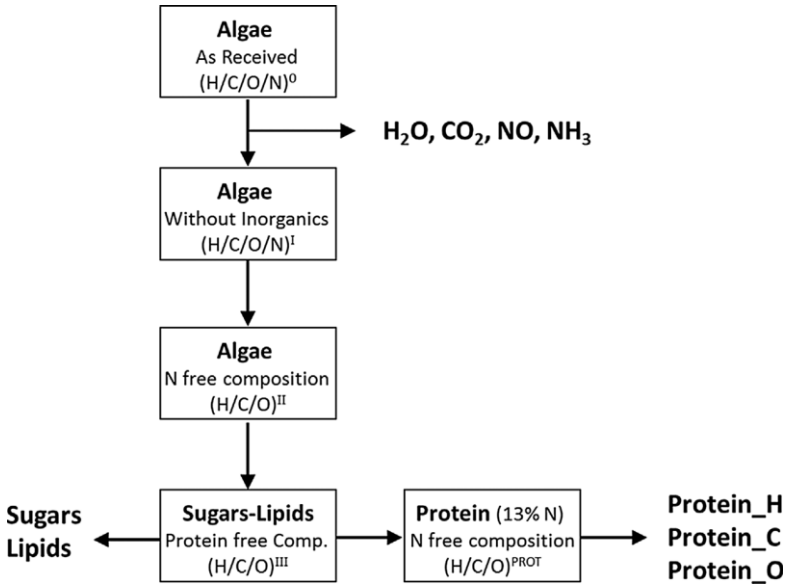

Figure 50 - Scheme of characterization procedure.

Starting from the proximate and elemental analysis, after the initial drying of the sample, the amounts of CO2, NO and NH3 is first defined by the ash and nitrogen content, and a new elemental composition without inorganics $(C/H/O/N)^{I}$ is derived. Here, nitrogen content is partially characterized in inorganic species, which for simplicity is assumed as an equimolar mixture of NH_3 and NO. Then, all the remaining nitrogen is assumed in proteins (organic bonded nitrogen), and the N-free composition of Algae $(C/H/O)^{II}$ is calculated. Global composition of the protein fraction $(C/H/O)^{PROT}$ is obtained by observing that the remaining composition of algae $(C/H/O)^{III}$ (proteins and inorganics-free) must be described in terms of the two reference species SUGAR and LIPID. Therefore, this composition must fall into the connecting line between them. Figure 51 shows the sequential steps of this procedure in the van Krevelen diagram. Several alternative paths are indeed possible to move from the

$(C/H/O)^{II}$ composition to the connecting line, and we arbitrarily shift the composition through the perpendicular line to find the $(C/H/O)^{III}$ composition, on the weight H/C plane. Moreover, the global amounts of lipids and sugars, as well as proteins, together with their global composition $(C/H/O)^{PROT}$, are also derived.

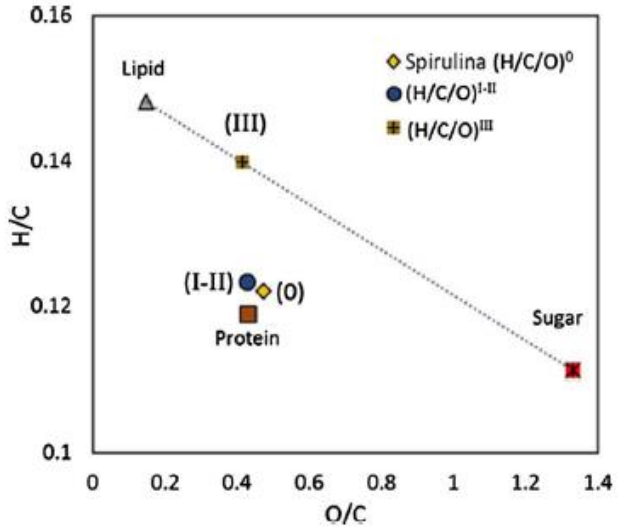

Figure 51 - Van Krevelen diagram showing the composition of Algae (initial, protein and inorganics-free)

Whereas the relative amount of sugar and lipid is simply obtained through the lever rule, the protein distribution among the three reference species is derived from their atomic H, C, and O balances. In a procedure very similar to lignin characterization, feasible solutions are only attainable when the protein composition falls within the triangle of Figure 52. For this reason, the reference proteins assume asymptotic chemical formulas. The solution is obtained by solving the same linear system of equations of atomic balances of Figure 40, using the PROT-C, PROT-H and PROT-O as the reference species

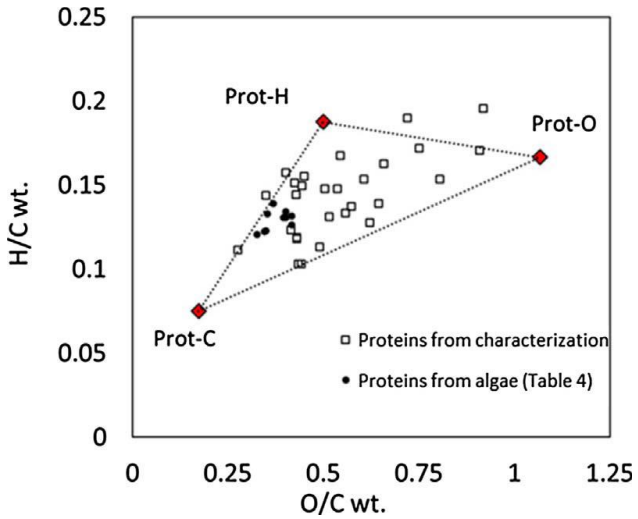

Figure 52 - Composition of proteins from algae (as reported in Chapter 2), proteins obtained with the characterization method, and reference protein species (PROT-C, PROT-H and PROT-O).

In order to better explain this procedure, reports the different steps in the characterization of an Arthrospira platensis sample (Spirulina: species #7 of the algae database), until the biochemical composition in terms of reference species is obtained, as reported in the last column. Further details and examples on this characterization procedure can be found in Trinchera [125].

Arthrospira platensis (Spirulina) #7						
STEP	Mass fraction	C	H	O	N	% initial
0	Algae (dry and ash-free)	0.556	0.068	0.264	0.112	100.00
I	Algae (CO_2-NH_3-NO-free)	0.573	0.070	0.252	0.105	95.98
	G{CO_2}	0.273	0.000	0.727	0.000	2.10
	G{NH_3NO}	0.000	0.064	0.340	0.596	1.92
II	Algae (N-CO_2-NH_3-NO-free)	0.640	0.078	0.282	0.000	85.92
	N	0.000	0.000	0.000	1.000	10.06
III	Algae (Proteins-N-CO_2-NH_3-NO-free)	0.648	0.089	0.273	0.000	18.62
PROT	Proteins	0.558	0.065	0.247	0.130	77.35
	Sugars	0.409	0.046	0.546	0.000	6.84
	Lipids	0.771	0.114	0.114	0.000	11.78
	Prot-C	0.697	0.052	0.121	0.130	36.39
	Prot-H	0.516	0.097	0.258	0.130	14.44
	Prot-O	0.389	0.065	0.415	0.130	26.52

Figure 53 – Characterization of Arthrospira platensis. Steps for definition of weight fraction of reference species. The first column refers to the C/H/O/N compositions of Figure 51.

4.2. Validation of the characterization procedure

Table 19 reports some comparisons between experimental and predicted biochemical compositions. In order to compare these data, the reference species, as obtained from the characterization procedure, are grouped in the following way:

- Proteins are the sum of PROT-C, PROT-H, and PROT-O;
- Sugars and Lipids are simply the values of reference species SUGAR and LIPID obtained from the characterization procedure;
- Inorganics sum up CO_2, NO and NH_3 contents.

	Wt.%	Spirulina #7		Chlorella #73		Porphyridium #123		Nannochloropsis #140	
C	Dry and ash-free	55.6		52.5		51.3		57.7	
H		6.8		7.1		7.6		8.0	
O		26.4		32.2		33.1		25.7	
N		11.2		8.2		8.0		8.6	
Ash	As received	7.6		7.0		24.4		26.4	
Moisture		8.0		8.0		5.0		7.0	
		Exp	Calc	Exp	Calc	Exp	Calc	Exp	Calc
Proteins	As received	58.6	65.2	50.9	48.1	30.9	38.8	36.0	39.3
Sugars		18.0	5.9	8.3	17.9	28.7	13	5.0	6.5
Lipids		4.5	10.1	23.1	16.3	5.7	12	20.2	15.4
Inorganics		n.a.	3.2	n.a.	2.7	n.a.	5.3	n.a.	5.4
Ash		7.6	7.6	7.0	7.0	24.4	24.4	26.4	26.4
Moisture		8.0	8.0	8.0	8.0	5.0	5.0	7.0	7.0

Table 19 - Comparison of algae samples characterization and experimental data. The numbers in parenthesis correspond to sample identification in the algae database.

These comparisons show that the proposed characterization procedure is able to predict the biochemical composition of algae with protein contents higher than 60% and lower than 40%, as a function of the different elemental compositions of the algae samples. It is also important to emphasize that the predicted biochemical composition is only scarcely affected by the assumptions in the characterization procedure. For instance, the selection of reference proteins having 13% of nitrogen content derives from the minimization of total protein content deviation. The scatter diagrams in Figure 54 compares model predictions and experimental values of protein, sugar and lipid content in algae samples. The complete set of experimental data of the algae database, containing both elemental and biochemical analysis, was used for this comparison.

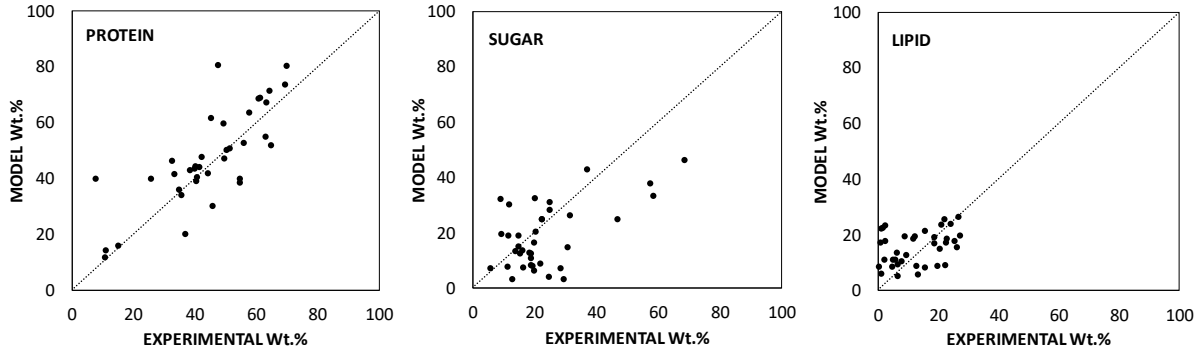

Figure 54 - Scatter diagram of experimental and predicted protein content.

5. Conclusions

The selection of a limited number of reference species is an essential step towards the development of general and reliable model for the thermochemical conversion of biomass. Characterization can be done directly by correlating the biochemical composition of the sample with the proper reference species. However, the reduced amount of these data, motivated the development of a characterization method that requires only the elemental analysis of the sample. The application is indeed of interest when considering the difficulties and uncertainties in biochemical analytical methods, which are not only complex, expensive, and time-consuming, but also affect and modify the original biomass structure [152]. Because of the large differences among lignocellulosic and algae biomass, two separate methods were proposed for their characterization. They are based in the same principles and require slightly different calculation procedures.

For lignocellulosic biomass, the procedure was optimized taking advantage of the large amount of experimental data available. To this aim, samples were further separated in two groups, one accounting for wood samples and the other comprehending grass and cereals. This allowed better correlation indexes between experimental and estimated biochemical composition.

Because of the larger exploration of lignocellulosic biomass, significantly more volume of experimental data, in comparison to algae biomass, is available. However, the possibilities of algae are promising and research on this field is recently becoming more intense. The available data was used to develop the characterization procedure, with includes also the content of nitrogen. This is an important step into describing the behavior of nitrogenated compounds in thermochemical conversion of biomass. The concepts and assumptions for nitrogen in algae can be implemented in lignocellulosic biomass. However,

nitrogen in lignocellulosic biomass still needs more investigation for more precisely describe in which chemical structure this element is present.

The method proved to be efficient in estimating the biochemical composition, requiring only widely available experimental data. The method remains flexible for further improvements. New experimental findings can be considered both for the selection of reference species and for characterization. The further step in the model development is the pyrolysis kinetic mechanism of the reference species, which will be discussed in the next chapter.

CHAPTER 4

KINETIC MECHANISM OF BIOMASS PYROLYSIS

The previous chapter described the selection of reference species that are able to characterize biomass and proposed characterization procedures that require only the simple elemental composition of the sample. Pyrolysis of these reference species will be discussed in the present chapter, highlighting the main reacting paths that take place in the process and the methods that were used to develop this modeling activity. Some reference species have large amounts of experimental data available, which allows to better develop the related kinetic mechanism. Some others require several lumping and simplifications, both because of the lack of literature data and also to keep the limited number of reacting steps and species produced. The kinetic mechanisms and validation will be presented separately for lignocellulosic and for algae biomass. Nevertheless, the mechanisms can be used together, as they are modular and structured in the same CHEMKIN format, using Arrhenius parameters for the rate of reaction.

1. Pyrolysis of Lignocellulosic Biomass Reference Species

1.1. Cellulose

Broido and coworkers developed the first global kinetic scheme of cellulose pyrolysis based on thermogravimetric studies [153-155]. Two parallel reactions lead to the formation of tars, char and gases. Subsequently, Bradbury, Sakai [69] modified this reaction scheme for cellulose pyrolysis including the formation of an intermediate, active cellulose, which then decomposes into gases, tars, and char. This is the most generally used and accepted Broido-Shafizadeh kinetic model (B-S model). It is nowadays well understood that the cellulose pyrolysis mechanism is characterized by a first depolymerization step producing active cellulose with an apparent activation energy of 47 kcal/mol [78, 156, 157]. Figure 55 shows a multistep kinetic scheme of cellulose pyrolysis. The first depolymerization reaction to form active cellulose reduces the polymerization degree without volatile release. Active cellulose then decomposes with two competitive reactions: a main reaction releasing levoglucosan and a slower decomposition reaction that produces char plus permanent gases. Only at high temperatures (T>750 K), decomposition reaction can prevail over tar release. A side charring and exothermic reaction of cellulose is also considered. This lumped and global multistep kinetic mechanism, reported in Table 20, roughly simplifies the complex nature and the concerted mechanisms of cellulose decomposition [158, 159].

Moving from their preliminary works [158, 160], Broadbelt's team extensively studied, both from a theoretical and experimental viewpoint, the fast pyrolysis of neat glucose-based carbohydrates [161-163]. They also developed a detailed mechanistic model for fast pyrolysis of glucose-based carbohydrates, involving about 100 species in more than 300 reactions. The mechanistic model describes the decomposition of cellulosic polymer chains, reactions of intermediates, and formation of several low molecular weight compounds. Similarly, Seshadri and Westmoreland [159] highlighted the implications of concerted molecular reactions for cellulose and hemicellulose kinetics. More recently, they also investigated the role of hydroxyls in the non-catalytic and catalyzed formation of levoglucosan from glucose [164]. A minor product of cellulose pyrolysis, still retaining all six carbons of glucose, is the 1,6-anhydroglucofuranose [165].

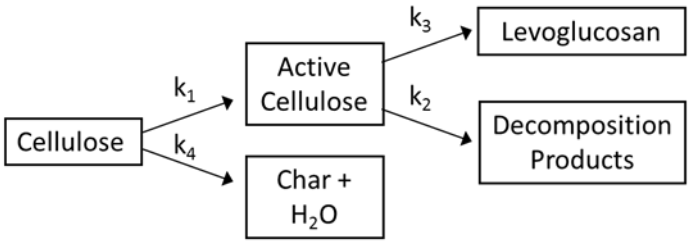

Figure 55 - Multistep kinetic mechanism of cellulose pyrolysis.

The global stoichiometry of active cellulose decomposition reaction to form lighter products accounts for the previous mechanistic studies, as well as further experimental and theoretical works [162, 163, 166, 167]. In this way, the lumped decomposition reaction of active cellulose to form hydroxyl-acetaldehyde, glyoxal, acetone, hydroxy-acetone, furfural, and 5-hydroxymethyl-furfural, together with lighter products such as formaldehyde, formic acid, CO and CO2 can be at least partially justified on mechanistic basis. As already discussed [168], while the tar release is an endothermic process and it absorbs ~500 kJ/kg, the char formation is an exothermic process releasing ~2000 kJ/kg of char formed [169]. Figure 26 shows a few comparisons between model predictions and experimental data of TGA of isolated cellulose at different heating rates. The model predictions agree with experimental data, within the experimental uncertainties in the whole range of heating rates from 1 up to 1000 K/min [170-172]. As a matter of facts, while model predictions are slightly slower for the first set of comparisons, an opposite deviation is observed in the remaining data.

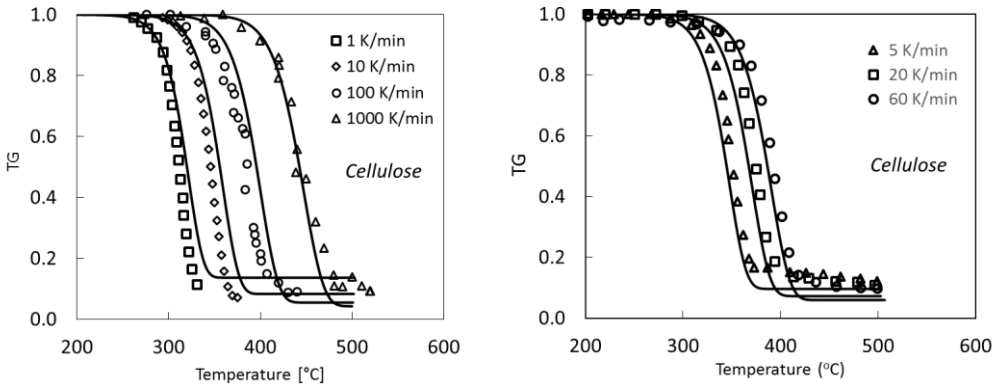

Figure 56 - Pyrolysis of cellulose. Left Panel: TGA at 1 and 10 °C/min[170], 100 and 1000 °C/min [171]. Right Panel: TGA at 5, 20, and 60 K/min [172].

Recently, [162, 173] studied the significant catalytic effect of NaCl and developed a mechanistic model of cellulose pyrolysis including Na interactions. The major Na effect on levoglucosan degradation will be further discussed in Section 2.22.2.

As a further complicating aspect of fast pyrolysis, active cellulose can be ejected as high molecular weight aerosols, mainly consisting of levoglucosan, cellobiosan and oligomers, together with other liquids formed inside the biomass sample[157, 174, 175].

1.2. Hemicelluloses

Together with cellulose, hemicelluloses are building components of the cell walls of higher plants, where they are associated with varying levels of proteins and phenolics. As already mentioned, the sugar units of hemicellulose consist of homopolymers (e.g. xylans), or heteropolymers (e.g. glucomannans). Many of the OH-groups at C2 and C3 of the xylanpyranosyl units are substituted by O-acetyl groups. Several units are often side groups of the main chain (e.g. 4-O-methylglucuronic acid, galactose). The average degree of polymerization (DP) of the hemicellulose is lower than that of cellulose, leading to a relatively faster decomposition process. As already shown in chapter 2, hemicellulose structures are largely different in hardwood and softwood. While glucomannans are mainly present in softwood, glucuronoxylans with a high percentage of acetyl substitutions are dominant in hardwood samples [176, 177].

With respect to the original multistep kinetic model discussed in previous papers [82] [Ranzi et al., 2008; Corbetta et al., 2014; Debiagi et al., 2015], three different reference components are here considered in order to account for the different pyrolysis behavior of the hardwood, softwood, and grass/cereals hemicellulose polymers. Grønli, Varhegyi [97] already highlighted these differences by observing the lower reactivity of hemicellulose components in softwood with respect to the reactivity of hardwood hemicellulose. Similarly, Prins, Ptasinski [178] and Prins, Ptasinski [179] analyzing torrefaction experiments observed that hemicellulose in softwood is less reactive than in hardwood. They also recommended research into thermal degradation of glucomannans, which constitute 60–70 wt% of the hemicellulose fraction in softwoods. In fact, a significant number of studies is available concerning the pyrolysis products of xylan, while glucomannans received a more limited attention, although the pyrolysis characteristics are different for hardwood or softwood species [177]. Thus, hemicellulose from hardwood is slightly more reactive, releases larger amounts of acetic acid, and shows a higher solid residue [180]. Figure 27 confirm this behavior by comparing several thermogravimetric analysis of xylans (hardwood) and glucomannans (softwood), at different heating rates from 3 to 80 K/min [181-192].

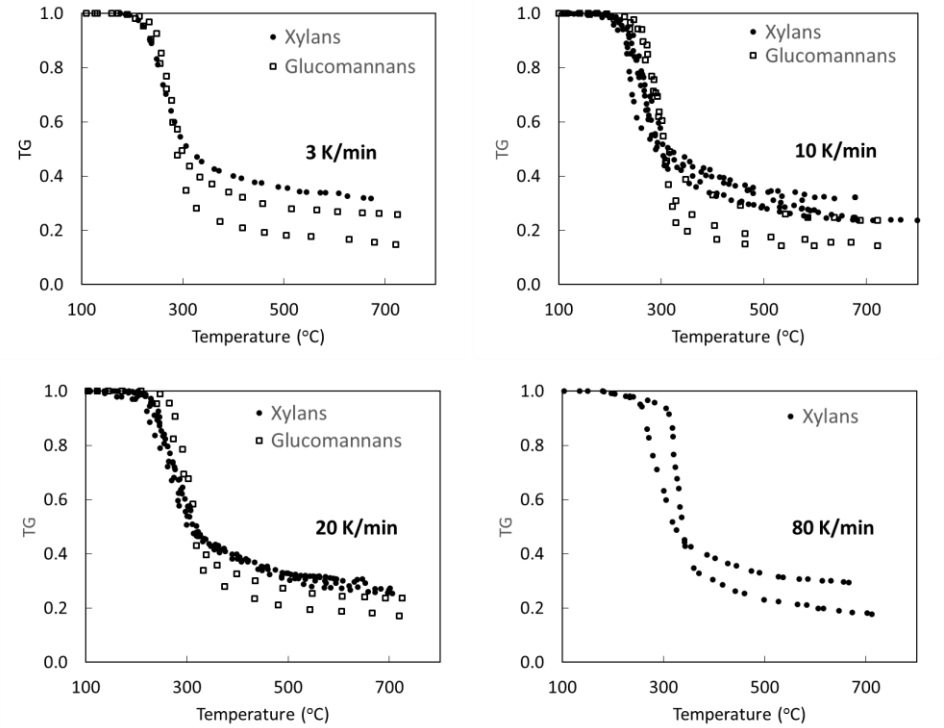

Figure 57 - Thermogravimetric analysis of xylan and glucomannan samples at 3, 10, 20, and 80 K/min. [181-192].

Figure 25 shows the multistep kinetic mechanism of hemicellulose. It is worth mentioning that it shares some similarities with the cellulose mechanism. The two intermediate species (HCE-1 and HCE-2) initially formed reflect the different compositions of softwood, hardwood and grass/cereal hemicelluloses and they allow to explain the progressive shift of sugar yields to furan-like compounds, the higher formation of acetic acid and residual char from hardwood samples, and the higher volatile yields from softwoods.

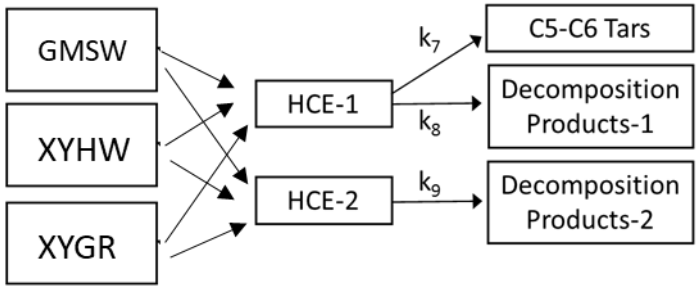

Figure 58 - Multistep kinetic mechanism of cellulose pyrolysis.

The yields of the main species from glucomannan pyrolysis, including acetic acid, hydroxyacetaldehyde, hydroxypropanone, formic acid, and furfuryl alcohol were recently presented by Branca, Di Blasi [177]. Both hemicelluloses are polysaccharydes, releasing

together with C5 and C6 tar components, permanent gases, a wide number of oxygenated species, including formic and acetic acid, hydroxy-acetaldehyde, acetone, acetol, furfural, 5-hydroxymethl-furfural [172]. The global and lumped stoichiometry of the multistep kinetic mechanism of hemicellulose pyrolysis accounts for these experimental and more detailed kinetic studies.

Figure 59 shows several thermogravimetric analysis of xylan and glucomannan (at 3, 10, 20, and 80 K/min) with comparisons between model predictions and the average experimental data reported in Figure 27.

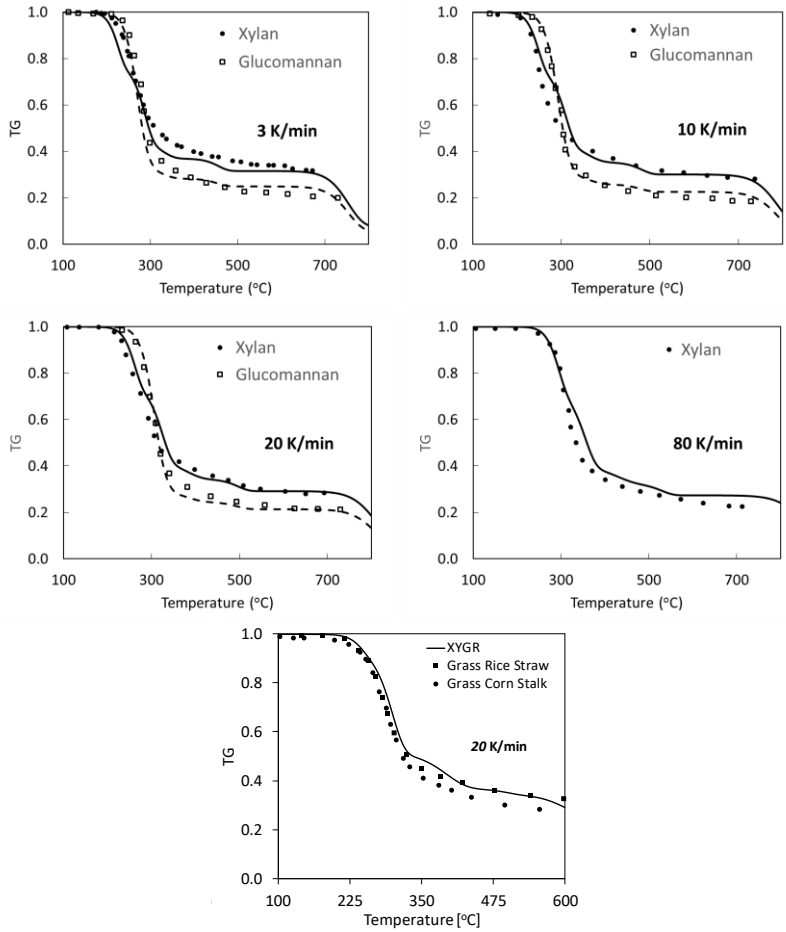

Figure 59 - Pyrolysis of Hemicellulose: thermogravimetric analysis of commercial xylan, glucomannan and hemicellulose extracted from two different cereals (rice husks and corn stalks)..

Comparisons between model predictions (lines) and average experimental data (symbols) of samples at 3, 10, 20, and 80 K/min.

Zhou, Nolte [163] very recently reviewed the status of hemicellulose pyrolysis in terms of experimental investigations, reaction mechanisms, and kinetic modeling. They also highlighted the composition and structural features of hemicellulose.

Hemicellulose is, among the lignocellulosic biomass components, the first to start thermal decomposition. In mild torrefaction processes, in which temperature treatment is not severe, this component is the main affected, while cellulose and lignin remain mostly undamaged. This condition is valid up to temperatures about 280°C, when the other compounds slowly start to decompose. It is useful to show some comparisons of experimental data and model predictions under these conditions. Figure 60 shows the torrefaction of xylan (commercial), analyzed in a temperature range of 200-300°C, with a successive pyrolysis up to 700 °C. The mass losses are reported as a function of temperature [193] and reaction time [194], and reveals the sensitivity of the model to slight temperature changes and its capability to satisfactorily predict torrefaction conditions.

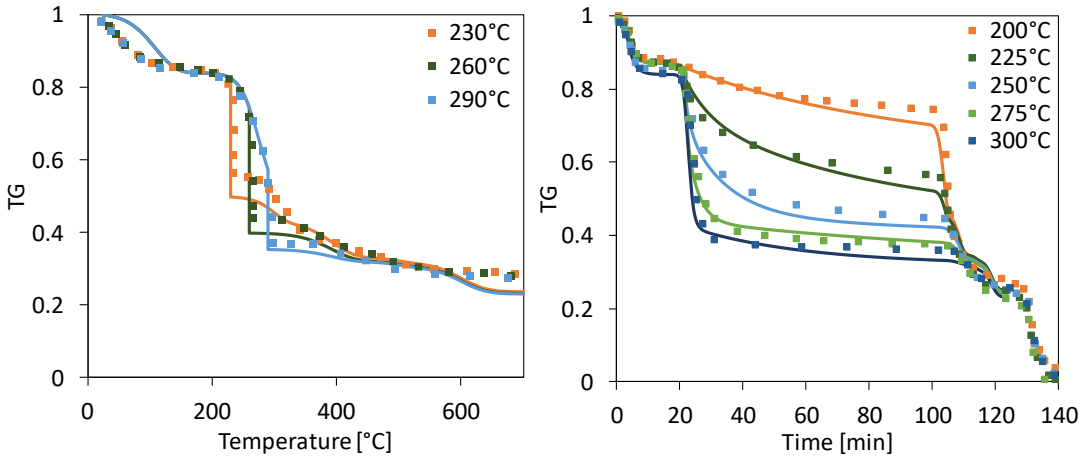

Figure 60 - Torrefaction of Xylan. Mass loss versus temperature program [193] and reaction time [194].

1.3. Lignins

Lignin pyrolysis products largely retain the structure of the monolignols from which they originate. Syringol derivatives are products derived from S-lignin units, while guaiacols are products derived from G-lignin units [165]. Klein and Virk [195] developed a lignin pyrolysis model based on a statistical characterization of the lignin structure. Lignin is assumed as the juxtaposition of methoxy phenol and a propanoid side chain attribute on an aromatic ring. Pyrolysis pathways and kinetics were derived from model substrates that mimicked the chemical moieties within lignin. The model was then extended to simulate Kraft lignin pyrolysis. Because of the changes in lignin structure which occur during the Kraft pulping process, the model was changed to accommodate a wider variety of side chains and inter-unit linkages [196]. The model was able to describe the temporal evolution of lignin thermolysis products in terms of gases (comprising methane and carbon monoxide) aqueous liquids (water and methanol), tars (guaiacol, catechol, and phenol), and a carbonaceous

residual char (multiple-ring aromatics) [197]. Klein and coworkers also used a Monte Carlo approach to generate a population of diverse lignin structures, whose average properties agree with experimental observables and analyzed their subsequent thermal decomposition. However, the lignin molecules exhibit a linear structure. In order to have a more explicit representation of the hyper-branched topology of lignin, [198] created a library of structural representations of lignin in order to enable more detailed computational studies in the areas of both kinetic modeling and molecular simulation. The complex structure of wheat straw lignin is used for demonstration purposes as a representative herbaceous lignin, even if the method seems sufficiently general and can be applied to any lignin source.

The multistep kinetic scheme of lignin decomposition here considered is a simplification of the detailed mechanism of Faravelli, Frassoldati [109] and it is schematically shown in Figure 61. This multistep kinetic mechanism fairly fits the one more recently discussed by Zhou, Pecha [173].

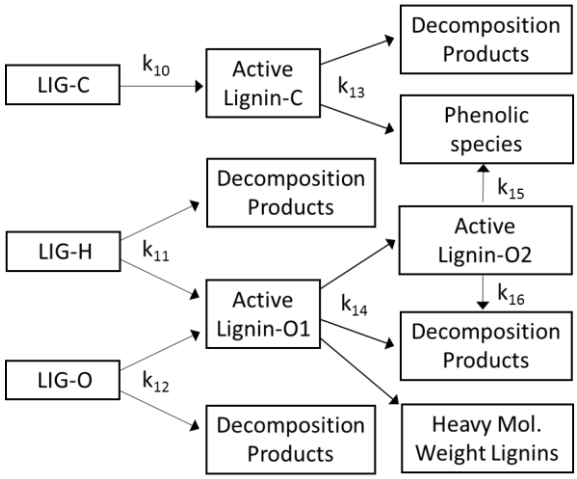

Figure 61 - Multistep kinetic mechanism of pyrolysis of the three reference lignins.

Figure 62 shows the thermogravimetric analysis of the three reference lignins at 20K/min. The thermal behavior of LIG-O and LIG-H promptly converges towards a common intermediate. The char residue of LIG-C is more abundant, because of its largest carbon content. The lignin pyrolysis reactions are active in a wide temperature range and release phenolic components. Phenol, anisole (metoxy-benzene), 2,6-dimethoxy-phenol, 4-(3-hydroxy-1-propenyl)phenol, and 3-(4-hydroxy-3,5-dimethoxy-phenyl)-acrylaldehyde are the selected lumped species representatives of these compounds. Heavy molecular weight lignins (HMWL) are also released and only one lumped component $C_{24}H_{28}O_4$ is considered.

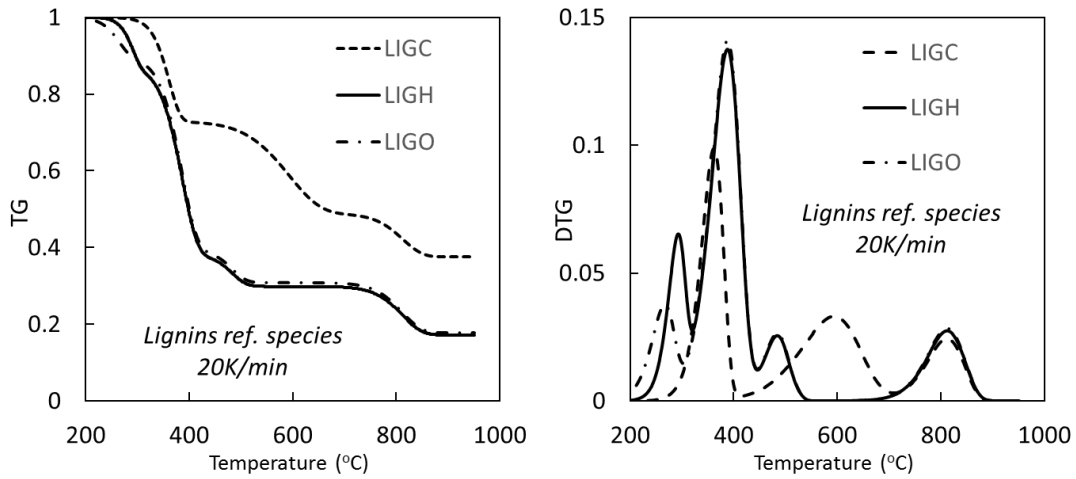

Figure 62 - Pyrolysis of Lignin: thermogravimetric analysis of the three reference species at 20K/min.

Figure 63 shows the trans-3-(3,4-dimethoxyphenyl)-4-((E)-3,4-dimethoxystyryl)-cyclohex-1-ene and the diethylstilbestrol-dipropionate as a couple of possible representative components.

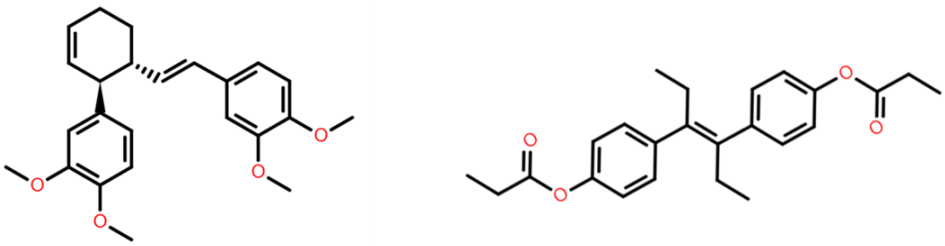

Figure 63 - Heavy molecular weight lignin (HMWL). Lumped components $C_{24}H_{28}O_4$

Figure 64 compares model predictions and experimental data of thermogravimetric analysis (TGA) of several different lignins, at heating rates of 20 K/min [199-201]. Observed deviations are within the experimental uncertainties, mainly when considering that lignins were extracted with different methods. Indeed, Yang et al. [2016] observed that different isolation processes affect both the thermal behavior and the properties of lignins.

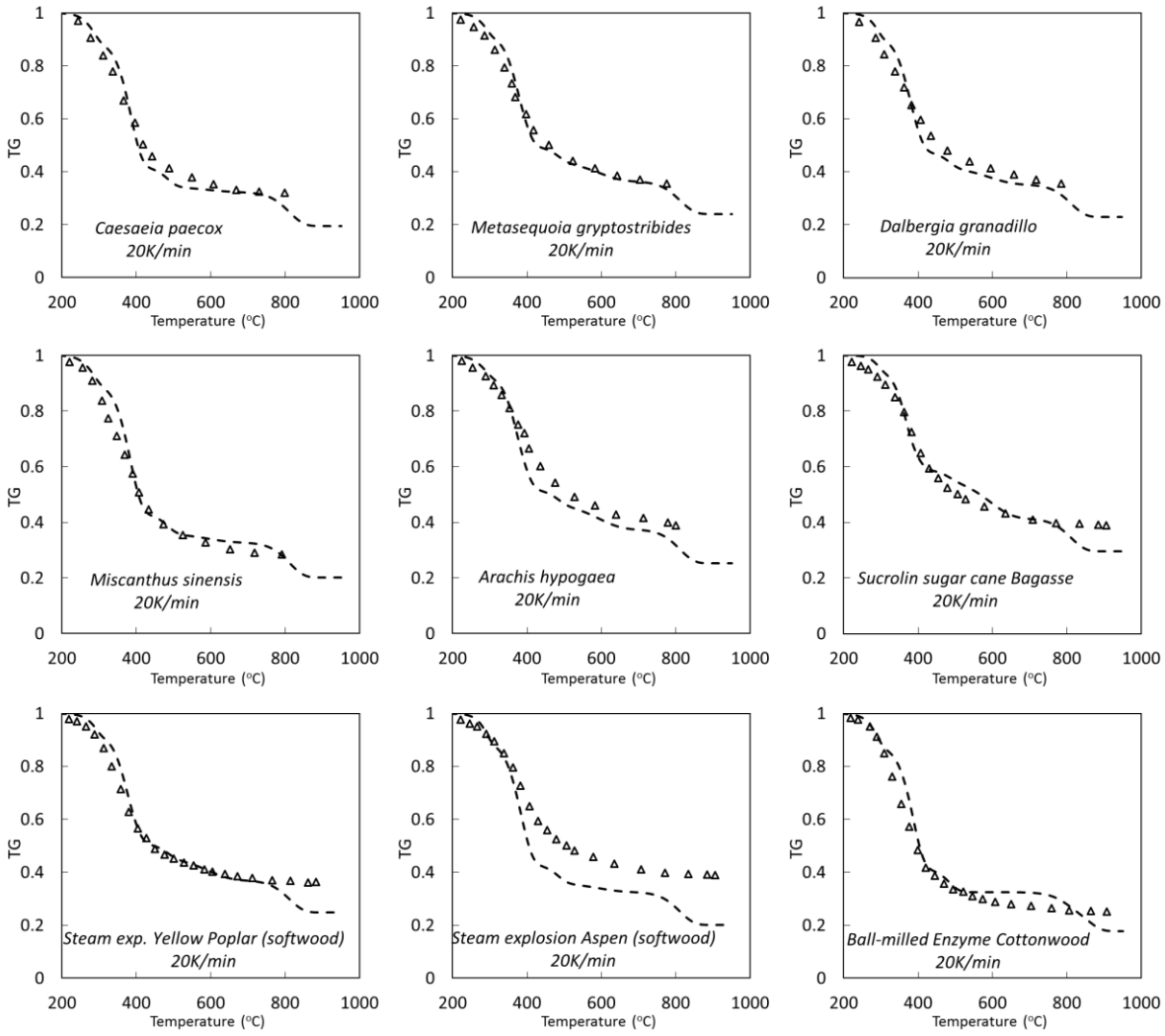

Figure 64 - Lignin pyrolysis (heating rates 20 K/min). Comparisons of model predictions (lines) and experimental data (marks) [199-201]

1.4. Extractives

1.4.1. Condensed Tannins

As already discussed in Chapter 2, several experimental data contributed to the definition of the reference species TANN, which releases relevant amounts of phenol and catechol species in the pyrolysis process. Apart from the initial removal of water, a first release of volatile species takes place at 300-400 °C, then there are slow and progressive crosslinking and charification reactions followed by a further peak in the DTG curve at temperatures higher than 700 °C [202]. A polymeric intermediate ITANN ($C_8H_4O_4$: 3,5-dihydroxy-benzofuranone) is the lumped species involved in the successive devolatilization and charification reactions.

Figure 33 shows a comparison between the model predicted at TG 10 °C/min under nitrogen and the average of several experimental data of condensed tannins. Experimental data refer to extracted condensed tannins from Tunisian Aleppo pine bark [203], Tunisian sumac root bark [204], Quebracho bark [202], Gambier [205], Schinopsis quebracho bark [206] and *Pinus radiata* bark [202, 207].

In agreement with the experiments, the kinetic mechanism is constituted by two successive reactions and it is reported in Table 20. First, there is a fission of the heterocyclic ring, with the release of phenolic species and the formation of an intermediate lumped species (ITANN: $C_8H_4O_4$), which contributes to a further release of volatiles with reticulation and charification process, at higher temperatures.

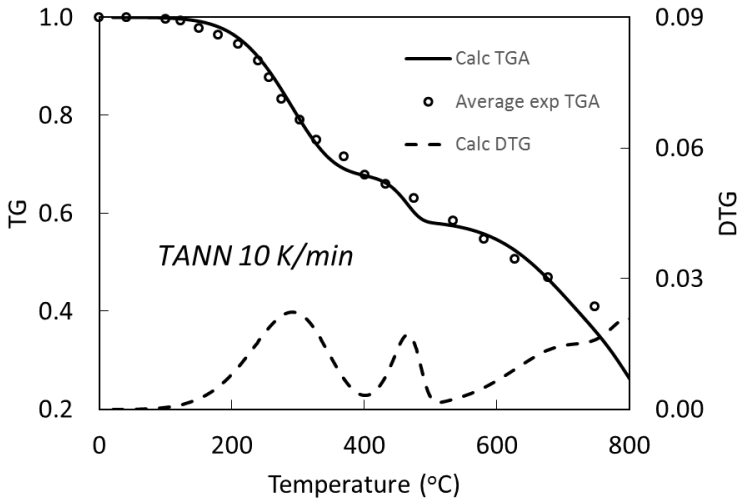

Figure 65 - TGA and DTG of condensed tannins samples heated at 10 K/min, model predictions (lines) and experimental data (marks).

1.4.2. Resins and Triglycerides

Thermogravimetric analysis of soybean [208] and corn oils [209] were very useful to understand the mass loss profile of triglycerides and support the development of the kinetic mechanism of the lumped reference species of resins and triglycerides (TGL). In line with the experiments, triglyceride devolatilization is well represented by a single step kinetics, without significant residue. Pyrolysis of triglycerides typically releases acrolein (C_2H_3CHO) together with two fatty acids and one aldehyde [210, 211]. In order to simplify the stoichiometries and the overall number of species in the mechanism, a lumping procedure is proposed.

First, one water molecule was added to the reference triglyceride species, for the simplification of the stoichiometries. Free-fatty acids have similar structure and reactivity as

the analogous methyl-esters, which were already studied and included in the CRECK mechanism [212]. Therefore, instead of increasing the number of species by releasing free-fatty acids, we consider that reference species TGL release analogous methyl-esters. Linoleic acid is then lumped as a combination of methyl-linoleate ($C_{19}H_{32}O_2$) and methyl-decanoate ($C_{11}H_{18}O_2$) in the mole ratio 0.875/0.125. This allows to satisfy both the elemental mass balances and account for the different chain lengths present.

In this way, the lumped stoichiometry of TGL decomposition simply involves the release of acrolein and two different chain-lengths methyl-esters. Figure 66 shows a satisfactory comparison between experimental data [210, 211] and model predictions of a TGA, with a heating rate of 10 K/min. In these conditions, the DTG curve peaks at ~400 °C.

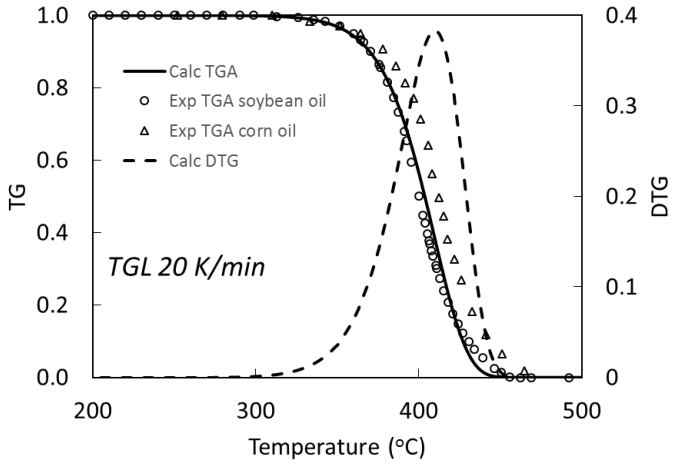

Figure 66 - TGA and DTG of lumped specie for resins (TGL) and natural vegetable oils, heated at 20 K/min, model predictions (lines) and experimental data (symbols) [210, 211]

Pyrolysis Reactions				Kinetic Parameters A (s^{-1}), Eact (kcal/kmol)
Cellulose				
1	CELL	->	CELLA	1.50 10^{14} x exp(-47000/RT)
2	CELLA	->	0.05CH2OHCH2CHO + 0.4CH2OHCHO + 0.03CHOCHO + 0.17CH3CHO + 0.25C6H6O3 + 0.35C2H5CHO + 0.2CH3OH + 0.15CH2O + 0.49CO + 0.43CO2 + 0.13H2 + 0.93H2O + 0.02HCOOH + 0.05CH4 + 0.66CHAR + 0.05G{CO} + 0.05G{COH2}$_{Loose}$ + 0.1G{H2}	2.50 10^{6}x exp(-19100/RT)
3	CELLA	->	C6H10O5	3.30 x T x exp(-10000/RT)
4	CELL	->	0.125H2 + 4.45H2O + 5.45CHAR + 0.12G{COH2}$_{Stiff}$ + 0.25G{CO} + 0.18G{COH2}$_{Loose}$ + 0.125G{H2}	9.00 10^{7} x exp(-31000/RT)
Hemicellulose				
5	GMSW	->	0.7HCE1 + 0.3HCE2	1.00 10^{10} x exp(-31000/RT)
6	XYHW	->	0.35HCE1 + 0.65HCE2	1.25 10^{11} x exp(-31400/RT)
7	XYGR	->	0.12HCE1 + 0.88HCE2	1.25 10^{11} x exp(-30000/RT)
8	HCE1	->	0.06CH2OHCH2CHO + 0.16FURFURAL + 0.1CHOCHO + 0.13C6H6O3 + 0.09CO2 + 0.02H2 + 0.54H2O + 0.25C6H10O5 + 0.1CH4 + 0.25C5H8O4 + 0.1CHAR	1.60 10^{1} x T x exp(-12900/RT)
9	HCE1	->	0.4CH2O + 0.49CO + 0.39CO2 + 0.1H2 + 0.4H2O + 0.05HCOOH + 0.1C2H4 + 0.3CH4 + 0.975CHAR + 0.37G{COH2}$_{Stiff}$ + 0.51G{CO2} + 0.01G{CO} + 0.325G{CH4} + 0.075G{C2H4} + 0.43G{COH2}$_{Loose}$ + 0.05G{H2} + 0.2G{C2H6}	3.00 10^{-3} x T x exp(-3600/RT)
10	HCE2	->	0.145FURFURAL + 0.105CH3CO2H + 0.035CH2OHCHO + 0.3CO + 0.5125CO2 + 0.5505H2 + 0.056H2O + 0.0175HCOOH + 0.049C2H5OH + 0.1895CH4 + 0.7125CHAR + 0.78G{COH2}STIFF + 0.45G{CO2} + 0.105G{CH3OH} + 0.05G{CH4} + 0.1G{C2H4} + 0.18G{COH2}$_{Loose}$ + 0.21G{H2} + 0.2G{C2H6}	7.00 10^{9} x exp(-30500/RT)
Lignins				
11	LIGH	->	0.2CH2OHCHO + 0.5C2H5CHO + 0.1CO + 0.4C2H4 + 0.1C2H6 + LIGOH	6.70 10^{12} x exp(-37500/RT)
12	LIGO	->	CO2 + LIGOH	3.30 10^{8} x exp(-25500/RT)
13	LIGC	->	0.1C6H5OCH3 + 0.22CH2O + 0.21CO + 0.1CO2 + H2O + 0.27C2H4 + 0.1VANILLIN + 0.35LIGCC + 5.85CHAR + 0.4G{COH2}$_{Stiff}$ + 0.36G{CH4} + 0.17G{COH2}$_{Loose}$ + 0.1G{H2} + 0.2G{C2H6}	1.00 10^{11} x exp(-37200/RT)
14	LIGCC	->	0.15C6H5OCH3 + 0.35CH2OHCHO + 1.15CO + 0.7H2 + 0.7H2O + 0.3C2H4 + 0.45CH4 + 0.25VANILLIN + 0.15CRESOL + 0.4C2H6 + 6.8CHAR + 0.4G{CO}	1.00 10^{4} x exp(-24800/RT)
15	LIGOH	->	0.025C24H28O4 + 0.1C2H3CHO + 0.6CH3OH + 0.65CO + 0.05CO2 + H2O + 0.05HCOOH + 0.1CH4 + 0.9LIG + 4.25CHAR + 0.4G{COH2}$_{Stiff}$ + 0.6G{CO} + 0.3G{CH3OH} + 0.25G{CH4} + 0.1G{C2H4} + 0.45G{COH2}$_{Loose}$ + 0.15G{C2H6}	1.50 10^{8} x exp(-30000/RT)
16	LIG	->	0.1C6H5OCH3 + 0.3CH3CHO + 0.6CO + 0.5C2H4 + VANILLIN + 0.1CHAR	4.00 x T x exp(-12000/RT)
17	LIG	->	0.4CH2O + 0.3CO + 0.1CO2 + 0.6H2O + 0.2CH4 + 6.1CHAR + 0.65G{COH2}$_{Stiff}$ + 0.2G{CO} + 0.4G{CH3OH} + 0.4G{CH4} + 0.5G{C2H4} + 1.25G{COH2}$_{Loose}$ + 0.1G{H2}	8.30 10^{-2} x T x exp(-8000/RT)
18	LIG	->	0.4CH3OH + 0.4CH2O + 2.6CO + 0.6H2O + 0.75C2H4 + 0.6CH4 + 0.5C2H6 + 4.5CHAR	1.50 10^{9} x exp(-31500/RT)

Extractives				
19	TGL	->	C2H3CHO + 0.5U2ME12 + 2.5MLINO	$7.00\ 10^{12}$ x exp(-45700/RT)
20	TANN	->	H2O + 0.85C6H5OH + ITANN + G{CO} + 0.15G{C6H5OH}	$2.00\ 10^{1}$ x exp(-10000/RT)
21	ITANN	->	2CO + H2O + 5CHAR + 0.45G{COH2}$_{Stiff}$ + 0.55G{COH2}$_{Loose}$	$1.00\ 10^{3}$ x exp(-25000/RT)
Metaplastic				
22	G{CO2}	->	CO2	$1.00\ 10^{6}$ x exp(-24500/RT)
23	G{CO}	->	CO	$5.00\ 10^{12}$ x exp(-52500/RT)
24	G{CH3OH}	->	CH3OH	$2.00\ 10^{12}$ x exp(-50000/RT)
25	G{COH2}$_{Loose}$	->	0.2CO + 0.2H2 + 0.8H2O + 0.8CHAR	$6.00\ 10^{10}$ x exp(-50000/RT)
26	G{C2H6}	->	C2H6	$1.00\ 10^{11}$ x exp(-52000/RT)
27	G{CH4}	->	CH4	$1.00\ 10^{11}$ x exp(-53000/RT)
28	G{C2H4}	->	C2H4	$1.00\ 10^{11}$ x exp(-54000/RT)
29	G{C6H5OH}	->	C6H5OH	$1.50\ 10^{12}$ x exp(-55000/RT)
30	G{COH2}$_{Stiff}$	->	0.8CO + 0.8H2 + 0.2H2O + 0.2CHAR	$1.00\ 10^{9}$ x exp(-59000/RT)
31	G{H2}	->	H2	$1.00\ 10^{8}$ x exp(-70000/RT)
H2O Evaporation				
32	ACQUA	->	H2O	1 x T x exp(-8000/RT)

Table 20 - Kinetic mechanism of lignocellulosic biomass pyrolysis

2. Validation of the kinetic mechanism of lignocellulosic biomass pyrolysis

2.1. Comparison with experimental data

As already mentioned, several detailed kinetic mechanisms of cellulose are available in the literature, while hemicellulose and lignin received a minor attention. The lumped kinetic scheme summarized in Table 20 and discussed in this work is very simplified, with the aim of an effective use not only at the particle scale[168], but also at the reactor scale in order to verify the effect of secondary gas-phase reactions. Computational time limitations are indeed very severe when simulating a gasifier or a biomass combustor at the reactor scale[213-215].

As already mentioned, biomass is characterized as a mixture of the seven reference components, whose internal composition either is obtained through the biochemical analysis, or is derived based on the elemental analysis. A couple of examples are useful to describe how to characterize different biomass samples.

A first example refers to Pinus radiata sawdust [201], whose biochemical composition determined with NMR, was: 55.5 of holocellulose, 32.8 of lignin, 5.8 of extractives, together with 5.24 of moisture and 0.7 of ash. This biomass is then characterized in terms of reference compounds considering some constraints. According to typical internal ratios, holocellulose is considered as 75% of cellulose and 25% of softwood hemicellulose (mainly glucomannans). Moreover, lignin is divided into 80% of LIG-O and 20% LIG-C, while extractives are considered as tannins (TANN), due to the high oxygen content of this biomass sample. The biomass is then characterized in the following way:

CELL	GMSW	LIG-C	LIG-H	LIG-O	TGL	TANN	Moisture	Ash
0.419	0.140	0.066	0.000	0.262	0.000	0.052	0.052	0.007

A second characterization example refers to a wheat straw sample, where only the elemental composition is reported (C/H/O=49.3/5.7/45.0 wt) [216]. The following three reference mixtures of reference components are first defined. RM1 is the holocellulose, with a molar ratio cellulose/hemicellulose=1.33, being a grass/cereal biomass sample. Reference mixtures RM-2 and RM-3 are mixtures of the three different lignins, with extractives (tannins and triglycerides). Due to the relatively low H content of this biomass, a linear combination 68% of RM-1 and 32% of RM-3 satisfies the elemental biomass composition. By splitting the reference mixtures, the biomass composition is:

CELL	XYGR	LIG-C	LIG-H	LIG-O	TGL	TANN	Moisture	Ash
0.373	0.230	0.025	0.000	0.164	0.000	0.099	0.090	0.019

Figure 35 shows the comparisons of predicted and experimental TGAs of these biomass samples at a heating rate of 80 K/min. The differential (DTG) curves are also reported, and they clearly show the peak of cellulose devolatilization at about 400 °C. *Pinus radiata* presents a shoulder before the cellulose peak, which correspond to GMSW hemicellulose decomposition. On the other hand, wheat straw has a smaller peak before 300 °C, corresponding to the thermal behavior of XYGR hemicellulose pyrolysis.

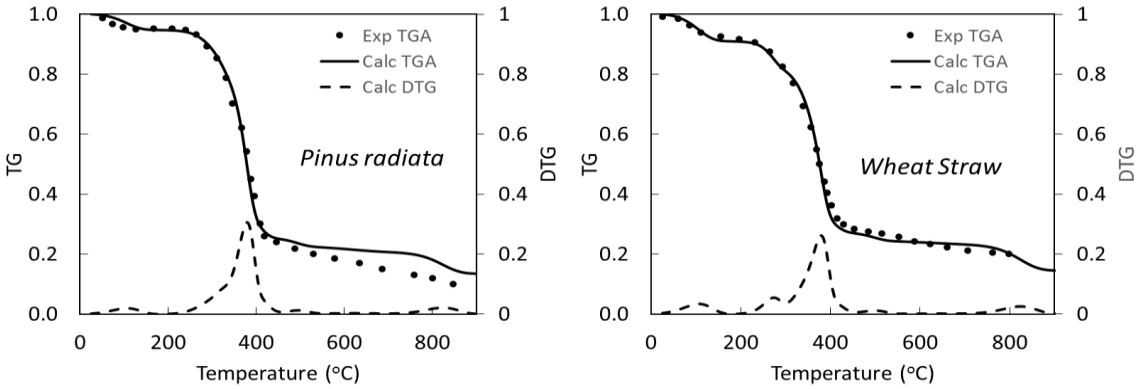

Figure 67 - Comparisons of predicted (lines) and experimental (marks) TGAs of Pinus radiata (Left Panel) and Wheat Straw (Right Panel) at heating rate of 80 K/min [201, 216].

Figure 68 show two more examples of TGA, this time two samples of waste biomasses, shells obtained from the extraction of palm oil and the bark of softwood. It is worthwhile to highlight the importance of characterizing these samples with extractives, as the shells are quite rich in hydrophobic species and the bark contains high amounts of both tannins and resins. From oil palm shell composition, it is clear that it requires some TGL for characterization, while for this bark sample, it is not necessary to include extractives. However, from the database, we can deduce that, because of the biomass type, extractives would provide better agreement on biochemical composition, the successive decomposition profile and released products.

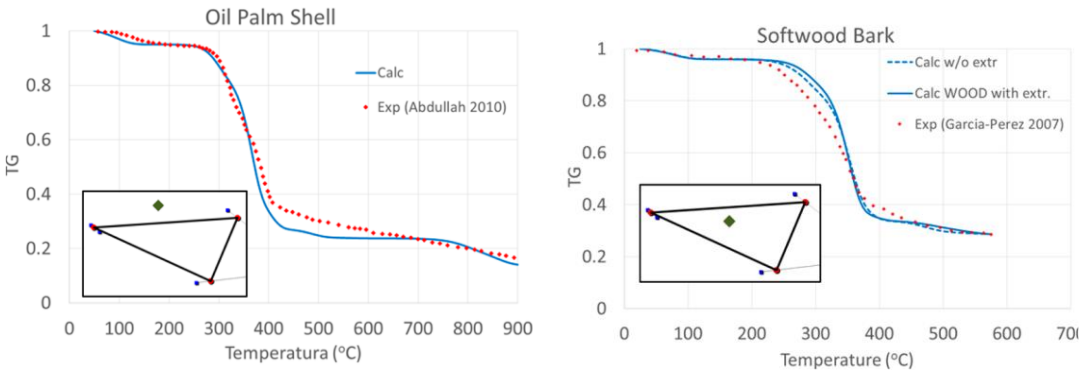

Figure 68 - Comparisons of predicted (lines) and experimental (marks) TGAs of Oil Palm Shell (Left Panel) at heating rate of 20 K/min and Softwood bark (Right Panel) at 10 K/min.

As already mentioned, the predicted pyrolysis profile is a linear combination of the weighted average of the reference species that characterize the sample. In order to better illustrate this feature, one more TGA is reported in Figure 69, showing the mass loss of almond shell, a typical residue from food industry. Together with the mass loss, the DTG of each reference species is reported, highlighting the differences in their individual pyrolysis behavior. In order to reduce the number of curves reported, the DTG of lignin corresponds to the combination of the three reference lignins.

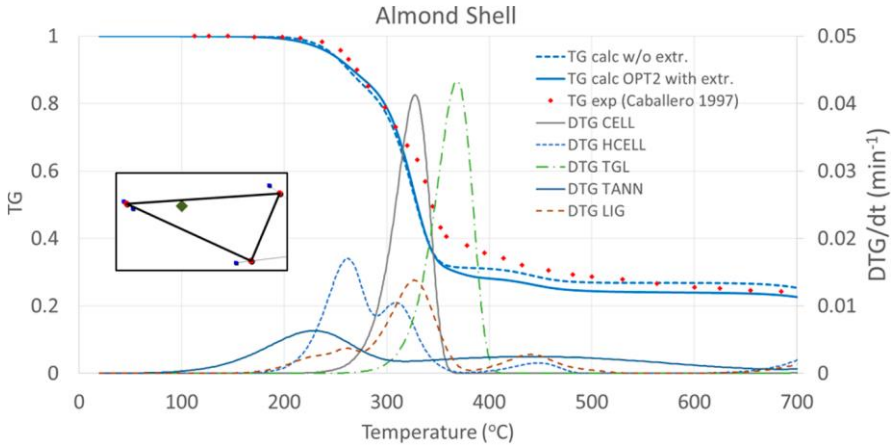

Figure 69 - Comparison of predicted (line) and experimental (marks) TGA of Almond shell at heating rate of 2 K/min. DTG of the reference species that characterize this sample.

Back to the first examples of TGA of *Pinus radiata* and Wheat Straw, from Figure 67, Table 21 compares the predicted volatile species from the pyrolysis of these two samples at 700 °C, at heating rate of 80 K/min. The amount and the C/H/O composition of the solid residue is also reported. Levoglucosan (LVG) is the most abundant volatile species for both the samples, because of the large amount of cellulose. The possible LVG degradation both for the catalytic effect of ash and for sample size will be discussed later on. Together with phenol, only a few species (anisole, coumaryl alcohol, synapyl aldehyde, and HMWL) lumped

phenolic derivatives, and they are more abundant from the pyrolysis of pine sawdust (softwood), because of the greatest amount of lignin. Direct comparisons of predictions of released species with experimental data will be discussed in the next chapter, because the presence and the effect of the secondary gas phase reactions needs to be accounted. Because of the moderate final temperature, still there is ∼20-25% of oxygen and ∼4-5% of hydrogen in the predicted weight composition of the residual char. Moreover, detailed description of the formation and evolution of residual char during pyrolysis will be explained in chapter 6.

The products reported in Table 21 represent the set of volatile species released by the biomass pyrolysis kinetic scheme reported in Table 20. These volatile species, once released in the gas phase can undergo successive decomposition and oxidation reactions. Table 22 reports the formation enthalpy ΔHf,298 and formation entropy ΔSf,298 of major oxygenated species released by biomass samples considered in the CRECK kinetic mechanism, which will be further discussed in the next chapter.

	Pine Sawdust	**Wheat Straw**
Temperature (°C)	700	700
Heating Rate (K/min)	80	80
Biomass Characterization (wt.%)		
CELL	41.7	37.3
HCELL	13.9	23.0
LIG (LIGH+LIGO+LIGC)	32.6	18.9
TANN	6.0	9.9
TGL	0.0	0.0
MOISTURE	5.2	9.0
ASH	0.7	1.9
Gases (wt.% of initial biomass)	**13.9**	**13.3**
CO	6.4	5.6
CO_2	6.2	7.1
H_2	0.0	0.0
C_2H_4	0.8	0.4
CH_4	0.5	0.3
Condensables (wt.% of initial biomass)	**65.6**	**64.5**
H_2O	11.5	14.5
CH_2O	2.3	2.9
CH_3OH	2.9	2.8
CH_3CHO	0.8	0.6
HCOOH	0.3	0.3
C_2H_5OH	0.2	0.5
Acrolein	0.3	0.2
Glyoxal	0.8	0.7
Hydroxy-acetaldehyde	3.0	2.8
Acetic acid	0.8	2.4
Propanal/Acetone	1.7	1.6
Acetol ($C_3H_6O_2$)	1.8	1.5
Furfural	0.9	0.7
C_5 sugars	4.7	3.7
Phenol	1.9	2.7
Hydroxy-methyl-furfural	3.2	2.8
Levoglucosan	22.0	19.7
Anisole	1.0	0.6
Coumaryl alcohol	0.7	0.3
Sinapyl Aldehyde	4.3	2.7
Heavy Mol. Weight Lignin (HMWL)	0.6	0.4
Solid residue (wt.% of initial biomass)	**20.3**	**21.7**
CHAR	**19.6**	**19.8**
C	77.1	70.9
H	4.1	4.7
O	18.9	24.3
ASH	0.7	1.9

Table 21 - Pyrolysis of Pinus radiata and Wheat Straw at 80 K/min. Characterization in terms of reference species and predicted composition of primary pyrolysis products and residual char, at 700 °C.

Chemical Name	Formula	ΔH_f	ΔS_f
Glyoxal	$C_2H_2O_2$	-50.6	65.4
Acetaldehyde	C_2H_4O	-39.5	63.0
Acetic Acid	$C_2H_4O_2$	-103.9	67.4
Hydroxy-acetaldehyde	$C_2H_4O_2$	-73.5	73.6
Ethylene-glycol	$C_2H_6O_2$	-92.0	76.3
Acrolein	C_3H_4O	-20.3	67.4
Propanedial	$C_3H_4O_2$	-62.4	73.7
3-Hydroxy-2-oxo-propanal	$C_3H_4O_3$	-102.7	88.4
Propanal	C_3H_6O	-45.3	72.8
1-Propanol	C_3H_8O	-60.9	76.4
2-Propanol	C_3H_8O	-65.5	74.5
Acetol	$C_3H_6O_2$	-87.4	80.6
3-Hydroxypropanal	$C_3H_6O_2$	-80.3	83.3
1,3-Propanediol	$C_3H_8O_2$	-45.5	86.0
Glycerol	$C_3H_8O_3$	-137.1	95.8
Furan	C_4H_4O	-10.2	60.2
Butanedione	$C_4H_6O_2$	-78.4	84.2
C4 O-heterocycles	C_4H_8O	-27.7	73.6
Furfural	$C_5H_4O_2$	-36.1	77.8
Xylosan	$C_5H_8O_4$	-151.6	104.8
Phenol	C_6H_6O	-23.0	75.3
Hydroxymethyl-furfural	$C_6H_6O_3$	-79.8	98.2
Levoglucosan	$C_6H_{10}O_5$	-200.9	113.5
Anisole	C_7H_8O	-17.1	84.0
Syringol	$C_8H_{10}O_3$	-95.3	111.0
Coumaryl alcohol	$C_9H_{10}O_2$	-49.2	109.0
Sinapyl aldehyde	$C_{11}H_{12}O_4$	-70.3	145.0
Heavy Molecular Weight Lignin (HMWL)	$C_{24}H_{28}O_4$	-0.2	186.7

Table 22 - Formation enthalpy $\Delta H_{f,298}$ [kcal/mol] and formation entropy $\Delta S_{f,298}$ [cal/mol/K] of major oxygenated species released from biomasses.

Anyway, it is evident that this multistep kinetic mechanism can be further improved in terms of new reaction steps, kinetic parameters, detail of reaction products [47, 217].

Shen, Jin [172] recently revised biomass fast pyrolysis discussing the yields of liquid and gas products, focusing on the primary and secondary formation pathways of oxygenated compounds. Moreover, gas chromatography with flame ionization detector and two-dimensional gas chromatography with time-of-flight mass spectrometry [218], as well as the application of tunable synchrotron vacuum ultraviolet photoionization mass spectrometry (SVUV-PIMS) [219], allows to identify and quantify more than hundreds of compounds, thus describing a large portion of bio-oil. All these continuous research efforts in the fast pyrolysis of biomass easily allow the extensions and improvements of the lumped kinetic mechanism [47, 180]. It is worth underlining that the interactions among reference species are not considered [220]. The ash influence will be discussed in the next section, because it is well known that they act as catalysts and significantly modify the overall biomass pyrolysis process [221].

2.2. Catalytic effect of ash

Biomass contains ashes, which act catalytically during fast pyrolysis and result in a decrease of the process selectivity towards the desired liquid product. In fact, while pyrolysis products form, they can interact with inorganic elements in the residual solid. Particularly, levoglucosan easily reacts on minerals present in the residual char from biomass pyrolysis, forming levoglucosenone, furan derivatives, and lighter oxygenates such as acetic acid, acetone, and acetol [165]. The pretreatment of biomass samples with water and acidic solutions can be carried out in order to reduce the content of inorganics, and this demineralization reduces the catalytic effects of the resulting metal oxides (ashes) [222-224].

Different inorganics are responsible for different types of secondary reactions [225, 226]. Generally, the presence of metal cations favors the homolytic cleavage of pyranose ring bonds over the heterolytic cleavage of glycosidic linkages, favoring in this way the formation of light oxygenate products at the expense of the direct release of levoglucosan. Relative to the reduction in levoglucosan yield the following reactivity trends were observed [227]:

Potassium (K) > Sodium (Na) > Calcium (Ca) > Magnesium (Mg)

While Na, K, Mg, and Ca cations all catalyze levoglucosan decomposition, their effects differ [165]. Na and K mainly favor the formation of formic acid, glycolaldehyde, and acetol through decomposition reactions, while Mg and Ca mainly promote furfural formation and dehydration reactions [228, 229].

Gargiulo, Giudicianni [230] further analyzed the catalytic effect of Na and K ions on steam assisted pyrolysis of Arundo donax. They observed and confirmed that the addition of Na and K ions to cellulose affects both pyrolysis and gasification proceses. Na promotes the pyrolysis reactions determining a reduced liquid yield, while both Na and K ions favor char gasification leading to the increase of gas production and a decrease of yields of levoglucosan and furans. The effect of Na ions seems more evident than that of K ions. Similar effects are observed on xylan pyrolysis, while there is a negligible effect of inorganics on the pyrolysis behavior of lignin fraction. This fact well agrees with the findings of Patwardhan, Brown [231].

Very recently, Zhou, Mayes [232], Zhou, Mayes [233] studied the effect of Na ions on the pyrolysis behavior of several biomasses. By using a micropyrolyzer, they investigated the catalytic effects of NaCl on fast pyrolysis of carbohydrates (glucose, cellobiose, maltohexaose and cellulose), and on a major product of cellulose pyrolysis, levoglucosan. They also developed a mechanistic model addressing the significant catalytic effects of NaCl on the product distribution. The model involves 768 reactions of 222 species, including the interactions of Na with cellulosic chains and low molecular weight species. The sharp reduction in the yield of levoglucosan (LVG) from fast pyrolysis of cellulose in the presence of NaCl was mainly caused by reduced decomposition of cellulose chains via end-chain initiation and depropagation due to Na favoring competing dehydration reactions.

The catalytic effect of alkaline earth metals on cellulose pyrolysis was studied by doping cellulose and levoglucosan with calcium or magnesium nitrate salts and their oxides [234]. Metal oxides have a negligible impact on the distribution of cellulose pyrolysis products, whereas metal ions doped by ion exchange were active for cellulose decomposition. Ca ions are more active than Mg ions and they promote the primary formation of char from cellulose, the conversion of levoglucosan to light oxygenates and furans, and the successive consumption of furans to char and permanent gases.

Together with the catalytic effects of inorganic elements [45], the possible factors affecting the yield of levoglucosan from biomass fast pyrolysis also include the interactions between cellulose and lignin. In fact, the interactions between cellulose and lignin during fast pyrolysis can inhibit the formation of levoglucosan due to the inherent covalent linkages between cellulose and lignin [224, 235].

Figure 70 shows the yields of bio-oil from fast pyrolysis of wood and agro-biomass, as obtained in the VTT's 20 kg/h pyrolyzer [236]. A high ash content in biomass leads to bio-oils with a higher water content and lower oil yield. This confirms the catalytic effect of ash promoting pyrolysis and dehydration reactions, decreasing bio-oil yield. It shows the effect of the ash content on the yield of organics and is based on over 20 years of experiments with bio-oils at VTT.

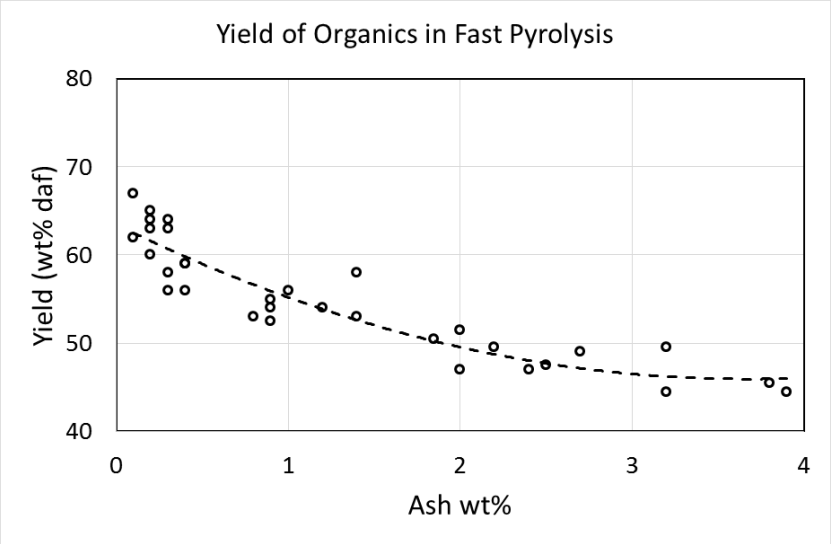

Figure 70 - Effect of ash content on the yields of bio-oil from fast pyrolysis of biomass in the VTT pyrolyzer [236].

The relevant catalytic effect of ash needs to be accounted for in the pyrolysis model. Trendewicz, Evans [221] already proposed a modification of the cellulose pyrolysis mechanism in order to include the effect of K on product yields and composition. They changed the kinetic parameters based on the experimental data collected from pyrolysis of cellulose samples treated with different K levels (0-1% mass fraction). In order to maintain a very flexible and simple kinetic model, it is convenient to modify the kinetic parameters of a few selected reactions of Table 20, based on a single ash parameter. The major catalytic effect of ash is the reduction of levoglucosan and xylan in favor of decomposition and dehydration products, together with a char increase. With reference to the cellulose decomposition scheme reported in Figure 55, it is clear that two splitting or selectivity parameters govern the product distribution. The first one (S_1) refers to the selectivity in the production of active cellulose, while the second one (S_2) refers to the selectivity of levoglucosan released by the active cellulose. Figure 71 shows how these selectivities vary as a function of the reaction temperature. These selectivities represent the average

selectivities, as obtained from the kinetic parameters reported in Table 20. The apparent and global catalytic effect of ash is to deplete both these selectivities.

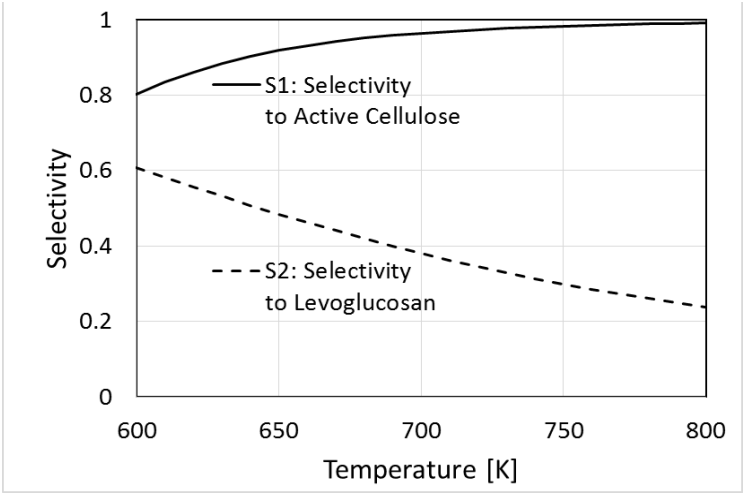

Figure 71 - Cellulose Pyrolysis: Selectivity towards active cellulose and levoglucosan as a function of the reaction temperature.

Therefore, once known the ash content of the biomass samples, a global Ash Factor (AF) (in adimensional form) is assigned, with values ranging between 0 (no Ash) and 1 (more than 5 wt.%). In a simplified form, it is assumed that this catalytic effect is saturated for biomasses with more than 5 wt.% of ash. For instance, it is possible to define AF as a function of the ash content (wt.%) with the following expression:

$$AF = \tanh(ash/2).$$

In this way, the ash factor ranges from zero (low ash content) to asymptotically 1 (ash content higher than 4-5 wt.%), and it assumes a value of about 0.5 for ash content in the order of 1 wt.%.

Figure 72 shows the modified selectivities for biomass samples without ash, and with the maximum ash content.

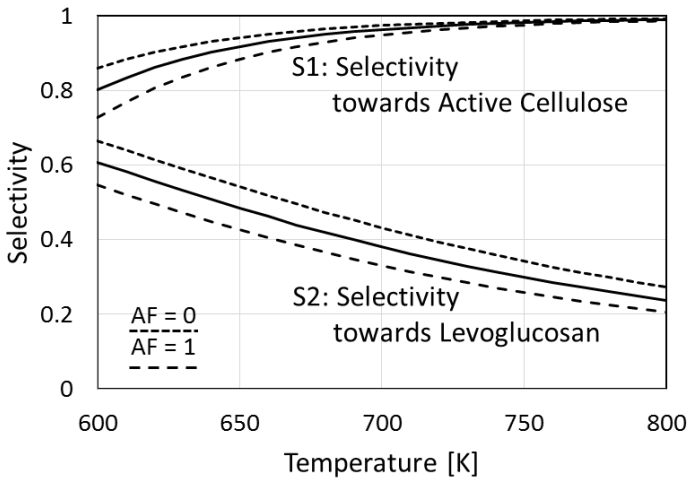

Figure 72 - Cellulose pyrolysis. Selectivity towards active cellulose and towards levoglucosan as a function of the ash parameter AF. Solid lines refer to the kinetic scheme of Table 20.

These corrections are obtained by simply modifying the activation energy of the decomposition reaction of active cellulose (E_2) and the activation energy of the charification reaction (E_4) as a function of the ash factor (AF):

$$E_2 = 19100 - 600 \times (AF-0.5) \qquad [kcal/mol]$$

$$E_4 = 30000 - 1000 \times (AF-0.5) \qquad [kcal/mol]$$

The reference kinetic parameters reported in Table 20 refer to the average of the biomass samples and they refer to an average ash content of 1 wt.% (AF=0.5).

In a very similar way, the decomposition reaction of hemicellulose intermediate (HCE1) is favored in presence of high ash content by correcting the activation energy of the corresponding decomposition reaction with the following correction:

$$E_{dec} = E_{dec} - 1000 \times (AF-0.5) \qquad [kcal/mol]$$

It is evident that these corrections are strongly simplified, but it is also clear that they can at least account for the catalytic effect of ash in a simplified way. Moreover, as the AF was supported by large amount of experimental data, the estimation of this parameter for a single biomass sample can be obtained easily by accessing its ash content.

3. Pyrolysis of Algae Biomass Reference Species

Ross, Jones [117] already discussed the large differences in pyrolysis behavior of algae and lignocellulosic biomass samples. Figure 73 shows that the TG onset of pyrolytic decomposition occurs at a lower temperature for algae compared to straws, grasses, and woody biomass.

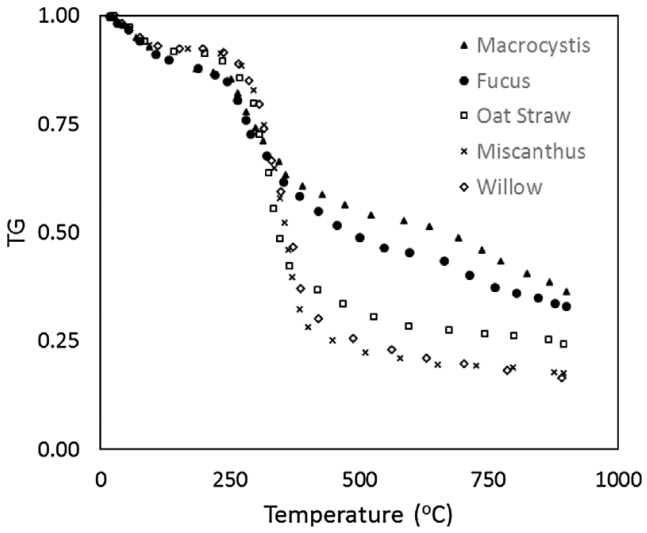

Figure 73 - Thermal gravimetric analysis of fuels in nitrogen showing mass loss at 25 K/min for Algae (Macrocystis pyrifera and Fucus Vesiculosus) and ligno-cellulosic biomass (Oat straw, Willow, and Miscanthus). [After Ross, Jones [117]].

The main weight loss in the region of 250 °C is consistent with high carbohydrate content. Pyrolysis undergoes a stepwise process corresponding to the biochemical composition. The first step of thermal degradation of lignocellulosic material is due to hemicellulose decomposition, whereas the second step is attributed to cellulose pyrolysis and to a wider degradation of lignin components [168]. The first step of mass loss for macroalgae represents the decomposition of carbohydrates, whereas the second one at ~300 °C relates to the pyrolysis of protein components. Pyrolysis of algae in a TGA also shows a gradual and final mass loss above 700 °C, which can be attributed to the high content of inorganics and their decomposition (metal carbonates and other salts) into ashes. Proteins reach the decomposition peak at 330–350 °C and their internal distribution mainly affects tar and gas composition, more than TG profiles, with final solid residues typically ranging from 20 to 30% [237]. In these experiments, the decomposition of lipids is not evident, as macroalgae are relatively poor in those compounds. This effect will be better observed in TG of microalgae.

3.1. Proteins

Protein pyrolysis is a very complex process, characterized by multiphase and multi-step phenomena. Solid phase pyrolysis and successive or secondary gas phase reactions involve very different time scales [238]. The primary decomposition reactions of the three reference species are here assumed as a first degradation and/or depolymerization step with the release, together with gas species, of a couple of intermediate proteins with a lower molecular weight (PROTCC: $C_{90}H_{70}O_{25}N_{10}$ and PROTOH: $C_{45}H_{70}O_{25}N_{10}$). Successive pyrolysis of these intermediate protein species forms nitrogen containing tar components (TARN), together with other gas and tar species. TARN is assumed as a fixed combination of pyrrole (C_4H_5N), pyridine (C_5H_4ON), and diketopiperazine (DKP: $C_4H_6O_2N_2$). Table 23 reports the proposed multistep kinetic mechanism of protein pyrolysis. The same kinetic parameters are assumed for the initial decomposition of the three reference proteins and also for the two intermediates. The rate parameters of this multistep kinetic mechanism of protein pyrolysis are first obtained by comparing model predictions with thermogravimetric data of pyrolysis of proteins taken from the literature.

PROTEIN PYROLYSIS	A [s^{-1}]	E [kcal/kmol]
PROT-O => 2.5 PROTOH + 0.6 PROTCC + TAR_N + 25 NH_3 + 9 NO + 12.75 C_2H_4 + 37.3 CO + 7.7 CO_2 + 71 H_2O	.10 10^5	17500
PROT-H => 5 PROTOH + .5 TAR_N + 20.75 G{H_2} + 27 NH_3 + 7 HCN + 21.5 CH_4 + 70 C_2H_4 + 23.5 H_2O	.10 10^5	17500
PROT-C => 4.5 PROTCC + .5 TAR_N + 7.5 HCN + 2 NH_3 + NO + 29 CO +5 CO_2 + 23.5 C_2H_4 + 10 H_2O	.10 10^5	17500
PROTOH => .5 TAR_N + 2$CHAR_N$ + 27.5CHAR + 3 G{NH_3} + 3 G{HCN} + 1.5 G{CO} +1.083333 C_6H_6 + 22 H_2O	.10 10^4	17000
PROTCC => .5 TAR_N + 42.75 CHAR + 2 $CHAR_N$ + 10 G{HCN} + 3.5 C_6H_6 + 3.375 C_2H_4 + 3 CH_4 + 1.5 H_2O + NH_3	.10 10^4	17000
G{H_2} => H_2	.50 10^{12}	75000
G{NH_3} => NH_3 ; G{HCN} => HCN	.55 10^1	13500
G{CO} => CO	.50 10^{13}	50000

Table 23 - Multistep kinetic mechanism of protein pyrolysis. First order reactions: k=A x exp(-E/RT) [s-1]

Figure 74 shows the comparisons of TG curves of an equal weight mixture of the three reference proteins with several protein samples, not only extracted from algae [239], but also from different feeds such as collagen [240], casein, whey protein concentrate, and gelatin[241], under inert atmosphere. Figure 75 highlight some important details on formation and decomposition of intermediate compounds PROTCC and PROTOH. For simplicity, we report only the fraction of reference protein PROTH decomposition. The same decomposition behavior is indeed observed for PROTC and PROTO, because of the same adopted kinetic parameters. Despite sharing the same kinetic parameters, reference species of proteins differ in composition and release a significant different product distribution, respecting the atomic mass balances.

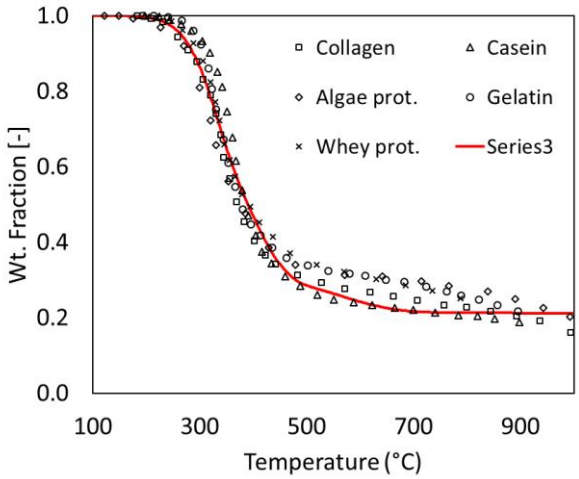

Figure 74 - Pyrolysis of proteins. Comparison of experimental pyrolysis of several protein samples (symbols) and predicted value (line) of TGA at 10 K/min.

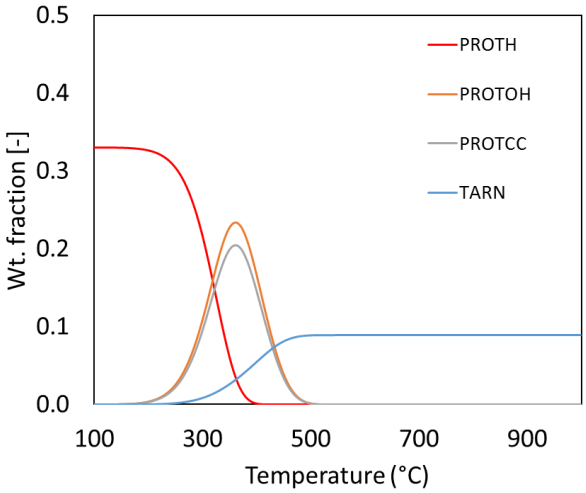

Figure 75 - Details on the evolution of important intermediate species.

Referring to the kinetic model of Table 23, species X referred as G{X} represent species adsorbed in the metaplastic phase. The quoted comparisons show that all the different proteins with different sequences of amino acids behave in a similar way. This fact seems to confirm that the pyrolysis mechanism of these proteins are similar, whereas differences are mainly arising from the distribution and composition of solid, tar and gas species. Stoichiometries of global and lumped reactions are derived by simply accounting for literature studies on protein and algae pyrolysis [117, 120]. Moreover, Purevsuren, Avid [242], Purevsuren and Davaajav [243] extensively analyzed the pyrolysate composition from casein decomposition using GC/MS. Proteins and amino acids release mainly CO2, CO, NH3, H2O, and organic volatiles by decarboxylation, deamination and dehydration reactions [244]. Dehydration, decarboxylation and deamination reactions, releasing H2O, CO2 and NH3 occur

in the first steps, while successive steps yield tars, CO, CH4, C2H4 and HCN [241, 245, 246]. Further slower mass loss is detected after 800 °C, mainly caused by the release of metaplastic species, which reduces the hydrogen, oxygen and nitrogen content in the residual char [240]. Proteins yield more HCN and residual char than their corresponding amino acid mixtures [241, 246], because of cyclization reaction paths (e.g. DKP formation).

3.2. Carbohydrates and Lipids

Different from proteins, the multistep kinetic mechanisms of carbohydrates and lipids were already discussed in the lignocellulosic biomass section. For those types of biomass, significantly higher amount of data is available, allowing to individuate the different polysaccharides present. For algae instead, one reference component for carbohydrates (SUGAR) is here considered and bring satisfactory results for the level of details expected. Sugars contained in algae share more structural similarities with hemicellulose than cellulose and the multistep kinetic mechanism of reference species SUGAR follows a similar decomposition path.

In a similar way, pyrolysis reactions of LIPID refer to the degradation model of TGL already discussed before, which predominantly results in the release of tar components before 350–400 °C, at heating rate of 10 K/min [247]. Moreover, as the lipids in algae contain not only free fatty acids, but also some other heavier compounds, the kinetics take into account two intermediates, and produce some solid residue.

3.3. Release of CO2, NO and NH3 from inorganics

Because of the large amounts of ashes found in algae, treating the ash-forming compounds as simply ashes would not be a good assumption. These ash-forming compounds, mostly inorganic carbonates, nitrates, nitrites and ammonium salts, can release CO2, NO and NH3 when heated, in general leaving oxides in the solid phase. Matsushita, Nakanishi [142] studied the pyrolysis process of basic calcium carbonate, mainly based on TG experiments. Comparison between experimental data and model results, as obtained by the release of CO2 from calcium carbonate and from the reference species G{CO2}, is reported in Figure 76. In a very similar way Vyazovkin, Clawson [248] studied the thermal decomposition process of ammonium nitrate. This TG experiment is compared to the release of NH3 and NO from the reference species G{NH3/NO} in Figure 77. The kinetic parameters of first order reactions of these species are obtained by fitting the experimental data of basic calcium carbonate and ammonium nitrate decomposition, respectively. The rate parameters

of G{CO2} decomposition is 10^7*exp(-40800/RT) [s−1], whereas k=2.5x10^{10}*exp(-27800/RT) [s−1] is the rate constant for G{NH3/NO}.

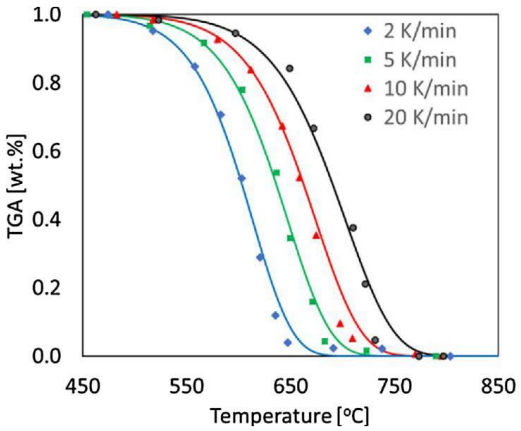

Figure 76 – CO_2 release from calcium carbonate at different heating rates. Comparison of predicted results (lines) and experimental data (marks)

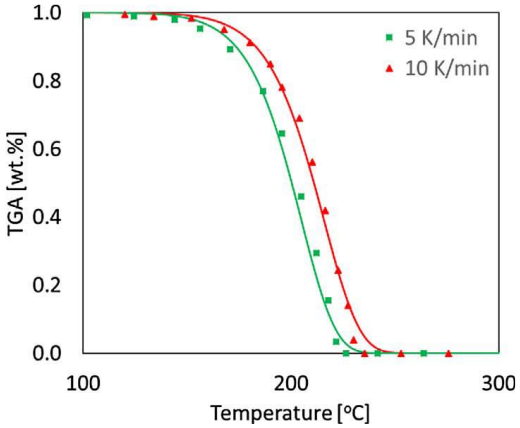

Figure 77 - Decomposition of NH_4NO_3 at different heating rates. Comparison of predicted results (lines) and experimental data (marks)

4. Validation of the kinetic mechanism of algae pyrolysis

Once the multistep kinetic mechanisms of reference species are defined, the pyrolysis of algae fuels is simply obtained by a weighted linear combination of these mechanisms. Figure 78 shows the predicted thermogravimetric analysis of reference species: proteins, sugars, lipids, and inorganics at 10 K/min. After their initial development and validation based on experimental data on pure components, the kinetic mechanism of reference species has been further tuned and validated based on the TG analysis of several algae samples. As an example of the kinetic modifications, let's consider the kinetic parameters of protein pyrolysis reported in Table 23. The activation energies of protein decomposition reactions have been decreased by 2000 kcal/kmol in order to reduce their onset temperature. Similar tuning activity was applied to SUGAR and LIPID mechanisms, and

to the release of CO2 from inorganics, which is again favored by reducing the activation energy of 2800 kcal/kmol.

Although the overall kinetic model remains a lumped and empirical kinetic model, these further kinetic modifications could possibly indicate either important interactions amongst the different components [230, 249], structural degradation effects of extraction methods [249], or finally reticulation and cross-linking reactions promoted by the catalytic effect of ash content. In order to confirm these possible effects, more experimental evidence is required.

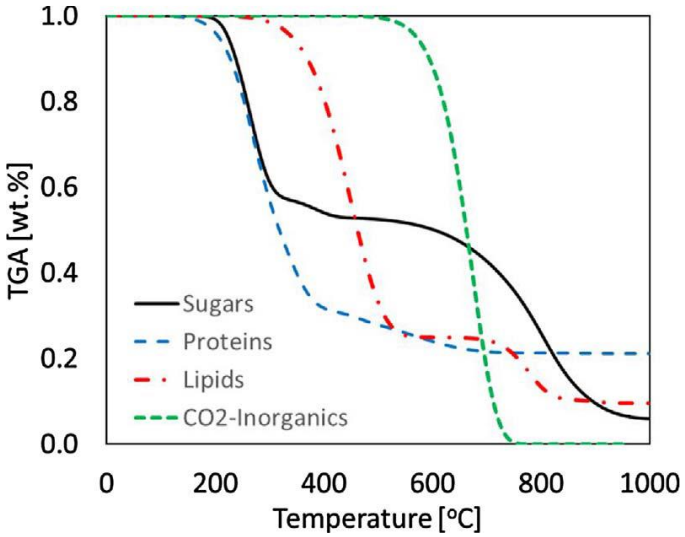

Figure 78 - Predicted thermogravimetric analysis of reference species: proteins, sugars, lipids, and inorganics at 10 K/min.

The final and complete mechanism with related kinetic parameters is reported in Table 24, and descriptions of the species involved with their molecular formula is reported in Table 25. The overall tuning of the kinetic mechanism has been organized and validated based on two different sets of experimental data. The first one refers to slow heating rate thermogravimetric experiments taken from the literature [117, 120, 250-253], whereas the second set of experiments was performed at IIT Madras laboratories in a single shot micro-pyrolyzer.

Algae Pyrolysis Reactions			Kinetic Parameters A (s^{-1}), Eact (kcal/kmol)
Proteins			
PROTO	=	2.5 PROTOH + 0.6 PROTCC + 25 NH_3 + 9 NO + TARN + 12.75C_2H_4 + 37.3 CO + 7.7 CO_2 + 71H_2O	.10 10^{05} × exp(−15500/RT)
PROTH	=	5 PROTOH + 27 NH_3 + 7 HCN + 0.5 TARN + 20.75 G(H_2) + 21.5 CH_4 + 70C_2H_4 + 23.5H_2O	.10 10^{05} × exp(−15500/RT)
PROTC	=	4.5 PROTCC + 7.5 HCN + 2 NH_3 + 0.5 TARN + 29 CO + NO + 23.5 C_2H_4 + 5 CO_2 + 10H_2O	.10 10^{05} × exp(−15500/RT)
PROTOH	=	27.5 CHAR + 2 CHARN + 0.5 TARN + 1.083333C_6H_6 + 3 G(NH_3) + 3 G(HCN) + 1.5 G(CO) + 22H_2O	.10 10^{04} × exp(−15000/RT)
PROTCC	=	42.75 CHAR + 2 CHARN + 0.5 TARN + 3.5 C_6H_6 + NH_3 + 10 G(HCN) + 3.375C_2H_4 + 3 CH_4 + 1.5H_2O	.10 10^{04} × exp(−15000/RT)
Sugars			
SUGAR	=	0.47 SUGAR1 + 0.53 SUGAR2	.80 10^{10} × exp(−26000/RT)
SUGAR1	=	0.6 TARO1 + 0.4 TARO2 + 0.4 G(CO_2) + 0.4H_2O	.15 10^{05} × exp(−16000/RT)
SUGAR2	=	1.6 CHAR + 0.25 G(CH_4) + 0.1 G(C_2H_4) + 0.73 G(COH_2) + 0.62 G(CO) + 1.3 G(CO_2) + 0.13 TARO3 + 0.88H_2O	.20 10^{02} × exp(−20000/RT)
Lipids			
LIPID	=	0.75 FFA + 0.25 HLIPID	.80 10^{03} × exp(−18000/RT)
HLIPID	=	9 CHAR + 2 G(COH_2) + 6 G(H_2) + 3 G(C_2H_4) + G(CH_4)	.70 10^{12} × exp(−49700/RT)
Inorganics			
G(CO_2),	=	CO_2	.10 10^{08} × exp(−38000/RT)
G(NH3NO)	=	NH_3 + NO	.25 10^{11} × exp(−27800/RT)
Metaplastics			
G(NH_3)	=	NH_3	.55 10^{01} × exp(−13500/RT)
G(HCN)	=	HCN	.55 10^{01} × exp(−13500/RT)
G(CO_2)	=	CO_2	.10 10^{07} × exp(−25000/RT)
G(CO)	=	CO	.50 10^{13} × exp(−50000/RT)
G(COH_2)	=	CO + H_2	.15 10^{13} × exp(−71000/RT)
G(H_2)	=	H_2	.50 10^{12} × exp(−75000/RT)
G(CH_4)	=	CH_4	.50 10^{13} × exp(−71500/RT)
G(C_2H_4)	=	C_2H_4	.50 10^{13} × exp(−71500/RT)
H_2O Evap. Moisture	=	H_2O	.10 10^{05} × exp(−10000/RT)

Table 24 – Kinetic mechanism of algae fuel pyrolysis

	SPECIES	MOLECULAR FORMULA	DESCRIPTION
Reference Species	PROTO	$C_{250}H_{500}O_{200}N_{72}$	Protein rich in Oxygen
	PROTH	$C_{400}H_{800}O_{150}N_{86}$	Protein rich in Hydrogen
	PROTC	$C_{500}H_{450}O_{65}N_{80}$	Protein rich in Carbon
	SUGAR	$C_6H_6O_6$	Sugars
	LIPID	$C_{18}H_{32}O_2$	Lipids
	G(CO2)i	CO_2	Volatile fraction of carbonates
	G(NH3NO)	NH_3 NO	Volatile fraction of ammonium salts and nitrates/nitrites
Solid Intermediates	PROTOH	$C_{45}H_{70}O_{25}N_{10}$	Intermediate species of proteins
	PROTCC	$C_{90}H_{70}O_{39}N_{15}$	Intermediate species of proteins
	SUGAR1	$C_6H_8O_6$	Loose intermediate of SUGAR
	SUGAR2	$C_6H_8O_6$	Stiff intermediate of SUGAR
	HLIPID	$C_{18}H_{32}O_2$	Intermediate species of LIPID
Tar species	TARO1	$C_6H_8O_6$	Anhydrous monomer of algae polysaccharides
	TARO2	$C_5H_6O_3$	Equimolar mixture of glyoxal. acetol and furfural
	TARO3	$C_{10}H_{26}O_9$	Molar mixture of methanol/ethanol/acetic acid in a 0.167/0.333/0.5 ratio
	FFA	$C_{18}H_{32}O_2$	Free-fatty acids
	TARN	$C_{13}H_{15}O_3N_4$	Equimolar mixture of DKP. Pyrrole and pyridone
	C6H6	C_6H_6	Benzene
	H2O	H_2O	Water
Gas species	HCN	HCN	Hydrogen cyanide
	NH3	NH_3	Ammonia
	NO	NO	Nitric Oxide
	CH4	CH_4	Methane
	CO2	CO_2	Carbon dioxide
	CO	CO	Carbon monoxide
	C2H4	C_2H_4	Ethylene
	H2	H_2	Hydrogen gas
Permanent solid species	CHAR	C	Char matrix
	CHARN	N	N atom bound to the char matrix

Table 25 – Description of the species present in the kinetic mechanism of algae pyrolysis (Table 24)

4.1. Slow Heating Rate Pyrolysis

The first set of comparison with experimental data refers to the TG behavior of some algae with different compositions. Rizzo, Prussi [251]analyzed the mass loss profiles of Chlorella spp. and Nannochloropsis samples under pyrolytic conditions in a Leco TGA 701 instrument in presence of nitrogen. TG analyses were repeated in triplicates from room temperature to 800 °C, at heating rates of 15 K/min. Ross, Jones [117] performed pyrolysis experiments at a N2 flow rate of 50 mL/min using a Stanton Redcroft differential thermal analyzer (DTA). Approximately 5 mg of macro algae samples were heated from 40°C to 950°C at a ramp rate of 25 K/min. Further comparison refers to the pyrolysis of microalga Aurantiochytrium sp. KRS101 reported by Vo, Lee [252] and Vo, Ly [253]. The last comparisons refer to pyrolysis of Spirulina reported by Anand, Sunjeev [120], and similar experiments by Gai, Zhang [250] referring to the TG decomposition of Spirulina and Chlorella at heating rate of 10 K/min. Based on proximate and elemental analysis, all the samples were first characterized in terms of the reference components, and then the predicted TG behaviors under slow and constant heating rate are obtained. Figure 79 reports the elemental and detailed composition of the algae based on the reference species, and the comparison of the model mass loss profiles with the experimental data, which relate to both micro and macroalgae. Microalgae are characterized by a larger amount of proteins, whereas macroalgae show a larger solid residue, because of their higher amount of sugars. Nevertheless, a general satisfactory agreement is observed for this whole set of experiments.

Chlorella spp. [Rizzo, 2013] - 15 K/min			
Elemental Composition		Reference Species	
C	0.591	PROTH	0.216
H	0.078	PROTO	0.024
O	0.245	PROTC	0.185
N	0.086	SUGAR	0.066
		LIPID	0.179
		G{NH3NO}	0.011
		G{CO2i}	0.038
		ASH	0.216
		MOISTURE	0.065

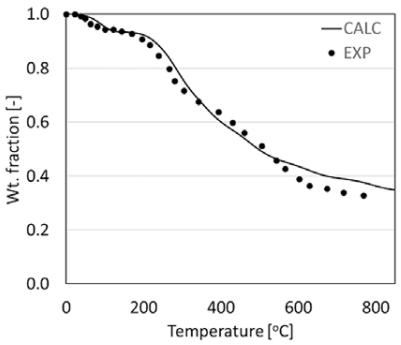

Nannochloropsis spp. [Rizzo, 2013]			
Elemental Composition		Reference Species	
C	0.562	PROTH	0.296
H	0.080	PROTO	0.058
O	0.270	PROTC	0.133
N	0.087	SUGAR	0.108
		LIPID	0.175
		G{NH3NO}	0.012
		G{CO2i}	0.026
		ASH	0.132
		MOISTURE	0.060

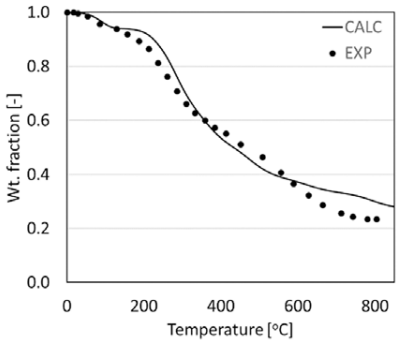

Fucus v.(6.5% water) [Ross, 2008] - 25 K/min			
Elemental Composition		Reference Species	
C	0.464	PROTH	0.000
H	0.060	PROTO	0.166
O	0.441	PROTC	0.021
N	0.036	SUGAR	0.424
		LIPID	0.121
		G{NH3NO}	0.005
		G{CO2i}	0.022
		ASH	0.118
		MOISTURE	0.123

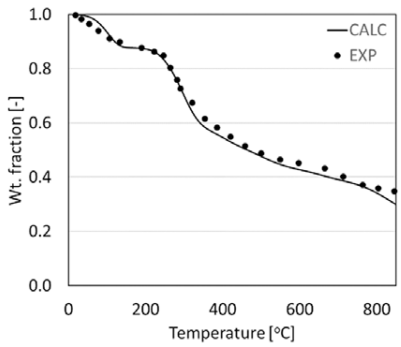

Macrocystis p. (8.5% water) [Ross, 2008] - 25 K/min			
Elemental Composition		Reference Species	
C	0.437	PROTH	0.000
H	0.055	PROTO	0.155
O	0.475	PROTC	0.005
N	0.033	SUGAR	0.441
		LIPID	0.077
		G{NH3NO}	0.004
		G{CO2i}	0.033
		ASH	0.185
		MOISTURE	0.100

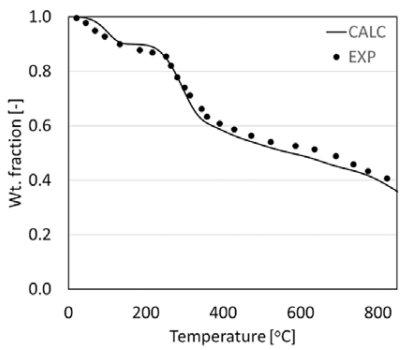

Aurantiochytrium sp. [Vo, 2017] - 20 K/min			
Elemental Composition		Reference Species	
C	0.528	PROTH	0.161
H	0.076	PROTO	0.075
O	0.356	PROTC	0.006
N	0.040	SUGAR	0.366
		LIPID	0.255
		G{NH3NO}	0.006
		G{CO2i}	0.015
		ASH	0.067
		MOISTURE	0.050

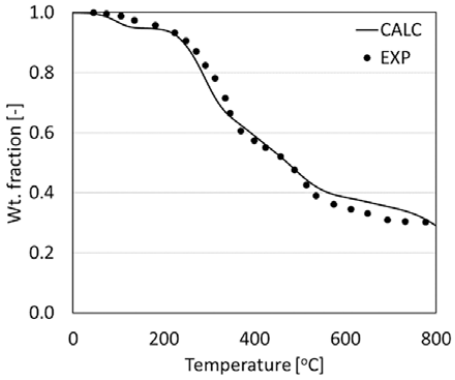

Arthrospira p. (Spirulina) [Anand, 2016] - 10 K/min			
Elemental Composition		Reference Species	
C	0.470	PROTH	0.175
H	0.070	PROTO	0.400
O	0.353	PROTC	0.090
N	0.107	SUGAR	0.135
		LIPID	0.073
		G{NH3NO}	0.016
		G{CO2i}	0.011
		ASH	0.050
		MOISTURE	0.050

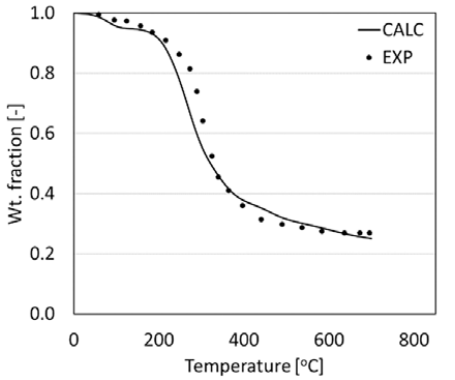

Arthrospira p. (Spirulina) [Gai, 2013] - 10 K/min			
Elemental Composition		Reference Species	
C	0.496	PROTH	0.000
H	0.062	PROTO	0.410
O	0.334	PROTC	0.212
N	0.108	SUGAR	0.098
		LIPID	0.079
		G{NH3NO}	0.015
		G{CO2i}	0.020
		ASH	0.096
		MOISTURE	0.070

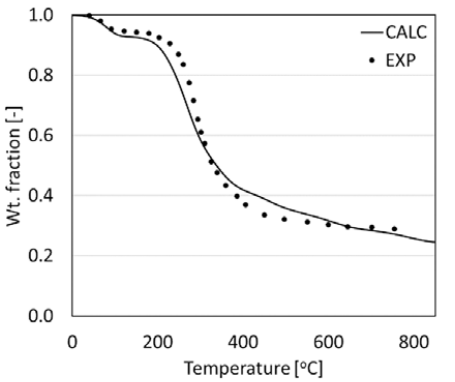

Chlorella [Gai, 2013] - 10 K/min			
Elemental Composition		Reference Species	
C	0.512	PROTH	0.126
H	0.068	PROTO	0.343
O	0.307	PROTC	0.221
N	0.113	SUGAR	0.083
		LIPID	0.080
		G{NH3NO}	0.017
		G{CO2i}	0.012
		ASH	0.057
		MOISTURE	0.060

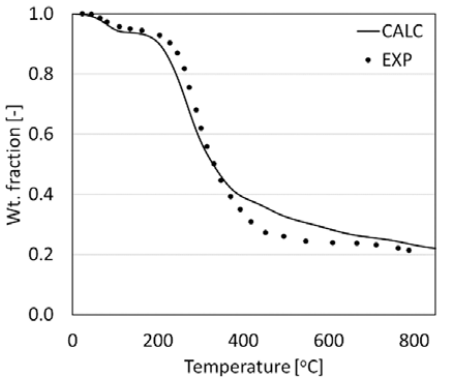

Figure 79 - Thermal gravimetric analysis of algae samples. Comparison of predicted results (lines) and experimental data (symbols) [117, 120, 250-253].

4.2. Isothermal fast pyrolysis experiments and model predictions

These set of comparisons are the result of a collaboration with the Indian Institute of Technology of Madras. The detailed experimental data was a courtesy of Prof. R. Vinu. Fast pyrolysis experiments were performed in an analytical Pyroprobe® 5150 pyrolyzer (CDS Analytical, U.S.A.) connected to the Brill cell. Typically, 4.5 ± 0.2 mg of the alga sample was taken in a quartz tube and inserted into the probe consisting of a resistively heated platinum coil. The probe was inserted into the Brill cell and heated at 20.000 K/s heating rate to the set temperature (400, 700 °C), and maintained for different time periods from 2 to 50 s. Argon was used as the inert gas at 110 mL/min. The actual heating rate experienced by the sample was calculated as 125–150 K/s. For every temperature and time period, the experiments were repeated for a minimum of three times, whereas five repetitions were performed to establish reasonable error bars for a few data points. Further details of the experimental set-up and the procedure can be found in Ojha, Viju [119]. Table 26 reports the obtained results for four algae samples in terms of conversion and residue, together with standard deviations.

Chlorella vulgaris			*Schizochytrium limacinum*			*Arthrospira platensis*			*Nannochloropsis oculata*		
T = 400 °C			T = 400 °C			T = 400 °C			T = 400 °C		
Time [s]	%Residue	St. dev.	Time [s]	%Residue	St. dev.	Time [s]	%Residue	St. dev.	Time [s]	%Residue	St. dev.
0	100	0	0	100	0	0	100	0	0	100	0
2	91.02	0.68	2	94.75	1.13	2	92.02	0.4	2	82.85	0.74
4	90.34	0.9	4	89.76	0.88	4	87.17	1.3	4	79.41	0.83
6	88.11	0.72	6	87.42	0.65	6	84.41	1.33	6	78.53	1.91
8	82.97	1.29	8	86.67	0.34	8	86.17	0.11	8	76.63	1.04
10	80.35	1.24	10	85.24	0.18	10	80.35	2.64	10	73.07	1.33
15	71.87	0.91	15	80.60	0.24	15	74.53	0.24	15	72.4	1.7
30	65.86	0.99	30	76.11	1.08	30	56.61	0.9	30	70.55	1.49
40	63.98	1.41	45	74.50	0.70	40	58.16	2.15	40	68.53	1.42
50	57.57	0.34	60	73.00	0.48	50	55.41	1	50	67.86	1.68
60	57.54	1.18							60	64.83	2.3
Chlorella vulgaris			*Schizochytrium limacinum*			*Arthrospira platensis*			*Nannochloropsis oculata*		
T = 700 °C			T = 700 °C			T = 700 °C			T = 700 °C		
Time [s]	%Residue	St. dev.	Time [s]	%Residue	St. dev.	Time [s]	%Residue	St. dev.	Time [s]	%Residue	St. dev.
0	100	0	0	100	0	0	100	0	0	100	0
2	79.79	1.28	2	85.71	0.57	2	70.69	1.35	2	73.06	1.3
4	61.66	1.89	4	76.47	0.94	4	66.99	0.73	4	69.01	2.15
6	53.98	0.79	6	62.50	1.51	6	58.24	0.8	6	60.78	0.41
8	47.97	1.59	8	54.55	1.45	8	45.27	0.6	8	59.97	0.86
10	45.55	1.1	10	53.85	1.15	10	42.36	0.12	10	58.28	0.86
15	41.8	1.96	15	50.30	2.52	15	38.67	0.33	15	54.47	1.4
30	40.11	1.39	30	49.76	1.23	30	36.59	1.22	30	49.73	2.11
40	40.08	1.54	45	48.97	1.02	40	36.43	1.73	40	49.64	1.21
50	39.15	1.43	60	48.28	1.13	50	36.39	0.43	50	48.39	1.94
60	39.03	0.58							60	48.14	0.91

Table 26 – Experimental data obtained with fast pyrolysis of four algae species

Figure 80 depicts the elemental and reference species composition, and the comparison of the model predictions with experimental data. It is important to underline that each experimental data point in the graph is an experiment performed at different temperature and hold time. It is evident that the match of the kinetic model with the

experimental data is good at 400 °C. At a higher temperature of 700 °C, there is a slight deviation in the initial time periods, although the mass loss at the end of 50s is reasonably well predicted by the model. It is worthwhile to observe that experiments performed in Pyroprobe® are potentially subject to some heat transfer limitations during pyrolysis. As a matter of fact, the recent work of Ojha, Viju [119] showed that diffusion models describe well the isothermal mass loss data of lignin under isothermal conditions in Pyroprobe® reactor. Therefore, the observed variation can be, at least partially, attributed to the diffusion effects into the experiments, whereas the model predicts pure kinetic behavior. This demonstrates the robustness of the kinetic model of algae pyrolysis.

Chlorella vulgaris			
Elemental Composition		Reference Species	
C	0.471	PROTH	0.229
H	0.072	PROTO	0.324
O	0.369	PROTC	0.025
N	0.087	SUGAR	0.244
		LIPID	0.114
		G{NH3NO}	0.014
		G{CO2i}	0.010
		ASH	0.041
		MOISTURE	0.000

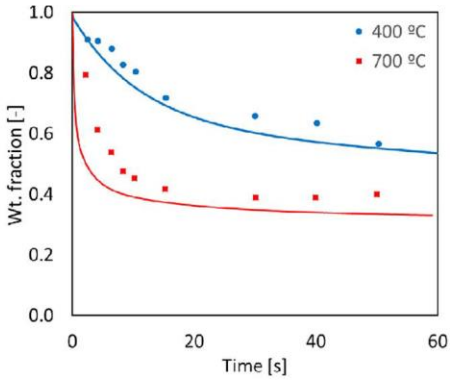

Schizochytrium limacinum (4% water)			
Elemental Composition		Reference Species	
C	0.612	PROTH	0.125
H	0.088	PROTO	0.000
O	0.279	PROTC	0.000
N	0.018	SUGAR	0.341
		LIPID	0.513
		G{NH3NO}	0.003
		G{CO2i}	0.003
		ASH	0.014
		MOISTURE	0.000

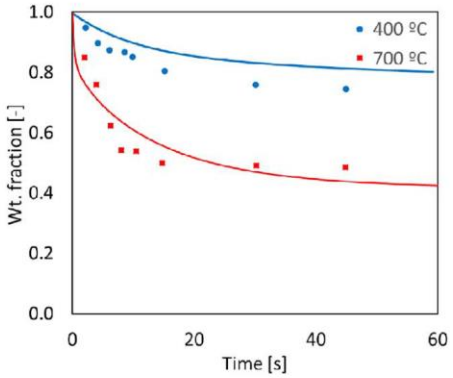

Arthrospira p. (Spirulina)			
Elemental Composition		Reference Species	
C	0.471	PROTH	0.207
H	0.071	PROTO	0.407
O	0.351	PROTC	0.089
N	0.107	SUGAR	0.141
		LIPID	0.078
		G{NH3NO}	0.017
		G{CO2i}	0.012
		ASH	0.050
		MOISTURE	0.000

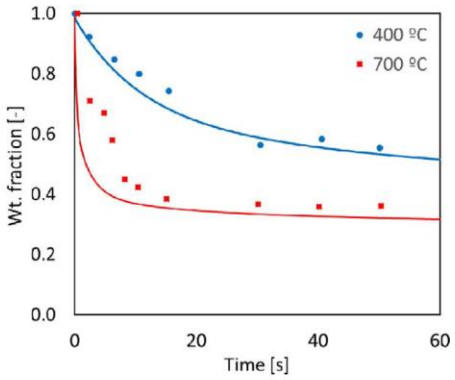

Nannochloropsis oculata			
Elemental Composition		Reference Species	
C	0.562	PROTH	0.276
H	0.080	PROTO	0.053
O	0.270	PROTC	0.128
N	0.087	SUGAR	0.098
		LIPID	0.165
		G{NH3NO}	0.012
		G{CO2i}	0.026
		ASH	0.182
		MOISTURE	0.060

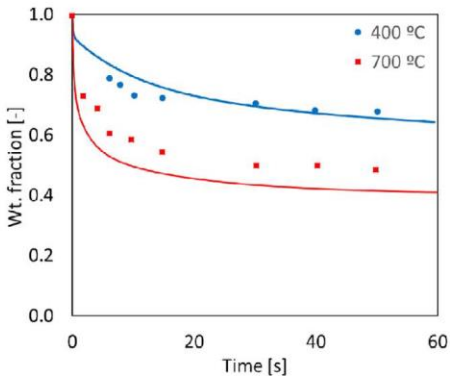

Figure 80 - Comparisons of isothermal tests.

5. Conclusions

In order to predictively and reliably describe the devolatilization step of biomass, it is crucial to well characterize the sample, accounting for the large variabilities found in these feedstocks. The kinetic mechanism of each reference species presented was supported by several experimental and modeling activities from the literature. Then, the pyrolysis of a biomass sample is described as a linear combination of the decomposition of the reference species, which was further validated for a wide range of feedstock compositions and operating conditions. The semi-detailed and lumped approach used allows to both predict a variety of information that is not present in other models, and remains computationally affordable for applications in the particle and reactor scales. Despite their simple expressions, these models allow the characterization of the degradation steps, their characteristic times, and the prediction of product distributions with real and lumped species. The good agreements with experimental data confirms the requirement of only the elemental composition of the sample, but also highlights that more details on the feedstock allow refined predictions.

The sub-mechanism of algae pyrolysis is, to our knowledge, the first attempt of modeling with this level of detail. It is relevant to emphasize that this lumped mechanism remains a first attempt to describe the complex behavior of algae pyrolysis, also including characterization of the decomposition products. Improvements and de-lumping should be introduced on the light of new experimental evidences, mainly on pyrolysis products distribution and better distinction between micro- and macro-algae. Also, the definition of reference components that describe the sulfur content and its successive decomposition remains a future task. This attempt opens new paths to investigating and developing new technologies for this promising source of fuels and chemicals.

All these aspects make the proposed mechanisms a useful tool in the design and optimization of industrial processes, where the optimal operating conditions must be defined a priori. The focus on products and byproducts formation is a further advantage when considering pollutant emission from such devices. The proper prediction of these aspects require the treatment of the fate of the resulting biochar and volatiles. For this reason, the next chapter will introduce the secondary gas-phase reactions that take place when these volatiles are released and face severe temperature conditions.

CHAPTER 5

SECONDARY GAS-PHASE REACTIONS OF RELEASED VOLATILES

Before discussing the secondary gas-phase reactions, it is important to explain their role in the present work. The biomass devolatilization process, discussed in chapter 4, produces large amounts of volatiles species, which are both fix gases and condensable tars. These species are often exposed to high temperatures (T>800K), conditions that gas phase pyrolysis and combustion reactions (secondary gas-phase reactions) play a significant role [100, 254]. For a residence time of just fractions of a second in these conditions, the less stable compounds further decompose in a process called tar cracking, producing other tar species and light gases. The global yield of tars reduces, resulting in a lower yield of bio-oil when the products are cooled down. Not only the yield, but also the composition of bio-oil significantly changes. Consequently, it is possible to find the optimal operating conditions that corresponds to the ideal yield and composition of bio-oil obtained [255-258]. In order to discuss this process, it is important to better introduce some important aspects of bio-oils.

Gas, tars and residual biochar are always the products of biomass pyrolysis, but their proportions are greatly dependent on biomass nature and process operating conditions. Moderate temperatures and short residence times optimize bio-oil yields. High temperatures

and long residence times for volatiles favor the successive conversion of tar species to syngas production. Low temperatures combined with long contact time between solid and volatiles favor cross-linking reactions, promoting biochar yields [13, 255].

In fast pyrolysis, the yields of bio-oil can reach 50-70 wt.%. Flash pyrolysis is characterized by higher heating rates (10^3-10^4 K/s) and shorter volatiles residence time (<0.5 s) reaching up to 75-80 wt.% [259].

As usual in chemical processes, the heart and crucial portion of the fast pyrolysis process is the reactor. It represents only a minor fraction of the capital cost of the overall system, nevertheless great research efforts are focused on developing new reactor configurations. Similar attention is nowadays devoted to the upgrading of the bio-oil quality [260-262]. Bridgwater [13] reports a widespread summary of fast pyrolysis reaction systems for liquids, recently and currently operational. He also discusses the different reactor types.

Bubbling fluid beds have the advantages of a proved technology, which is simple in construction and operation, with an efficient heat transfer and good temperature control. The biochar yield is typically ~15 wt.%, and can be used to provide the pyrolysis heat by combustion. Circulating fluidized bed and transported bed reactors are similar to the previous ones, except that the residence time of the char is lower and similar to the one of vapors and gas. Due to the high velocities, char attrition can become an issue. The rotating cone reactor effectively operates as a transported bed reactor, but with transport effected by centrifugal forces in a rotating cone rather than by a fluidizing gas [263].

In ablative pyrolysis heat is transferred from the hot reactor wall to the wood surface. The pyrolysis front moves through the biomass particle. The reaction rate is strongly dependent on the pressure of the wood onto the heated surface. Some other apparatuses are also mentioned, such as the auger pyrolysis reactor, hydro-pyrolysis and microwave heating. In the last one, the process is largely different from the previous techniques as the biomass particles receive heat from high-frequency waves, consequently heating the feedstock from within and not externally by heat conduction, convection or high temperature wall radiation. There is a very rapid heating with a penetration of microwaves limited to about 1-2 cm. One interesting

aspect is the absence of thermal gradients and the possibility for studying fundamentals of fast pyrolysis process. However, different reacting paths can be favored by this heating procedure, and more investigation is still needed to validate the applicability of the present work in such conditions. Therefore, experiments using such technology are not considered.

1. Bio-oil: Liquid Biomass Pyrolysis Product

1.1. Bio-oil composition and physical properties

As already discussed and clearly summarized by [264], the properties of fast pyrolysis bio-oils differ significantly from those of fossil fuels. Bio-oil is not suitable as transportation fuel without a relevant upgrading. Pyrolysis bio-oil is a dark-brown acidic liquid (pH 2÷3) with high water and solid content, and has a heating value which is less than half of liquid petroleum fuels [236, 265]. Because of their acidic nature, bio-oils are corrosive for several metals, such as carbon steel and aluminum. High instability during storage is due to the ongoing polymerization reactions to form larger molecules [259]. The water content and the large amount of oxygen, up to 45-50 wt.% explain the low heating value [236]. It is possible to increase the heating value of the bio-oil only through expensive deoxygenation processes [266]. Usually catalysts are also added during the fast pyrolysis step to obtain bio-oil of a better quality, with a lower oxygen content [13, 267, 268].

Figure 81 shows that currently there are two broad approaches for improving the quality of bio-oil. The first one is to use catalytic processes to eliminate the oxygen in the fuel. The catalytic cracking processes use zeolite catalysts to achieve the deoxygenation[269, 270]. The catalytic reaction eliminates the oxygen by forming CO and CO_2 while simultaneously producing a gasoline fuel. However, significant coke deposition and deactivation of the catalyst are observed, also due to the alkali content of the fuel. The typical yield for the catalytic cracking of pyrolysis liquid is about 40% [271]. To date, various zeolites have been tried to upgrade bio-oils. Lee, Choi [272] found that HZSM-5 zeolites can selectively convert oxygenates species in the bio-oil to aromatics compounds due to their small pore opening and strong acidity. However, they indicated that HZSM-5 zeolites cannot completely decompose large oxygenate species, and suggested that zeolites with larger pore such as Hβ and HY are more useful for this purpose [273].

An alternative route for upgrading bio-oils is the catalytic hydrodeoxygenation (HDO) commonly applied to reduce the oxygen content and acidity of crude bio-oils [274]. The

catalytic reactions eliminate oxygen by producing water while simultaneously cracking and hydrogenating the fuel producing a conventional hydrocarbon fuel. Compared to catalytic cracking, this process has the ability to convert about 50% of the original bio-oil. A sulfided NiMo/CoMo catalyst supported on gamma alumina was recently used as a benchmark catalyst for a hydrodesulfurization reaction in refineries and is considered the reference catalyst for HDO in the production of renewable diesel. The properties of renewable diesel made through hydroprocessing are similar to those of petro-diesel [275]. The main disadvantages are the requirement of an external hydrogen source, catalyst fouling and deactivation and the production of waste water. Applying syngas in the hydrotreating step can significantly reduce the cost of the whole process and make it more competitive [276]. Even if the technical problems with catalytic cracking and hydrotreating are solved, the low liquid yields and high capital expense make these methods economically not completely viable [277].

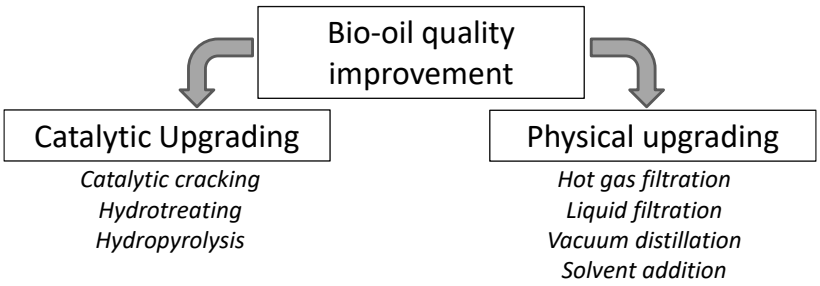

Figure 81 - Overview of the major approaches used to improve the quality of the pyrolysis bio-oils. Adapted from [271].

Before analyzing the physical upgrading of bio-oil, it seems important to recall the physical, thermal, and the chemical pre-treatment of the biomass, which is very useful to improve the bio-oil yield and quality [259]. Physical pre-treatment involves reduction of particle size to cut intra-particle heat and mass transfer resistances and enhance bio-oil production. Thermal pre-treatment and torrefaction involves reduction in the moisture and oxygen content in the biomass, in order to improve the energy efficiency and product quality. Chemical pre-treatment finally reduces the ash content, so that the pyrolysis bio-oil yields can be further enhanced.

The second and more suitable approaches to increase the oil quality are based on physical upgrading. These methods include hot gas filtration, liquid filtration, distillation, and solvent addition. They do not convert bio-oil into a hydrocarbon fuel, but they provide a

much cheaper and less energy intensive means of improving liquid fuel quality for use in combustion systems. Biomass pretreatments such as washing/leaching and torrefaction are another class of strategies to improve bio-oil quality by changing biomass composition [225]. For example, by washing biomass with detergent (Triton) or acid to remove minerals, the yield of bio-oil is increased and reaction water content is reduced [226]. Most of these techniques also have a number of technical problems and disadvantages [271]. By far, the simplest and most effective physical upgrading method for bio-oil is polar solvent addition, usually using alcohol fuels.

It is worthwhile to compare bio-oil with petroleum fuels and discuss the challenges in bio-oil combustion resulting both from its physical and chemical characteristics. Bio-oils contain a tar and an aqueous fraction, which makes them immiscible with conventional liquid hydrocarbon fuels. The aqueous fraction contains the low molecular mass (LMM) oxygenated compounds, while the tar fraction is constituted by high molecular mass (HMM), water-insoluble lignin fragments (pyrolytic lignin). As already discussed, the composition of the bio-oil is related to that of biomass, but also depends on the operating conditions and severity of the pyrolysis process. Bio-oils derived from different biomass streams are much more uniform compared to the original biomass resources and have typically 5-20 times higher volumetric energy density than the original biomass [278] . Thus, they offer the potential to de-couple liquid fuel production (scale, time, and location) from its utilization [279]. Moreover, this allows a better fuel standardization and market development. This process also enables the separation of residual biochar and minerals which can be recycled to the soil as a nutrient. Bio-oils can be used as a liquid energy carrier or as a renewable raw material for the chemical industry in the production of high-value chemicals [280, 281]. Lehto, Oasmaa [282] give a recent review of the existing bio-oil production technologies and a comparison between the properties of bio-oil and mineral oils.

Table 27 contains a comparison between the typical composition of a bio-oil and fossil fuels. The unusual characteristics of the bio-oil have to be taken into account because they have an impact on the combustion technology in terms of burner design, flame stability, emissions and materials compatibility. Because of the elevated number of compounds present, the evaporation of bio-oils start below 100 °C and continues until 250-280 °C. The low-boiling point compounds evaporate slightly before water vapor suppresses the ignition [282]. Bio-oils ignite only at high temperatures, mainly because of the large presence of water and the limited volatility.

	Typical bio oil	HFO 180/420	LFO EN 590
Water (% wt)	20-30	-	-
Solids (% wt)	<0.5	-	-
Ash (%wt)	0.01-0.1	0.08 max	0.01 max
Oxygen (%wt)	35-40	-	-
Nitrogen (wt)	<0.4	0.4	0.02
Sulphur (%wt)	<0.05	1.0 max	0.001 max
Density@15 °C (g/cm3)	1.10-1.30*	0.99/0.995 max	0.845 max
Viscosity@40 °C (cSt)	15-35*	180/420 max @50 °C	2-4.5
LHV (MJ/kg)	13-18	40.6 min	42.6
Distillability/Stability (heating and long term storage)	Non distillable/Unstable	Distillable/Stable	Distillable/Stable
* depending on water content			

Table 27 - Comparison of physical properties of bio- oil and mineral oils: Heavy Fuel Oil (HFO) and Light Fuel Oil (LFO) [282].

In particular, density, viscosity and surface tension are important parameters that affect pump design and atomization quality, which directly affects the efficiency of the combustion and emissions. Since the droplet size in a spray increases with the viscosity, surface tension and density of the liquid, it is clear that atomization is a major concern for bio-oil combustion. Some degree of preheating can be used to reduce bio-oil viscosity thus improving the atomization quality. However, due to the low thermal stability, the preheating should be limited to temperatures below 80°C and achieved only just before the atomizer. Premature or excessive preheating quickly leads to plugging in the fuel line and atomizing nozzles. Due to the low volatility, air preheating is also suggested in order to promote spray droplets evaporation, ignition and combustion [271, 282].

Figure 82 shows and compares the chemical composition of several bio-oils [283]. The single most abundant bio-oil component is water. It results from the original moisture in the feedstock and as a pyrolysis product of the dehydration reactions. Therefore, the water content varies in a wide range (15-30%) depending on the feedstock and process conditions [277]. The presence of water obviously reduces the heating value of the bio-oil, but it also has desirable effects, such as the reduction of the liquid viscosity, which has a positive impact on the atomization characteristics. Moreover, water also reduces the thermal NOx-emissions by lowering the flame temperature, and may also contribute to reduce the amount of unburned particulate emissions, like in the case of water emulsions in heavy fuel oil combustion. However, elevated water content in bio-oil may decrease the flame

temperature and reduce combustion stability, which might ultimately lead to higher total emissions of sub-products of incomplete combustion [282].

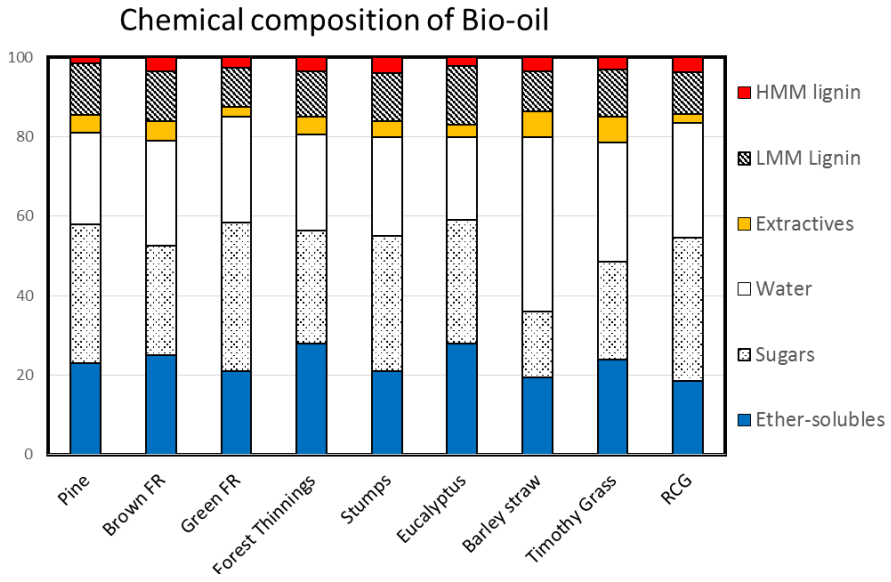

Figure 82 - Chemical composition of several bio-oils (weight fraction of total bio-oil) [283].

Beside water, bio-oils are complex mixtures of hundreds of organic compounds that belong to acids, aldehydes, ketones, alcohols, esters, anhydrosugars, furans, phenols, guaiacols, syringols, nitrogen containing compounds. Oxygenated compounds (mostly acids, aldehydes, ketones and phenols) represent between 50 and 60 wt.% of the products. Djokic, Dijkmans [284] reported quantitative analysis of crude and stabilized bio-oils by comprehensive two-dimensional gas-chromatography, and identified about 150 compounds, describing approximately 80% of total peak volume. Similarly, Bertero, de la Puente [285] measured the composition of the bio-oil using gas chromatography-mass spectrometry techniques. More recently, Cheng, Han [286] used a three-step supercritical CO_2 extraction for selective fractionation of fast pyrolysis bio-oil. More than 100 oxygen-containing compounds in bio-oil were characterized using combined analytical techniques. The molecular composition of different components in lipids, hemicellulose, lignin, and condensed aromatics were characterized by enriching their presence in the three different fractions.

1.2. Impact of bio-oil properties on combustion systems

The complexity of the bio-oil composition and the chemical nature of its components are the main reason for the challenging behavior of these fuels in terms of stability, combustion, and corrosion. For these reasons, the existing burners/units require some modifications to handle the different physical and chemical properties of these alternative

bio-fuels. First, all the parts in contact with bio-oil should be replaced with parts made of stainless steel, and the suitability of all gaskets and instruments needs to be checked [287]. Moreover, the variability and the lack of standard quality specifications of these bio-oils also delayed their direct commercial applications. While the use of bio-oil to replace heavy fuel oil has already been proven, the next step is to replace light fuel oil. Fuel standards for bio-oil is already available in ASTM D7544 (Standard Specification for Pyrolysis Liquid Biofuel) [282].

Storage and handling of the bio-oil is also challenging, due to the "aging" of the bio-oil [277] [288]. For this reason, the storage temperature has to be carefully controlled in order to prevent polymerization of unsaturated components, etherification and esterification reactions between hydroxyl, carbonyl, and carboxyl group components of the bio-oil. These aging reactions lead to the formation of water and higher molecular weight components. These phenomena are unwanted because they further increase the viscosity of the oil, reduce its volatility, and can also lead to complete phase separation of the aqueous and pyrolytic lignin fractions [277]. Biochar and ash particles in bio-oil increase the aging phenomena acting as catalytic sites for the polymerization reactions [289], and particles can agglomerate during storage and form a sludge layer on the bottom of the container [282]. Erosion and clogging in the pumps and atomizing nozzles is also a concern.

It is evident that the quality of biomass pyrolysis oils is inferior to that of conventional fossil fuels. However, their characteristics can be improved by adding polar solvents, such as methanol and ethanol. Alcohol addition has a beneficial effect on the storage stability of the bio-oil because it inhibits the polymerization reactions that cause aging phenomena [290]. Moreover, the addition of alcohols increases the fuel volatility, reduces the viscosity and thus promote of the flame stability. Tzanetakis, Moloodi [271] showed that by mixing the bio-oil with 20% of ethanol, the viscosity of the bio-oil is reduced from 12.1 to 7.3 (cSt, at 40 °C).

Among other requirements of bio-oil fuels, which are mainly related to physical properties (distillation range), burning characteristics, ignition delay times, flame stability and pollutant emissions are mainly related to the chemical composition and reactivity of the system.

Bio-oils are mainly composed by scarcely volatile components; therefore, significant energy is required for ignition. The fuel composition is also relevant in controlling the flame speed of the fuel/air mixtures, because it influences not only the exothermicity of the

combustion reaction, but also the tendency to form relatively stable combustion intermediates, such as resonantly-stabilized radicals [291] which lower the mass burning rate. Moreover, due to the high oxygen content, the stoichiometric air to fuel ratio differs significantly from the corresponding one of conventional fossil fuels. This also has an impact on the burner design. Visual observations of bio-oil flames indicate the presence of a stable combustion zone followed by a region where biochar particles formed from individual droplets undergo burnout [292, 293]. The flame length and stability depends on a number of factors, including atomization quality, fuelling rate, spray inlet velocity, flame swirl and recirculation. Bio-oil flames have a similar or longer flame length compared to conventional fossil fuels [269]. Although flame temperature is lower than in the case of hydrocarbon flames [294], bio-oils produce more luminous flames, primarily because of the higher particulate concentration [293].

The behavior of bio-oil in the gas-phase can be described with detail detailed kinetic mechanism of pyrolysis and combustion of its constituting chemical species. Due to the modular structure, the extension of the CRECK detailed kinetic mechanism to the species released from biomass fuels simply requires to include the primary reactions of the new species. The reaction classes to be included are initiation, H-abstraction and addition reactions, together with molecular and successive radical decompositions until the formation of intermediate products already considered in the kinetic mechanism.

The overall dimensions of the kinetic scheme, in terms of species and reactions, need always to be a reasonable compromise between model accuracy and computational efforts. For this reason, a limited number of lumped components are representative and group several tar and heavy species and/or isomers with similar reactivity. For example, as already mentioned in chapter 4, the free-fatty acids that are usually released by the triglycerides (TGL) in the biomass pyrolysis mechanism. Their structures and reactivities are very similar to the analogous methyl-esters. The sub-mechanism of heavy methyl-esters was already investigated and included in the CRECK kinetic model, first presented by Saggese, Frassoldati [212]. Therefore, instead of increasing the number of species by releasing free-fatty acids, we consider that reference species TGL release analogous methyl-esters. Linoleic acid is then lumped as a combination of methyl-linoleate ($C_{19}H_{32}O_2$) and methyl-decanoate ($C_{11}H_{18}O_2$) in the mole ratio 0.875/0.125. This allows to satisfy both the elemental mass balances and account for the different chain lengths present. Moreover, pyrolysis and oxidation of methyl esters of stearic, oleic, linoleic, and linolenic acids allow to investigate the effect of the

unsaturation degree of fatty acid methyl esters. All these methyl-esters contain 19 C atoms. In the next session, we briefly introduce the approach for the development of the kinetic mechanism and the validation for the prediction of biomass volatiles behavior.

2. Kinetic Mechanism of Gas-Phase Reactions

2.1. Chain radical reactions. Generic rate rules for initiation and H-abstraction reactions.

It is worth to briefly describe the methods used to build detailed kinetic mechanisms of gas-phase reactions, even though the development of the mechanism was not part of the activities of this thesis. The gas-phase mechanism was applied in order to process the fate of nascent volatiles from biomass pyrolysis, strongly affecting the global yields of gas and tar species.

In the modeling of secondary gas-phase reactions of volatile from biomass pyrolysis, Carstensen and Dean [254] highlighted that it is not feasible to perform ab-initio high-level calculations of the rate constants for all the reactions, because of the large dimension of the kinetic model. From first principle calculations, they systematically derived kinetic laws on a series of small reactants for several reaction classes and used these data to generate rate estimation rules, to be extrapolated to all members of the same reaction class. Similarly, in modeling steam cracking reactions, Dente, Pierucci [295], Dente, Ranzi [296] highlighted that the rate constant of initiation and H-abstraction reactions of pure hydrocarbons can be obtained, with reasonable accuracy, by adopting generic rate rules. These rules mainly rely on the bond dissociation energy (BDE) of the reacting molecules.

Favored chain initiation reactions are the ones involving the breaking of the weakest bonds. From the microscopic reversibility principle, and assuming the rate constant for the reverse radical recombination, it is practical to evaluate the rate constant of initiation reactions. If the activation energy of the radical recombination reactions is zero, the activation energy of the corresponding unimolecular dissociation reaction becomes directly the BDE.

H-abstraction, or metathesis reactions, can be written in the generic form [297]:

$$R\bullet + R'H \leftrightarrow RH + R\bullet'$$

where R● is the H-abstracting radical. Rate constant of this reaction is conveniently decomposed as the following product:

$$k_f = k_{(ref,R)0} \cdot (n_H \, C_{R'H})$$

where $k_{(ref,R)0}$ represents the reference rate constant of R radical to abstract a single H-atom from a methyl group, and (n_H $C_{R'H}$) is the number and the relative reactivity of the H-atoms of R'H with respect to the primary ones. Table 28 reports a series of BDEs of different C-H bonds in hydrocarbon and oxygenated species. From these BDE values, it is quite evident that all the radicals abstract acyl and allyl H-atoms with the greatest selectivity, whereas the removal of vinyl H-atoms is largely more difficult.

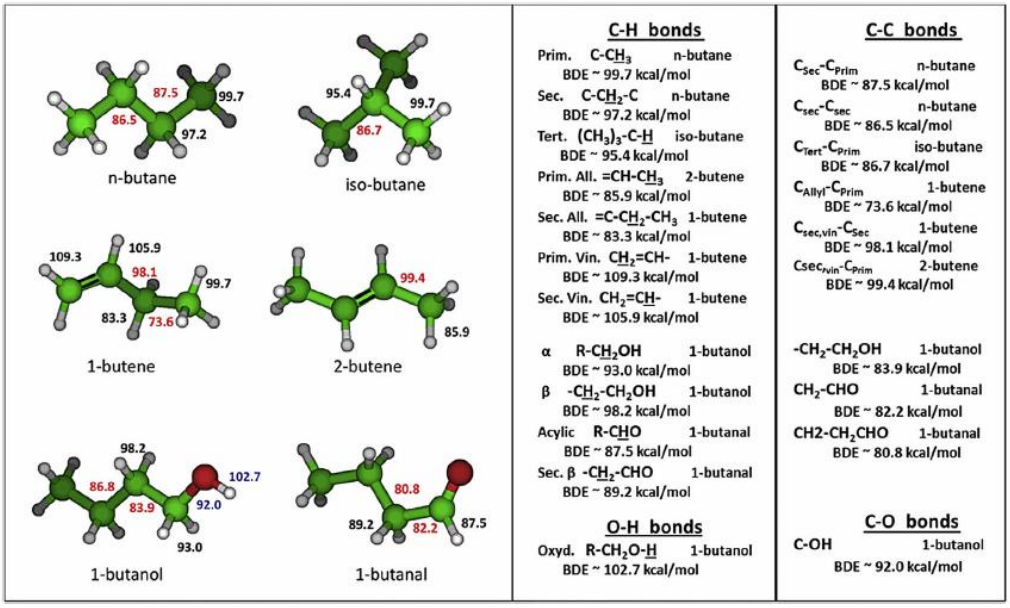

Table 28 - Bond dissociation energies of C4 hydrocarbon and oxygenated species. C-H (black), C-C (red), and C-O & O-H (blu) bond dissociation energies (kcal/mol) calculated at G4 level (298 K) [298].

CH3-CH2-CH2-CH3	n-butane	99.7	Primary H atom in alkanes
CH3-CH2-CH2-CH3	n-butane	97.2	Secondary H atom in alkanes
(CH3)3-CH	iso-butane	95.4	Tertiary H atom in alkanes
CH2=CH-CH3	propylene	85.9	Primary allyl H atom in alkenes
CH2=CH-CH2-CH3	1-butene	83.3	Secondary allyl H atom in alkenes
CH2=CH-CH2-CH3	1-butene	109.3	Primary vinyl H atom in alkenes
CH2=CH-CH2-CH3	1-butene	105.9	Secondary vinyl H atom in alkenes
CH3-CH2-CH2-CH2-OH	1-butanol	93	Primary α H atom in alcohols
CH3-CH2-CH2-CH2-OH	1-butanol	98.2	Secondary β H atom in alcohols
CH3-CH2-CH2-CHO	n-butanal	87.5	Acyl H atom in aldehydes
CH3-CH2-CH2-CHO	n-butanal	89.2	Secondary β H atom in aldehydes

Table 29 - C-H bond dissociation energy (kcal/mol) of hydrocarbon and oxygenated species calculated at G4 level (298 K)

H, OH and CH_3 are the dominant reactive radicals in pyrolysis and oxidation conditions. Figure 83 compares the rates constants of H-abstraction of H, OH and CH_3 from primary, secondary, tertiary, allyl, and vinyl positions. These rate constants confirm the great correlation with the corresponding C-H bond dissociation energies. Similar generic rate rules are formulated not only for abstraction reactions involving different H-sites in hydrocarbons but also in oxygenated species [298].

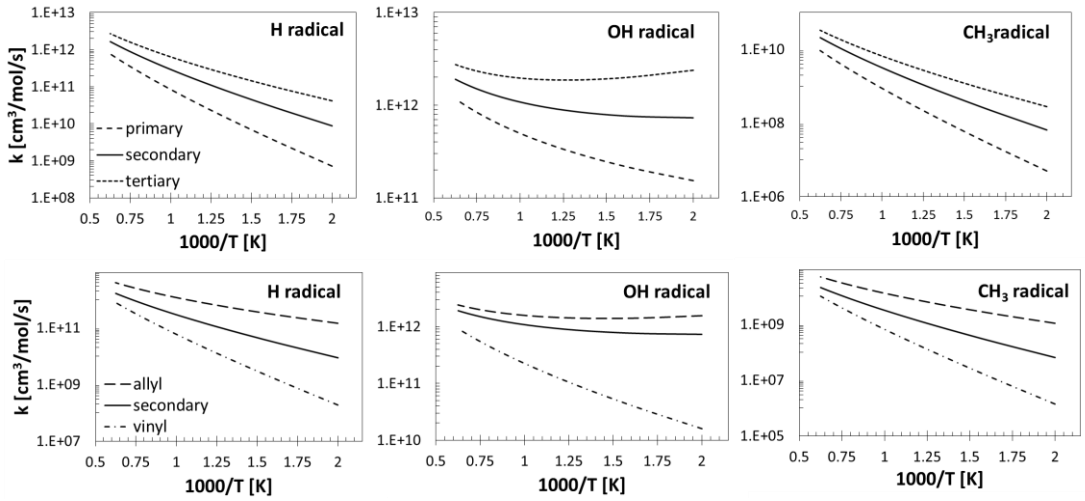

Figure 83 - H-abstraction reactions. Rate constants of H, OH and CH3 (per H-atom) for single primary, secondary, tertiary H-atoms (top) and for secondary H-atoms in alkyl, vinyl and allyl-sites (bottom).

These generic rate rules, both for initiation and for H-abstraction reactions, have been and are very useful to create a first reasonable set of rate parameters for the secondary gas phase reactions of all the primary products of biomass pyrolysis.

2.2. Molecular reactions and water elimination reactions. Alcohols, Glycerol, and Carbohydrates

The importance of molecular reactions and water elimination reactions in cellulose decomposition mechanism [158, 159, 162] was highlighted by Carstensen and Dean [254]. These reactions were detailed discussed in previous papers on alcohol fuels [299-301], but it is worth to describe a simple example. Figure 84 shows the four center molecular dehydration reactions of 2-butanol to form 1-butene and 2-butene.

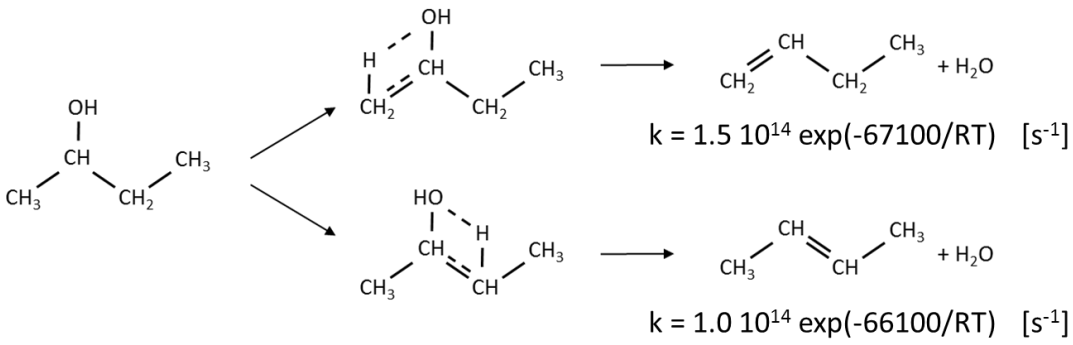

Figure 84 - Dehydration reactions of 2-butanol to form 1-butene and 2-butene, via four center molecular reactions.

In agreement with the recent review of Sarathy, Oßwald [302] for different butanol isomers, the reference rate parameters for this reaction class are site specific, i.e. they are affected by the position of the OH group inside the carbon skeleton. While these differences are rather limited, large deviations are observed for substituted aldehydes, when water elimination reactions form unsaturated species with conjugated double bonds. The two successive molecular dehydration reactions in glycerol pyrolysis constitute a clear example [303], as shown in Figure 85.

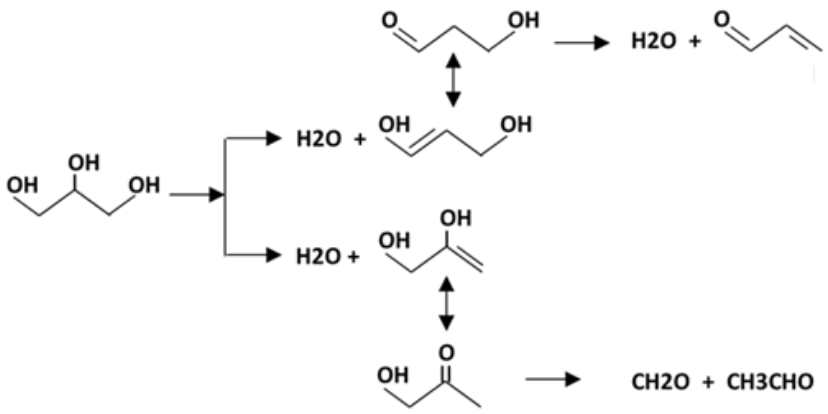

Figure 85 - Glycerol pyrolysis. Successive water elimination reactions

The first dehydration reaction again refers to the previous reference parameters:

Glycerol → 1propene1,3-diol + H_2O k = 0.2 10^{14} exp(-65000/RT) [s^{-1}]

Then, the keto-enol tautomerism transforms 1-propene-1,3-diol into 3-hydroxypropanal, which rapidly forms acrolein through a second dehydration reaction:

3-hydroxy-propanal → Acrolein + H_2O k = 10^{14} exp(-51000/RT) [s^{-1}]

The aldehyde moiety strongly influences the reactivity and it stabilizes the transition state and the products with a reduction of the activation energy of more than 10 kcal/mol [254].

Kawasaki and Yamane [304] studied the effect of reaction temperature on the pyrolysis of a mixture glycerol/N_2 inside a quartz flow reactor at atmospheric pressure. Figure 86 shows a comparison between the experimental measurements and model predictions. Since liquid glycerol is injected, the residence time in the plug flow reactor simulation is assumed to be only one half of the nominal residence time to take into account the non-ideal behavior of the system.

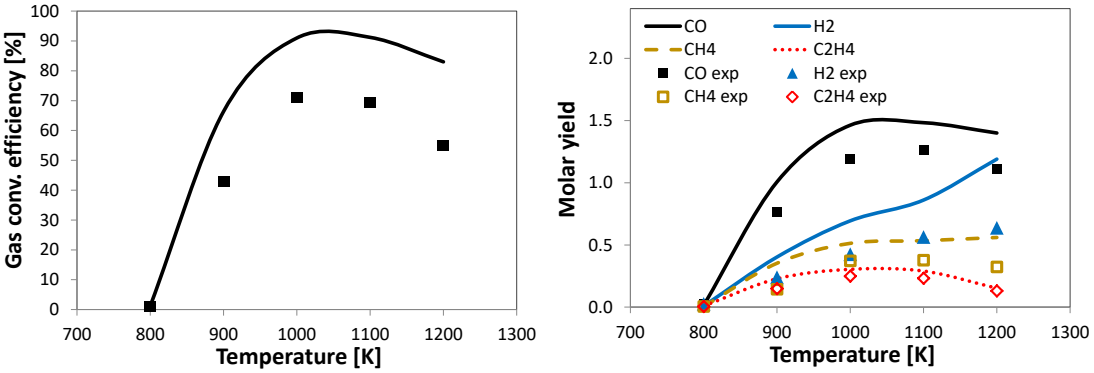

Figure 86 - Pyrolysis of glycerol at 1 atm. Effect of temperature on gaseous product yields. Comparisons of experimental data (symbols) [304] and model predictions (lines).

It is possible to observe that the model is able to predict the effect of temperature on the gas conversion efficiency and on the relative yields of the major gas phase species. The gas conversion efficiency is defined by the authors as the % of glycerol conversion to CO, CO_2, CH_4, C_2H_4, and C_2H_6, on carbon basis. The increasing formation of acetylene, C_4's, and aromatic species explains the reduction of the efficiency at higher temperatures. Syngas formation is overestimated with respect to these experimental data.

Fukutome, Kawamoto [305] studied the pyrolysis of glycerol in the gas phase at 400, 600, and 800°C under a N_2 flow at residence times ranging from 0.9 to 1.4 s by using an experimental setup consisting of an evaporator and a pyrolyzer. Glycerol conversion at 800°C was complete and the intermediate condensable products were largely decomposed. Figure 87 shows a comparison between the experimental and the predicted gas composition. Contrary to the previous comparisons, syngas production seems here slightly underestimated (~10%).

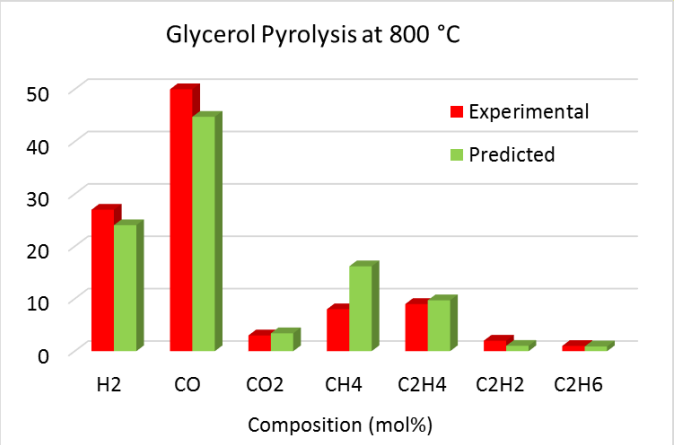

Figure 87 - Pyrolysis of glycerol at 1 atm. Comparisons of experimental data and model predictions [305]

The dehydration reactions also rule the first molecular decomposition of carbohydrates, specifically of levoglucosan and xylan. Successive levoglucosan dehydration reactions produce the 5-hydroxymethyl-furfural ($C_6H_6O_3$: HMFU), whose successive reactions form furfural ($C_5H_4O_2$) and furfuryl-alcohol ($C_5H_6O_2$) [172, 306]. According to Carstensen and Dean [254], retro-Diels Alder reactions are further molecular reactions forming C_2-C_4 oxygenated species. Together with these molecular reactions, chain initiation and H-abstraction reactions are considered with the usual rules of chain radical propagation reactions, well defined for hydrocarbon and oxygenated species [295, 296, 307]. Primary radicals progressively decompose forming the major intermediates, such as formaldehyde, hydroxyl-acetaldehyde, glyoxal, acetol, and other small-oxygenated components.

Shin, Nimlos [306] analyzed the kinetics of gas-phase pyrolysis of levoglucosan, together with 5-hydroxymethyl furfural, and hydroxyacetaldehyde, by using a quasi-isothermal tubular quartz reactor equipped with a molecular beam mass spectrometer for product detection. Figure 88 shows a comparison of model predictions and experimental data of LVG decomposition at 898 and 973 K, in the flow reactor of Shin, Nimlos [306]. The same figure also shows the effect of successive reactions to form 5-hydroxymethyl furfural, furfural, and furan. The predicted, successive benzene formation is also reported.

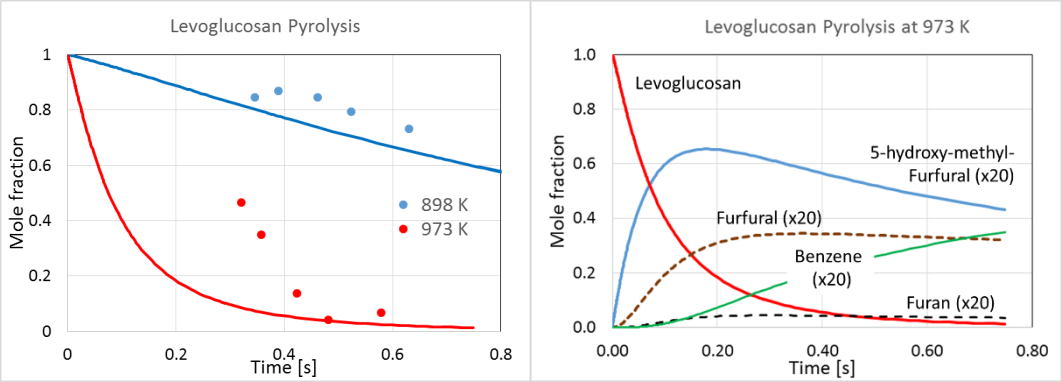

Figure 88 - Levoglucosan pyrolysis in a flow reactor [306]. Left panel. Levoglucosan fractions at 898 and 973 K. Right Panel. Successive decomposition reactions of LVG and predicted yields of 5-hydroxymethyl-furfural, furfural, furan, and benzene at 973 K.

Similarly, Kawamoto, Murayama [308] extensively studied the reactivity of levoglucosan, as well as glyceraldehyde (CH_2OH-$CHOH$-CHO) and acetol (CH_3-CO-CH_2OH), as simple surrogates of cellulose [305, 309]. They used the previously referred two-stage tubular reactor. The liquid LVG was vaporized completely under a N_2 flow in the evaporator then was fed to the pyrolyzer in the temperature range of 400-900°C, at residence times 0.8-1.4 s. Condensable and non-condensable products were recovered and analyzed. Figure 89 shows a detailed comparison between model predictions and experimental data in terms of the major gas products and also minor condensable species. While oxygenated C_1 and C_2 species were properly measured, the details of heavy C_4-C_6 species are not reported. An overall selectivity of more than 10% is predicted, as a result of the successive dehydration reactions to form initially 5-hydroxy-methyl-furfural, then furfural and furan. Again, the kinetic model predicts a relevant formation of benzene, which is mainly formed via propargyl radical recombination reactions.

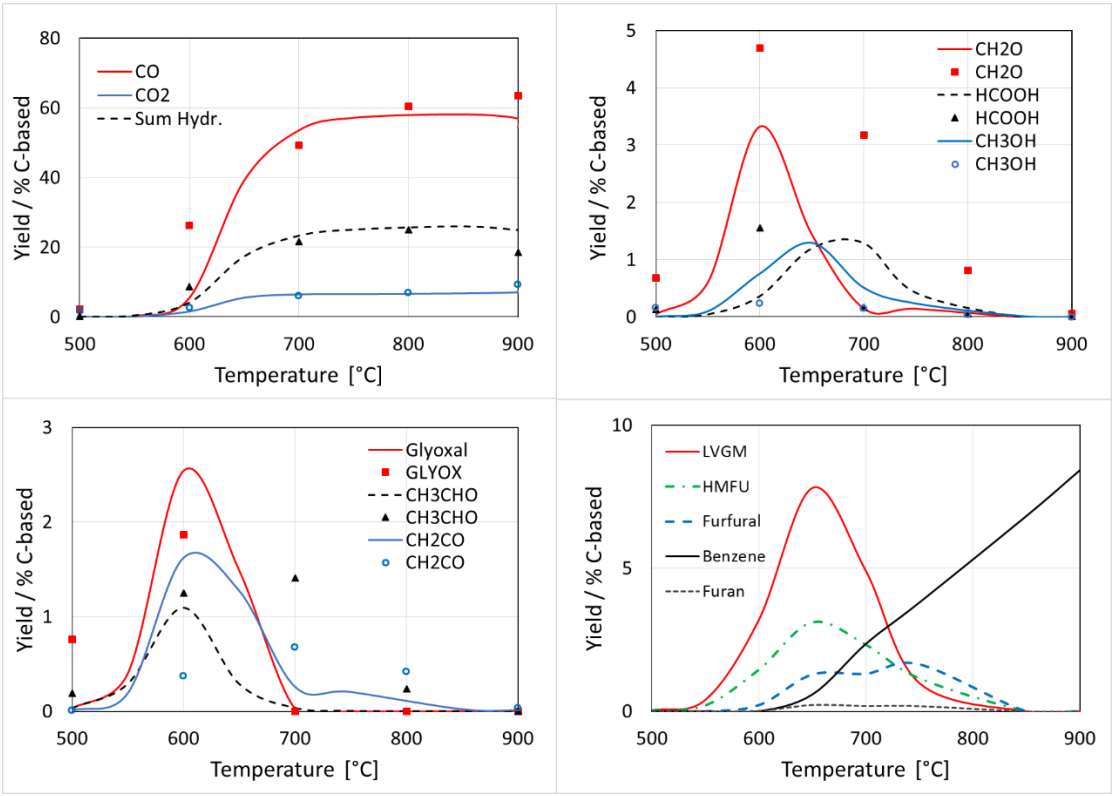

Figure 89 - Pyrolysis of levoglucosan. Comparisons between experimental data (symbols) [309] and model predictions (lines).

To better validate the kinetic mechanism and to analyze the successive fate of these intermediate species, it is useful to refer to the experimental data of 5-hydroxymethyl-furfural pyrolysis of Shin, Nimlos [306]. Together with the comparisons of 5-hydroxymethyl-furfural pyrolysis in the flow reactor at 898 and 973 K, Figure 90 shows the predicted yields of intermediate and aromatic species: furfural, furan, and benzene. Although furfural is a primary intermediate, benzene is mainly the result of the successive recombination and condensation reactions of propargyl radicals.

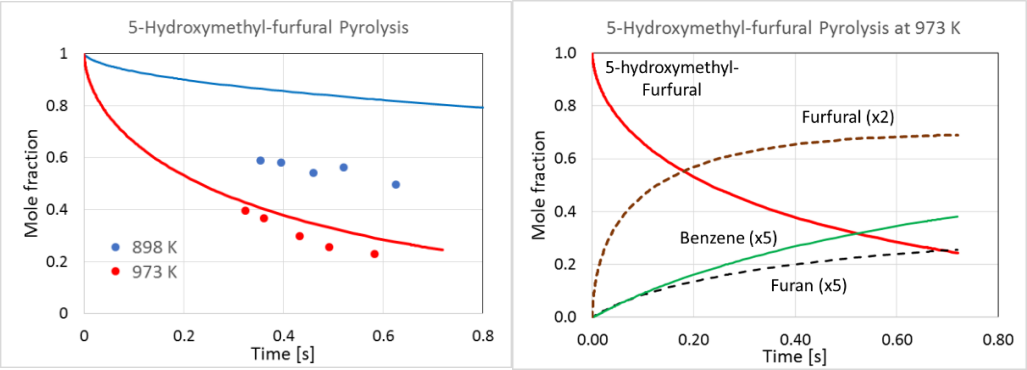

Figure 90 - Hydroxymethyl-furfural pyrolysis in a flow reactor at 898 and 973 K [306]. Left panel: comparisons of experimental data (symbols) and model predictions (lines). Right panel: predicted successive decomposition products.

The decomposition mechanism of 5-hydroxymethyl-furfural proceeds through both a molecular and a radical reaction path. Following these reactions, 5-hydroxymethyl-furfural forms furfural which in turn, via H abstraction reactions and CO formation, explains the successive formation of furan. Furan pyrolysis reactions have been investigated experimentally by Organ and Mackie [310] and theoretically with ab initio quantum chemical techniques by Sendt, Bacskay [311]. More recently, the kinetics of furan and furan derivatives received a particular attention [312-314]. Principal products of furan decomposition are carbon monoxide, and C_3H_4 (propyne and allene), together with acetylene and ketene. In fact, furan decomposition is mostly ruled by 1,2-H transfers with the formation of cyclic carbene intermediates whose successive decomposition forms CO and propyne as a major channel, and C_2H_2 and ketene.

2.3. Aromatics, phenolics, and successive reactions to form polycyclic aromatic hydrocarbons (PAH) and soot

Phenolic species deserve a special attention, not only for their presence as tar components released by lignins, but also as possible precursors of dibenzofurans and dibenzodioxins. Kinetic studies on phenol, cresol, and anisole chemistry highlighted the importance of CO elimination from unsubstituted and substituted phenoxy radicals:

$$C_6H_5O \rightarrow cyC_5H_5 + CO \qquad k = 5.\ 10^{11} \exp(-43920/RT) \qquad [s^{-1}]$$

Similar reactions to form CO and cyclopentadienyl radicals from phenoxy-substituted species were discussed by Carstensen and Dean [254]. While phenol and cresol were extensively investigated for their interest in combustion systems, anisole ($C_6H_5OCH_3$) was mainly studied as a very simple surrogate of tar from lignin pyrolysis [315-318]. These studies

allowed to verify the importance of the ipso-addition reactions. Reference rate parameters for this reaction class are derived from these simple reactions:

H + Anisole → Phenol + CH_3	k =1. 10^{13} exp(-6000/RT)	[cm^3/s/mol]
H+ Phenol → Benzene + OH	k =1.2 10^{13} exp(-6000/RT)	[cm^3/s/mol]
H+ Anisole → Benzene + OCH_3	k =1. 10^{13} exp(-8000/RT)	[cm^3/s/mol]
OH + Toluene → Cresol + H	k =1.1 10^{12} exp(-11000/RT)	[cm^3/s/mol]
OH + Toluene → Phenol + CH_3	k =4.4 10^{12} exp(-6700/RT)	[cm^3/s/mol]
CH_3 + Phenol → Cresol + H	k =1.3 10^{12} exp(-16200/RT)	[cm^3/s/mol]
CH_3 + Phenol → Toluene + OH	k =1. 10^{12} exp(-15000/RT)	[cm^3/s/mol]

All these reactions progressively convert the aromatic and phenolic species and their rate values mainly derive from the kinetic studies of pyrolysis and oxidation of anisole and phenol [317, 319]. More recently, anisole pyrolysis and oxidation were studied by Nowakowska, Herbinet [318] in a jet-stirred reactor under diluted conditions at 673–1173 K, residence time 2 s, and 106.7 kPa. Figure 91 shows selected comparisons between these experimental data and the predictions of the proposed model.

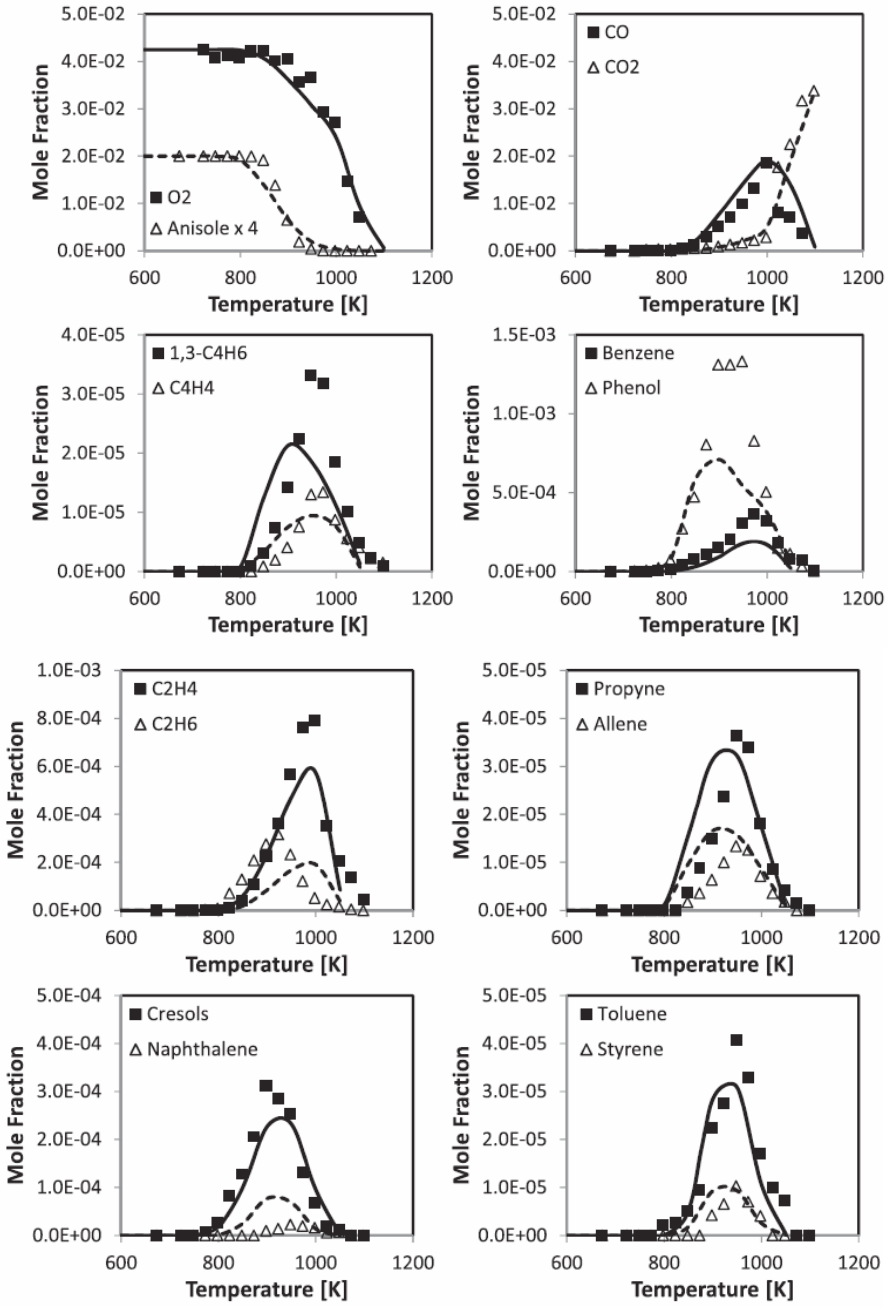

Figure 91 - Mole fraction profiles of major species during the stoichiometric oxidation of anisole at residence time 2 s and 106.7 kPa. Symbols refer to experiments [318] and lines to model predictions.

Moreover, sinapyl and coniferyl alcohols as intermediates of lignin monomers from hardwood species were recently investigated by Kotake, Kawamoto [320]. Recently, Norinaga, Yang [321] discussed the reaction pathways to form benzene, toluene, and naphthalene from levoglucosan and cellulose pyrolysis. These experimental data clearly indicate that the formation of aromatic species from the high temperature biomass pyrolysis is largely due to first to the recombination of propargyl radicals, then to the successive addition reactions of acetylenic species. For several years these kinetic mechanisms of

formation of polycyclic aromatic hydrocarbons (PAHs) and soot have been extensively investigated [322-326]. Still there is a great attention to this research topic and also CRECK kinetic mechanism was recently revised and improved [327-329]. Saggese, Frassoldati [319] also revised and discussed the intermediate and high temperature reactions of benzene with particular attention not only to the successive reaction paths to form PAHs, but also to the chemistry of phenol species.

2.4. Secondary gas-phase reactions of volatiles from cellulose and lignin pyrolysis.

Norinaga, Shoji [31] and Yang, Appari [33] studied the kinetics of secondary vapor-phase decomposition of volatiles generated from the fast pyrolysis of cellulose and lignin in a two-stage tubular reactor, while minimizing volatile-biochar interactions. Cellulose with particle sizes ranging from 74 to 105 µm was used by Norinaga, while the lignin samples used by Yang had particle sizes in the range of 75–150 µm. These particle sizes allow to neglect mass and heat transfer limitations.

Norinaga, Shoji [31] provided experimental data of tar and gas compositions during secondary pyrolysis of cellulose volatiles, at temperatures of 700 and 800 °C. The most abundant product is always CO, along with major species such as H_2O, CH_4, and H_2. These data are useful not only to verify the primary released species, but mainly to analyze the effect of the secondary gas phase reactions studied with residence times up to 6s. Figure 92 shows a satisfactory comparison between experimental data and model predictions in terms of time evolution of major pyrolysis products. The model correctly predicts the time evolution of the most abundant products (CO, H_2O, CH_4, H_2, and methane) as well as the decomposition of tar and intermediate species, properly accounting for the formation of benzene and aromatics

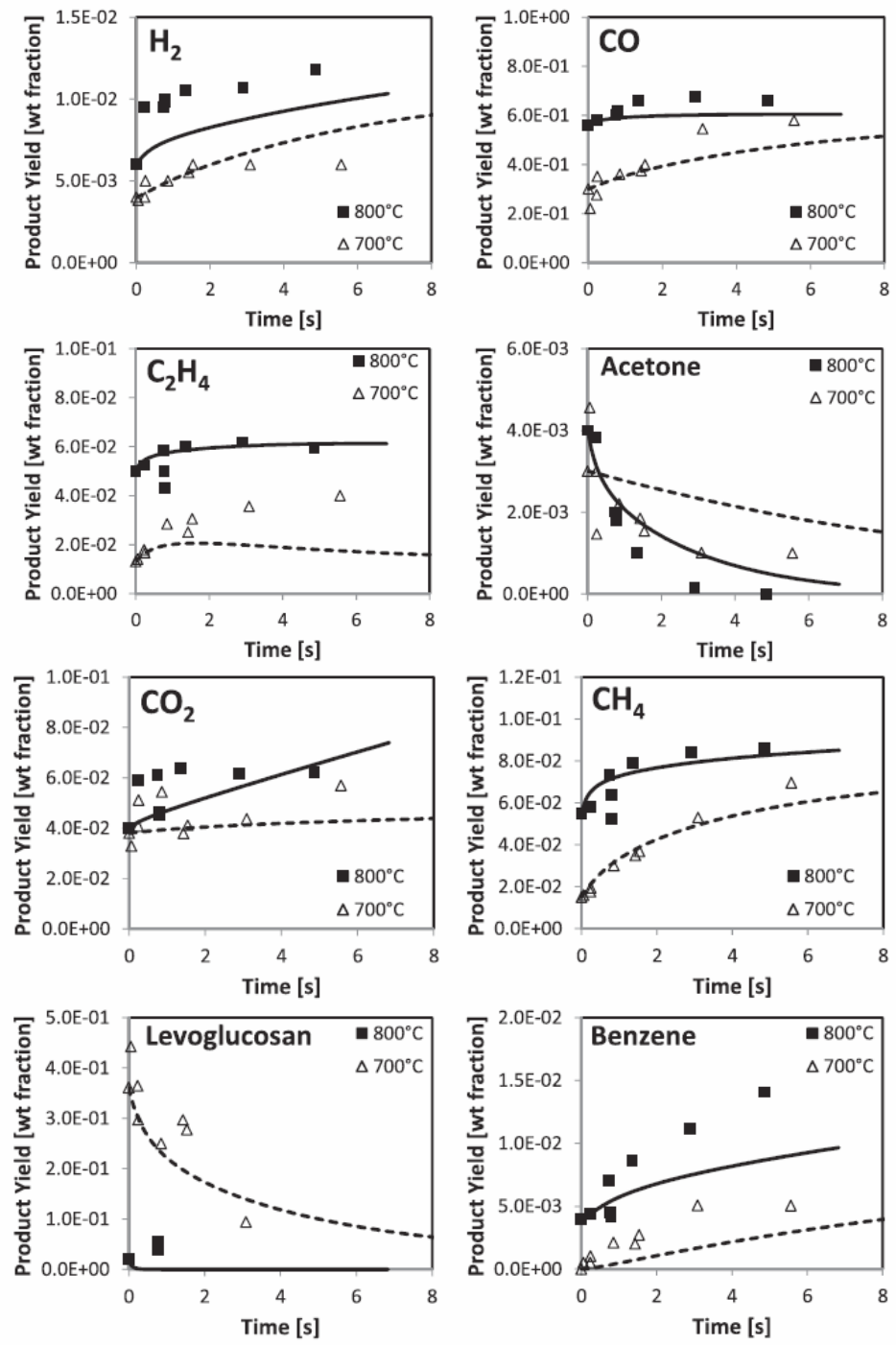

Figure 92 - Effect of secondary gas-phase reactions on volatile species released from cellulose pyrolysis at 700°C and 800°C. Comparison between experimental data (symbols) [31] and model predictions (lines).

Yang, Appari [33] investigated the vapor-phase reactions of nascent volatiles derived from the fast pyrolysis of lignin at temperatures from 500°C to 900°C, at 241 kPa. A two-stage micro-tubular reactor was used modifying the residence time of volatiles inside the secondary pyrolysis reactor from 0.1 s up to 3.6 s. The lignin sample, prepared by enzymatic

hydrolysis (EHL) of empty fruit bunches, has the elemental C/H/O composition of 63.5/5.93/30.57 (on a dry basis). Fast pyrolysis was realized in the first reactor, where together with detected primary volatile products there was a large amount of heavy undetectable phenolic species (>30% at 773 K). Table 30 reports the primary volatile products released from fast pyrolysis of lignin as experimentally measured after 0.1 s [33].

	EXPERIMENTAL			PREDICTED		
	Gas Phase (0.1 s)			Prim. Pyrolysis + 0.1 s (gas-phase)		
Temperature [K]	773	1023	1223	773	1023	1223
Products (wt.% of initial)						
H_2	0.0	0.3	1.2	0.0	0.2	1.3
CO	1.0	15.0	33.1	7.6	13.1	32.0
CO_2	4.5	6.4	8.3	5.5	5.6	6.2
CH_4	1.2	4.1	6.7	0.3	1.3	5.9
C_2	0.3	2.5	3.6	2.2	2.8	5.9
C_3-C_5	0.3	3.5	0.4	0.0	0.2	0.8
Aromatics (C_6+)	0.2	3.3	8.4	0.0	1.5	5.6
Light Oxygenated	5.7	3.8	0.1	7.1	6.6	2.1
Phenolic compounds*	28.0	14.2	4.5	17.5	17.0	5.0
H_2O	7.6	6.8	6.2	6.1	7.0	7.3
Total Volatiles	48.8	59.9	72.5	46.3	55.3	72.1
Char* (wt.%)	51.2	39.6	27.6	53.6	44.8	28.1
C (wt.%)	75.3	80.9	97.7	77.5	82.3	98.1
H (wt.%)	3.6	3	2.3	4.6	4.1	0.9
O (wt.%)	21.1	16	0	17.9	13.6	1.0

Table 30 - Primary volatile products released from fast pyrolysis of lignin at 0.1 s. Comparisons between experimental data [Yang et al., 2015] and model.

Because of the lumping approach, very heavy phenolic species are not considered in the kinetic model. Therefore, the experimental data are here corrected by assuming the undetected heavy species as equally distributed between the phenolic species and biochar residue. Predicted pyrolysis products as obtained from lignin pyrolysis after 0.1 s at the pyrolysis temperature are also reported and they show an overall reasonable agreement with experimental data. At high temperatures and residence time of 0.1 s, there is an effect of

secondary gas phase reactions. A significant decomposition of oxygenated species to form CO and H_2, and a relevant formation of aromatic species, up to heavy PAHs is noteworthy. The oxygen and hydrogen content in the char residue, as a function of the pyrolysis temperature, well agrees with experimental measurements.

Figure 93 compares experimental and model predictions of volatile species released from lignin pyrolysis at different temperatures with residence time of 3.6 s in the second tubular reactor [33]. Two different sets of model predictions are reported in Figure 93. The former set refers and uses the experimental information of product distribution from primary lignin pyrolysis reported in Table 30. Phenolic species, together with the undetected ones, were distributed according to the predicted primary pyrolysis products of the EHL sample. The second simulation results were obtained by directly feeding the EHL lignin sample to the two-stage tubular reactor. In this case, after the first pyrolysis stage, the predicted lignin pyrolysis products were fed to the second tubular reactor with the residence time of 3.6 s

The reasonable agreement obtained with both these simulation procedures further confirms the predictive feature of the whole pyrolysis model, i.e. it is not necessary to use the experimental information on the primary decomposition products from lignin. In fact, the direct and coupled use of primary biomass pyrolysis together with successive gas-phase reactions give satisfactory predictions, very similar to the ones obtained by feeding the experimental primary products to the second reactor.

[330] observed that feedstocks with high lignin content, and possible interactions with polysaccharides, tend to produce high yields of oxygenated (hydroxyacetaldehyde and acetic acid). The characterization of this sample was done with the reference species of lignin only. If we consider that residual amounts of hemicellulose are often bonded chemically to the extracted lignin samples, some GMSW/XYHW/XYGR could be added to the characterization, promoting the release of acetic acid during pyrolysis step. However, this experimental information was not available, and any tentative of including hemicellulose to the characterization would be based only in guessing.

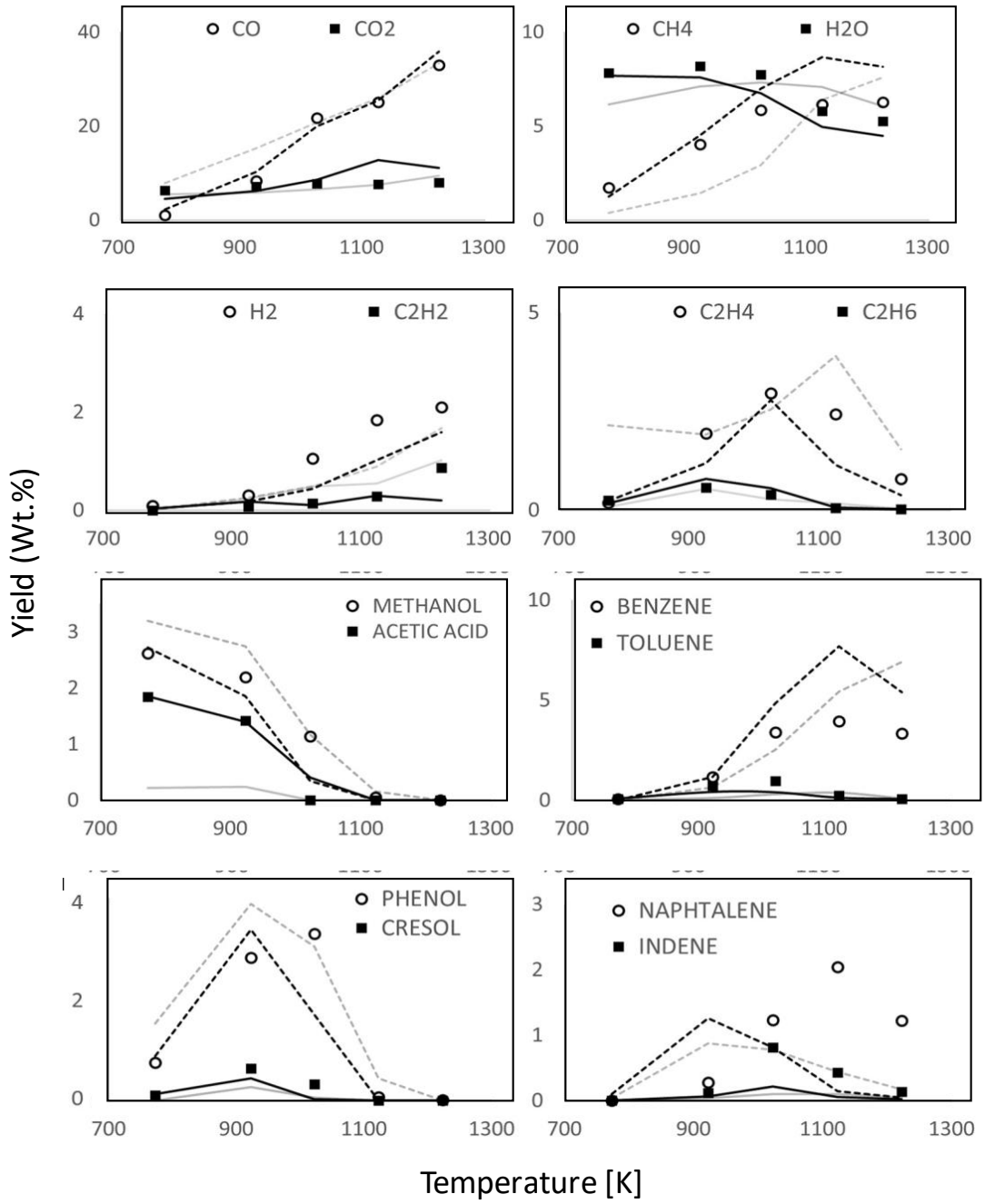

Figure 93 - Volatile species released from lignin pyrolysis at different temperatures with residence time of 3.6 s in the second tubular reactor. Comparison between experimental data [33] (symbols) and model predictions (lines) with (dark lines) and without using the experimental intermediate data of lignin pyrolysis (light lines).

The observed under-prediction of acetic acid which deserves a special attention and a better analysis of its possible formation path from lignin pyrolysis. Recently, Mante et al.

An additional important aspect of these experiments relates to the very severe pyrolysis conditions, which cause significant formation of heavy PAHs and soot. Again, model results indicate in a predictive way the formation of ~5% of species heavier than C_{20}, in

agreement with the experimental observation of soot deposition on reactor walls above 1023 K. The heaviest C_{20} PAH species act as the final sink of heavy carbonaceous species, because of the very severe pyrolysis conditions.

2.5. The Effect of Secondary Gas-Phase in Bio-Oil

This section will show some comparisons with experimental data regarding the yield of gas, solid and bio-oil, highlighting the model sensitivity to major process parameters such as temperature, solid and vapor residence times, and biomass composition.

Aguado, Olazar [331] studied the flash pyrolysis of sawdust with N_2 in a conical spouted bed reactor at 350-700 °C and with 50 ms of gas residence time. They studied the effect of pyrolysis temperature on the obtained yields and composition of gas, liquid, and solid, assuming a residence time of the solid particles of about 10 min [332]. A maximum yield of liquid of about 70 wt % was observed at 450 °C. The proximate analysis of the sawdust was: fixed carbon=16.04; volatile matter=83.74; ash=0.22. The ultimate analysis are as follows: C/H/O=44.80/6.56/48.49; with N=0.05 S, and S=0.1 (in wt %). According to this analysis and assuming 6 wt.% of moisture, the characterization method described in chapter 3 gives the following detailed composition (weight fractions) in terms of reference species:

CELL	GMSW	LIGC	LIGH	LIGO	TGL	TANN	Moist	Ash
0.516	0.226	0.041	0.136	0.011	0.012	0.002	0.05	0.006

Figure 94 compares experimental data and model predictions in terms of organic oil, water, gas, and residual biochar yields on weight basis. While the maximum liquid yield of 70 wt.% is properly predicted by the model, large deviations are observed mainly at the low temperatures. These deviation allows to highlight the importance of the residence time, as well as of the thermal resistances, of the solid particles. By halving the residence time of the solid to 5 min, instead of 10 min, there is a clear effect, more evident up to 700K, and it would be possible to strongly reduce the observed deviations, as shown in Figure 94. This effect, here obtained by reducing the residence time of the solid particles, could be also due to the presence of biomass particles with larger sizes, i.e. requiring more time for finishing the devolatilization process. In order to complete this sensitivity analysis to the heating of biomass particles, the predicted profiles for a residence time of 2 minutes are also reported in the same figure. These model predictions are obtained without considering the effect of secondary gas-phase reactions of released products.

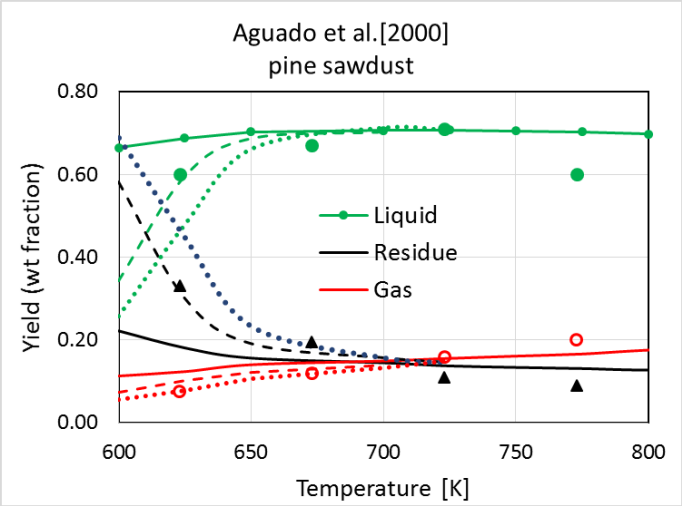

Figure 94 - Fast pyrolysis of pine sawdust. Comparisons of experimental data (symbols) [331] and model predictions in terms weight yields of bio-oil (including water), gas, and residual biochar vs reactor temperature. Effect of residence time of biomass particles: 10 min (solid lines), 5 min (dashed lines), and 2 min (dotted lines).

Similar experiments were also reported by [333]. They treated pine wood particles in a small fluidized bed fast pyrolysis reactor with a biomass particle residence time up to 25 min, at temperatures between 330 and 580 °C to study the effect on product yields and oil composition. Pine wood particles of 1 mm, a density of 570 kg/m^3, and a moisture content of 9-10 wt.% were used, together with silica sand particles of 250 µm as fluidized bed material. Accurate mass balance closure was achieved in the laboratory scale bubbling fluidized bed reactor. The bio-oil yield initially increases up to about 56-58 dry wt.%, then is nearly constant between 450 and 530 °C, and finally decreases at higher pyrolysis temperatures. Biomass biochemical composition was given as cellulose / hemicellulose / lignin =35/29/28 (wt.%, dry). The ultimate analysis of the same biomass was C/H/O = 46.58/6.34/46.98 (wt.%, daf), total ash 2600 mg/kg, on a dry basis, and only traces of N and S. Figure 95 compares experimental data and model predictions in terms of organic oil, water, gas, and residual char yields on weight basis. The residence time for the solid particles is 5 minutes, while only 1 s is assumed for the released gas and tar species.

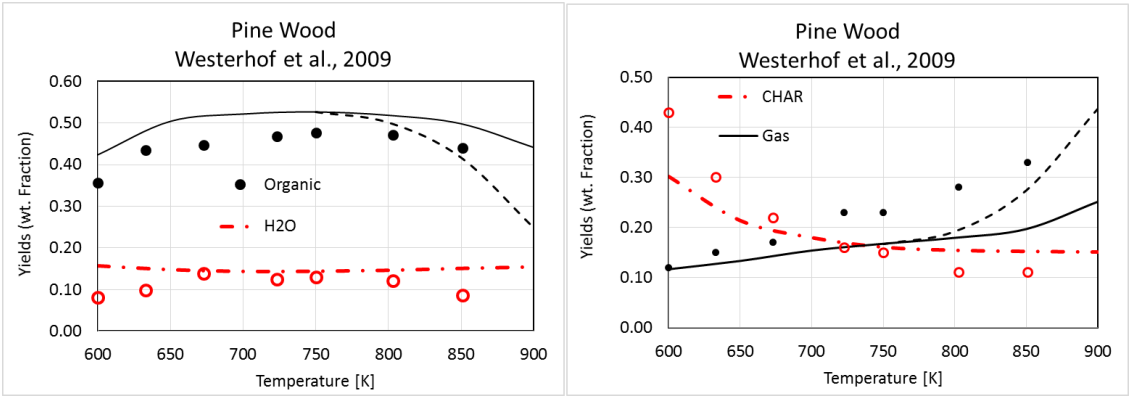

Figure 95 - Pine wood pyrolysis. Comparisons between experimental data (symbols) and model predictions (lines) in terms of organic oil, water, gas, and residual biochar yields respect to the initial biomass [333]. Oil and gas profiles are reported for gas residence time of 1 s (solid lines) and 5 s (dashed lines).

At temperatures higher than 800 K, there are the largest deviations, in these experiments. By assuming a residence time of the gas phase of 5 s, it is possible to account for these deviations. In fact, the effect of secondary gas-phase reactions with relevant oil decomposition significantly reduces the deviations in organic and gas yields, at temperatures higher than 800 K. As already discussed in the previous example, the deviations at low temperatures can be explained based on a lower residence time of the solid particles, or on a size distribution involving larger diameters.

Both these examples refer to fast pyrolysis of a softwood biomass, consequently the model predictions are similar, because of the similar feed and similar operating conditions. Deviations between experiments and model predictions are limited and partially contradictory for the two sets of data. It seems relevant to emphasize the importance, as well as the difficulty, in the complete and correct simulation of these data. It is necessary to properly account for the reactor conditions, typically in terms of the average residence time both of the gas and of solid particles. Moreover, the size distribution of the solid particle, together with the characterization of the transport properties during the pyrolysis process, are further features to be properly defined for a correct simulation of the reactor behavior, and are outside of the range of this work. Both these examples show a maximum liquid yield of about 65-70 wt %, with about 10-15% of water, as a global value due to the initial moisture and the pyrolysis water.

In order to highlight the possibilities of the model, Figure 96 compares the model predictions on yields of organics (bio-oil without moisture), biochar and gas, obtained with pyrolysis at different temperatures. The residence times used were 5 minutes for the solid

and 2 seconds for the volatiles. It is clear that the model is able to account for the differences between feedstock, predicting maximum bio-oil yields between 40% and 80%, mainly because of the different cellulose and hemicellulose content of different biomass samples. Biomasses with high cellulose content produce more bio-oil (e.g. untreated wood and sawdust feedstocks), because of the elevated release of levoglucosan and HMFU from cellulose. Biomass with elevated content of inorganics and hemicellulose (e.g. grass and residues from agriculture) typically produce low bio-oil. As already observed, the presence of a maximum is due to the primary biomass pyrolysis (at low temperatures) and, on the other side, to the successive decomposition reactions of tar species, at high temperatures. Gas yields increase continuously with temperature. At temperatures below 700 K, and mainly depending on particle dimensions, an appropriate residence time is essential to complete the pyrolysis process and maximize bio-oil yields.

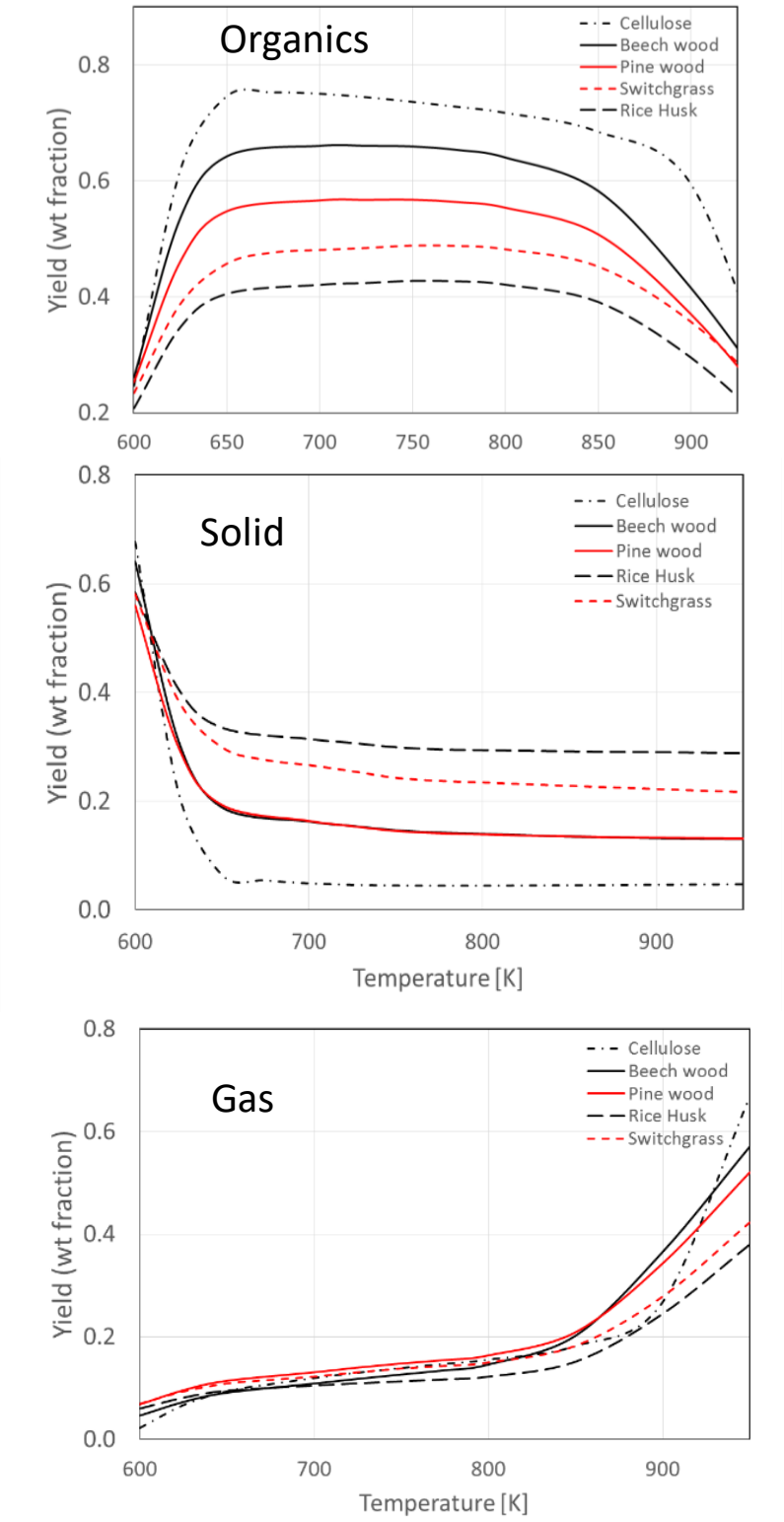

Figure 96 - Predicted typical yields of bio-oil, biochar and gas from fast pyrolysis of different biomass samples (residence time: solid 5 min, gas 2 s)

In order to further validate the validity of these model predictions, we report a few more comparisons. Zhao, Jiang [334] performed pyrolysis experiments of commercial

cellulose, xylan and lignin using a tubular reactor. Samples of 25g were inserted in the tube once it has achieved the desired temperature and have been kept there for 20 minutes under a N_2 flow of 80ml/min (99.99% purity). The liquid products collected after the condenser were analyzed by an Agilent 6890 GC-MS with a HP-35 capillary column to exploit its composition. The gas composition was analyzed by an Agilent 7890A gas chromatography with a thermal conductivity detector (TCD) and hydrogen flame ionization detector (FID) attached directly to the sampling point. Simulations have been carried out at 300-700°C. Despite the fact that this experiment is not fully on a kinetically-limited regime, it is also worthwhile to evaluate the model predictions.

	Cellulose	Xylan	Lignin
Proximate analysis (wt.%)			
Moisture	3.31	3.96	3.42
Ash	-	5.59	3.85
Volatile matter	94.65	79.42	67.23
Fix carbon	2.04	11.03	25.50
Elemental analysis (wt.%)			
C	43.08	42.14	61.81
H	6.40	6.22	5.63
O	46.71	41.40	23.57
N	0.50	0.69	1.72
HHV [MJ/kg]	17.28	16.81	25.51

Figure 97 – Analysis of the three samples

The simulations were carried out with the reference species CELL and XYHW forcellulose and xylan samples, respecting the experimental moisture and ashes content. With an oddly high content of hydrogen, a mixture of LIG-C=78.0, LIG-H=8.3, TGL=6.5 wt.% was used to characterize the lignin sample, also respecting the experimental ash and moisture contents. The inclusion of a few amounts of TGL aids the characterization of such a sample with high H content. A residence time of 2 s for the volatiles was estimated. Since no information about the volumes of the units were provided, this value has been assumed as typical value for gas phase residence time in experiments of this nature. Figure 98 shows the comparison between experiments and model predictions for gas and bio-oil from the three different samples. It confirms once more the higher yield of bio-oil from cellulose, producing about 50% more than the other compounds in the maximum bio-oil yield. The lignin

experimental values for gas yields is at least questionable in the range of 400-600°C, as no changes are observed, while the bio-oil keeps increasing, reaching a maximum at 600°C. If volatiles are still being released until these temperatures, gases are expected to follow the trend. However we only see an increase in gases at 700°C, when tar cracking becomes significant.

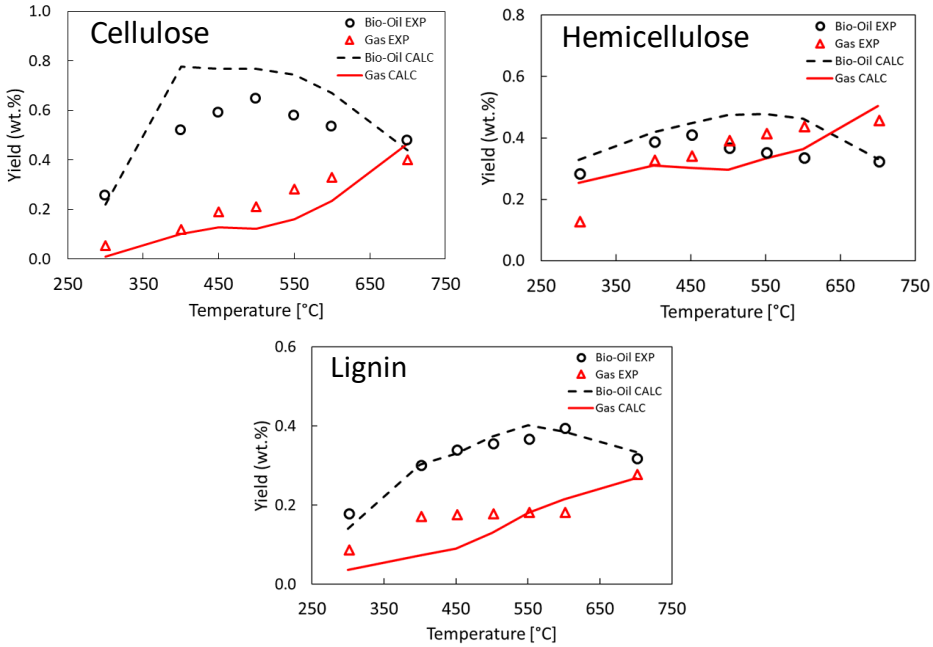

Figure 98 – Cellulose, Hemicellulose and Lignin Pyrolysis. Comparisons between experimental data (symbols) and model predictions (lines) in terms of bio-oil and gas. Oil and gas profiles are reported for gas residence time of 2 s (solid lines).

These set of comparisons were very useful for observing the model flexibility to distinguish these aspects for the different samples. It is very important to be able to well predict the behavior of the single species, as complex biomasses are assumed in this model as a linear combination of the thermal degradation of the reference components.

To further validate these model predictions, we compare with experimental data on solid, gas and tar, together with CO and CO_2 yields for pyrolysis of another sample of xylan pyrolysis [182] from 400 to 700°C. The model follows the experiments trends: tars exhibit a maximum yield at ~450°C, where devolatilization is almost complete. At higher temperatures, bio-oil yield reduction is caused by the progressive importance of secondary gas-phase-reactions (tar cracking), leading to increase in gas yields. In order to obtain these results the temperature and residence times mentioned by Shen, Gu [182] were applied. The residence time for the volatiles in the reactor was about 0.5-1s, which showed to be long

enough to triple the CO yields, and increase by one third the overall light gases yield, mainly above 650°C, when compared to the values at 500°C.

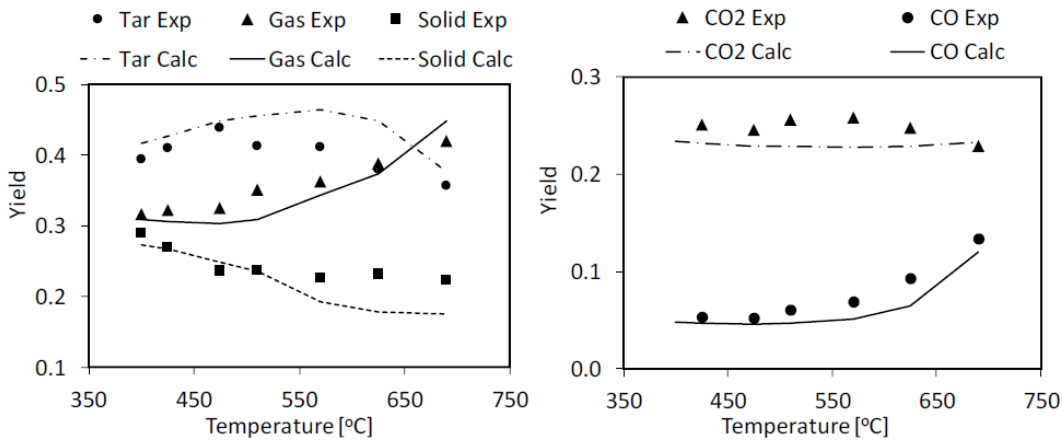

Figure 99 - Xylan pyrolysis. Yield of biochar, gas and bio-oil, CO and CO_2 [182].

The following comparisons refer to the bio-oil organic compounds obtained from hemicellulose extracted from different types of biomass. The bar plot in Figure 100 shows the distribution of tar species produced from the pyrolysis of the three different hemicelluloses at 550°C, and compares the model predictions with the experimental data of Wang et al [335, 336] in terms of sugars, furanic and light oxygenated species. The authors applied an improved method using detergents for hemicellulose extraction, without causing relevant structure damage. The method also obtains low-ash content extracted samples, when compared to commercial available hemicellulose model compounds. This is important to hinder the catalytic effect of inorganics on sugar decomposition. The comparisons highlight the higher sugar monomers release from softwood, and the higher content of light oxygenated from grass/cereals. This is the consequence of the higher presence of 6-carbon sugar monomers and less branched structure of softwood hemicellulose (HCE1). The 6-carbon sugars are more easily released as anhydrous monomers, more similar to the decomposition of cellulose, while 5-carbon sugars tend to decompose into furanics and light oxygenated compounds (HCE2). These comparisons highlight that hemicelluloses are not homogeneous in tar distribution, as well as in thermal stability and yield of solids, as already showed in chapter 4. These aspects reinforce the necessity to characterize hemicellulose according to the biomass origin, for obtainin more reliable predictions.

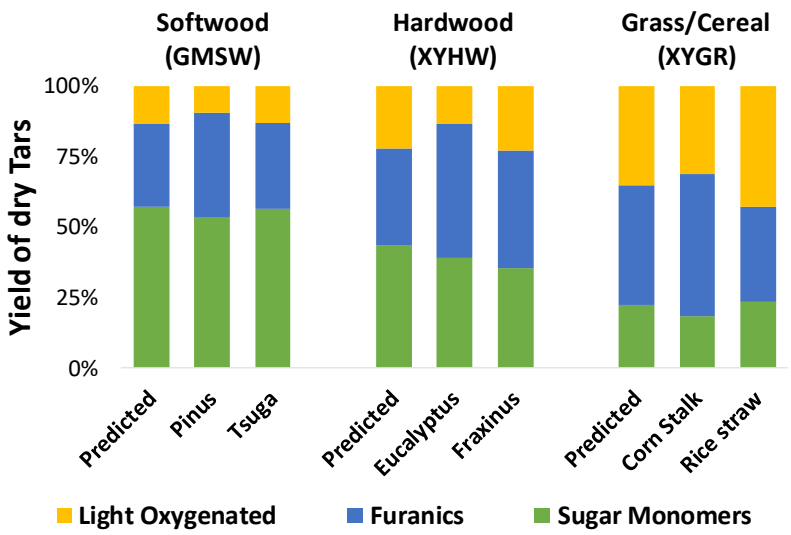

Figure 100 - Distribution of condensable products of hemicellulose from different types of biomass. Comparison between predicted (GMSW, XYHW, XYGR) and experimental data of Softwood (Pinus, Tsuga), Hardwood (Eucalyptus, Fraxinus) [336] and Grass/Cereals (Corn stalk, rice straw) [335]

Furthermore, Figure 101 satisfactory compares experimental and predicted products yields from the fast pyrolysis of three different typical biomass samples: softwood (pine sawdust), hardwood (eucalyptus log), and grass (reed canary grass). Simulation results refer to pyrolysis temperature of 700 K, with a residence time of 2 s for the secondary gas phase reactions of released products. Higher phenolic species content (~30 wt.% higher) in grass is the result of higher initial lignin content. Moreover, it is clear that sugars are lower in grass samples, first because of lower cellulose content, but also because of the effect of higher ash content on sugars decomposition, which will be highlighted in the next discussion.

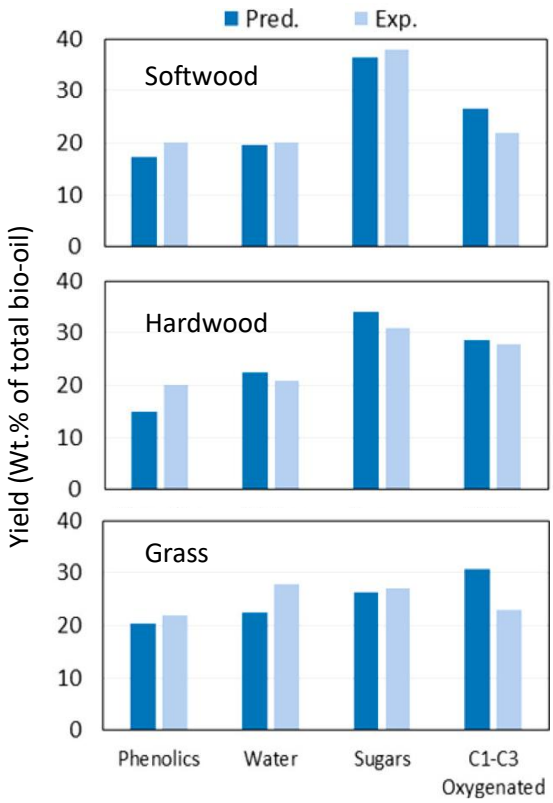

Figure 101 - Comparison of experimental [283] and predicted products from the fast pyrolysis of softwood (pine), hardwood (eucalyptus), and grass samples.

The large variability in bio-oil yields shows the effect of incomplete pyrolysis of biomass at low temperatures, along with the effect of secondary decomposition reactions, at high temperatures. Another aspect that is worth to be discussed is the effect of inorganics in the predictions of bio-oil. The yields of organics in Figure 96 refer to average ash conditions, i.e. the predictions refer to the results obtained using the unchanged kinetic parameters. On the other hand, Figure 102 clearly shows the effect of ash on the yield of organics. The three yield curves refer to values of ash factor (AF) equal to 0, 0.5, and 1.0, showing the extremes of this factor on model predictions. Cellulose predictions are reported because this component is the one releasing major amounts of tar species, and therefore, the effects are highlighted. The maximum of bio-oil yield span in this way between 70 and 80 wt.% of the original dry biomass. As this effect is not caused by the secondary gas-phase reactions, but directly on the release of volatile species, accounting for this ash effect is essential to achieve better predictions.

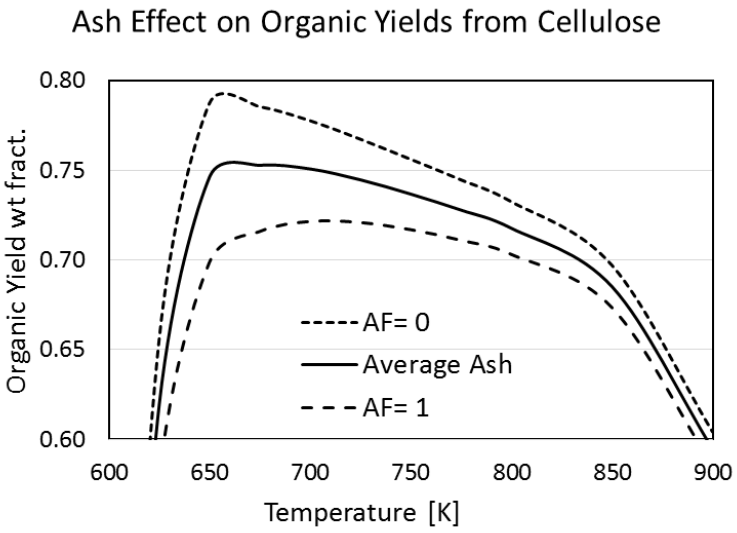

Figure 102 - Cellulose Pyrolysis and the effect of ash on organic yield.

3. Conclusions

This chapter discussed the fate of the volatile fraction of products from biomass pyrolysis. The importance of accounting for the secondary gas-phase reactions of these species for the proper prediction of products was explained. The methods used in the development of such kinetic mechanisms of these oxygenated compounds were explained with several examples and validation with experimental data for single compounds. The successful coupling of the biomass pyrolysis with the gas-phase mechanism was presented, showing the robustness of the model to account for the different yields from the biomass reference species, and consequently account for the large variability of biomasses. While the biomass pyrolysis model involves tens of species species in the solid and metaplastic phase, more than 400 species are involved in the gas phase reactions. The complexity of the gas phase can be further reduced by proper methods depending on the computational cost that can be afforded [337-339]. The satisfactory comparisons with several experimental data on broad range of conditions prove the model reliability. As the model's target after validation is the use on non-kinetically limited situations, many simplifications are required. A comprehensive mathematical model of biomass pyrolysis, both at reactor and particle scale, is then required to characterize bio-oil formation properly accounting for the coupling of the chemistry and transport resistances in real scale reactors. In fact, not only the kinetics of pyrolysis reactions, but also the heat diffusivity inside biomass particle, the heat transfer coefficients, as well as the fluid dynamics inside the reactor, play a crucial role in determining bio-oil production in fast pyrolysis processes at the industrial scale. The next chapter will

discuss the applications of biochar and the formation and evolution of this fuel on the pyrolysis step. Then, the most important physical and chemical properties that influence its combustion and gasification will be explained together with a kinetic mechanism of these heterogeneous reactions.

CHAPTER 6

BIOCHAR FORMATION AND OXIDATION

Human kind has been using biochar, which Is a very versatile material since the discovery and mastery of fire. It was used in order to avoid the spread of diseases and odors from human wastes. The addition of biochar into human feces creates, after some period of fermentation, a good source of natural soil fertilizers. The structural characteristics of biochar provides interesting features to this material. For being highly porous, it can hold high amounts of moisture and other substances, which makes it useful for carrying nutrients and moisture to the soil. It also helps on water treatment by capturing undesirable substances. As plants fix the CO_2 during their growth, biochar keeps part of this CO_2 in its structure, acting as a carbon-capture method. It has elevated calorific value, mostly when the ash and oxygen contents are not elevated. Biochar can be used in these and many other highly valuable applications [20].

In the previous chapters, we proposed a predicted kinetic mechanism for the pysolysis of biomass. This process generates gases, tars and a solid product, which is the

biochar. Understanding the characteristics of the biochar and being able to predict them is a key aspect of the modeling of thermochemical conversion of biomass.

1. Biochar yield and composition

Cellulose, hemicellulose and lignin produce biochar in different amounts. Their different molecular structure and composition are the main reason for these differences. In fast pyrolysis processes, when temperature is about 550 °C, cellulose yields the lowest amount of solids, producing about 5 wt.% of the initial mass. Hemicellulose from grasses and cereals produce about 38 wt.%. Hardwood and softwood hemicelluloses produce about 33 and 25 wt.%, respectively [340]. Inorganic matter in increase the yield of biochar for two reasons. The first is that they remain in the solid phase as ashes. The second is that they promote the decomposition of sugars into biochar and gases, inhibiting the release of tars [341]. The inorganics in biochar have a negative effect in the high heating value of the solid fuel, but some metals have a positive effect of catalyzing the gasification reactions. The yield of biochar from a biomass is usually well described by the linear combination the biochar yield of the biomass components. Interactions between these components can influence the overall biochar yield, but these effects are not yet completely clear and require further investigation.

The solid residue is an amorphous carbon structure containing significant amounts of oxygen and hydrogen, minor amounts of nitrogen and sulfur, together with metal oxides (i.e. ashes), which are formed from the inorganic matter present in the raw material during pyrolysis. The carbon content usually ranges from 65 to 95% depending on the initial biomass composition and pyrolysis operating conditions. Hydrogen and oxygen contents progressively drop when pyrolysis temperature rises by the release of gases.

The content of hydrogen and oxygen directly influences the biochar reactivity in oxidation and gasification processes. In particular, H and O sites disturb the organization of the crystalline carbon matrix through the formation of amorphous areas and weakly bonded functional groups. These factors enhance the surface area, the amount of volatile matter in the biochar and the density of surface active sites, which are directly correlated to the biochar reactivity.

Both char from coal and from biomass can undergo a progressive graphitization at high temperatures (T>1000-1200°C) [342], a processes called annealing. This process is schematically shown in Figure 103, where four stages take place. At temperatures below 770

K, the basic structural components are present; between 1070 and 1770 K the basic structures rearrange themselves face-to-face in distorted columns; at temperatures between 1873 and 2270 K, the adjacent columns coalesce into crumpled layers and at the end, at temperatures above 2370, these layers harden, becoming flat and perfect [343].

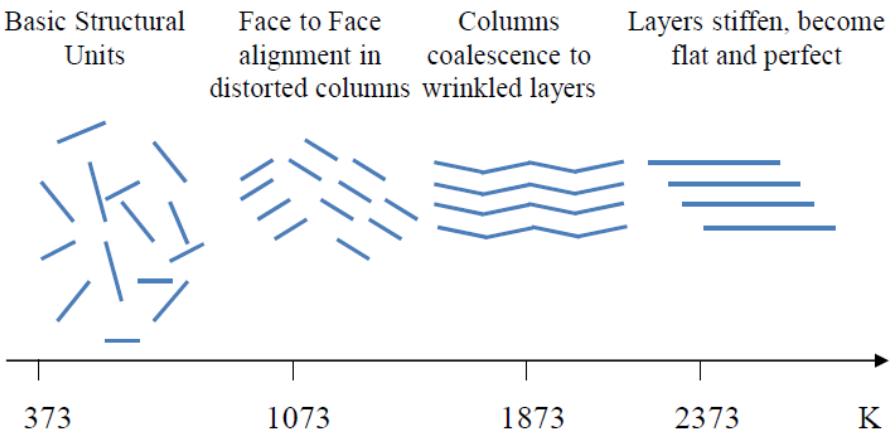

Figure 103 - Four stages of structural rearrangements leading to crystalline order (after [344].

However, this process should be between the first and the beginning of second stage in biochar, mainly because of the typical lower operating temperatures, which hinder the annealing process. Moreover, the operating conditions analyzed in the present work do not fall into the annealing severity conditions. For these reasons, this effect will not be here considered.

As already mentioned in the previous chapters, the experimental data on elemental composition of the raw biomass and of the pyrolysis products obtained were essential for the development of this model. From this simple information, many other can be predicted if the model proves to be in accordance to experiments. Most of the models of biomass thermochemical conversion describe the yield of biochar, but do not pay attention to its elemental composition.

Neves, Thunman [345] extensively analyzed the characterization and prediction of biomass pyrolysis products, with particular attention to the residual biochar. From a large collection of experiments, they derived empirical correlations to predict the yield and composition of the gas, bio-oil and biochar as a function of the peak pyrolysis temperature. They considered a variety of fuels over a wide range of pyrolysis conditions, providing

correlations also for the yields of gas-phase volatiles and thermochemical properties of char, tar and gas.

Figure 104 shows the elemental composition of several samples of biochar (on a dry and ash-free basis), in terms of C, H and O, as a function of the pyrolysis peak temperature. The elemental composition varies roughly from the one of the parent fuel to about 100% carbon, being highly dependent on the pyrolysis temperature. The carbon content of biochar increases with temperature increase, meanwhile there is a loss of oxygen and hydrogen. Typically, the amount of O decreases from 20-40 to 5-10%, while the H content is lower than 1-2%. The investigation divided the samples into wood (raw and residues of wood) and non-wood biomass (grasses, cereals, residues from agriculture and industry processes). Neves, Thunman [345] proposed these all-inclusive temperature-dependent regressions for the yield of char and for its composition in terms of C, H, and O mass fractions, in the temperature range of 250-1000 °C:

$$Y_{Char} = 0.106 + 2.43 \cdot e^{-0.0066 \cdot T} \qquad R^2=0.56 \qquad (1)$$

$$Y_C = 0.93 - 0.92 \cdot e^{-0.0042 \cdot T} \qquad R^2=0.65 \qquad (2)$$

$$Y_O = 0.07 + 0.85 \cdot e^{-0.0048 \cdot T} \qquad R^2=0.56 \qquad (3)$$

$$Y_H = -0.0041 + 0.1 \cdot e^{-0.0024 \cdot T} \qquad R^2=0.75 \qquad (4)$$

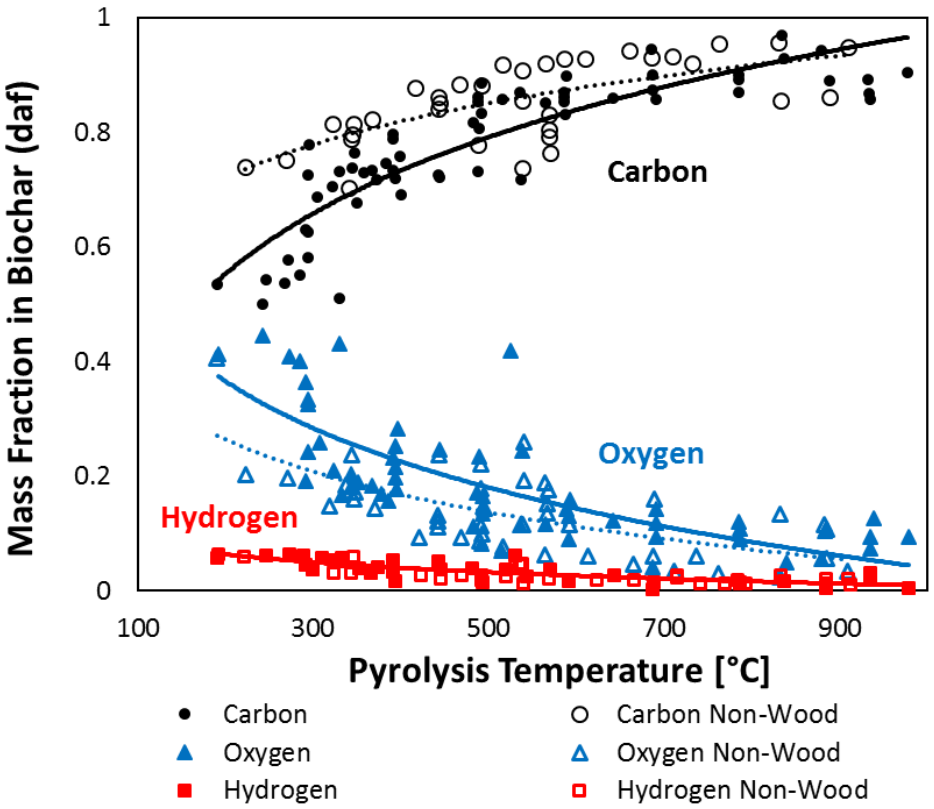

Figure 104 - Elemental C/O/H composition of dry ash-free biochar as a function of the pyrolysis peak temperature. Dashed lines are given in eq. (2)-(4). Open symbols: wood. Solid symbol: non-wood. After Neves, Thunman [345].

It is quite clear that the correlation indexes obtained from this general temperature-dependent approach is very low (R^2 ~0.5-0.75). The accuracy of such predictions can be slightly improved by separating the samples into wood and non-wood fuels. The lines in

Figure 104 show the predictions of an exponential correlation distinguishing the two sub-set of samples and they indicate a tendency of non-wood biomasses to generate chars with higher carbon content. This fact can be at least partially explained by the higher carbon of the parent fuels, and elevated ash matter that promotes dehydration reactions by catalytic effect of the inorganics. Indeed, not only the parent biomass atomic composition and the peak temperature but also operating conditions strongly influence the pyrolysis process. Biochemical composition, heating rate and peak temperature are the most influencing process conditions [10, 11].

As already observed by Anca-Couce [47], at low temperatures (<800 K) and low heating rates most of the volatiles have been already released and char and tar are the most abundant products, whereas the gas yield is lower. When charring is promoted, as in slow pyrolysis or when a high ash content acts as catalyst, total tar yield is reduced while the yields

of char, CO_2 and H_2O are enhanced. At higher temperatures (>800 K), the CO and H_2 yields increase drastically, while tar and char yields are reduced. This is due both to secondary decomposition reactions of tar species (already discussed in chapter 5) and also to the progressive char devolatilization processes. Thus, higher heating rates promote production of higher liquid yields, whereas lower heating rates enhance biochar formation. Higher amounts of cellulose favor bio-oil production and higher lignin contents enhance biochar yields.

We believe that, in order to have reliable predictions of the thermochemical conversion of biomass, a model must account for the effect of all these variables. As already reported in the previous chapters, the present model is able to predictively process these variations in feedstock and operating conditions. The next session will further validate the model predictions, now focusing on the characteristics of the biochar formed after pyrolysis step. The reliable description of the biochar characteristics is essential for the modeling of the further gasification and oxidation of this material

1.1. Predictions of the Model

Biochar structures and functional groups were studied by several authors [43-45, 346]. Supported by solid-state ^{13}C and ^{31}P NMR (Nuclear Magnetic Resonance), the chemical moieties can be investigated. In-situ rheology allows to understand the metaplastic phase formation, involving the softening and shrinking of the material. The ^{1}H NMR allows to understand the mobility of protons in the material, which stabilize the free radicals formed when bonds are broken. The molecular weight and degree of polymerization can be identified by gel permeation chromatography with ultra-violet absorption (GPC-UV). These and several other analytical methods are being employed for the study of raw biomass, the biochar formation process and the biochar structure itself.

In Raman spectroscopy, the IV, ID and IG bands refer to amorphous, large aromatic cluster with defects, and graphitic biochar structures, respectively. Figure 105 shows the Raman spectra of the biochars obtained from beech wood pyrolysis in different temperatures [346]. The ID and IG bands correspond to the peaks at ~1350 and ~1582 cm^{-1}, whereas the IV band corresponds to the signals between ID and IG. The decrease of IV band reflects the devolatilization of weakly bonded functionalities, while the increase of ID bands refers to the reordering of smaller aromatic clusters, forming a larger carbonaceous structure. The IG band does not increase because the pyrolysis temperature does not reach graphitization

conditions. The process of char devolatilization is thus characterized by a strong decrease of IV/ID ratios at lower temperatures and an increase of ID/IG at higher temperatures [346].

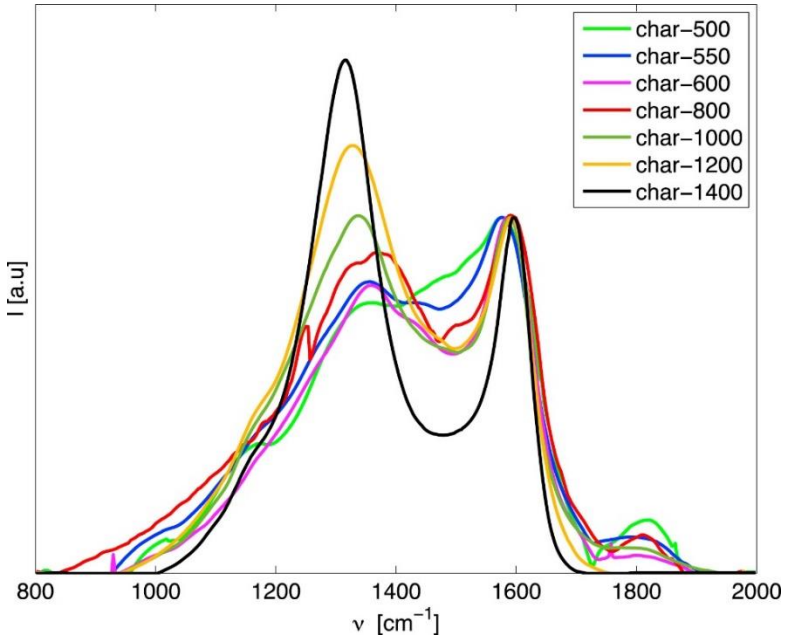

Figure 105 - Raman spectra of the biomass chars. (after Guizani, Haddad [346])

A wide range of chemical functionalities, whose distribution depends on the sample composition, characterizes the structure of the raw biomass. The typical bands detected in NMR spectra of biomass indicate groups of aliphatic carbon (primary, secondary and tertiary), carbonyl, carboxyl, aldehyde/ketone, methoxyl, methylene, methyl acetates, protonated and non-protonated aromatics, and aromatics linked with methoxyl groups and with oxygen [43].

Biomass components, cellulose, hemicellulose, lignin, and extractives have characteristic functional groups, which can be identified in these bands. Along with the decomposition of these components, their characteristic bands reduce in intensity, increasing the band intensity of biochar characteristic structures: aliphatics, and aromatic C-H, C-O, C-O-C, and C-C.

The formation of aliphatic carbon is typical in pyrolysis at 300-350°C when most of the sugar structures of cellulose and hemicellulose already decomposed. Carboxyl, carbonyl and acetates bands quickly diminish with increasing pyrolysis temperature. Aliphatic carbon bands significantly reduce after 400°C with the release of light hydrocarbons, because of the breakage of weaker bonds in the forming biochar.

Progressively, the size of aromatic clusters grows with the loss of C-H, C-O and C-O-C aromatic groups, increasing C-C aromatic bands, as non-edge carbon. These are the preliminary steps describing the biomass evolution to a less ordered biochar; then, there is a progressive ordering of aromatic clusters to more turbostratic and graphitic-like structures. Cao, Pignatello [43] measured clusters with about 20, 40, 60 and 80 carbon atoms for pyrolysis of maple wood at 400, 500, 600 and 700°C, respectively. Moreover, Brewer, Schmidt-Rohr [44] report significant differences in the functional groups found for pyrolysis performed under low and high heating rates. The low heating process allowed to reach more ordered structures with higher carbon content, because of a more complete release of the weaker bonded groups. The slow pyrolysis experiments at 500°C produced a biochar with 40% larger clusters (16 vs. 23 C atoms), when compared to the fast pyrolysis at the same temperature [44]. This fact further confirms that the structural evolution of the biochar, and its composition, is not only sensitive to temperature, but also on operating conditions. Therefore, the compositional data together with these more advanced analytical methods allow to better describe the nascent biochar and its evolution throughout the increase of temperature.

From the kinetic mechanism of pyrolysis, we describe the biochar residue as a mixture of pure carbon species (CHAR) and many other G{..} species that contain hydrogen and oxygen. CHAR species represents the carbonaceous matrix, made of aromatic rings. The other species represent both the metaplastic species, which are the volatiles that remained trapped in the solid, and the chemical functionalities bonded to the carbonaceous matrix.

The reason to have several species is to represent, in a simplified approach, the many chemical moieties present, such as carbonyls, carboxyls, methoxyl, hydroxyls. They have different composition and bond strength, resulting in different temperature and products released. These species are formed during the decomposition of the biomass reference species. The solid residue is then represented by the sum of pure carbon (CHAR) and the G{..} species. The progressive release of these species causes the decrease of biochar yield, the rising of its carbon content, together with a corresponding reduction of oxygen and hydrogen content.

The release of these lumped G{..} species accounts for the structural information mentioned before. Figure 106 shows the rate of release of G{..} species in the temperature range 500-1333 K. The lumped oxygenated species G{CO2}, G{CH3OH} and G{CO}, representing alcohol/aldehyde/ketone/carboxylic acid functional groups, are first released.

G{CH3OH} and G{CO} species are released with very similar rates. For keeping the easy reading of the plot, we report only the G{CO}. For the same reason, G{C6H5OH} is not reported, having a similar releasing rate as $G\{COH2\}_{Loose}$. Then, the aliphatic carbon groups G{CH4}, G{C2H6}, and G{C2H4} follow, together with the release of $G\{COH2\}_{Loose}$ group. G{H2} and the stiff G{COH2} groups, with different releasing rates, describe the final oxygen and hydrogen content in the residual biochar. Whereas the $G\{COH2\}_{Loose}$ group release mainly H2O with a charification process, the stiff G{COH2} group contributes to the final release of CO and H2, gases detected typically at high temperature during biomass pyrolysis.

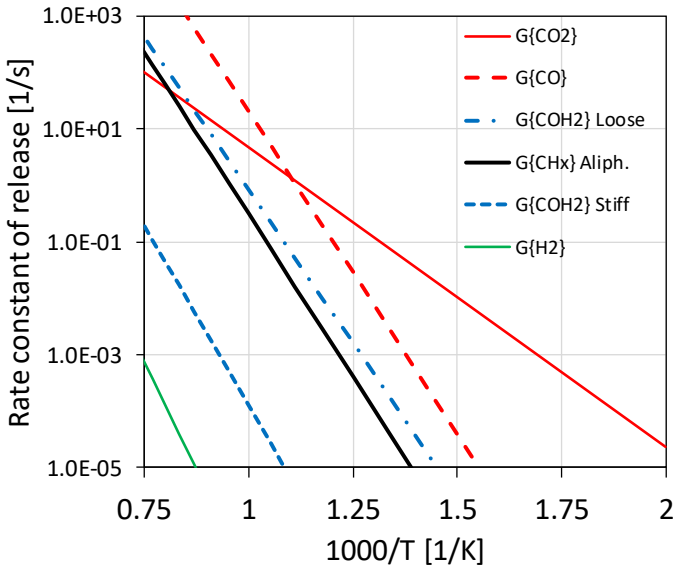

Figure 106 - Rate constant of the release of metaplastic species.

In fact, as shown in Figure 106, the final release of metaplastic species $G\{COH2\}_{Stiff}$ and G{H2} groups typically takes place only at temperatures higher than 1400 K and 1800 K, respectively, where their half life time is about 1 s. These species are also released in lower temperatures, but require long exposure time. This progressive release of these last two metaplastic species globally agrees with the decrease of C-H, and the increase of C-C bond bands in NMR.

The model also accounts for competing reactions that have different selectivities under different temperatures, defining the main path under low and high temperatures. These features are present for the reference components of cellulose, hemicellulose and lignin, while extractives were not accounted for these differences because of their reduced amount in the samples and less importance in the global biomass pyrolysis. In general, the low temperature mechanisms produce more biochar and gases, while high temperature yield more tars.

In order to validate the predictions of the model in terms of yield and composition of biochar, all the selected biomass samples taken from the database (available in the Appendix A) were first characterized in terms of reference species, based on the biochemical composition either specified or estimated through the characterization method. Then the biomass pyrolysis model predicts the time evolution of the yield and composition of the residual biochar, according to the specified operating conditions. As said, the predicted solid residue (biochar) is the sum of the fixed carbon (CHAR) and all the residual lumped species (G{..}) still trapped in metaplastic phase. Elemental (C/H/O) composition of the biochar is calculated simply taking into account mass fraction and composition of each residual species. To better show the model performance, feedstock composition and characterization of some biomass samples are reported in Table 31.

Mass Fraction	Spruce Wood	Birch Wood	Peanut Shell	Waste Wood	Maple Wood
C (daf)	0.498	0.478	0.484	0.467	0.534
H (daf)	0.064	0.064	0.062	0.058	0.068
O (daf)	0.438	0.458	0.454	0.474	0.398
Ash (dry)	0.007	0.006	0.017	0.015	0.017
CELL	0.482	0.558	0.579	0.519	0.251
XYHW	-	0.303	0.202	-	0.205
GMSW	0.262	-	-	0.181	-
LIGO	0.001	0.000	0.046	0.116	0.002
LIGH	0.173	0.072	0.097	0.004	0.349
LIGC	0.026	0.011	0.021	0.018	0.051
TANN	0.000	0.000	0.010	0.070	0.001
TGL	0.049	0.050	0.028	0.001	0.089
Moisture	-	0.030	-	0.075	0.035
ASH	0.007	0.003	0.017	0.015	0.017

Table 31 - Biomass elemental composition and characterization in terms of reference components. Spruce wood, birch wood [347], peanut shell [348], waste wood shavings [349], and maple wood [43].

Figure 107 shows the comparison yield and composition of the residual solid after torrefaction (220-300°C) of (A) Spruce (Softwood) and (B) Birch (hardwood) wood samples from Table 31. The experiments [347] were performed in a TGA at heating rates of 40 °C/min, with 2 hours of hold time after reaching peak temperature. The characterization was done considering the different typical hemicelluloses of these two samples.

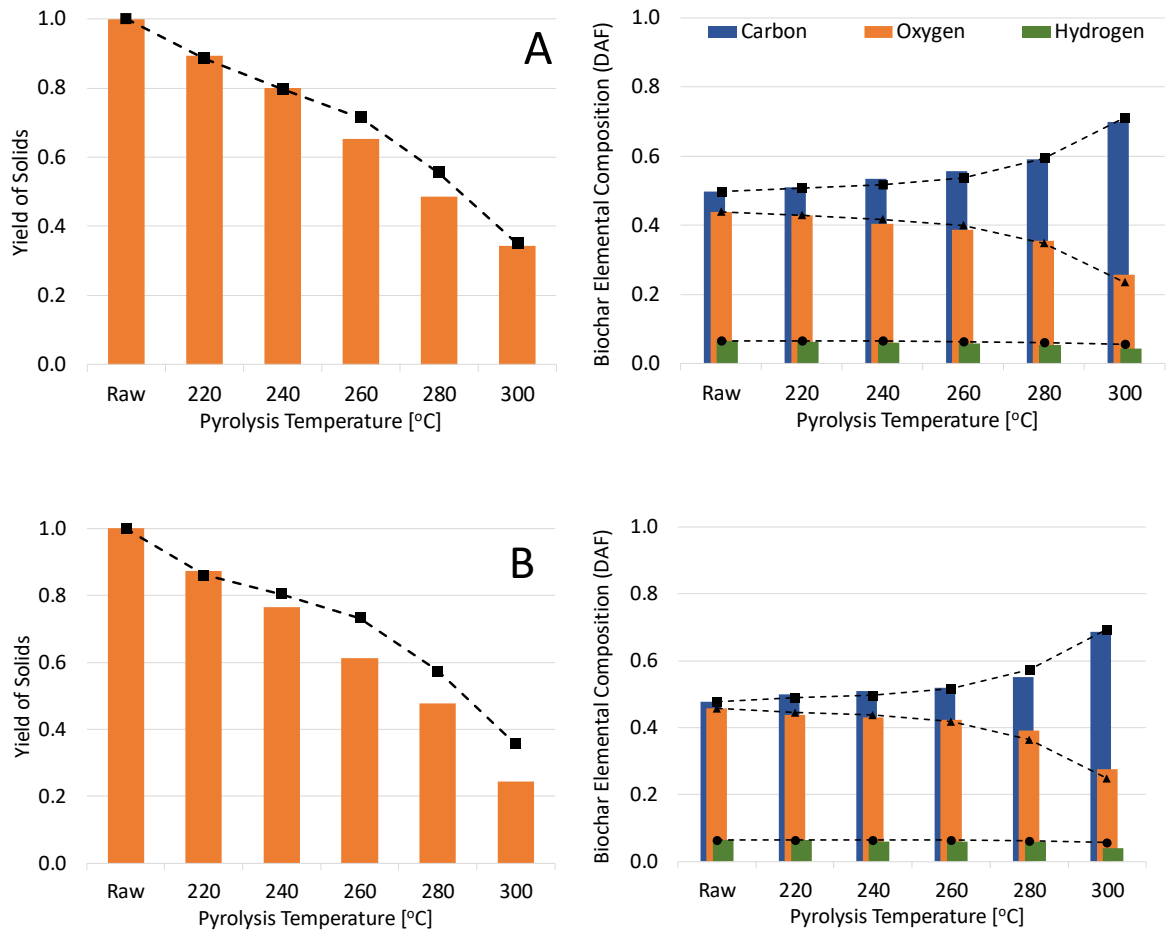

Figure 107 - Torrefaction of (A) Spruce (Softwood) and (B) Birch (Hardwood) [347]. Comparison of experimental data (bars) and model predictions (lines) in terms of biochar yield and composition vs pyrolysis temperature.

The experimental data is reported in the bars and model predictions are reported in the lines. The plots on the left show the evolution of the residual mass of solids and elemental composition is reported on the right. Mass fraction of Carbon, Oxygen and Hydrogen in the biochar at each temperature are represented with different colors. The sum of C/H/O are on a dry and ash-free basis and sum up to 1 for both experiments and model predictions. It is clear that at lower temperatures, typical from mild torrefaction processes, the mass loss is limited, and the composition of the residual solid discreetly changes. After reaching severe torrefaction conditions, the solid yield drastically reduces and significant changes can be observed in the composition. The model is able to track both the discreet and the more significant changes.

In Figure 108, severe pyrolysis conditions are reported for three different biomass samples. The results are organized in the same way as in Figure 107. However, these set of

experimental data contained only the elemental composition of the biochar. Therefore, the solid yield reported are only the model predictions. The characterization of these samples is also reported in Table 31. Figure 108 (A) refers to pyrolysis of peanut shells [348] in a fixed bed reactor heated by electrical furnace at 15°C/min. Figure 108 (B) refers to waste wood shavings in a fluidized bed reactor at different constant temperatures [349]. Finaly, Figure 108 (C) shows the results of pyrolysis of Maple wood shavings in a stainless steel tube furnace at temperatures from 300 to 700°C [43] with heating rates of 25 °C /min.

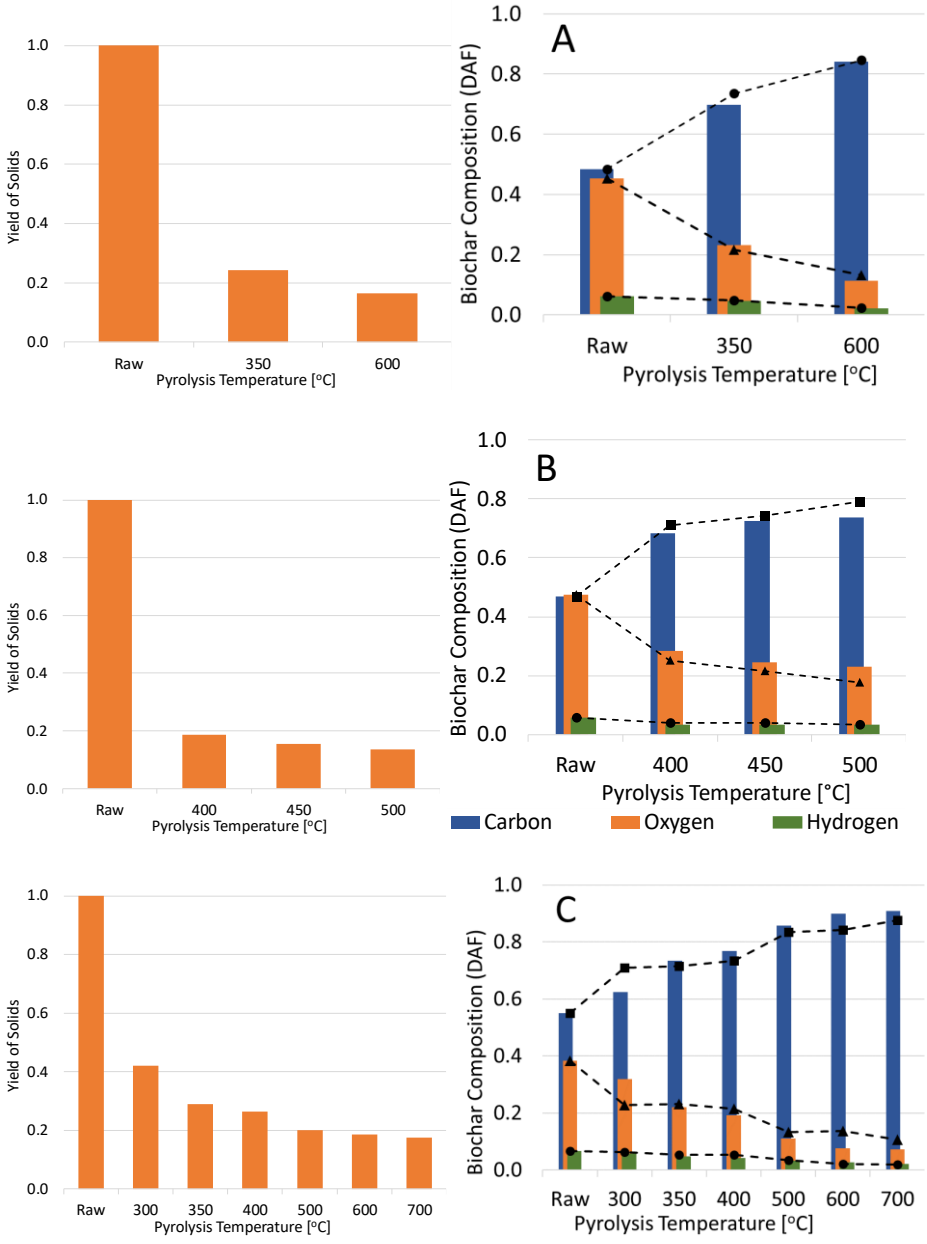

Figure 108 - Pyrolysis of peanut shell (A) [348], waste wood shavings (B) [349], and maple wood (C) [43]. Comparison of experimental data (bars) and model predictions (lines).

At temperatures above 500 °C the reference species are already decomposed, and the further mass loss and compositional change of the solids are caused by the release of the G{..} species. As temperature rises, the oxygen and hydrogen content drops, caused by the breakage of weaker bonds releasing light gases, resulting in a reduction of the biochar yield and an increase of the carbon content. This effect is less evident in the torrefaction process, whereas it is very clear in the high temperature pyrolysis treatments.

The parity diagrams in Figure 109 and

Figure 110 highlight the global correlation indexes obtained with the model predictions when compared to the whole set of comparisons processed (80 samples). In order to better analyze these data, experiments are first divided into:

- Low heating rate (LHR): experiments in TGA and reactors with programmed heating rate.
- High heating rate (HHR): experiments in fluidized bed, drop tube, pyroprobe and similar devices.

Both these categories are further subdivided depending on low and high final temperature (550°C is the threshold temperature). Finally, TGA category refers to TGA experiments in which C/H/O data of biochar is not provided.

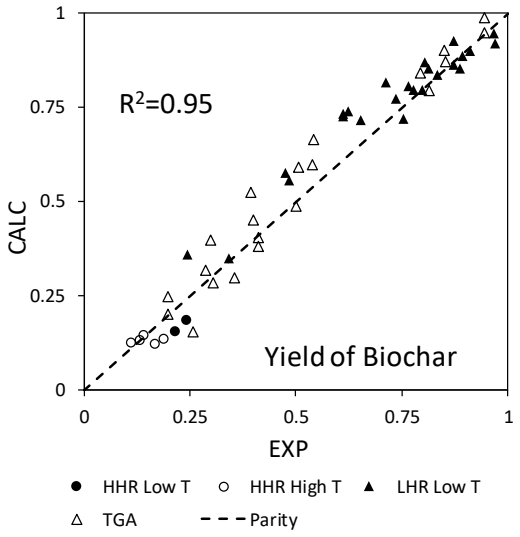

Figure 109 - Parity diagram of experimental and predicted values of biochar yield

Figure 109 shows the parity diagram of biochar yield, which has a correlation index (R^2) of 0.95. A correct prediction not only of biochar yield, but also its elemental composition

is of utmost importance, because it strongly affects successive biochar reactivity in combustion and gasification processes [350].

Figure 110 show the parity diagrams for carbon, hydrogen and oxygen composition of the biochar, with correlation index of 0.94, 0.9, and 0.9 respectively. The good prediction of elemental composition is essential but remains only a first feature because it is indeed necessary to correctly define the oxygenated and aliphatic surface functionalities, the catalytic active sites as well as the porosity and specific surface [43, 351].

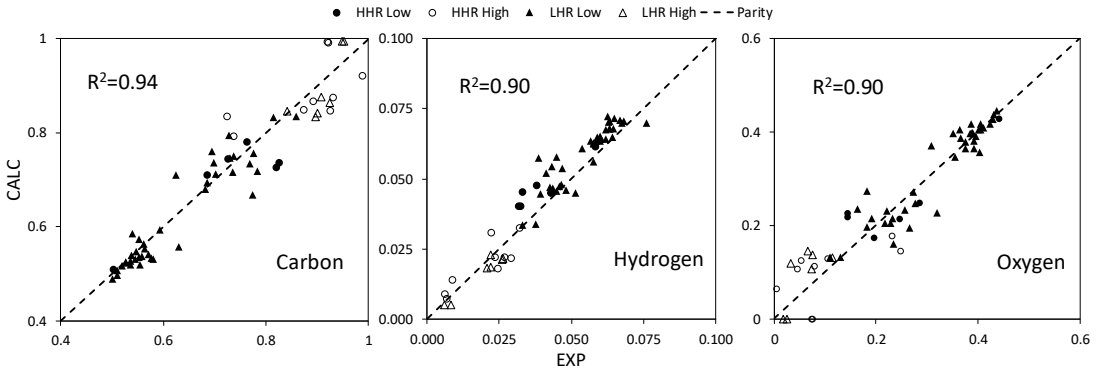

Figure 110 - Parity diagrams of experimental and predicted values of biochar elemental composition

These comparisons show that the model is capable of providing reliable prediction of both biochar yield and its elemental composition at several different temperatures and heating conditions. Of course the simplifications and assumptions used for the development of the model limit the accuracy of the predictions. However, the absence of significant systematic deviations indicates the robustness of the model.

This fact is well evident in Figure 111, where the residuals (experimental – predictions) are reported as a function of the temperature. Larger hydrogen residuals are present at low temperatures, also because of a higher sensitivity of model results to operating and simulation parameters. Moreover, this fact is not anymore true when considering relative instead of absolute errors.

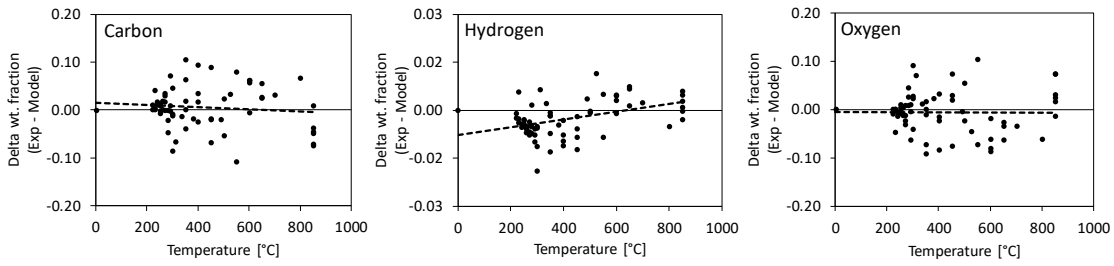

Figure 111 - Distribution of residuals (experimental-prediction) of elemental composition and yields of biochar vs peak pyrolysis temperature.

However, some scatter still persists caused not only by the large simplifications of the biomass characterization and the pyrolysis model, but also to the experimental uncertainties, including the poor knowledge of the biomass origin and composition, and the incomplete description of the reactors and operating conditions in many cases.

Moreover, the scatter of the HHR experiments in Figure 109 highlights a minor systematic biochar underpredictions, whereas an opposite deviation is observed for the LHR data. At high temperatures and high heating rates, the release of metaplastic species could be partially reduced, but more experimental data is required to confirm the trends. Jia, Dufour [352] also reached similar conclusions, when investigating the performance of our model under HHR conditions.

2. Biochar Oxidation

The large majority of kinetic models of both char from coal and from biomass propose empirical or semi-empirical mechanisms of reactions which are usually able to describe one or a few samples under a strict range of conditions. While efforts were directed to the development of general models for characterization, pyrolysis and gas phase reactions, the biochar oxidation/gasification still lacks predictive approaches. Coal and biomass chars significantly differ in structural and compositional aspects, which lead to different behaviors and properties.

Char from coal is usually much less reactive than biochars. The first are less porous and have lower surface area per mass unit. This is mostly a consequence of the pore size distribution. The amount of volatile matter in biomass typically ranges from 60 to 90 wt.% of initial mass, against 5-40 wt.% in coal. The devolatilization step, mainly in biomass, creates large amounts of micropores in the residual char, which confer large surface areas to the solid.

The surface is a determining characteristic on the reactivity of the solid to oxidation and gasification. The reactions taking place are the result of interactions between the surrounding oxidizing agents and the surface of the solid. Thus, the process is a heterogeneous system of reactions. The surface is important, but these reactions occur in specific sites of the surface, the edge atoms present in the structure. In the present work, these edge atoms will be described as the active sites of the surface. The amount of these active sites per unit of area will be referred to a general density of active sites (γ).

2.1. Density of Active Sites

The previous section described the model predictions on yield and composition of the biochar. The combination of the predicted elemental composition with the evidences from Raman Spectroscopy and NMR experiments allow us to correlate the possible structures that are formed during the biomass pyrolysis step, and their successive evolution along the temperature.

In order to estimate the density of active sites, it is necessary to estimate the number of active sites and the total surface area in a certain cluster structure. Therefore, Figure 112 shows the predicted pyrolysis of a typical wood biomass, heated at 20 K/min, and the evolution of the elemental composition of the solid residue.

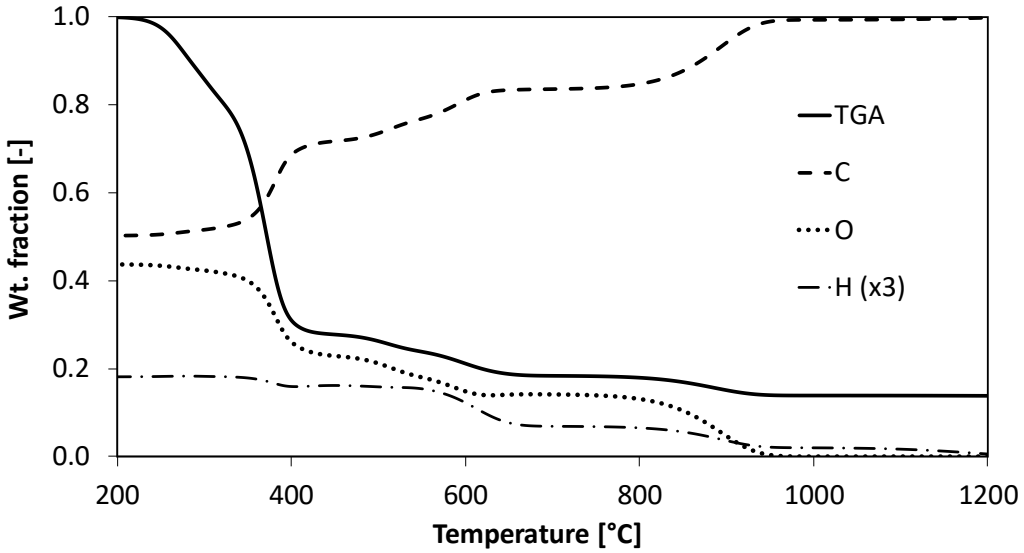

Figure 112 - Predicted pyrolysis of a typical wood biomass, heated at 20 K/min, and the evolution of the elemental composition of the solid residue.

From these composition predictions, using the cluster sizes reported by Cao, Pignatello [43], molecular structures of these clusters were estimated, as reported in Table 32. Structures obtained for pyrolysis temperatures above 700 °C were not described by the author, so we estimated clusters of 100 carbon atoms, which are equivalent to 38 aromatic rings. We considered the same number of carbon atoms for all the structures at higher temperatures, but with a progressive reduction on the number of oxygen and hydrogen atoms, according to the model predictions.

	Mass Fraction			Molecular Formula					
Temp [°C]	C	H	O	C	H	O	MW	Cluster Area [Å^2]	γ [#sites/m^2]
200	0.503	0.060	0.437	8	12	5	188	81.3	2.1 10^{19}

300	0.516	0.061	0.423	13	18	8	302	130.4	$2.0\ 10^{19}$
400	0.686	0.053	0.260	20	19	6	355	165.2	$1.5\ 10^{19}$
500	0.735	0.053	0.212	40	34	9	658	313.7	$1.4\ 10^{19}$
600	0.811	0.041	0.149	65	39	9	963	471.6	$1.0\ 10^{19}$
700	0.836	0.023	0.141	76	25	10	1097	532.8	$8.4\ 10^{18}$
800	0.847	0.022	0.131	100	31	12	1423	694.4	$8.2\ 10^{18}$
900	0.941	0.012	0.047	100	16	4	1280	646.4	$8.0\ 10^{18}$
1000	0.993	0.007	0.000	100	8	0	1208	622.0	$7.9\ 10^{18}$
1200	0.998	0.002	0.000	100	2	0	1202	617.3	$7.8\ 10^{18}$

Table 32 – Biochar elemental composition, cluster molecular formula and estimated density of active sites.

From these estimated structures, we calculated the cluster areas considering two different approaches, which returned very similar results (± 10%). The first considers the clusters inside the equivalent rectangular prisms (box method). The sides of the prism are calculated through the diameter of a carbon atom, which is 1.4 Å in an aromatic ring. Oxygen and hydrogen atom diameters are assumed as 1.2 and 0.5 Å, respectively. The resulting cluster surface area is equivalent to the surface area of the box.

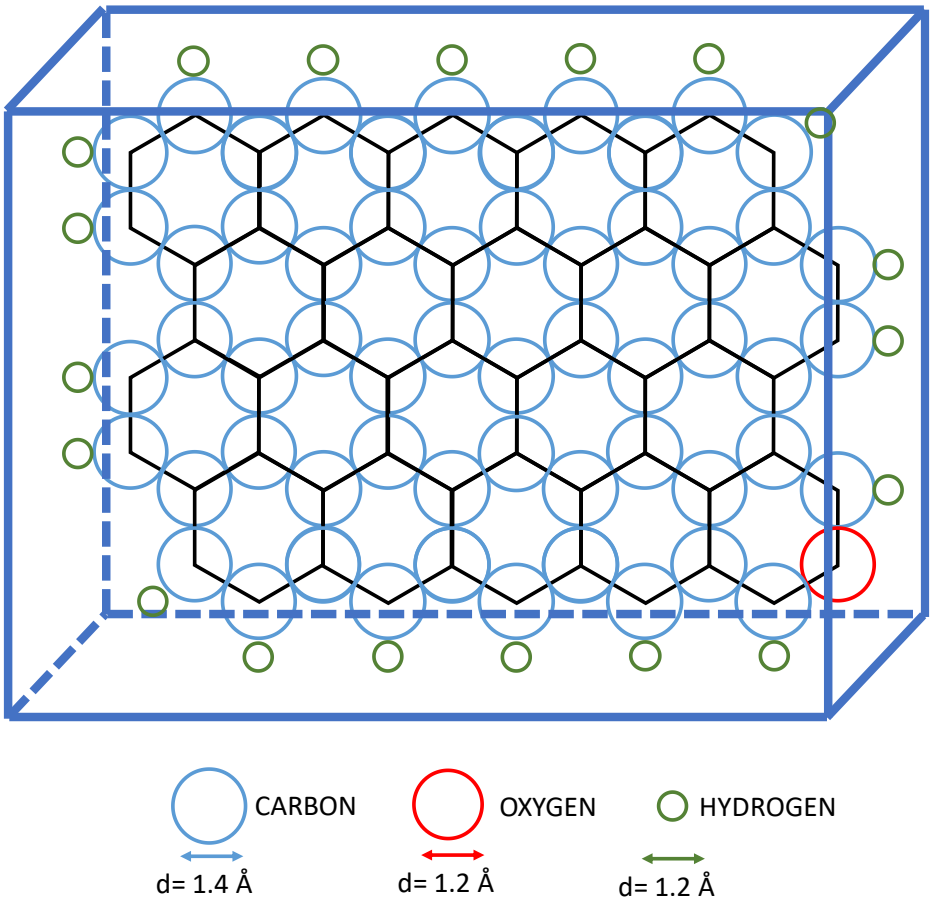

Figure 113 - Rectangular prism approach used to estimate the cluster areas.

The second method assumes the cluster area as the sum of the surface area of all atoms composing the cluster. The atoms are considered perfect spheres and the surface area of each atom was estimated using the same diameters. As the results are quite similar we assumed the results obtained by the second method. Figure 114 shows, for illustration purposes, some possible biochar cluster structures with the increase of the pyrolysis temperature.

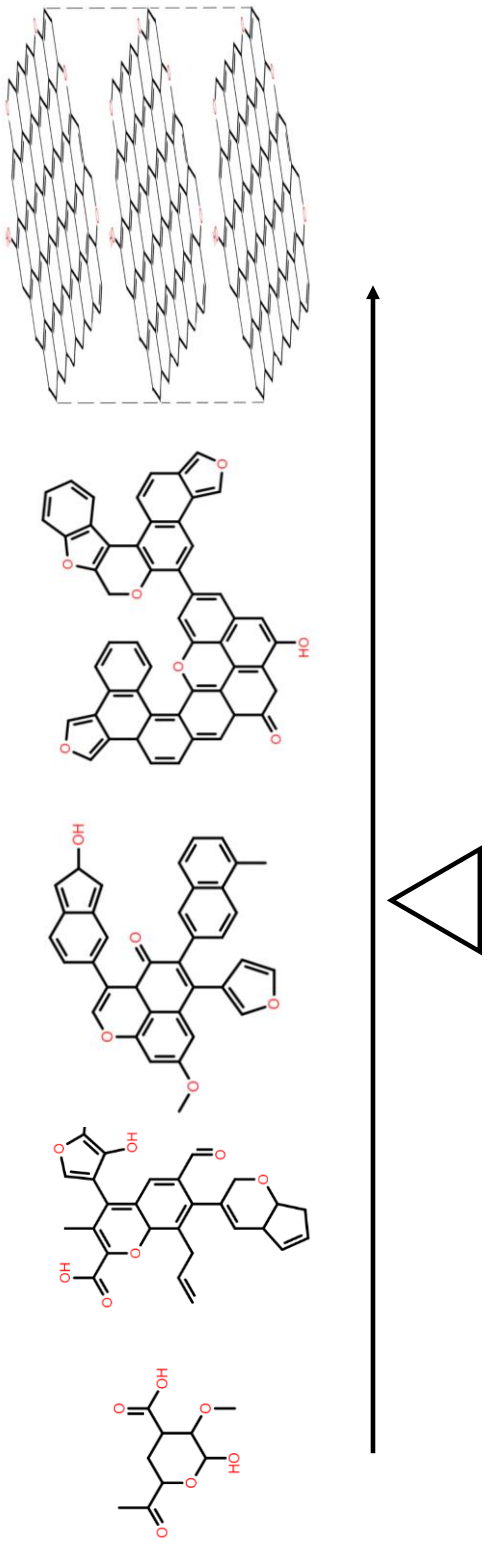

Figure 114 – Possible cluster structures of biochar at increasing pyrolysis temperatures.

Only edge atoms of each structure are considered active sites, whereas the inner atoms are not accounted. For this reason, the increase in the cluster size leads to a reduction of total active sites per unit of area, as more atoms are located internally. The inner atoms

are also called bulk atoms. The increase of cluster area progressively raise the ratio bulk/edge atoms. This is one of the reasons for the reduced reactivity of chars obtained at more severe temperatures. Figure 115 shows the estimated values of γ (as obtained through the cluster structures). Estimating the structures for each possible biochar composition is unnecessary, as a clear trend appears as a function of the carbon content. Therefore, in order to provide a predictive estimation of this parameter, a simple correlation was obtained through an exponential regression of these values, as a function of biochar carbon content. However, this simple approach does not account for the 3D arrangement of biochars, which brings further complexities such as the number of stacked layers. Graphite, for example, is composed very large clusters arranged in elevated number of stacked layers. This is one of the reasons for the very low reactivity of graphite to oxidation.

Haynes [353] estimated 10^{19} sites/m^2, Feng and Bhatia [354] reports 1.2 10^{19} sites/m^2, Darmstadt and Roy [355] used 3.8 10^{19} sites/m^2, and Campbell and Mitchell [356] reports 6.5 10^{19} sites/m^2. The values obtained by the methods used in this work are in line with the ones proposed by these authors, offering the advantage of predicting variable values, depending on the char characteristics.

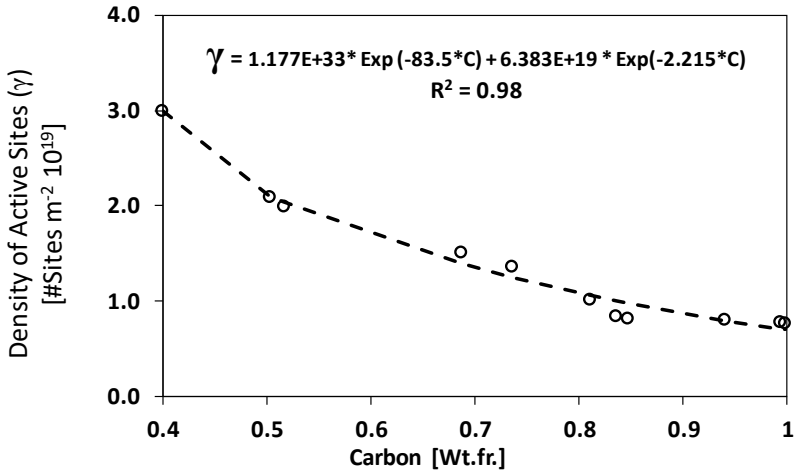

Figure 115 –Estimated values of γ (density of active sites) and the exponential correlation in function of the carbon content.

2.2. Surface evolution

Biochars are porous solid carbonaceous structure with different pore sizes and distributions. During solid conversion, pores evolve in different ways, depending on their initial size and shape. Also, new micropores can be created in early conversion. They grow along conversion, until reaching mesopores size range. The creation of new pores and the growth of the existing ones stops at mid-conversion, when the pores start to coalesce, leading to a reduction of the surface area per unit of volume. There are two main approaches used to model this phenomena, namely the grain and the pore model. The first is only able to predict a diminution of the specific surface area. The second, depending on the characteristics of the initial pores, predict a first increase in specific surface area, followed by a decrease in this value.

The most accurate model available is the adaptive random pore model, which requires the distribution of pore sizes in the biochar. However, this information is not widely available. Therefore, we apply the simpler random pore model, which considers only some structural information, which are easier available or estimated.

In this model, the specific surface area follows the equations (1) and (2) The characteristics of the solid are simplified in a single structural parameter φ, which is a function of porosity, initial surface area and total pore length.

$$S_v = S_{v0} \times (1 - x) \times \sqrt{1 - \varphi \ln(1 - x)} \qquad (1)$$

with

$$\varphi = \frac{4\pi L_{v0}(1-\varepsilon_0)}{S_{v0}} \qquad (2)$$

In which

L_{v0} is the total pore length per unit of volume (m/m^3) at time 0;

S_{v0} is the total surface area per unit of volume (m^2/m^3) at time 0;

ε_0 is the porosity at time 0;

x is the conversion of the solid.

Microporous biochars are characterized by high L_{v0} and low ε_0, resulting in higher values of φ. Samples with φ values above 2 implies that micropores are present, and therefore shows an evolution with S_v reaching maximum values. For φ between 0-2, pores

are already large and their growth leads to coalescence, progressively reducing the value of S_v.

When using the random pore model, different behaviors for the evolution of the surface are obtained, depending on the value of φ. These behaviors can be better observed in Figure 116, where the evolution of the surface are per unit of volume is reported for values of φ from 0 to 50. Chars obtained from coals usually have φ in the range of 2-8, mostly because of the reduced amount of volatiles and micropores. Biochars produced at low temperature pyrolysis will typically have φ above 15. This means that the increase in surface area along the conversion, for biochars, should be much higher than for chars from coal.

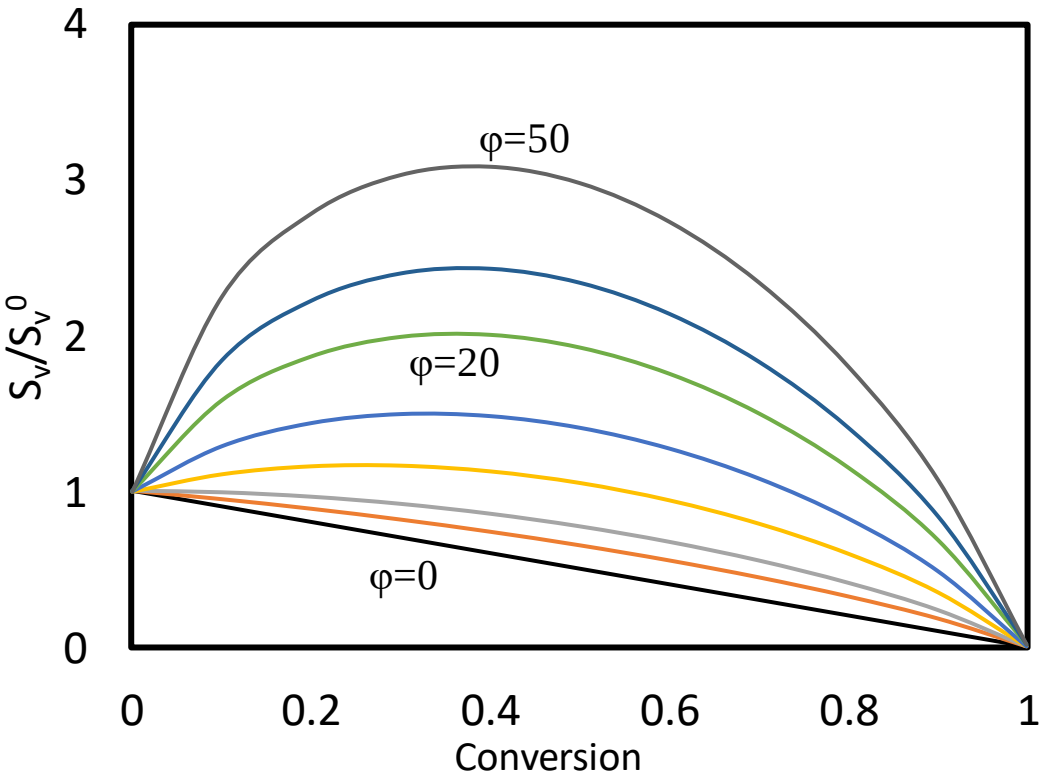

Figure 116 – Evolution of the surface area per unit of volume, as a function of the conversion, for several values of φ.

The reactions taking place are result of heterogeneous reactions between the solid and the surrounding atmosphere, so biochar reactivity is strictly related to the extension of the surface. Therefore, a proper description and reliable prediction of the surface evolution is crucial for modeling biochar oxidation.

Supported by tens of experiments on coals and the successive chars, Maffei [344] proposed some correlations for estimating the initial surface area and the values of φ for a

certain char sample, based on their elemental composition and pyrolysis operating conditions. However, the correlation indexes are quite low (R^2=0.56 surface area and 0.46 for φ). In order to obtain better correlations, a deeper investigation of the subject is still required.

A collection of ~200 experiments from the literature [357-373] containing the measurements of surface area through BET analysis was organized and is shown in Figure 107 (A). It is clear that the resulting surface area of a biochar evolves with the peak pyrolysis temperature, reaching maximum values at about 500 °C. However, the large spread of data reveals that these values are not only temperature-dependent, but are also influenced by the residence time and the heating rate. Moreover, the initial content of cellulose, hemicellulose, lignin and ashes significantly change these values. Figure 107 (B) shows this collection of data simply divided into wood and non-wood biochars, and reinforce the influence of the initial composition of biomass. Wood biomass are typically rich in cellulose and have low ash content, whilst non-wood biomasses typically have higher amounts of lignin, hemicellulose and ashes. Pure cellulose is known for generating high surface area biochars, and this effect is also observed on high cellulose content biomasses.

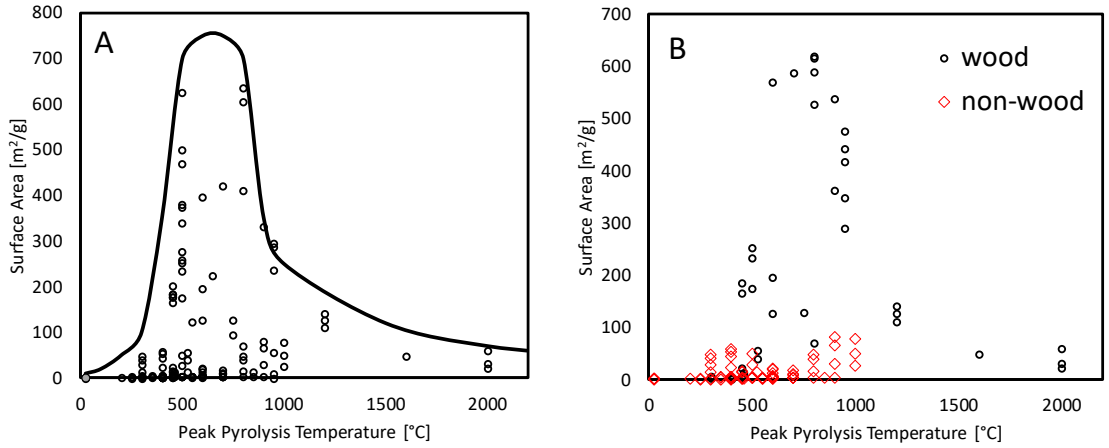

Figure 117 - Surface area per unit of mass of Biochars.

On the other hand, lignin, hemicellulose and ashes form a viscous liquid phase during pyrolysis, which occlude the nascent micropores. The pyrolysis of these components lead to the formation of larger bubbles from the volatilization of components. These bubbles further stabilize, generating the meso and macro-porous structure observed. As already discussed, the presence of large amount of micropores increase the solid surface area and its successive reactivity on oxidation. In order to validate the kinetic mechanism proposed in this chapter,

the experimental data on surface area from this collection will be applied. Nevertheless, future works will put efforts on predicting the resulting surface area of the solid together with the simulation, avoiding the input of external data.

Having an estimation of the surface area, the structural aspects of the solid and the active sites distribution through the biochar area is essential. However, these active sites have different reactivities to oxidizing agents. These differences can be accounted through specific kinetics attributed to each chemical functionality.

2.3. Kinetic Mechanism of Char Oxidation

The heterogeneous reactions taking place between the edge atoms of char and the oxidizing agents can be correlated to analogous homogeneous gas phase reactions. Soot particle growth was already proposed by other authors, using similar approach [322, 374]. Soot formation occurs under pyrolytic conditions, in a reduction process in which gaseous molecules feed atoms to build the solid structure. This process cannot be easily described by homogenous gas phase reactions, as the soot particles size increase and the resulting surface area start to control the process. Soot particles are composed of turbostratically arranged polycyclic aromatic molecules (graphene flakes)[325, 375]. Discovery of fullerenes [376] led Kroto and co-workers to propose that a spherical soot particle could form through a continuously grown fullerene [377]. While such a single-molecule mechanism was not well accepted to explain particle inception, it was proposed by Frenklach and Ebert [378] that a curved graphene-edge front, once formed, can propagate surface growth retaining particle sphericity.

Similar to soot formation and growth, the surface characteristics are also very important in the oxidation step of soot. The successful kinetic modeling of polycyclic aromatic hydrocarbons and soot is very important, as they are the transition between the gas and solid phase approach. In a more recent work, Singh, Mebel [379] used an analogy approach to propose a reaction mechanism of successive oxidation of the soot particles. In this mechanism, the activation energy of the molecular reactions were obtained using quantum chemistry calculations, using the pyrene geometry ($C_{16}H_{10}$) as the reference gas-phase molecule. Successively, $C_{16}H_9$ (Pyrenyl) is formed after the abstraction of a hydrogen atom. The formation of this radical allows oxygen to adsorb into this active surface site (Carbon). The peroxide formed releases one oxygen radical and forms an unstable complex. This complex that further rearranges into a $C_{15}H_9$ structure that contains one 5-carbon ring, releases a CO molecule, and finally stabilize. This is the main reaction path that describes the

adsorption/desorption mechanism proposed by this author. This mechanism is schematically shown in Figure 118.

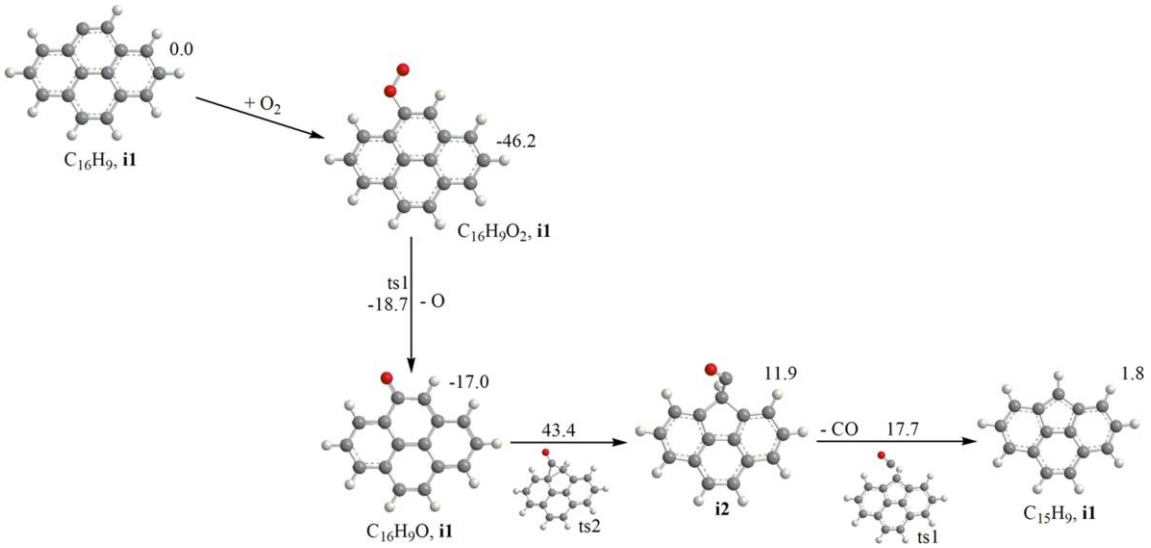

Figure 118 - Potential energy diagram for oxidation of pyrenyl radical by O_2. Potential energies calculated at the G3(MP2,CC) level are shown in kilocalories per mole relative to the C16H9|i1 + O_2. (After Singh, Mebel [379])

This approach can be applied also to describe the conversion of biochar in combustion and gasification. The activation energy for the reacting steps of H-Abstractions reactions in graphene edges were investigated by Zhao-Bin Ding [380], which observed different values from the analogous gas-phase steps. However, clear trends were noticed and they proposed correlations for obtaining the activation energy of the gas-solid reactions from the gas-phase reactions.

Supported by these investigations, we propose a first attempt to describe a detailed functional-group based kinetic mechanism for the heterogeneous reactions of oxidation and gasification of biochar. The functional groups, represented by the G{..} species, that are formed in the pyrolysis step, undergo analogous reactions that are present in the CRECK gas-phase mechanism. A correction factor must be applied both for the activation energy and for the frequency factor. The activation energies were adjusted using the correlations proposed by Zhao-Bin Ding [380]. The frequency factor must be corrected to account the per-site frequency, instead of per-molecule.

For example, as shown in Table 33, when considering the H-Abstraction of a Naphthalene ($C_{10}H_8$) molecule, the frequency factor considers the eight hydrogen atoms that can be extracted to form the naphthyl radical ($C_{10}H_7$). The Gas-solid reaction must be adjusted to consider a per-site basis, resulting in a frequency factor 0.125 times the gas-phase

analogous. In the gas-solid reaction we consider the hydrogen as an active surface site (H(S)), whereas the carbon bonded is a bulk species (C(B)). The abstraction of this surface hydrogen forms the radical HO_2, exposing the bulk carbon to the surface (C(S)). The surface carbon (C(S)) is then accounted as a surface active site, that can be attacked by oxidizing species.

Reaction	Mechanism	A	E_{act}	Reference
$C_{10}H_8 + O_2 \rightarrow C_{10}H_7 + HO_2$	Gas-phase	2.165E+07	8781.96	Pelucchi, Cavallotti [381]
$C(B) + H(S) + O_2 \rightarrow C(S) + HO_2$	Gas-solid	2.710E+06	6419.14	This work

Table 33 - H-abstraction from naphtalene and equivalent path on gas-solid.

In a very similar way, Figure 119 schematically shows the analogous path comparing H-Abstraction from benzene, forming phenyl radical.

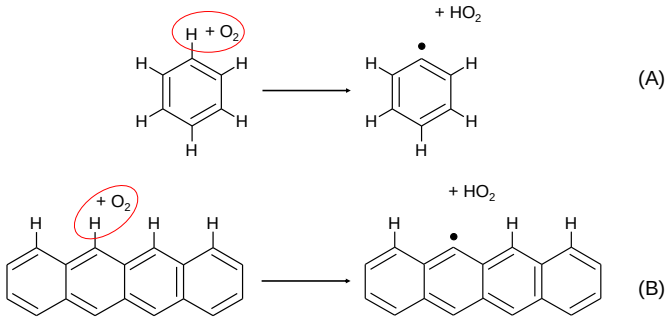

Figure 119 - H-abstraction from benzene (A) and equivalent path on gas-solid (B).

Using the same approach, a kinetic mechanism was developed and is reported in Table 34, involving the chemical moieties typically found in biochars. The description of the species involved are reported in Table 35. For the species whose main reaction path is H-Abstraction reactions by O radial, we report the kinetic constant at 400 °C. This is the typical temperature of biochar oxidation to observe the kinetically controlled regime. The compared reactivities of these groups are:

$$CHO(S) > OH(S) > CH3(S) > H(S)$$

This information is useful to understand which groups will be reacting first. As expected, the oxygenated group are more reactive, typical groups found in biochars obtained at low temperature pyrolysis. Then aliphatics, which remain in the char at intermediate temperature pyrolysis. Finally, hydrogen directly connected to the aromatic clusters is the less reactive, typical from more ordered biochars, which are only released by severe pyrolysis conditions.

The kinetic mechanism provides the rate constants of each reaction. The rate of reaction per unit of surface area of biochar, for reaction i is given by:

$$r_i = k_i \prod_{j=1} [X_j]^{\nu_{j,i}}$$

Where the generic concentration X is obtained by the following expressions:

$[X_j] = \frac{P}{RT} y_j$ if the species j is in the gas phase;

$[X_j] = \gamma \theta_j$ for the surface species;

γ is the density of active sites;

θ_j is the fraction of sites occupied by species j;

The non-surface species, namely bulk species, are not considered in the rate of reactions calculations. We assume unitary value for their activity in the reactions. In fact the concentration of bulk species does not influence the rate of reactions, but needs to be accounted in the stoichiometries in order to provide the resulting free carbon sites.

The rate of production or consumption of species j is given by

$$R_j = \sum_{i=1}^{nR} \nu_{j,i}\, r_i$$

As the surface increases, in the lower conversion part, more sites are being generated by the creation of new pores and by the enlargement of the existing ones. This is accounted for on each time step of the calculation. The new surface sites created keep the density of active sites constant by converting bulk carbon atoms C(B) into surface carbon atoms C(S). In this way, the mass balances are respected. Similar procedure is applied during the surface decrease part.

		Kinetic constant $K=A \times T^{\beta} \times \exp(-Eact/RT)$					
#	Reactions	A	beta	Eact	Analogy	Source	K 673K
	H(S)						
1	C(B) + H(S) => C(S) + H	1.50E+17	0	114000	Benzene	CRECK WEBSITE	
2	C(B) + H(S) + O => C(S) + OH	2.71E+06	2	6219	Naphtalene	CRECK 1710	1.21E+10
3	C(B) + H(S) + OH => C(S) + H2O	6.25E+12	0	2499.09	Naphtalene	CRECK WEBSITE	9.76E+11
4	C(B) + H(S) + HO2 => C(S) + H2O2	1.08E+05	2	19135	Naphtalene	CRECK 1710	3.26E+04
5	C(B) + H(S) + H => C(S) + H2	4.81E+06	2	9303	Naphtalene	CRECK 1710	2.17E+09
6	C(B) + H(S) + O2 => C(S) + HO2	3.41E+06	2	52513.74	Naphtalene	CRECK 1710	1.76E-05
	OH(S)						
7	C(B) + OH(S) => C(S) + OH	5.00E+16	0	115000	Phenol	CRECK WEBSITE	3.92E-21
8	C(B) + OH(S) + O => CO(A) + OH	1.35E+07	2	3575.94	Naphtol	CRECK 1710	4.30E+11
9	C(B) + OH(S) + OH => CO(A) + H2O	1.00E+14	0	-1039.41	Naphtol	CRECK WEBSITE	2.16E+14
10	C(B) + OH(S) + HO2 => CO(A) + H2O2	5.39E+05	2	14075.94	Naphtol	CRECK 1710	7.01E+06
11	C(B) + OH(S) + H => CO(A) + H2	5.48E+06	2.147	9849	PAH	Frenklach 2015	4.29E+09
12	C(B) + OH(S) + H => C(S) + H2O	2.00E+14	0	3759	PAH	Frenklach 2015	1.23E+13
13	C(B) + OH(S) + O2 => CO(A) + HO2	1.70E+07	2	45575.94	Naphtol	CRECK 1710	1.52E-02
	CHO(S)						
14	C(B) + CHO(S) => C(S) + HCO	5.00E+16	0	98900	Benzaldehyde	CRECK 1710	6.14E-16
15	CHO(S) => CO(Su) + H	1.00E+16	0	89300	Benzaldehyde	CRECK 1710	1.54E-13
16	CHO(S) + O => CO(Su) + OH	9.47E+06	2	1094.46	same as other aldehydes	Pelucchi et al. 2017	1.90E+12
17	CHO(S) + OH => CO(Su) + H2O	2.00E+13	0	630	same as other aldehydes	Pelucchi et al. 2017	1.25E+13
18	CHO(S) + HO2 => CO(Su) + H2O2	5.00E+12	0	12460	same as other aldehydes	Pelucchi et al. 2017	4.77E+08
19	CHO(S) + H => CO(Su) + H2	1.60E+14	0	6360	same as other aldehydes	Pelucchi et al. 2017	1.42E+12
20	CHO(S) + O2 => CO(Su) + HO2	1.36E+07	2	38109.91	same as other aldehydes	Pelucchi et al. 2017	3.12E+00
21	C(B) + CO(Su) => C(S) + CO	4.00E+14	0	29500	Benzaldehyde	CRECK 1710	1.21E+05
	CH3(S)						
22	CH3(S) + O => CH2(Su) + OHi	4.91E+07	1.635	3795.67	Toluene	CRECK 1710	1.23E+11
23	CH3(S) + OH => CH2(Su) + H2O	6.12E+07	1.587	220.318	Toluene	CRECK 1710	1.60E+12
24	CH3(S) + HO2 => CH2(Su) + H2O2	2.718	3.546	11323.604	Toluene	CRECK 1710	6.44E+06
25	CH3(S) + H => CH2(Su) + H2	2.14E+06	2.268	4392.371	Toluene	CRECK 1710	2.12E+11
26	CH3(S) + O2 => CH2(Su) + HO2i	1.81E+02	3.365	38473.24	Toluene	CRECK 1710	2.29E-01
27	CH3(S) + OH => OH(S) + CH3	8.29E+01	2.884	3221	Toluene	CRECK 1710	1.08E+09
27	CH2(Su) + O2 => CHO(S) + OH	1.00E+13	0	26500	Benzyl	CRECK WEBSITE	2.82E+04
28	C(B) + CH2(Su) + O2 => C(S) + CH2O + O	6.00E+11	0	14500	Benzyl	CRECK WEBSITE	1.26E+07
29	CH2(Su) + O => CHO(S) + H	1.80E+14	0	0	Benzyl	CRECK WEBSITE	1.80E+14
30	C(B) + CH2(Su) + O => C(S) + CH2O	1.80E+14	0	0	Benzyl	CRECK WEBSITE	1.80E+14

	C2H3(S)						
31	C2H3(S) + O => C2H2(S) + OH	1.35E+07	2	8781.96	Styrene	CRECK WEBSITE	8.99E+09
32	C2H3(S) + OH => C2H2(S) + H2O	3.99E+06	2	-53.76	Styrene	CRECK WEBSITE	1.88E+12
33	C2H3(S) + OH => CH2(Su) + CH2O	1.00E+11	0	0	Styrene	CRECK WEBSITE	1.00E+11
34	C2H3(S) + HO2 => C2H2(S) + H2O2	5.39E+05	2	16656.36	Styrene	CRECK WEBSITE	1.03E+06
35	C2H3(S) + H => C2H2(S) + H2	2.41E+07	2	10160.27	Styrene	CRECK WEBSITE	5.74E+09
36	C2H3(S) + H => H(S) + C2H3	2.00E+13	0	5000	Styrene	CRECK WEBSITE	4.87E+11
37	C2H3(S) + O2 => C2H2(S) + HO2	1.70E+07	2	37366	Styrene	CRECK WEBSITE	6.78E+00
38	C2H2(S) + O => C2H(S) + OH	2.00E+14	0	0			2.00E+14
39	C2H2(S) + H => C2H(S) + H2	2.00E+14	0	0	Styrene radicals	CRECK WEBSITE	2.00E+14
40	C2H2(S) + H => H(S) + C2H2	4.00E+14	0	0	Styrene radicals	CRECK WEBSITE	4.00E+14
41	C2H2(S) + OH => C2H(S) + H2O	1.50E+13	0	0	Styrene radicals	CRECK WEBSITE	1.50E+13
42	C2H2(S) + O2 => CHO(S) + HCO	6.00E+10	0	3000	Styrene radicals	CRECK WEBSITE	6.46E+09
43	C(B) + C2H2(S) + O => 2 H(S)+ 2 C(B) + CO(A)	1.00E+13	0	0	Styrene radicals	CRECK WEBSITE	1.00E+13
44	C(B) + C2H2(S) + OH => 2 H(S)+ 2 C(B) + CO(A)+ H	1.00E+13	0	0	Styrene radicals	CRECK WEBSITE	1.00E+13
45	C(B) + C2H(S) + O2 => C(S) + CO + HCO	3.00E+11	0	22000	Ph-acetylene	CRECK WEBSITE	2.39E+04
46	C(B) + C2H(S) + OH => C(S) + CH2CO	5.00E+12	0	2000	Ph-acetylene	CRECK WEBSITE	1.13E+12
47	C2H(S) + OH => CH2(Su) + CO	1.00E+13	0	7000	Ph-acetylene	CRECK WEBSITE	5.51E+10
	CO(S)						
48	CO(S) => CO(A)	1.00E+13	0	0	Migration of radicals		
	COOH(S)						
49	C(B) + COOH(S) + O => HO + CO(A) + CO	3.79E+06	2	1094.46	Propanoic Acid	CRECK WEBSITE	7.61E+11
50	C(B) + COOH(S) + OH => H2O + CO(A) + CO	1.12E+06	2	-3343.83	Propanoic Acid	CRECK WEBSITE	6.07E+12
51	C(B) + COOH(S) + HO2 => H2O2 + CO(A) + CO	1.51E+05	2	9982.61	Propanoic Acid	CRECK WEBSITE	4.11E+07
52	C(B) + COOH(S) + H => H2 + CO(A) + CO	6.74E+06	2	2387.18	Propanoic Acid	CRECK WEBSITE	5.18E+11
53	C(B) + COOH(S) + O2 => HO2 + CO(A) + CO	4.77E+06	2	38109.91	Propanoic Acid	CRECK WEBSITE	1.09E+00
	O(S)						
54	2C(B) + O(S) + O => CO + CO(A)	1.35E+07	2	2579.54	O-heter-pent	CRECK WEBSITE	9.02E+11
55	C(B) + O(S) + OH => CO + OH(S)	3.99E+06	2	-2259.83	O-heter-pent	CRECK WEBSITE	9.70E+12
56	2C(B) + O(S) + HO2 => CO + CO(A) + OH	5.39E+05	2	11887.73	O-heter-pent	CRECK WEBSITE	3.56E+07
57	C(B) + O(S) + H => CO + H(S)	2.41E+07	2	3950.57	O-heter-pent	CRECK WEBSITE	5.79E+11
58	2C(B) + O(S) + O2 => CO + CO(A) + O	1.70E+07	2	40722.49	O-heter-pent	CRECK WEBSITE	5.60E-01
	C(S)						
59	C(S) + O2 => CO(A) + O	3.17E+13	0	2000	Frenklach 2015	Frenklach 2015	7.17E+12
60	C(B) + CO(A) => C5A(S) + CO	1.08E+02	3.28	43500	Frenklach 2015	Frenklach 2015	1.88E-03
61	C(B) + C5A(S) + O2 => C5B(S) + CO2	3.45E+11	0	26800	Frenklach 2015	Frenklach 2015	7.77E+02
62	C(B) + C5B(S) + O2 => C(S) + CO2	3.45E+11	0	26800	Frenklach 2015	Frenklach 2015	7.77E+02

Table 34 – Kinetic mechanism of biochar oxidation

Species	Molecular Formula			Description	H-Abstraction by O (K at 400 °C)
	C	H	O		
H(S)	0	1	0	Hydrogen bonded to an aromatic carbon	1.2e+10
OH(S)	0	1	1	Hydroxyl bonded to an aromatic carbon	4.3e+11
CHO(S)	1	1	1	Aldehyde functional group	1.9e+12
CH3(S)	1	3	0	Methyl functional group	1.23e+11
C2H3(S)	2	3	0	Vinyl functional group	-
CO(S)	1	0	1	Carbonyl functional group	-
COOH(S)	1	1	2	Carboxyl functional group	-
O(S)	0	0	1	O-heteroatom in aromatic ring	-
C(S)	1	0	0	Free aromatic atom of carbon	-
C5A(S)	1	0	0	Free atom of carbon in a 5 member-ring type A	-
C5B(S)	1	0	0	Free atom of carbon in a 5 member-ring type B	-

Table 35 - Description of species in the mechanism.

2.4. Validation

In order to validate the model predictions of biochar oxidation, this section compares some experimental data, mainly on the temporal evolution of the conversion of biochars, under different operating conditions. The aim is to observe that no systematic deviations are present, and if the model responds well to different heating programs and feedstock characteristics.

Branca and Di Blasi [382] pyrolyzed samples of wood in a packed-bed reactor at 800K, obtaining 23 wt.% of char, which were milled to reduce particle size. The work also evaluated the effect of impregnating the samples in ammonium salts. For these reasons the raw wood was demineralized by washing in hot distilled water for 2 h, in order to eliminate alkali compounds. To avoid heat and mass transfer effects, the final temperature was maintained below 873 K, the heating rate below 15 °C/min, using particle sizes smaller than 110 µm. The samples were oxidized in a TGA, under air at atmospheric pressure. The authors report that a residual 25.3 wt.% of volatiles was present in the samples and proposed a three-step mechanism, involving two steps of devolatilization (25.3 wt.%), followed by one oxidation (74.7 wt.%). In order to validate the kinetics proposed, we consider only the oxidation, which prevails after the devolatilization. Therefore, simulations account for only the 74.7% of total biochar mass. The three plots in Figure 120 show the different heating rates applied to the

oxidation experiments and the model predictions. From the onset until reaching final conversion, the process took about 1600 s, 1000 s, and 500 s, for 5, 10 and 15 °C/min experiments. As the experiments used the same samples of biochar, this set of comparisons were useful to validate the ability of the model to follow the different heating speeds.

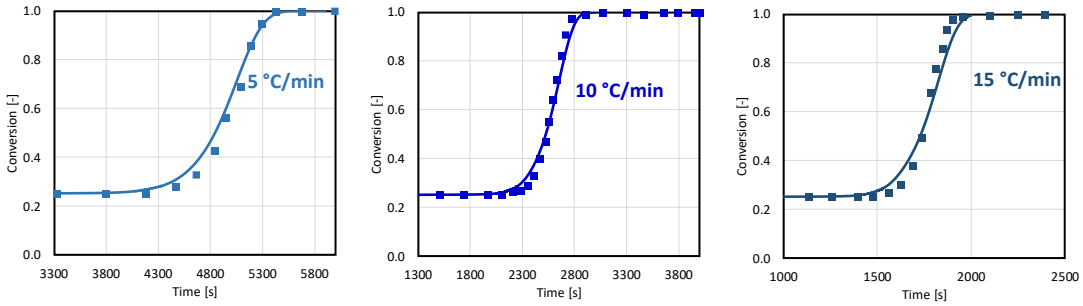

Figure 120 – Oxidation of biochar under air atmosphere at 5, 10 and 15 °C/min. The biochars were obtained by pyrolysis of raw wood at 527 °C.

In another work, Di Blasi, Branca [383] again demineralized fir wood (softwood) and pyrolyzed the sample using the same procedure of the examples of Figure 120. The authors reported that the fir biochar had 24 wt.% of volatiles. Figure 121 shows the comparison with model predictions, which is indeed very similar to the previous comparison. This example is useful to validate the predictions for another kind of biomass under similar operating conditions, and to compare the model with experiments in low-mineral content samples.

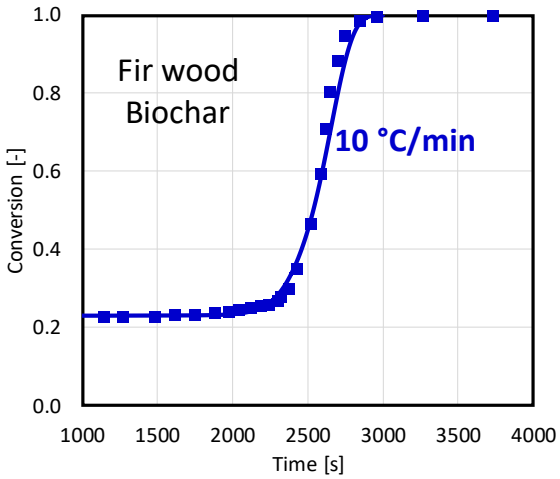

Figure 121 - Oxidation of fir wood biochar under air atmosphere at 10 °C/min. Demineralized fir wood was pyrolyzed at 527 °C to produce the biochar.

Later, Branca, Iannace [384] performed similar experiments, this time observing the behavior of biochar from beech wood and oak bark (*Quercus cerris*). In this case, the samples analyzed are significantly different from each other. Bark has a total of 44 wt.% of extractive compounds and 14 wt.% of ashes, on a dry basis. Beech has 0.2 wt.% of ashes, 2 wt.% of

extractives, and almost 80 wt.% of holocellulose. The authors also mention that raw bark has 65% of volatile matter. Therefore, the comparisons are only accounting for the 35 wt.% of solid residue (biochar). In this way the behavior of beech and bark chars can be compared in Figure 122, showing also the model predictions for these two samples.

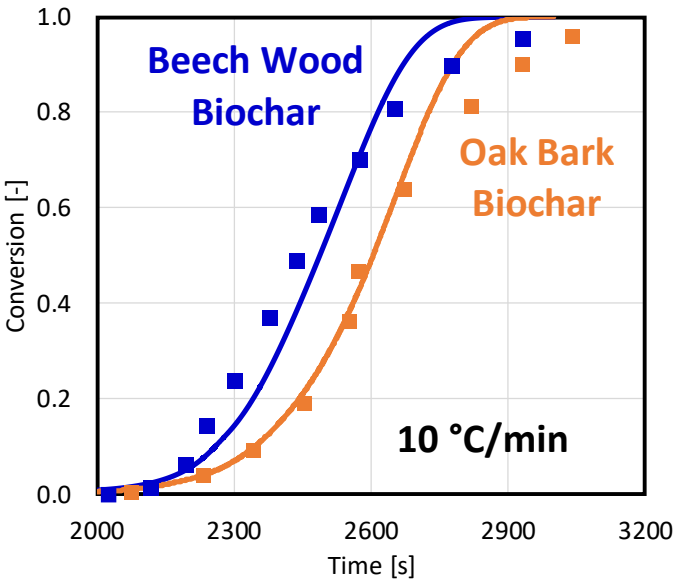

Figure 122 - Oxidation of beech wood and oat bark biochar under air atmosphere at 10 °C/min.

Both examples are satisfactory compared to the model predictions, mainly in early stage conversion. Oak bark biochar is less reactive, reaching 50% of conversion only some minutes after beech wood biochar. The first reason is the great difference in their composition. The high amounts of ashes in the bark sample (14 wt.%) resulted in a biochar with about 40 wt.% of ashes. The effect of such high amount of ashes can become determining in the rate of biochar conversion.

The ash problem is indeed complex, as it both acts as catalyst and depletes the reactivity. As a catalyst, the metals in ash aid the transfer of atmospheric oxygen to the carbons in the surface, reducing the activation energy of some reacting steps. On the other hand, ashes can melt during the formation of char, obstructing the pores in biochar, decreasing both the pore size aperture and the carbonaceous surface area [239]. Indeed the author [384] mentions that the massive presence of calcium and transparent solidified material over the porous surface and the reduced porosity, with respect to wood char, certainly contribute to diminishing the extension of the carbonaceous surface area. This, together with the limited penetration of oxygen in the solid, reduced the apparent reactivity of the material. As it is a physical problem, properly accounting for this effect requires a

completely different approach as the one from this work. However, in the present work, we accounted for this effect by assuming that half of the expected surface area was obstructed (by halving the value of S_{v0} and that this obstruction also reduced the microporosity (by halving the value of φ). This was a very rough assumption, but it was able to well describe this lower reactivity.

After this set of comparisons with experimental data, it is also useful to verify the sensitivity of the model to the input parameters, such as biochar characteristics and operating conditions. For this aim, we defined the biochar obtained from pyrolysis of maple wood [43] as the benchmark. The elemental composition of this sample is C/H/O = 0.551/0.067/0.382, which resulted in the characterization in terms of reference species:

CELL	XYHW	LIG-C	LIG-H	LIG-O	TGL	TANN	Moisture	Ash
0.251	0.205	0.052	0.348	0.002	0.089	0.001	0.035	0.017

After pyrolysis at 527 °C, the predicted biochar resulted with an elemental composition of C/H/O = 0.834/0.034/0.132. The molar fractions of the surface species in this biochar was H(S)=0.20, CHO(S)=0.6, CH3(S)=0.09, C2H3(S)=0.11. The plots in Figure 123 show the conversion of this biochar in air atmosphere by changing some of the operating conditions.

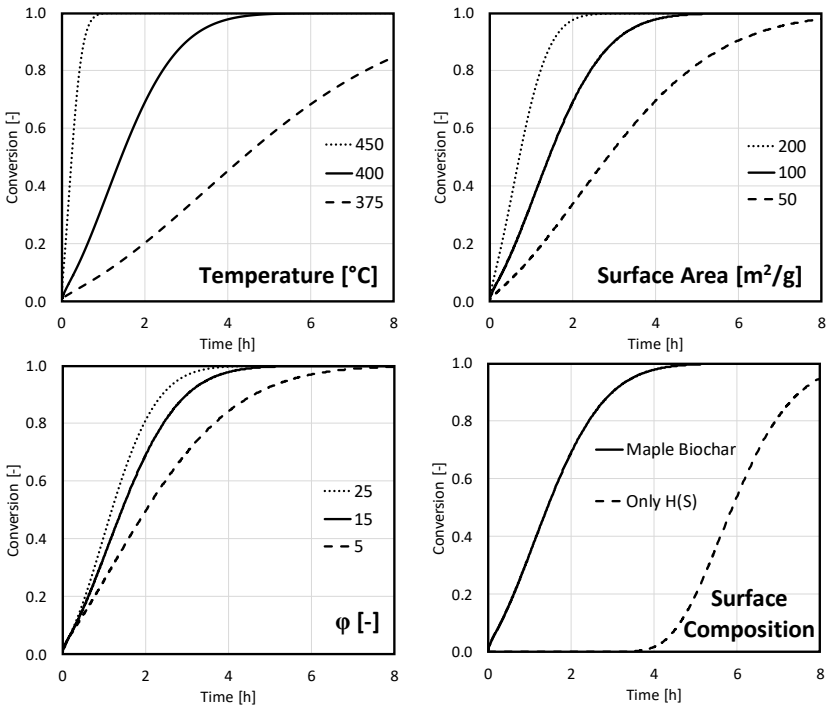

Figure 123 – Sensitivity analysis to the main parameters of the reacting system.

The benchmark is reported with a solid line. Each plot in Figure 123 reports the results after changing one parameter only. It is clear that all the model is sensitive to all these parameters, but in special the temperature. The main reason is that the kinetics increase exponentially with the increase of temperature. This confirms the importance of having an accurate kinetic mechanism and kinetic constants.

The surface parameters S_{v0} and φ are less sensitive than the temperature, but are extremely important even outside of the kinetically-controlled regime. The density of active sites has the same sensitivity as the surface area, because the product of these two aspects provides the total number of site per unit of mass/volume of biochar. For this reason, only one parameter was analyzed. Finally, the surface composition, which is the main novelty of this model, significantly affects the reactivity. The simulation guessing a surface only composed by hydrogen sites, is drastically less reactive than the regular biochar. This is totally in agreement with the fact that after releasing all the chemical moieties, char remains only a disordered arrangement of large aromatic clusters, with hydrogen atoms in the edges. A graphene layer and graphite, for example, are significantly less reactive than chars, mainly because of the lack of weakly-bonded groups.

3. Conclusions

The reliable prediction of yield and composition of biochar was validated in this chapter. The satisfactory agreement with the database collected, together with essential experimental evidence on the char physical-chemical structure allowed the estimation of biochar cluster structures at different pyrolysis temperatures. From these clusters, the density of active sites was estimated, obtaining values that are in line with the literature. The advantage of the estimations of this work is that this parameter can be estimated based on the carbon content of the sample.

Then, an innovative mechanism of reactions was proposed to describe the oxidation process of the biochar. This mechanism considers individually each chemical functionality bonded to the biochar. This allows to account not only for the elemental composition of the biochar, but also the reactivity of these different groups. This mechanism opens the path to the development of detailed kinetics of the heterogeneous gas-solid reaction. This approach is useful also to unify the kinetic mechanisms of both char from coal and biochars, creating a tool that can be more easily implemented in the design of reactors for co-combustion.

This is just a first attempt of proposing detailed kinetics for gas-solid reactions. Much information still need to be obtained, both through experiments and from theoretical calculations. Quantum chemistry investigations are becoming progressively more affordable in terms of computational cost. DFT calculations are essential to estimate with better precision the activation energies of essential reacting steps.

The effect of ashes, both in the chemical and physical aspects, must still be investigated and implemented in this model. Better methods for the estimation of both surface area and pore distributions are essential for enhancing the applicability and reliability of the predictions of this model.

REFERENCES

1. Gowlett, J.A., The discovery of fire by humans: a long and convoluted process. Phil. Trans. R. Soc. B, 2016. 371(1696): p. 20150164.

2. NAS, N.A.o.S., Materials and Man's Needs: Materials Science and Engineering. Vol. Volume I. The History, Scope, and Nature of Materials Science and Engineering. 1975, Washington, DC: The National Academies Press. 288.

3. Balch, J.K., et al., Global combustion: the connection between fossil fuel and biomass burning emissions (1997–2010). Phil. Trans. R. Soc. B, 2016. 371(1696): p. 20150177.

4. Smil, V., Prime movers of globalization: The history and impact of diesel engines and gas turbines. 2010: MIT press.

5. EIA, U.S.E.I.A., Petroleum and Other Liquids -Product Supplied. 2017.

6. Brennan, L. and P. Owende, Biofuels from microalgae—a review of technologies for production, processing, and extractions of biofuels and co-products. Renewable and sustainable energy reviews, 2010. 14(2): p. 557-577.

7. Chen, W.-H., J. Peng, and X.T. Bi, A state-of-the-art review of biomass torrefaction, densification and applications. Renewable and Sustainable Energy Reviews, 2015. 44: p. 847-866.

8. IEA, I.E.A., Key World Energy Statistics 2017. 2017, OECD Publishing.

9. EIA, U.S.E.I.A., International Energy Outlook 2017 - IEO2017. 2017.

10. WEC, W.E.C., World Energy Trilemma Index 2017: Monitoring the Sustainability of National Energy Systems. 2017: London, UK.

11. BP, B.P., BP Statistical Review of World Energy - June 2017. 2017.

12. Heidenreich, S. and P.U. Foscolo, New concepts in biomass gasification. Progress in energy and combustion science, 2015. 46: p. 72-95.

13. Bridgwater, A.V., Review of fast pyrolysis of biomass and product upgrading. Biomass and bioenergy, 2012. 38: p. 68-94.

14. Singh, A., P.S. Nigam, and J.D. Murphy, Renewable fuels from algae: an answer to debatable land based fuels. Bioresource technology, 2011. 102(1): p. 10-16.

15. Dragone, G., et al., Third generation biofuels from microalgae. Current research, technology and education topics in applied microbiology and microbial biotechnology, 2010. 2: p. 1355-1366.

16. Mohan, D., C.U. Pittman, and P.H. Steele, Pyrolysis of wood/biomass for bio-oil: a critical review. Energy & fuels, 2006. 20(3): p. 848-889.

17. French, R. and S. Czernik, Catalytic pyrolysis of biomass for biofuels production. Fuel Processing Technology, 2010. 91(1): p. 25-32.

18. Elliott, D.C., Historical developments in hydroprocessing bio-oils. Energy & Fuels, 2007. 21(3): p. 1792-1815.

19. Corma, A., et al., Processing biomass-derived oxygenates in the oil refinery: Catalytic cracking (FCC) reaction pathways and role of catalyst. Journal of Catalysis, 2007. 247(2): p. 307-327.

20. Schmidt, H.-P. and K. Wilson, 55 uses of biochar. Ithaka J., 2012. 1: p. 286-289.

21. Basu, P., Biomass gasification and pyrolysis: practical design and theory. 2010: Academic press.

22. McKendry, P., Energy production from biomass (part 3): gasification technologies. Bioresource technology, 2002. 83(1): p. 55-63.

23. Knoef, H. and J. Ahrenfeldt, Handbook biomass gasification. 2005: BTG biomass technology group The Netherlands.

24. Behrendt, F., et al., Direct liquefaction of biomass. Chemical engineering & technology, 2008. 31(5): p. 667-677.

25. Vaz Jr, S., Analytical techniques for the chemical analysis of plant biomass and biomass products. Analytical Methods, 2014. 6(20): p. 8094-8105.

26. Carrier, M., et al., Thermogravimetric analysis as a new method to determine the lignocellulosic composition of biomass. Biomass and Bioenergy, 2011. 35(1): p. 298-307.

27. Choi, Y.S., et al., Manipulation of chemical species in bio-oil using in situ catalytic fast pyrolysis in both a bench-scale fluidized bed pyrolyzer and micropyrolyzer. Biomass and Bioenergy, 2015. 81: p. 256-264.

28. Proano-Aviles, J., et al., Heat and Mass Transfer Effects in a Furnace-Based Micropyrolyzer. Energy Technology, 2017. 5(1): p. 189-195.

29. Ronsse, F., et al., Optimization of platinum filament micropyrolyzer for studying primary decomposition in cellulose pyrolysis. Journal of analytical and applied pyrolysis, 2012. 95: p. 247-256.

30. Kousoku, A., K. Norinaga, and K. Miura, Extended detailed chemical kinetic model for benzene pyrolysis with new reaction pathways including oligomer formation. Industrial & Engineering Chemistry Research, 2014. 53(19): p. 7956-7964.

31. Norinaga, K., et al., Detailed chemical kinetic modelling of vapour-phase cracking of multi-component molecular mixtures derived from the fast pyrolysis of cellulose. Fuel, 2013. 103: p. 141-150.

32. Qi, S.-C., et al., Theoretical Study on Hydrogenolytic Cleavage of Intermonomer Linkages in Lignin. The Journal of Physical Chemistry A, 2017. 121(15): p. 2868-2877.

33. Yang, H.-M., et al., Detailed Chemical Kinetic Modeling of Vapor-Phase Reactions of Volatiles Derived from Fast Pyrolysis of Lignin. Industrial & Engineering Chemistry Research, 2015. 54(27): p. 6855-6864.

34. Yang, H., et al., Experimental investigation of thermal decomposition of dihydroxybenzene isomers: Catechol, hydroquinone, and resorcinol. Journal of analytical and applied pyrolysis, 2016. 120: p. 321-329.

35. Thangalazhy-Gopakumar, S., et al., Influence of pyrolysis operating conditions on bio-oil components: a microscale study in a pyroprobe. Energy & Fuels, 2011. 25(3): p. 1191-1199.

36. Hankalin, V., T. Ahonen, and R. Raiko, On thermal properties of a pyrolysing wood particle. Finnish-Swedish Flame Days, 2009. 16.

37. Dauenhauer, P.J., et al., Reactive boiling of cellulose for integrated catalysis through an intermediate liquid. Green Chemistry, 2009. 11(10): p. 1555-1561.

38. Scheer, A.M., et al., Radical chemistry in the thermal decomposition of anisole and deuterated anisoles: an investigation of aromatic growth. The Journal of Physical Chemistry A, 2010. 114(34): p. 9043-9056.

39. Scheer, A.M., et al., Unimolecular thermal decomposition of phenol and d5-phenol: Direct observation of cyclopentadiene formation via cyclohexadienone. The Journal of chemical physics, 2012. 136(4): p. 044309.

40. Scheer, A.M., et al., Thermal decomposition mechanisms of the methoxyphenols: formation of phenol, cyclopentadienone, vinylacetylene, and acetylene. The Journal of Physical Chemistry A, 2011. 115(46): p. 13381-13389.

41. Buckingham, G.T., et al., The thermal decomposition of the benzyl radical in a heated micro-reactor. I. Experimental findings. The Journal of Chemical Physics, 2015. 142(4): p. 044307.

42. Chen, P., Unimolecular and bimolecular reaction dynamics. 1994, John Wiley & Sons: New York.

43. Cao, X., et al., Characterization of wood chars produced at different temperatures using advanced solid-state 13C NMR spectroscopic techniques. Energy & Fuels, 2012. 26(9): p. 5983-5991.

44. Brewer, C.E., et al., Characterization of biochar from fast pyrolysis and gasification systems. Environmental Progress & Sustainable Energy, 2009. 28(3): p. 386-396.

45. Le Brech, Y., et al., Characterization of biomass char formation investigated by advanced solid state NMR. Carbon, 2016. 108: p. 165-177.

46. Prakash, N. and T. Karunanithi, Kinetic modeling in biomass pyrolysis–a review. Journal of Applied Sciences Research, 2008. 4(12): p. 1627-1636.

47. Anca-Couce, A., Reaction mechanisms and multi-scale modelling of lignocellulosic biomass pyrolysis. Progress in Energy and Combustion Science, 2016. 53: p. 41-79.

48. Miyanami, K., et al., A mathematical model for pyrolysis of a solid particle—effects of the heat of reaction. The Canadian Journal of Chemical Engineering, 1977. 55(3): p. 317-325.

49. Fan, L., et al., A mathematical model for pyrolysis of a solid particle: Effects of the lewis number. The Canadian Journal of Chemical Engineering, 1977. 55(1): p. 47-53.

50. Wichman, I.S. and A. Atreya, A simplified model for the pyrolysis of charring materials. Combustion and Flame, 1987. 68(3): p. 231-247.

51. Kung, H.-C., A mathematical model of wood pyrolysis. Combustion and flame, 1972. 18(2): p. 185-195.

52. Kansa, E.J., H.E. Perlee, and R.F. Chaiken, Mathematical model of wood pyrolysis including internal forced convection. Combustion and flame, 1977. 29: p. 311-324.

53. Kanury, A.M., Thermal decomposition kinetics of wood pyrolysis. Combustion and Flame, 1972. 18(1): p. 75-83.

54. Lee, C.K., R.F. Chaiken, and J.M. Singer. Charring pyrolysis of wood in fires by laser simulation. in Symposium (International) on Combustion. 1977. Elsevier.

55. Thurner, F. and U. Mann, Kinetic investigation of wood pyrolysis. Industrial & Engineering Chemistry Process Design and Development, 1981. 20(3): p. 482-488.

56. Alves, S. and J. Figueiredo, A model for pyrolysis of wet wood. Chemical Engineering Science, 1989. 44(12): p. 2861-2869.

57. Grønli, M.G., A theoretical and experimental study of the thermal degradation of biomass. 1996.

58. Larfeldt, J., B. Leckner, and M.C. Melaaen, Modelling and measurements of heat transfer in charcoal from pyrolysis of large wood particles. Biomass and Bioenergy, 2000. 18(6): p. 507-514.

59. Svenson, J., J. Pettersson, and K. Davidsson, Fast pyrolysis of the main components of birch wood. Combustion science and technology, 2004. 176(5-6): p. 977-990.

60. Shafizadeh, F. and P.P. Chin, Thermal deterioration of wood. 1977, ACS Publications.

61. Chan, W.-C.R., M. Kelbon, and B.B. Krieger, Modelling and experimental verification of physical and chemical processes during pyrolysis of a large biomass particle. Fuel, 1985. 64(11): p. 1505-1513.

62. Font, R., et al., Kinetics of the pyrolysis of almond shells and almond shells impregnated with cobalt dichloride in a fluidized bed reactor and in a pyroprobe 100. Industrial & engineering chemistry research, 1990. 29(9): p. 1846-1855.

63. Di Blasi, C. and G. Russo, Modeling of transport phenomena and kinetics of biomass pyrolysis, in Advances in thermochemical biomass conversion. 1993, Springer. p. 906-921.

64. Liden, A., F. Berruti, and D. Scott, A kinetic model for the production of liquids from the flash pyrolysis of biomass. Chemical Engineering Communications, 1988. 65(1): p. 207-221.

65. Boroson, M.L., et al., Product yields and kinetics from the vapor phase cracking of wood pyrolysis tars. AIChE Journal, 1989. 35(1): p. 120-128.

66. Janse, A., R. Westerhout, and W. Prins, Modelling of flash pyrolysis of a single wood particle. Chemical engineering and processing: process intensification, 2000. 39(3): p. 239-252.

67. Mousques, P., J. Dirion, and D. Grouset, Modeling of solid particles pyrolysis. Journal of Analytical and Applied Pyrolysis, 2001. 58: p. 733-745.

68. Broido, A., M. Evett, and C.C. Hodges, Yield of 1, 6-anhydro-3, 4-dideoxy-β-d-glycero-hex-3-enopyranos-2-ulose (levoglucosenone) on the acid-catalyzed pyrolysis of cellulose and 1, 6-anhydro-β-d-glucopyranose (levoglucosan). Carbohydrate Research, 1975. 44(2): p. 267-274.

69. Bradbury, A.G., Y. Sakai, and F. Shafizadeh, A kinetic model for pyrolysis of cellulose. Journal of Applied Polymer Science, 1979. 23(11): p. 3271-3280.

70. Di Blasi, C., Influences of physical properties on biomass devolatilization characteristics. Fuel, 1997. 76(10): p. 957-964.

71. Koufopanos, C., A. Lucchesi, and G. Maschio, Kinetic modelling of the pyrolysis of biomass and biomass components. The Canadian Journal of Chemical Engineering, 1989. 67(1): p. 75-84.

72. Koufopanos, C., et al., Modelling of the pyrolysis of biomass particles. Studies on kinetics, thermal and heat transfer effects. The Canadian journal of chemical engineering, 1991. 69(4): p. 907-915.

73. Jalan, R. and V. Srivastava, Studies on pyrolysis of a single biomass cylindrical pellet—kinetic and heat transfer effects. Energy Conversion and Management, 1999. 40(5): p. 467-494.

74. Babu, B. and A. Chaurasia. Modeling & simulation of pyrolysis: effect of convective heat transfer & orders of reactions. in Proceedings of International Symposium and 55th Annual Session of IIChE (CHEMCON-2002), OU, Hyderabad, India. 2002. Citeseer.

75. Babu, B. and A. Chaurasia, Dominant design variables in pyrolysis of biomass particles of different geometries in thermally thick regime. Chemical Engineering Science, 2004. 59(3): p. 611-622.

76. Babu, B. and A. Chaurasia, Pyrolysis of biomass: improved models for simultaneous kinetics and transport of heat, mass and momentum. Energy conversion and Management, 2004. 45(9-10): p. 1297-1327.

77. Chaurasia, A. and B. Kulkarni, Most sensitive parameters in pyrolysis of shrinking biomass particle. Energy conversion and management, 2007. 48(3): p. 836-849.

78. Varhegyi, G., E. Jakab, and M.J. Antal Jr, Is the Broido-Shafizadeh model for cellulose pyrolysis true? Energy & Fuels, 1994. 8(6): p. 1345-1352.

79. Boutin, O., M. Ferrer, and J. Lédé, Flash pyrolysis of cellulose pellets submitted to a concentrated radiation: experiments and modelling. Chemical Engineering Science, 2002. 57(1): p. 15-25.

80. Branca, C. and C. Di Blasi, Kinetics of the isothermal degradation of wood in the temperature range 528–708 K. Journal of Analytical and applied Pyrolysis, 2003. 67(2): p. 207-219.

81. Branca, C., A. Albano, and C. Di Blasi, Critical evaluation of global mechanisms of wood devolatilization. Thermochimica Acta, 2005. 429(2): p. 133-141.

82. Ranzi, E., et al., Chemical kinetics of biomass pyrolysis. Energy & Fuels, 2008. 22(6): p. 4292-4300.

83. Ranzi, E., P.E.A. Debiagi, and A. Frassoldati, Mathematical modeling of fast biomass pyrolysis and bio-oil formation. Note I: Kinetic mechanism of biomass pyrolysis. ACS Sustainable Chemistry & Engineering, 2017. 5(4): p. 2867-2881.

84. NREL, National Renewable Energy Laboratory - Biomass Feedstock Composition and Property Database. 2015.

85. Parikh, J., S. Channiwala, and G. Ghosal, A correlation for calculating elemental composition from proximate analysis of biomass materials. Fuel, 2007. 86(12): p. 1710-1719.

86. Aiken, A.C., P.F. DeCarlo, and J.L. Jimenez, Elemental analysis of organic species with electron ionization high-resolution mass spectrometry. Analytical Chemistry, 2007. 79(21): p. 8350-8358.

87. Xu, F., et al., Qualitative and quantitative analysis of lignocellulosic biomass using infrared techniques: a mini-review. Applied Energy, 2013. 104: p. 801-809.

88. Lupoi, J.S., et al., Assessment of lignocellulosic biomass using analytical spectroscopy: an evolution to high-throughput techniques. BioEnergy Research, 2014. 7(1): p. 1-23.

89. Demirbas, A., Combustion characteristics of different biomass fuels. Progress in energy and combustion science, 2004. 30(2): p. 219-230.

90. Williams, A., et al., Pollutants from the combustion of solid biomass fuels. Progress in Energy and Combustion Science, 2012. 38(2): p. 113-137.

91. Templeton, D.W., et al., Separation and quantification of microalgal carbohydrates. Journal of Chromatography A, 2012. 1270: p. 225-234.

92. Yang, L., et al., Effect of different isolation methods on structure and properties of lignin from valonea of Quercus variabilis. International journal of biological macromolecules, 2016. 85: p. 417-424.

93. Bi, Z. and B.B. He, Characterization of microalgae for the purpose of biofuel production. Trans. ASABE, 2013. 56(4): p. 1529-1539.

94. Batista, A.P., et al., Comparison of microalgal biomass profiles as novel functional ingredient for food products. Algal Research, 2013. 2(2): p. 164-173.

95. Tibbetts, S.M., J.E. Milley, and S.P. Lall, Chemical composition and nutritional properties of freshwater and marine microalgal biomass cultured in photobioreactors. Journal of Applied Phycology, 2015. 27(3): p. 1109-1119.

96. Lane, D.J., et al., Combustion behavior of algal biomass: carbon release, nitrogen release, and char reactivity. Energy & Fuels, 2013. 28(1): p. 41-51.

97. Grønli, M.G., G. Varhegyi, and C. Di Blasi, Thermogravimetric analysis and devolatilization kinetics of wood. Industrial & Engineering Chemistry Research, 2002. 41(17): p. 4201-4208.

98. Zhao, X., L. Zhang, and D. Liu, Biomass recalcitrance. Part I: the chemical compositions and physical structures affecting the enzymatic hydrolysis of lignocellulose. Biofuels, Bioproducts and Biorefining, 2012. 6(4): p. 465-482.

99. Bidlack, J. Molecular structure and component integration of secondary cell walls in plants. in Proceedings of the Oklahoma Academy of Science. 1992.

100. Mettler, M.S., D.G. Vlachos, and P.J. Dauenhauer, Top ten fundamental challenges of biomass pyrolysis for biofuels. Energy & Environmental Science, 2012. 5(7): p. 7797-7809.

101. O'sullivan, A.C., Cellulose: the structure slowly unravels. Cellulose, 1997. 4(3): p. 173-207.

102. Himmel, M.E., et al., Biomass recalcitrance: engineering plants and enzymes for biofuels production. science, 2007. 315(5813): p. 804-807.

103. Wang, Z., et al., Effect of cellulose crystallinity on solid/liquid phase reactions responsible for the formation of carbonaceous residues during pyrolysis. Industrial & Engineering Chemistry Research, 2014. 53(8): p. 2940-2955.

104. Mukarakate, C., et al., Influence of crystal allomorph and crystallinity on the products and behavior of cellulose during fast pyrolysis. ACS Sustainable Chemistry & Engineering, 2016. 4(9): p. 4662-4674.

105. Ebringerová, A. Structural diversity and application potential of hemicelluloses. in Macromolecular symposia. 2005. Wiley Online Library.

106. Dutta, S., et al., Advances in conversion of hemicellulosic biomass to furfural and upgrading to biofuels. Catalysis Science & Technology, 2012. 2(10): p. 2025-2036.

107. Zhou, X., et al., A critical review on hemicellulose pyrolysis. Energy Technology, 2017. 5(1): p. 52-79.

108. Vanholme, R., et al., Lignin biosynthesis and structure. Plant physiology, 2010. 153(3): p. 895-905.

109. Faravelli, T., et al., Detailed kinetic modeling of the thermal degradation of lignins. Biomass and bioenergy, 2010. 34(3): p. 290-301.

110. Garcia-Perez, M., et al., Vacuum pyrolysis of softwood and hardwood biomass: comparison between product yields and bio-oil properties. Journal of Analytical and Applied Pyrolysis, 2007. 78(1): p. 104-116.

111. Hillis, W.E., Wood extractives and their significance to the pulp and paper industries. 2014: Academic press.

112. Selleby, L., Birch wood constituents. Part 2. The ether extract. Svensk Papperstidning, 1960. 63(4): p. 81-5.

113. Ververidis, F., et al., Biotechnology of flavonoids and other phenylpropanoid-derived natural products. Part I: Chemical diversity, impacts on plant biology and human health. Biotechnology journal, 2007. 2(10): p. 1214-1234.

114. Chen, P., et al., Review of biological and engineering aspects of algae to fuels approach. International Journal of Agricultural and Biological Engineering, 2010. 2(4): p. 1-30.

115. Alam, F., et al., Biofuel from algae-Is it a viable alternative? Procedia Engineering, 2012. 49: p. 221-227.

116. Martínez-Fernández, E., H. Acosta-Salmón, and P.C. Southgate, The nutritional value of seven species of tropical microalgae for black-lip pearl oyster (Pinctada margaritifera, L.) larvae. Aquaculture, 2006. 257(1): p. 491-503.

117. Ross, A., et al., Classification of macroalgae as fuel and its thermochemical behaviour. Bioresource technology, 2008. 99(14): p. 6494-6504.

118. Tibbetts, S.M., et al., Biochemical characterization of microalgal biomass from freshwater species isolated in Alberta, Canada for animal feed applications. Algal Research, 2015. 11: p. 435-447.

119. Ojha, D.K., D. Viju, and R. Vinu, Fast Pyrolysis Kinetics of Alkali Lignin: Evaluation of Apparent Rate Parameters and Product Time Evolution. Bioresource Technology, 2017.

120. Anand, V., V. Sunjeev, and R. Vinu, Catalytic fast pyrolysis of Arthrospira platensis (spirulina) algae using zeolites. Journal of Analytical and Applied Pyrolysis, 2016. 118: p. 298-307.

121. Lorenzetti, C., et al., A comparative study on the catalytic effect of H-ZSM5 on upgrading of pyrolysis vapors derived from lignocellulosic and proteinaceous biomass. Fuel, 2016. 166: p. 446-452.

122. Lourenço, S.O., et al., Amino acid composition, protein content and calculation of nitrogen-to-protein conversion factors for 19 tropical seaweeds. Phycological Research, 2002. 50(3): p. 233-241.

123. Lourenço, S.O., et al., Distribution of intracellular nitrogen in marine microalgae: calculation of new nitrogen-to-protein conversion factors. European Journal of Phycology, 2004. 39(1): p. 17-32.

124. Wong, K. and P.C. Cheung, Nutritional evaluation of some subtropical red and green seaweeds: Part I—proximate composition, amino acid profiles and some physico-chemical properties. Food chemistry, 2000. 71(4): p. 475-482.

125. Trinchera, M., Biomasse di terza generazione : Caratterizzazione e pirolisi delle alghe. 2017, Politecnico di Milano. p. 105.

126. Boyd, C., Amino acid composition of freshwater algae. Archiv fur Hydrobiologie, 1973.

127. Fleurence, J., Seaweed proteins: biochemical, nutritional aspects and potential uses. Trends in food science & technology, 1999. 10(1): p. 25-28.

128. NCBI Resouce Coordinators, Database Resources of the National Center for Biotechnology Information. Nucleic Acids Research, 2016. 44(Database issue D7–D19).

129. Guaratini, T., et al., Comparison of diode array and electrochemical detection in the C30 reverse phase HPLC analysis of algae carotenoids. Journal of the Brazilian Chemical Society, 2009. 20(9): p. 1609-1616.

130. Brown, M.R. and S. Jeffrey, Biochemical composition of microalgae from the green algal classes Chlorophyceae and Prasinophyceae. 1. Amino acids, sugars and pigments. Journal of experimental marine biology and ecology, 1992. 161(1): p. 91-113.

131. Dawczynski, C., R. Schubert, and G. Jahreis, Amino acids, fatty acids, and dietary fibre in edible seaweed products. Food Chemistry, 2007. 103(3): p. 891-899.

132. Black, W., E. Dewar, and F. Woodward, Manufacture of algal chemicals. II. Laboratory-scale isolation of mannitol from brown marine algae. Journal of Applied Chemistry, 1951. 1(9): p. 414-424.

133. Chen, C.-Y., et al., Microalgae-based carbohydrates for biofuel production. Biochemical Engineering Journal, 2013. 78: p. 1-10.

134. Dunstan, G.A., M.R. Brown, and J.K. Volkman, Cryptophyceae and Rhodophyceae; chemotaxonomy, phylogeny, and application. Phytochemistry, 2005. 66(21): p. 2557-2570.

135. Zhukova, N.V. and N.A. Aizdaicher, Fatty acid composition of 15 species of marine microalgae. Phytochemistry, 1995. 39(2): p. 351-356.

136. Pratoomyot, J., P. Srivilas, and T. Noiraksar, Fatty acids composition of 10 microalgal species. Songklanakarin J Sci Technol, 2005. 27(6): p. 1179-1187.

137. Chakraborty, S. and S. Santra, Biochemical composition of eight benthic algae collected from Sunderban. Indian Journal of Geo-Marine Sciences, 2008. 37(3): p. 329-332.

138. Gressler, V., et al., Lipid, fatty acid, protein, amino acid and ash contents in four Brazilian red algae species. Food Chemistry, 2010. 120(2): p. 585-590.

139. Kumari, P., et al., Fatty acid profiling of tropical marine macroalgae: an analysis from chemotaxonomic and nutritional perspectives. Phytochemistry, 2013. 86: p. 44-56.

140. Debiagi, P.E.A., et al., Extractives extend the applicability of multistep kinetic scheme of biomass pyrolysis. Energy & Fuels, 2015. 29(10): p. 6544-6555.

141. Anastasakis, K., A. Ross, and J. Jones, Pyrolysis behaviour of the main carbohydrates of brown macro-algae. Fuel, 2011. 90(2): p. 598-607.

142. Matsushita, I., et al., Effect of atmosphere on the pyrolysis process of basic calcium carbonate. Journal of the Ceramic Society of Japan, 1995. 103(1195): p. 240-244.

143. Hurt, R.H. Structure, properties, and reactivity of solid fuels. in Symposium (International) on Combustion. 1998. Elsevier.

144. BIOBIB, et al., BIOBIB - a Database for Biofuels. 1996.

145. Demirbaş, A., Fuel characteristics of olive husk and walnut, hazelnut, sunflower, and almond shells. Energy Sources, 2002. 24(3): p. 215-221.

146. Buzzi-Ferraris, G. and F. Manenti, Outlier detection in large data sets. Computers & chemical engineering, 2011. 35(2): p. 388-390.

147. Buzzi-Ferraris, G. and F. Manenti, BzzMath: Library overview and recent advances in numerical methods. Computer Aided Chemical Engineering, 2012. 30(2): p. 1312-1316.

148. Sheng, C. and J. Azevedo, Modeling biomass devolatilization using the chemical percolation devolatilization model for the main components. Proceedings of the Combustion Institute, 2002. 29(1): p. 407-414.

149. Fletcher, T.H., et al., A chemical percolation model for devolatilization: summary. Brigham Young University, 1992.

150. Vizzini, G., et al., Prediction Of Rapid Biomass Devolatilization Yields With An Upgraded Version Of The Bio-CPD Model. Combustion Institute Italian section, 2008.

151. Buzzi-Ferraris, G. and F. Manenti, A combination of parallel computing and object-oriented programming to improve optimizer robustness and efficiency. Computer Aided Chemical Engineering, 2010. 28: p. 337-342.

152. Laurens, L.M., et al., Algal biomass constituent analysis: method uncertainties and investigation of the underlying measuring chemistries. Analytical chemistry, 2012. 84(4): p. 1879-1887.

153. Kilzer, F.J. and A. Broido, Speculations on the nature of cellulose pyrolysis. Pyrodynamics. 2: 151-163, 1965. 2: p. 151-163.

154. Shafizadeh, F. and Y. Fu, Pyrolysis of cellulose. Carbohydrate Research, 1973. 29(1): p. 113-122.

155. Broido, A. and M.A. Nelson, Char yield on pyrolysis of cellulose. Combustion and Flame, 1975. 24: p. 263-268.

156. Antal, M.J.J. and G. Varhegyi, Cellulose pyrolysis kinetics: the current state of knowledge. Industrial & Engineering Chemistry Research, 1995. 34(3): p. 703-717.

157. Lédé, J., Cellulose pyrolysis kinetics: An historical review on the existence and role of intermediate active cellulose. Journal of Analytical and Applied Pyrolysis, 2012. 94: p. 17-32.

158. Vinu, R. and L.J. Broadbelt, A mechanistic model of fast pyrolysis of glucose-based carbohydrates to predict bio-oil composition. Energy & Environmental Science, 2012. 5(12): p. 9808-9826.

159. Seshadri, V. and P.R. Westmoreland, Concerted reactions and mechanism of glucose pyrolysis and implications for cellulose kinetics. The Journal of Physical Chemistry A, 2012. 116(49): p. 11997-12013.

160. Mayes, H.B. and L.J. Broadbelt, Unraveling the reactions that unravel cellulose. The Journal of Physical Chemistry A, 2012. 116(26): p. 7098-7106.

161. Mayes, H.B., et al., The Alpha–Bet (a) of Glucose Pyrolysis: Computational and Experimental Investigations of 5-Hydroxymethylfurfural and Levoglucosan Formation Reveal Implications for Cellulose Pyrolysis. ACS Sustainable Chemistry & Engineering, 2014. 2(6): p. 1461-1473.

162. Zhou, X., et al., Experimental and mechanistic modeling of fast pyrolysis of neat glucose-based carbohydrates. 1. Experiments and development of a detailed mechanistic model. Industrial & Engineering Chemistry Research, 2014. 53(34): p. 13274-13289.

163. Zhou, X., et al., Experimental and mechanistic modeling of fast pyrolysis of neat glucose-based carbohydrates. 2. Validation and evaluation of the mechanistic model. Industrial & Engineering Chemistry Research, 2014. 53(34): p. 13290-13301.

164. Seshadri, V. and P.R. Westmoreland, Roles of hydroxyls in the noncatalytic and catalyzed formation of levoglucosan from glucose. Catalysis Today, 2016. 269: p. 110-121.

165. Lin, F., et al., Relationships between biomass composition and liquid products formed via pyrolysis. Frontiers in Energy Research, 2015. 3: p. 45.

166. Shen, D. and S. Gu, The mechanism for thermal decomposition of cellulose and its main products. Bioresource Technology, 2009. 100(24): p. 6496-6504.

167. Paulsen, A.D., M.S. Mettler, and P.J. Dauenhauer, The role of sample dimension and temperature in cellulose pyrolysis. Energy & Fuels, 2013. 27(4): p. 2126-2134.

168. Corbetta, M., et al., Pyrolysis of centimeter-scale woody biomass particles: Kinetic modeling and experimental validation. Energy & Fuels, 2014. 28(6): p. 3884-3898.

169. Milosavljevic, I., V. Oja, and E.M. Suuberg, Thermal effects in cellulose pyrolysis: relationship to char formation processes. Industrial & Engineering Chemistry Research, 1996. 35(3): p. 653-662.

170. Antal, M.J., G. Varhegyi, and E. Jakab, Cellulose pyrolysis kinetics: revisited. Industrial & engineering chemistry research, 1998. 37(4): p. 1267-1275.

171. Milosavljevic, I. and E.M. Suuberg, Cellulose thermal decomposition kinetics: global mass loss kinetics. Industrial & Engineering Chemistry Research, 1995. 34(4): p. 1081-1091.

172. Shen, D., et al., An overview on fast pyrolysis of the main constituents in lignocellulosic biomass to valued-added chemicals: Structures, pathways and interactions. Renewable and Sustainable Energy Reviews, 2015. 51: p. 761-774.

173. Zhou, S., et al., Slow and fast pyrolysis of Douglas-fir lignin: Importance of liquid-intermediate formation on the distribution of products. Biomass and Bioenergy, 2014. 66: p. 398-409.

174. Teixeira, A.R., et al., Spontaneous aerosol ejection: origin of inorganic particles in biomass pyrolysis. ChemSusChem, 2016. 9(11): p. 1322-1328.

175. Lédé, J., et al., The nature and properties of intermediate and unvaporized biomass pyrolysis materials, in Developments in thermochemical biomass conversion. 1997, Springer. p. 27-42.

176. Moreira, L., An overview of mannan structure and mannan-degrading enzyme systems. Applied microbiology and biotechnology, 2008. 79(2): p. 165.

177. Branca, C., et al., Products and kinetics of glucomannan pyrolysis. Industrial & Engineering Chemistry Research, 2013. 52(14): p. 5030-5039.

178. Prins, M.J., K. Ptasinski, and F.J. Janssen, Torrefaction of wood: Part 1. Weight loss kinetics. Journal of analytical and applied pyrolysis, 2006. 77(1): p. 28-34.

179. Prins, M.J., K. Ptasinski, and F. Janssen, Torrefaction of wood Part 2. Analysis of products J. Anal. Appl. Pyrolysis, 2006. 77: p. 35-40.

180. Anca-Couce, A. and I. Obernberger, Application of a detailed biomass pyrolysis kinetic scheme to hardwood and softwood torrefaction. Fuel, 2016. 167: p. 158-167.

181. Fisher, T., et al., Pyrolysis behavior and kinetics of biomass derived materials. Journal of analytical and applied pyrolysis, 2002. 62(2): p. 331-349.

182. Shen, D., S. Gu, and A.V. Bridgwater, Study on the pyrolytic behaviour of xylan-based hemicellulose using TG–FTIR and Py–GC–FTIR. Journal of analytical and applied pyrolysis, 2010. 87(2): p. 199-206.

183. Kong, W., et al., A promising strategy for preparation of cationic xylan by environment-friendly semi-dry oven process. Fibers and Polymers, 2014. 15(5): p. 943-949.

184. Li, S., S. Chen, and J. Mu. Influence of UF resin on pyrolysis characteristics of biomass components: A thermogravimetric study. in Biobase Material Science and Engineering (BMSE), 2012 International Conference on. 2012. IEEE.

185. Moriana, R., et al., Thermal degradation behavior and kinetic analysis of spruce glucomannan and its methylated derivatives. Carbohydrate polymers, 2014. 106: p. 60-70.

186. Tanodekaew, S., S. Channasanon, and P. Uppanan, Xylan/polyvinyl alcohol blend and its performance as hydrogel. Journal of applied polymer science, 2006. 100(3): p. 1914-1918.

187. Williams, P.T. and S. Besler, The influence of temperature and heating rate on the slow pyrolysis of biomass. Renewable energy, 1996. 7(3): p. 233-250.

188. Yang, H., et al., Thermogravimetric analysis− Fourier transform infrared analysis of palm oil waste pyrolysis. Energy & fuels, 2004. 18(6): p. 1814-1821.

189. Yang, H., et al., Characteristics of hemicellulose, cellulose and lignin pyrolysis. Fuel, 2007. 86(12-13): p. 1781-1788.

190. Yu, H., et al., Preparation and characterization of a quaternary ammonium derivative of konjac glucomannan. Carbohydrate polymers, 2007. 69(1): p. 29-40.

191. Zhang, X.-Q., et al., Dual-component system dimethyl sulfoxide/LiCl as a solvent and catalyst for homogeneous ring-opening grafted polymerization of ε-caprolactone onto xylan. Journal of agricultural and food chemistry, 2014. 62(3): p. 682-690.

192. Zhou, H., et al., The pyrolysis simulation of five biomass species by hemi-cellulose, cellulose and lignin based on thermogravimetric curves. Thermochimica acta, 2013. 566: p. 36-43.

193. Chen, W.-H. and P.-C. Kuo, Torrefaction and co-torrefaction characterization of hemicellulose, cellulose and lignin as well as torrefaction of some basic constituents in biomass. Energy, 2011. 36(2): p. 803-811.

194. Chen, W.-H. and P.-C. Kuo, Isothermal torrefaction kinetics of hemicellulose, cellulose, lignin and xylan using thermogravimetric analysis. Energy, 2011. 36(11): p. 6451-6460.

195. Klein, M. and P. Virk, Modeling of lignin thermolysis. Energy & Fuels, 2008. 22(4): p. 2175-2182.

196. Serio, M.A., et al., Measurement and modeling of lignin pyrolysis. Biomass and Bioenergy, 1994. 7(1-6): p. 107-124.

197. Hou, Z., et al., Approaches and Software Tools for Modeling Lignin Pyrolysis†. Energy & Fuels, 2009. 24(1): p. 58-67.

198. Yanez, A.J., et al., A stochastic method to generate libraries of structural representations of lignin. Energy & Fuels, 2016. 30(7): p. 5835-5845.

199. Jakab, E., O. Faix, and F. Till, Thermal decomposition of milled wood lignins studied by thermogravimetry/mass spectrometry. Journal of Analytical and Applied Pyrolysis, 1997. 40: p. 171-186.

200. Jakab, E., et al., Thermogravimetry/mass spectrometry study of six lignins within the scope of an international round robin test. Journal of Analytical and Applied Pyrolysis, 1995. 35(2): p. 167-179.

201. Moore, A.M., The Effect of Biomass Characteristics on Bio-oil Produced via Fast Pyrolysis. 2015.

202. Luo, C., et al., Synthesis, characterization, and thermal behaviors of tannin stearates prepared from quebracho and pine bark extracts. Journal of applied polymer science, 2010. 117(1): p. 352-360.

203. Saad, H., et al., Characterization of Tunisian Aleppo pine tannins for a potential use in wood adhesive formulation. Industrial Crops and Products, 2014. 61: p. 517-525.

204. Mahmoud, S.B., et al., Characterization of sumac (Rhus tripartitum) root barks tannin for a potential use in wood adhesives formulation. Wood Science and Technology, 2015. 49(1): p. 205-221.

205. Arbenz, A. and L. Avérous, Oxyalkylation of gambier tannin—Synthesis and characterization of ensuing biobased polyols. Industrial Crops and Products, 2015. 67: p. 295-304.

206. Pantoja-Castro, M.A. and H. González-Rodríguez, Study by infrared spectroscopy and thermogravimetric analysis of tannins and tannic acid. Revista latinoamericana de química, 2011. 39(3): p. 107-112.

207. Gaugler, M. and W.J. Grigsby, Thermal degradation of condensed tannins from radiata pine bark. Journal of wood chemistry and technology, 2009. 29(4): p. 305-321.

208. Na, J.-G., et al., Rapid estimation of triacylglycerol content of Chlorella sp. by thermogravimetric analysis. Biotechnology letters, 2011. 33(5): p. 957-960.

209. Dantas, M., et al., Thermal and kinetic study of corn biodiesel obtained by the methanol and ethanol routes. Journal of Thermal Analysis and Calorimetry, 2007. 87(3): p. 835-839.

210. Moldoveanu, S.C., Pyrolysis of organic molecules: applications to health and environmental issues. 2009: Elsevier.

211. Meier, H., et al., A kinetic model for thermal cracking of waste cooking oil based on chemical lumps. Fuel, 2015. 144: p. 50-59.

212. Saggese, C., et al., A lumped approach to the kinetic modeling of pyrolysis and combustion of biodiesel fuels. Proceedings of the Combustion Institute, 2013. 34(1): p. 427-434.

213. Ranzi, E., et al., Comprehensive and detailed kinetic model of a traveling grate combustor of biomass. Energy & Fuels, 2011. 25(9): p. 4195-4205.

214. Ranzi, E., et al., Kinetic modeling of the thermal degradation and combustion of biomass. Chemical Engineering Science, 2014. 110: p. 2-12.

215. Stark, A.K., et al., Prediction and validation of major gas and tar species from a reactor network model of air-blown fluidized bed biomass gasification. Energy & Fuels, 2015. 29(4): p. 2437-2452.

216. Pasangulapati, V., Devolatilization characteristics of cellulose, hemicellulose, lignin and the selected biomass during thermochemical gasification: experiment and modeling studies. 2012, Oklahoma State University.

217. Anca-Couce, A., et al., Kinetic scheme of biomass pyrolysis considering secondary charring reactions. Energy Conversion and Management, 2014. 87: p. 687-696.

218. Yildiz, G., et al., Validation of a new set-up for continuous catalytic fast pyrolysis of biomass coupled with vapour phase upgrading. Journal of Analytical and Applied Pyrolysis, 2013. 103: p. 343-351.

219. Weng, J., et al., Pyrolysis study of poplar biomass by tunable synchrotron vacuum ultraviolet photoionization mass spectrometry. Proceedings of the Combustion Institute, 2013. 34(2): p. 2347-2354.

220. Mikkelsen, D., et al., Interactions of arabinoxylan and (1, 3)(1, 4)-β-glucan with cellulose networks. Biomacromolecules, 2015. 16(4): p. 1232-1239.

221. Trendewicz, A., et al., Evaluating the effect of potassium on cellulose pyrolysis reaction kinetics. Biomass and Bioenergy, 2015. 74: p. 15-25.

222. Fahmi, R., et al., The effect of alkali metals on combustion and pyrolysis of Lolium and Festuca grasses, switchgrass and willow. Fuel, 2007. 86(10-11): p. 1560-1569.

223. Ronsse, F., et al., Secondary reactions of levoglucosan and char in the fast pyrolysis of cellulose. Environmental Progress & Sustainable Energy, 2012. 31(2): p. 256-260.

224. Stefanidis, S.D., et al., Optimization of bio-oil yields by demineralization of low quality biomass. Biomass and Bioenergy, 2015. 83: p. 105-115.

225. Banks, S., D. Nowakowski, and A. Bridgwater, Fast pyrolysis processing of surfactant washed Miscanthus. Fuel Processing Technology, 2014. 128: p. 94-103.

226. Banks, S.W., D.J. Nowakowski, and A.V. Bridgwater, Impact of potassium and phosphorus in biomass on the properties of fast pyrolysis bio-oil. Energy & Fuels, 2016. 30(10): p. 8009-8018.

227. Patwardhan, P.R., et al., Influence of inorganic salts on the primary pyrolysis products of cellulose. Bioresource technology, 2010. 101(12): p. 4646-4655.

228. Müller-Hagedorn, M., et al., A comparative kinetic study on the pyrolysis of three different wood species. Journal of analytical and Applied Pyrolysis, 2003. 68: p. 231-249.

229. Eom, I.-Y., et al., Effect of essential inorganic metals on primary thermal degradation of lignocellulosic biomass. Bioresource technology, 2012. 104: p. 687-694.

230. Gargiulo, V., et al., Influence of possible interactions between biomass organic components and alkali metal ions on steam assisted pyrolysis: a case study on Arundodonax. Journal of Analytical and Applied Pyrolysis, 2015. 112: p. 244-252.

231. Patwardhan, P.R., R.C. Brown, and B.H. Shanks, Understanding the fast pyrolysis of lignin. ChemSusChem, 2011. 4(11): p. 1629-1636.

232. Zhou, X., et al., Fast pyrolysis of glucose-based carbohydrates with added NaCl part 1: Experiments and development of a mechanistic model. AIChE Journal, 2016. 62(3): p. 766-777.

233. Zhou, X., et al., Fast pyrolysis of glucose-based carbohydrates with added NaCl part 2: Validation and evaluation of the mechanistic model. AIChE Journal, 2016. 62(3): p. 778-791.

234. Zhu, C., et al., Alkaline-Earth-Metal-Catalyzed Thin-Film Pyrolysis of Cellulose. ChemCatChem, 2016. 8(4): p. 818-829.

235. Zhang, L. and S.-C. Kong, Multicomponent vaporization modeling of bio-oil and its mixtures with other fuels. Fuel, 2012. 95: p. 471-480.

236. Oasmaa, A., et al., Controlling the phase stability of biomass fast pyrolysis bio-oils. Energy & Fuels, 2015. 29(7): p. 4373-4381.

237. Shuping, Z., et al., Pyrolysis characteristics and kinetics of the marine microalgae Dunaliella tertiolecta using thermogravimetric analyzer. Bioresource Technology, 2010. 101(1): p. 359-365.

238. Debiagi, P.E.A., et al., Detailed kinetic mechanism of gas-phase reactions of volatiles released from biomass pyrolysis. Biomass and Bioenergy, 2016. 93: p. 60-71.

239. Raheem, A., et al., Thermogravimetric study of Chlorella vulgaris for syngas production. Algal Research, 2015. 12: p. 52-59.

240. Kamińska, A. and A. Sionkowska, The effect of UV radiation on the values of thermal parameters of collagen containing β-carotene. Polymer degradation and stability, 1999. 65(1): p. 87-90.

241. Barreto, P., A. Pires, and V. Soldi, Thermal degradation of edible films based on milk proteins and gelatin in inert atmosphere. Polymer Degradation and Stability, 2003. 79(1): p. 147-152.

242. Purevsuren, B., et al., Estimation of the molecular mass range of the tar from pyrolysis of casein by gas chromatographymass spectrometry, probe mass spectrometry and size-exclusion chromatography with 1-methyl-2-pyrrolidinone as eluent. European Journal of Mass Spectrometry, 2004. 10(1): p. 101-108.

243. Purevsuren, B. and Y. Davaajav, Thermal analysis of casein. Journal of Thermal Analysis and Calorimetry, 2001. 65(1): p. 147-152.

244. Wanjun, T., W. Cunxin, and C. Donghua, An investigation of the pyrolysis kinetics of some aliphatic amino acids. Journal of analytical and applied pyrolysis, 2006. 75(1): p. 49-53.

245. Smith, W.T., T.B. Harris, and J.M. Patterson, Pyrolysis of soybean protein and an amino acid mixture having the same amino acid composition. Journal of Agricultural and Food Chemistry, 1974. 22(3): p. 480-483.

246. Hansson, K.-M., et al., Formation of HNCO, HCN, and NH 3 from the pyrolysis of bark and nitrogen-containing model compounds. Combustion and Flame, 2004. 137(3): p. 265-277.

247. Shen, L. and K.S. Alexander, A thermal analysis study of long chain fatty acids. Thermochimica acta, 1999. 340: p. 271-278.

248. Vyazovkin, S., J.S. Clawson, and C.A. Wight, Thermal dissociation kinetics of solid and liquid ammonium nitrate. Chemistry of materials, 2001. 13(3): p. 960-966.

249. Yang, H., et al., In-depth investigation of biomass pyrolysis based on three major components: hemicellulose, cellulose and lignin. Energy & Fuels, 2006. 20(1): p. 388-393.

250. Gai, C., et al., Thermogravimetric and kinetic analysis of thermal decomposition characteristics of low-lipid microalgae. Bioresource technology, 2013. 150: p. 139-148.

251. Rizzo, A.M., et al., Characterization of microalga Chlorella as a fuel and its thermogravimetric behavior. Applied energy, 2013. 102: p. 24-31.

252. Vo, T.K., et al., Kinetics study of the hydrothermal liquefaction of the microalga Aurantiochytrium sp. KRS101. Chemical Engineering Journal, 2016. 306: p. 763-771.

253. Vo, T.K., et al., Pyrolysis characteristics and kinetics of microalgal Aurantiochytrium sp. KRS101. Energy, 2017. 118: p. 369-376.

254. Carstensen, H.-H. and A.M. Dean, Development of detailed kinetic models for the thermal conversion of biomass via first principle methods and rate estimation rules. Computational Modeling in Lignocellulosic Biofuel Production, 2010: p. 201-243.

255. Bridgwater, A.V., Renewable fuels and chemicals by thermal processing of biomass. Chemical Engineering Journal, 2003. 91(2): p. 87-102.

256. Di Blasi, C., Modeling chemical and physical processes of wood and biomass pyrolysis. Progress in Energy and Combustion Science, 2008. 34(1): p. 47-90.

257. Di Blasi, C., Combustion and gasification rates of lignocellulosic chars. Progress in energy and combustion science, 2009. 35(2): p. 121-140.

258. Calonaci, M., et al., Comprehensive kinetic modeling study of bio-oil formation from fast pyrolysis of biomass. Energy & Fuels, 2010. 24(10): p. 5727-5734.

259. Kan, T., V. Strezov, and T.J. Evans, Lignocellulosic biomass pyrolysis: A review of product properties and effects of pyrolysis parameters. Renewable and Sustainable Energy Reviews, 2016. 57: p. 1126-1140.

260. Isahak, W.N.R.W., et al., A review on bio-oil production from biomass by using pyrolysis method. Renewable and Sustainable Energy Reviews, 2012. 16(8): p. 5910-5923.

261. Xiu, S. and A. Shahbazi, Bio-oil production and upgrading research: A review. Renewable and Sustainable Energy Reviews, 2012. 16(7): p. 4406-4414.

262. Mahadevan, R., et al., Physical and chemical properties and accelerated aging test of bio-oil produced from in situ catalytic pyrolysis in a bench-scale fluidized-bed reactor. Energy & Fuels, 2015. 29(2): p. 841-848.

263. Wagenaar, B., et al., Rotating Cone Bio-Oil Production and Applications. Progress in thermochemical biomass conversion, 2001: p. 1268-1280.

264. Lindfors, C., et al., Fractionation of bio-oil. Energy & Fuels, 2014. 28(9): p. 5785-5791.

265. Tzanetakis, T., et al., Spray combustion characteristics and gaseous emissions of a wood derived fast pyrolysis liquid-ethanol blend in a pilot stabilized swirl burner. Energy & Fuels, 2010. 24(10): p. 5331-5348.

266. Ringer, M., V. Putsche, and J. Scahill, Large-scale pyrolysis oil production: a technology assessment and economic analysis. 2006, National Renewable Energy Laboratory (NREL), Golden, CO.

267. Pecha, B., P. Arauzo, and M. Garcia-Perez, Impact of combined acid washing and acid impregnation on the pyrolysis of Douglas fir wood. Journal of Analytical and Applied Pyrolysis, 2015. 114: p. 127-137.

268. Ruddy, D.A., et al., Recent advances in heterogeneous catalysts for bio-oil upgrading via “ex situ catalytic fast pyrolysis”: catalyst development through the study of model compounds. Green Chemistry, 2014. 16(2): p. 454-490.

269. Czernik, S. and A. Bridgwater, Overview of applications of biomass fast pyrolysis oil. Energy & fuels, 2004. 18(2): p. 590-598.

270. Mortensen, P.M., et al., A review of catalytic upgrading of bio-oil to engine fuels. Applied Catalysis A: General, 2011. 407(1-2): p. 1-19.

271. Tzanetakis, T., et al., Spray combustion and particulate matter emissions of a wood derived fast pyrolysis liquid-ethanol blend in a pilot stabilized swirl burner. Energy & Fuels, 2011. 25(4): p. 1405-1422.

272. Lee, H.W., et al., Catalytic conversion of Laminaria japonica over microporous zeolites. Energy, 2014. 66: p. 2-6.

273. Widayatno, W.B., et al., Upgrading of bio-oil from biomass pyrolysis over Cu-modified β-zeolite catalyst with high selectivity and stability. Applied Catalysis B: Environmental, 2016. 186: p. 166-172.

274. Marsman, J., et al., Identification of components in fast pyrolysis oil and upgraded products by comprehensive two-dimensional gas chromatography and flame ionisation detection. Journal of Chromatography A, 2007. 1150(1-2): p. 21-27.

275. Patel, M. and A. Kumar, Production of renewable diesel through the hydroprocessing of lignocellulosic biomass-derived bio-oil: A review. Renewable and Sustainable Energy Reviews, 2016. 58: p. 1293-1307.

276. Luo, Y., et al., Upgrading of syngas hydrotreated fractionated oxidized bio-oil to transportation grade hydrocarbons. Energy Conversion and Management, 2016. 115: p. 159-166.

277. Oasmaa, A. and S. Czernik, Fuel oil quality of biomass pyrolysis oils state of the art for the end users. Energy & Fuels, 1999. 13(4): p. 914-921.

278. Venderbosch, R., et al., Stabilization of biomass-derived pyrolysis oils. Journal of Chemical Technology and Biotechnology, 2010. 85(5): p. 674-686.

279. Venderbosch, R. and W. Prins, Fast pyrolysis technology development. Biofuels, bioproducts and biorefining, 2010. 4(2): p. 178-208.

280. Kim, J.-S., Production, separation and applications of phenolic-rich bio-oil–a review. Bioresource technology, 2015. 178: p. 90-98.

281. Toraman, H.E., et al., Potential of genetically engineered hybrid poplar for pyrolytic production of bio-based phenolic compounds. Bioresource technology, 2016. 207: p. 229-236.

282. Lehto, J., et al., Review of fuel oil quality and combustion of fast pyrolysis bio-oils from lignocellulosic biomass. Applied Energy, 2014. 116: p. 178-190.

283. Oasmaa, A., et al., Fast pyrolysis bio-oils from wood and agricultural residues. Energy & Fuels, 2009. 24(2): p. 1380-1388.

284. Djokic, M.R., et al., Quantitative analysis of crude and stabilized bio-oils by comprehensive two-dimensional gas-chromatography. Journal of Chromatography A, 2012. 1257: p. 131-140.

285. Bertero, M., G. de la Puente, and U. Sedran, Fuels from bio-oils: Bio-oil production from different residual sources, characterization and thermal conditioning. Fuel, 2012. 95: p. 263-271.

286. Cheng, T., et al., Molecular composition of oxygenated compounds in fast pyrolysis bio-oil and its supercritical fluid extracts. Fuel, 2016. 172: p. 49-57.

287. Oasmaa, A., M. Kytö, and K. Sipilä, Pyrolysis oil combustion tests in an industrial boiler. Progress in thermochemical biomass conversion, 2001: p. 1468-1481.

288. Czernik, S., D.K. Johnson, and S. Black, Stability of wood fast pyrolysis oil. Biomass and Bioenergy, 1994. 7(1-6): p. 187-192.

289. Diebold, J.P., A review of the chemical and physical mechanisms of the storage stability of fast pyrolysis bio-oils. 1999, National Renewable Energy Lab., Golden, CO (US).

290. Diebold, J.P. and S. Czernik, Additives to lower and stabilize the viscosity of pyrolysis oils during storage. Energy & Fuels, 1997. 11(5): p. 1081-1091.

291. Ranzi, E., et al., Hierarchical and comparative kinetic modeling of laminar flame speeds of hydrocarbon and oxygenated fuels. Progress in Energy and Combustion Science, 2012. 38(4): p. 468-501.

292. Krumdieck, S. and J. Daily, Evaluating the feasibility of biomass pyrolysis oil for spray combustion applications. Combustion science and technology, 1998. 134(1-6): p. 351-365.

293. Stamatov, V., D. Honnery, and J. Soria, Combustion properties of slow pyrolysis bio-oil produced from indigenous Australian species. Renewable Energy, 2006. 31(13): p. 2108-2121.

294. Kytö, M., P. Martin, and S. Gust, Development of combustors for pyrolysis liquids. Pyrolysis and gasification of biomass and waste, 2003: p. 187-190.

295. Dente, M., et al., New improvements in modeling kinetic schemes for hydrocarbons pyrolysis reactors. Chemical engineering science, 1992. 47(9): p. 2629-2634.

296. Dente, M., E. Ranzi, and A. Goossens, Detailed prediction of olefin yields from hydrocarbon pyrolysis through a fundamental simulation model (SPYRO). Computers & Chemical Engineering, 1979. 3(1): p. 61-75.

297. Ranzi, E., et al., Prediction of kinetic parameters for hydrogen abstraction reactions. Combustion science and technology, 1993. 95(1-6): p. 1-50.

298. Pelucchi, M., et al., Relative Reactivity of Oxygenated Fuels: Alcohols, Aldehydes, Ketones, and Methyl Esters. Energy & Fuels, 2016. 30(10): p. 8665-8679.

299. Frassoldati, A., et al., An experimental and kinetic modeling study of n-propanol and iso-propanol combustion. Combustion and Flame, 2010. 157(1): p. 2-16.

300. Grana, R., et al., An experimental and kinetic modeling study of combustion of isomers of butanol. Combustion and Flame, 2010. 157(11): p. 2137-2154.

301. Frassoldati, A., et al., Detailed kinetic modeling of the combustion of the four butanol isomers in premixed low-pressure flames. Combustion and Flame, 2012. 159(7): p. 2295-2311.

302. Sarathy, S.M., et al., Alcohol combustion chemistry. Progress in Energy and Combustion Science, 2014. 44: p. 40-102.

303. Hemings, E.B., et al., A detailed kinetic study of pyrolysis and oxidation of glycerol (propane-1, 2, 3-triol). Combustion Science and Technology, 2012. 184(7-8): p. 1164-1178.

304. Kawasaki, K. and K. Yamane. A309 Thermal Decomposition of Waste Glycerol (Fuel). in The Proceedings of the International Conference on Power Engineering (ICOPE) 2009.3. 2009. The Japan Society of Mechanical Engineers.

305. Fukutome, A., H. Kawamoto, and S. Saka, Gas-Phase Reactions of Glyceraldehyde and 1, 3-Dihydroxyacetone as Models for Levoglucosan Conversion during Biomass Gasification. ChemSusChem, 2016. 9(7): p. 703-712.

306. Shin, E.-J., M.R. Nimlos, and R.J. Evans, Kinetic analysis of the gas-phase pyrolysis of carbohydrates. Fuel, 2001. 80(12): p. 1697-1709.

307. Ranzi, E., et al., Kinetic modeling of polyethylene and polypropylene thermal degradation. Journal of Analytical and Applied Pyrolysis, 1997. 40: p. 305-319.

308. Kawamoto, H., M. Murayama, and S. Saka, Pyrolysis behavior of levoglucosan as an intermediate in cellulose pyrolysis: polymerization into polysaccharide as a key reaction to carbonized product formation. Journal of Wood Science, 2003. 49(5): p. 469-473.

309. Fukutome, A., H. Kawamoto, and S. Saka, Processes forming Gas, Tar, and Coke in Cellulose Gasification from Gas-Phase Reactions of Levoglucosan as Intermediate. ChemSusChem, 2015. 8(13): p. 2240-2249.

310. Organ, P.P. and J.C. Mackie, Kinetics of pyrolysis of furan. Journal of the Chemical Society, Faraday Transactions, 1991. 87(6): p. 815-823.

311. Sendt, K., G.B. Bacskay, and J.C. Mackie, Pyrolysis of furan: Ab initio quantum chemical and kinetic modeling studies. The Journal of Physical Chemistry A, 2000. 104(9): p. 1861-1875.

312. Wei, L., et al., Shock-tube experiments and kinetic modeling of 2-methylfuran ignition at elevated pressure. Energy & Fuels, 2013. 27(12): p. 7809-7816.

313. Liu, D., et al., Combustion chemistry and flame structure of furan group biofuels using molecular-beam mass spectrometry and gas chromatography–Part I: Furan. Combustion and flame, 2014. 161(3): p. 748-765.

314. Somers, K.P., et al., The pyrolysis of 2-methylfuran: a quantum chemical, statistical rate theory and kinetic modelling study. Physical Chemistry Chemical Physics, 2014. 16(11): p. 5349-5367.

315. Brezinsky, K., M. Pecullan, and I. Glassman, Pyrolysis and oxidation of phenol. The Journal of Physical Chemistry A, 1998. 102(44): p. 8614-8619.

316. Pecullan, M., K. Brezinsky, and I. Glassman, Pyrolysis and oxidation of anisole near 1000 K. The Journal of Physical Chemistry A, 1997. 101(18): p. 3305-3316.

317. Hemings, E.B., et al., Detailed kinetics of the pyrolysis and oxidation of anisole. Chem. Eng. Trans., 2011. 24: p. 61-66.

318. Nowakowska, M., et al., Detailed kinetic study of anisole pyrolysis and oxidation to understand tar formation during biomass combustion and gasification. Combustion and Flame, 2014. 161(6): p. 1474-1488.

319. Saggese, C., et al., A wide range kinetic modeling study of pyrolysis and oxidation of benzene. Combustion and Flame, 2013. 160(7): p. 1168-1190.

320. Kotake, T., H. Kawamoto, and S. Saka, Pyrolytic formation of monomers from hardwood lignin as studied from the reactivities of the primary products. Journal of Analytical and Applied Pyrolysis, 2015. 113: p. 57-64.

321. Norinaga, K., et al., A mechanistic study on the reaction pathways leading to benzene and naphthalene in cellulose vapor phase cracking. Biomass and Bioenergy, 2014. 69: p. 144-154.

322. Frenklach, M. and H. Wang. Detailed modeling of soot particle nucleation and growth. in Symposium (International) on Combustion. 1991. Elsevier.

323. D'Alessio, A., et al. Precursor formation and soot inception in premixed ethylene flames. in Symposium (International) on Combustion. 1992. Elsevier.

324. Glassman, I. Soot formation in combustion processes. in Symposium (international) on combustion. 1989. Elsevier.

325. Haynes, B.S. and H.G. Wagner, Soot formation. Progress in energy and combustion science, 1981. 7(4): p. 229-273.

326. Neoh, K., J. Howard, and A. Sarofim, Soot oxidation in flames, in Particulate Carbon. 1981, Springer. p. 261-282.

327. Djokic, M.R., et al., An experimental and kinetic modeling study of cyclopentadiene pyrolysis: First growth of polycyclic aromatic hydrocarbons. Combustion and Flame, 2014. 161(11): p. 2739-2751.

328. Saggese, C., et al., Kinetic modeling of particle size distribution of soot in a premixed burner-stabilized stagnation ethylene flame. Combustion and Flame, 2015. 162(9): p. 3356-3369.

329. Saggese, C., et al., Kinetic modeling study of polycyclic aromatic hydrocarbons and soot formation in acetylene pyrolysis. Energy & Fuels, 2014. 28(2): p. 1489-1501.

330. Mante, O.D., S.P. Babu, and T.E. Amidon, A comprehensive study on relating cell-wall components of lignocellulosic biomass to oxygenated species formed during pyrolysis. Journal of Analytical and Applied Pyrolysis, 2014. 108: p. 56-67.

331. Aguado, R., et al., Pyrolysis of sawdust in a conical spouted bed reactor. Yields and product composition. Industrial & Engineering Chemistry Research, 2000. 39(6): p. 1925-1933.

332. Olazar, M., et al., Pyrolysis of sawdust in a conical spouted-bed reactor with a HZSM-5 catalyst. AIChE Journal, 2000. 46(5): p. 1025-1033.

333. Westerhof, R.J., et al., Effect of temperature in fluidized bed fast pyrolysis of biomass: oil quality assessment in test units. Industrial & Engineering Chemistry Research, 2009. 49(3): p. 1160-1168.

334. Zhao, C., E. Jiang, and A. Chen, Volatile production from pyrolysis of cellulose, hemicellulose and lignin. Journal of the Energy Institute, 2017. 90(6): p. 902-913.

335. Wang, S., et al., Pyrolysis mechanism study of minimally damaged hemicellulose polymers isolated from agricultural waste straw samples. Bioresource technology, 2015. 190: p. 211-218.

336. Wang, S., et al., Pyrolysis behaviors of four O-acetyl-preserved hemicelluloses isolated from hardwoods and softwoods. Fuel, 2015. 150: p. 243-251.

337. Frassoldati, A., et al., Reduced kinetic mechanisms of diesel fuel surrogate for engine CFD simulations. Combustion and Flame, 2015. 162(10): p. 3991-4007.

338. Ranzi, E., et al., Reduced kinetic schemes of complex reaction systems: fossil and biomass-derived transportation fuels. International Journal of Chemical Kinetics, 2014. 46(9): p. 512-542.

339. Stagni, A., et al., Lumping and reduction of detailed kinetic schemes: an effective coupling. Industrial & Engineering Chemistry Research, 2013. 53(22): p. 9004-9016.

340. Demirbas, A., Effects of temperature and particle size on bio-char yield from pyrolysis of agricultural residues. Journal of analytical and applied pyrolysis, 2004. 72(2): p. 243-248.

341. Ranzi, E., P.E.A. Debiagi, and A. Frassoldati, Mathematical Modeling of Fast Biomass Pyrolysis and Bio-Oil Formation. Note II: Secondary Gas-Phase Reactions and Bio-Oil Formation. ACS Sustainable Chemistry & Engineering, 2017. 5(4): p. 2882-2896.

342. Senneca, O. and P. Salatino, A semi-detailed kinetic model of char combustion with consideration of thermal annealing. Proceedings of the Combustion Institute, 2011. 33(2): p. 1763-1770.

343. Russell, N., et al., Coal char thermal deactivation under pulverized fuel combustion conditions. Energy & fuels, 2000. 14(4): p. 883-888.

344. Maffei, T., Kinetic model of coal combustion. 2013, Politecnico di Milano.

345. Neves, D., et al., Characterization and prediction of biomass pyrolysis products. Progress in Energy and Combustion Science, 2011. 37(5): p. 611-630.

346. Guizani, C., et al., New insights on the structural evolution of biomass char upon pyrolysis as revealed by the Raman spectroscopy and elemental analysis. Carbon, 2017. 119: p. 519-521.

347. Bach, Q.-V., et al., Predictions of biochar yield and elemental composition during torrefaction of forest residues. Bioresource Technology, 2016. 215: p. 239-246.

348. Bonelli, P.R., Slow pyrolysis of nutshells: characterization of derived chars and of process kinetics. Energy Sources, 2003. 25(8): p. 767-778.

349. Horne, P.A. and P.T. Williams, Influence of temperature on the products from the flash pyrolysis of biomass. Fuel, 1996. 75(9): p. 1051-1059.

350. Morin, M., et al., Pyrolysis of biomass in a batch fluidized bed reactor: Effect of the pyrolysis conditions and the nature of the biomass on the physicochemical properties and the reactivity of char. Journal of Analytical and Applied Pyrolysis, 2016. 122: p. 511-523.

351. Lee, J., K.-H. Kim, and E.E. Kwon, Biochar as a catalyst. Renewable and Sustainable Energy Reviews, 2017. 77: p. 70-79.

352. Jia, L., et al., On-line analysis of primary tars from biomass pyrolysis by single photoionization mass spectrometry: Experiments and detailed modelling. Chemical Engineering Journal, 2017. 313: p. 270-282.

353. Haynes, B.S., A turnover model for carbon reactivity I. development. Combustion and flame, 2001. 126(1-2): p. 1421-1432.

354. Feng, B. and S.K. Bhatia, On the validity of thermogravimetric determination of carbon gasification kinetics. Chemical Engineering Science, 2002. 57(15): p. 2907-2920.

355. Darmstadt, H. and C. Roy, Surface spectroscopic study of basic sites on carbon blacks. Carbon, 2003. 41(13): p. 2662-2665.

356. Campbell, P. and R. Mitchell, The impact of the distributions of surface oxides and their migration on characterization of the heterogeneous carbon–oxygen reaction. Combustion and Flame, 2008. 154(1-2): p. 47-66.

357. Angın, D., Effect of pyrolysis temperature and heating rate on biochar obtained from pyrolysis of safflower seed press cake. Bioresource technology, 2013. 128: p. 593-597.

358. Bonelli, P., et al., Effect of pyrolysis temperature on composition, surface properties and thermal degradation rates of Brazil Nut shells. Bioresource Technology, 2001. 76(1): p. 15-22.

359. Cetin, E., R. Gupta, and B. Moghtaderi, Effect of pyrolysis pressure and heating rate on radiata pine char structure and apparent gasification reactivity. Fuel, 2005. 84(10): p. 1328-1334.

360. Chen, Y., et al., Biomass-based pyrolytic polygeneration system on cotton stalk pyrolysis: influence of temperature. Bioresource technology, 2012. 107: p. 411-418.

361. Fu, P., et al., Study on the gas evolution and char structural change during pyrolysis of cotton stalk. Journal of analytical and applied pyrolysis, 2012. 97: p. 130-136.

362. Fu, P., et al., Effect of temperature on gas composition and char structural features of pyrolyzed agricultural residues. Bioresource Technology, 2011. 102(17): p. 8211-8219.

363. Guerrero, M., et al., Pyrolysis of eucalyptus at different heating rates: studies of char characterization and oxidative reactivity. Journal of Analytical and Applied Pyrolysis, 2005. 74(1-2): p. 307-314.

364. Kim, K.H., et al., Influence of pyrolysis temperature on physicochemical properties of biochar obtained from the fast pyrolysis of pitch pine (Pinus rigida). Bioresource technology, 2012. 118: p. 158-162.

365. Tushar, M.S.H.K., et al., Production, characterization and reactivity studies of chars produced by the isothermal pyrolysis of flax straw. Biomass and bioenergy, 2012. 37: p. 97-105.

366. Zeng, K., et al., The effect of temperature and heating rate on char properties obtained from solar pyrolysis of beech wood. Bioresource technology, 2015. 182: p. 114-119.

367. Raveendran, K. and A. Ganesh, Adsorption characteristics and pore-development of biomass-pyrolysis char. Fuel, 1998. 77(7): p. 769-781.

368. Mohanty, P., et al., Evaluation of the physiochemical development of biochars obtained from pyrolysis of wheat straw, timothy grass and pinewood: effects of heating rate. Journal of analytical and applied pyrolysis, 2013. 104: p. 485-493.

369. Ronsse, F., et al., Production and characterization of slow pyrolysis biochar: influence of feedstock type and pyrolysis conditions. Gcb Bioenergy, 2013. 5(2): p. 104-115.

370. Kloss, S., et al., Characterization of slow pyrolysis biochars: effects of feedstocks and pyrolysis temperature on biochar properties. Journal of environmental quality, 2012. 41(4): p. 990-1000.

371. Onay, O., Influence of pyrolysis temperature and heating rate on the production of bio-oil and char from safflower seed by pyrolysis, using a well-swept fixed-bed reactor. Fuel Processing Technology, 2007. 88(5): p. 523-531.

372. Guerrero, M., et al., Characterization of biomass chars formed under different devolatilization conditions: differences between rice husk and eucalyptus. Energy & Fuels, 2008. 22(2): p. 1275-1284.

373. Sharma, R.K., et al., Characterization of chars from pyrolysis of lignin. Fuel, 2004. 83(11-12): p. 1469-1482.

374. Frenklach, M., Reaction mechanism of soot formation in flames. Physical chemistry chemical Physics, 2002. 4(11): p. 2028-2037.

375. Palmer, H.B. and C.F. Cullis, The formation of carbon from gases. Chemistry and physics of carbon, 1965. 1: p. 265-325.

376. Kroto, H., et al., C60: buckminsterfullerene. Nature, v. 318, p. 162-163. 1985.

377. Zhang, Q.-L., et al., Reactivity of large carbon clusters: spheroidal carbon shells and their possible relevance to the formation and morphology of soot. The Journal of Physical Chemistry, 1986. 90(4): p. 525-528.

378. Frenklach, M. and L.B. Ebert, Comment on the proposed role of spheroidal carbon clusters in soot formation. The Journal of Physical Chemistry, 1988. 92(2): p. 561-563.

379. Singh, R.I., A.M. Mebel, and M. Frenklach, Oxidation of graphene-edge six-and five-member rings by molecular oxygen. The Journal of Physical Chemistry A, 2015. 119(28): p. 7528-7547.

380. Zhao-Bin Ding, E.d.M., Matteo Pelucchi, Tiziano Faravelli, Matteo Maestri, First-principles assessment of the analogy between gas phase and gas-solid H-abstraction reactions at graphene edges. Chemical Engineering Journal, 2018(under review).

381. Pelucchi, M., et al., Detailed kinetics of substituted phenolic species in pyrolysis bio-oils. Energy & Environmental Science, 2018. (Submited).

382. Branca, C. and C. Di Blasi, Oxidation characteristics of chars generated from wood impregnated with (NH4) 2HPO4 and (NH4) 2SO4. Thermochimica Acta, 2007. 456(2): p. 120-127.

383. Di Blasi, C., C. Branca, and A. Galgano, Flame retarding of wood by impregnation with boric acid–pyrolysis products and char oxidation rates. Polymer degradation and stability, 2007. 92(5): p. 752-764.

384. Branca, C., A. Iannace, and C. Di Blasi, Devolatilization and Combustion Kinetics of Quercus cerris Bark. Energy & fuels, 2007. 21(2): p. 1078-1084.